# Degassing behavior and eruptive dynamics in rhyolitic melts: Geochemical, textural and numerical analyses of hybrid eruptions

Dissertation

zur Erlangung des Akademischen Grades
“Doktor der Naturwissenschaften”
im Promotionsfach Geologie/Paläontologie

am Fachbereich für Chemie, Pharmazie, Geographie und Geowissenschaften
der Johannes Gutenberg-Universität, Mainz

**Sebastian Carl Walter**

geb. in Frankenthal (Pfalz)

Mainz, 2026

1. Gutachter: **Prof. Dr. Jonathan M. Castro (JGU Mainz)**
2. Gutachter: **Dr. Christoph Helo (JGU Mainz)**

Tag der mündlichen Prüfung: 11.05.2026

# Abstract

Degassing, the exsolution of volatiles—with water being the predominant component—from magma into a co-existing vapor phase, is a crucial mechanism, controlling behavior and evolution of volcanic eruptions. Accordingly, water concentrations and hydrogen isotopic signatures (expressed as δD) are frequently applied to trace degassing histories to detect the progress of eruptions. Specifically silicic melts can produce highly explosive eruptions, venting vast quantities of gas, ash, and pyroclastic material, with profound impacts on the ecosystem, environment and life. This thesis particularly focuses on studying the degassing behavior of rhyolitic melts and investigates pre-historic eruptions at Big Glass Mountain (BGM), California, USA, and three eruptions at Lipari, Sicily, Italy. Through field studies, texture and geochemical analyses, and degassing modeling, this thesis provides new insights into eruption dynamics. Moreover, the boron isotope system was explored as a potential additional degassing tracer.

A vital outcome of this work is the development of “VolcDeGas”, a user-friendly program which is designed to iteratively model degassing systems for the hydrogen and boron isotopic systems, which also enables best-fit modeling for natural data. The accuracy of the program was confirmed by verification against data and models of previous studies. Results reveal that batched-degassing models most accurately reproduce observed eruption trends. This batched-system can mimic both closed- and open-degassing system behaviors by varying the step size during degassing. It is also linked to hybrid activity—characterized by simultaneous explosive and effusive phases—a pattern which was recently observed in eruptions such as Chaitén (2008) and Cordón Caulle (2011) in Chile. A batched system with gradually decreasing step sizes explains explosive impulses and their declining intensities, and both are linked to the successive dominance of effusive activity over the course of the hybrid sequence. These findings furthermore support the recently proposed “cryptic fragmentation” hypothesis in which fragmentation and subsequent sintering of clastic material in tuffisites or conduits could initiate batched degassing conditions fostering hybrid eruption behavior.

Field studies, textural analyses, $H_2O$ and hydrogen isotopic measurements at BGM and Lipari reveal evidence for hybrid activity. Both sites reveal that a batched-system with variable step size represents the degassing history best, and both exhibit textures indicative of tuffisites and sintering processes. Additionally, deposits show similarities to the hybrid deposits of Chaitén and Cordón Caulle. At Lipari, the δD-$H_2O$ degassing histories of all three eruptions establish a singular coherent trend, and their textures and eruption chronology exhibit strong similarities, indicating a co-eruption. Moreover, two outlier samples with elevated deuterium concentrations were identified at Lipari. While the dataset is limited, these anomalies may be the result of

regassing that could enrich the sample in deuterium, possibly occurring during the hybrid activity.

Boron isotopic signatures and concentrations were measured in BGM samples and compared to their corresponding δD and $H_2O$ contents. Furthermore, theoretical models were generated by “VolcDeGas” and best-fitted to published boron data. The goal was to assess whether the boron isotopic system can serve as a tracer for degassing. Comparisons between the boron and hydrogen system in the same BGM samples showed that, while the hydrogen system tracks an apparent degassing history, boron data appears scattered and random. While theoretically feasible, the fractionation and partitioning effects associated with boron during degassing appear to be inhibited by slow diffusion rates, making them too subtle to be detected in natural systems as they are concealed by other geochemical processes. Consequently, boron can be employed as a tracer for such processes without the need to account for degassing variations.

The discoveries of this thesis provide significant insights into degassing mechanisms and eruption dynamics. By linking field observations, geochemical analyses, and modeling, this work establishes guidelines for identifying hybrid eruptions in pre-historic volcanoes. The VolcDeGas program introduces a robust tool for future studies, enabling rapid and precise modeling of degassing histories. Furthermore, these findings raise important questions about processes such as cryptic fragmentation, regassing, and hybrid eruption mechanisms, which all demand further investigations. They also contribute to improved hazard assessments and more effective volcanic risk management.

# Zusammenfassung

Entgasung, die Entmischung von flüchtigen Bestandteilen—mit Wasser als Hauptkomponente—aus der Magma heraus in eine koexistierende Gasphase, ist ein entscheidender Mechanismus, der Verhalten und Entwicklung von Vulkanausbrüchen steuert. Folglich werden Wasserkonzentrationen und Wasserstoffisotopensignaturen (dargestellt durch δD) häufig genutzt, um Entgasungsgeschichten nachzuverfolgen und den Verlauf von Ausbrüchen zu erfassen. Insbesondere silikatische Schmelzen können hoch explosive Eruptionen erzeugen, bei denen große Mengen an Gas, Asche und pyroklastischem Material freigesetzt werden, was beträchtliche Auswirkungen auf Ökosysteme, Umwelt und Lebewesen hat. Diese Dissertation konzentriert sich insbesondere auf die Untersuchung des Entgasungsverhaltens von rhyolithischen Schmelzen und analysiert dazu die prähistorischen Eruptionen von Big Glass Mountain (BGM) in Kalifornien, USA, sowie drei Eruptionen auf Lipari, in Sizilien, Italien. Mithilfe von Feldstudien, Textur und geochemischen Analysen sowie Entgasungsmodellierungen liefert diese Arbeit neue Erkenntnisse zu den Eruptionsdynamiken. Darüber hinaus wurde das Borisotopensystem als möglicher zusätzlicher Entgasungstracer untersucht.

Ein wesentliches Ergebnis dieser Arbeit ist die Entwicklung von „VolcDeGas“, einem benutzerfreundlichen Programm, das zur iterativen Modellierung von Entgasungssystemen für die Wasserstoff- und Borisotopensysteme konzipiert wurde, welches auch Bestpassungsmodellierung auf Basis von Daten aus natürlichen Systemen ermöglicht. Die Genauigkeit des Programms wurde durch den Vergleich mit Daten und Modellen früherer Studien verifiziert. Die Ergebnisse zeigen, dass „Batched“-Entgasungsmodelle die aufgezeigten Eruptionstrends am besten reproduzieren können. Dieses „Batched“-System kann durch Variationen in den Schrittgrößen während des Entgasungsprozesses sowohl geschlossenes als auch offenes Entgasungssystemverhalten nachahmen. Es steht auch in Verbindung mit hybrider Aktivität, die durch das gleichzeitige Auftreten von explosiven und effusiven Phasen gekennzeichnet ist—ein Muster, welches jüngst bei den Eruptionen von Chaitén (2008) und Cordón Caulle (2011) in Chile beobachtet wurde. Ein „Batched“-System mit stetig abnehmenden Schrittgrößen erklärt explosive Impulse und deren abnehmende Intensität, die beide über den Verlauf der hybriden Sequenz mit einer zunehmenden Dominanz effusiver Aktivität verbunden sind. Diese Ergebnisse stützen zudem die kürzlich formulierte Hypothese der „kryptischen Fragmentierung“, wonach die Fragmentierung und anschließende Sinterung von klastischem Material in Tuffisite oder Vulkanschlote, „Batched“-Entgasungsbedingungen erzeugen könnte, die hybride Eruptionsverhalten fördern.

Feldstudien, Texturanalysen und Messungen von $H_2O$ und Wasserstoffisotopen an Proben der Eruptionszentren BGM und Lipari liefern Hinweise auf hybride Aktivität. Beide Standorte offenbaren, dass ein „Batched“-System mit variabler Schrittgröße die Entgasungsgeschichte am besten darstellt, und beide zeigen auch Texturen, die auf Sinterungsprozesse und Tuffisite hinweisen. Darüber hinaus weisen die Ablagerungen Ähnlichkeiten mit den Hybridablagerungen von Chaitén und Cordón Caulle auf. Auf Lipari bilden die $\delta D$-$H_2O$-Entgasungsgeschichten aller drei Eruptionen einen singulären kohärenten Trend ab und ihre Texturen sowie ihre Eruptionschronologien weisen starke Ähnlichkeiten auf, was auf eine Ko-Eruption hinweist. Zudem wurden auf Lipari zwei anomale Proben mit erhöhten Deuteriumkonzentrationen identifiziert. Obwohl der Datensatz begrenzt ist, könnten diese Anomalien auf Rückbegasung zurückzuführen sein, die die Proben mit Deuterium anreichern könnte, und möglicherweise während der hybriden Aktivität auftrat.

Borisotopensignaturen und -Konzentrationen wurden in BGM-Proben gemessen und mit den entsprechenden $\delta D$- und $H_2O$-Gehalten verglichen. Darüber hinaus wurden theoretische Modelle mit „VolcDeGas“ erstellt und an veröffentlichte Bordaten angepasst. Ziel war es zu untersuchen, ob das Borisotopensystem als Tracer für Entgasungsprozesse geeignet ist. Ein Vergleich zwischen dem Bor- und dem Wasserstoffisotopensystem an denselben BGM-Proben zeigt, dass das Wasserstoffisotopensystem eine klare Entgasungsgeschichte abbildet, während die Bor-Daten verstreut und zufällig erscheinen. Obwohl theoretisch möglich, scheint die Fraktionierung und Partitionierung von Bor während der Entgasung durch langsame Diffusionsraten gehemmt zu sein, wodurch die Effekte zu subtil sind, um in natürlichen Systemen nachgewiesen zu werden, da sie von anderen geochemischen Prozessen überlagert werden. Folglich kann Bor als Tracer für solche Prozesse verwendet werden, ohne dass die Auswirkungen der Entgasung berücksichtigt werden müssten.

Die Ergebnisse dieser Arbeit liefern wichtige Einblicke in Entgasungsmechanismen und Eruptionsdynamiken. Durch die Kombination aus Feldbeobachtungen, geochemischen Analysen und Modellierungen etabliert diese Arbeit Richtlinien zur Identifizierung hybrider Eruptionen in prähistorischen Vulkanen. Das VolcDeGas-Programm stellt ein robustes Werkzeug für zukünftige Studien dar, da es eine schnelle und präzise Modellierung von Entgasungsgeschichten ermöglicht. Zudem werfen die gewonnenen Erkenntnisse Fragen zu Prozessen wie kryptischer Fragmentierung, Rückbegasung und hybriden Eruptionsmechanismen auf, die weitere Untersuchungen erfordern. Sie tragen somit auch zur Verbesserung der Gefährdungsbewertung und zu einem effektiveren Risikomanagement von Vulkanen bei.

# Preamble

Several parts of the content of this thesis have already been published or are currently under review in peer-reviewed scientific journals. The references of those are listed below:

Walter, S., Castro, J., 2020. VolcDeGas: A program for modelling hydrogen isotope fractionation during degassing of rhyolitic melts. Volcanica 3 (1), 155–168, doi: 10.30909/vol.03.01.155168

Castro, J., Walter, S.C., 2021. Hybrid rhyolitic eruption at Big Glass Mountain, CA, USA. Volcanica 4 (2), 257–277, doi: 10.30909/vol.04.02.257277

Walter, S.C., Castro, J., Bindeman, I.N. Hydrous geochemical evolution of the Lipari rhyolites during multi-vent, hybrid volcanic activity. Under review at Bulletin of Volcanology.

# Table of contents

**Abstract**……III
**Zusammenfassung** ……V
**Preamble**……VII
**Table of contents**……IX
**List of tables**……XV
**List of figures**……XVII

**Chapter 1 – Introduction**……23
**1.1 Early studies on eruptions**……24
**1.2 Degassing and hydrogen isotopic signature**……25
1.2.1 Introduction into degassing simulations……32
**1.3 Hybrid eruptions** ……33
1.3.1 Dynamics of batched degassing……36
**1.4 Cryptic fragmentation model** ……37
**1.5 Rehydration**……38
1.5.1 Rehydration prevention……39
**1.6 Boron isotopic system overview**……40

**Chapter 2 – Background**……43
**2.1 Degassing modeling**……43
2.1.1 Closed-system degassing ……43
2.1.2 Open-system degassing……45
2.1.3 Batched-system degassing……46
2.1.4 Buffered-system degassing……48
2.1.5 Alpha-factor and water speciation……49
**2.2 Boron system information**……51
2.2.1 Boron degassing theory……53
2.2.2 Boron degassing modeling ……56
**2.3 Numerical modeling** ……56

**Chapter 3 – Thesis outline**……59
**3.1 Thesis aims**……59
**3.2 Chapters outline**……59
**3.3 Authors contributions** ……61

**3.4 Software.....62**

**Chapter 4 – Analytical techniques.....65**
**4.1 FTIR spectroscopy.....65**
**4.2 Isotope-ratio mass spectrometry.....68**
4.2.1 TCEA-MS .....68
4.2.2 SIMS.....69

**Chapter 5 – VolcDeGas: A program for modeling hydrogen isotope fractionation during degassing of rhyolitic melts.....73**
**Abstract.....73**
**5.1 Introduction .....74**
5.1.1 Natural context: rhyolitic volcanism.....74
5.1.2 $H_2O$ speciation in rhyolitic melts.....76
5.1.3 Observations of rhyolitic eruptions.....77
5.1.4 Modeling theory and degassing path calculations.....77
*5.1.4.1 Closed-system degassing.....78*
*5.1.4.2 Open-system degassing .....79*
*5.1.4.3 Batched-system degassing.....79*
*5.1.4.4 $\alpha_{v-m}$ factor and speciation of $H_2O$ in rhyolitic melts.....80*
**5.2 Results.....83**
5.2.1 Program functionality and verification.....83
*5.2.1.1 Relation between bulk $H_2O$ and alpha factors.....84*
*5.2.1.2 Modeling pyroclastic $H_2O$-δD patterns in the Mono Craters 1340 C.E. eruption.....86*
*5.2.1.3 Modeling pyroclastic $H_2O$-δD patterns in the Chaitén 2008 eruption.....86*
**5.3 Discussion.....90**
**5.4 Summary and conclusions.....93**
**5.5 Acknowledgements.....93**
**5.6 Author contributions.....93**
**5.7 Data availability.....93**
**5.8 Software requirements .....94**
**5.9 Size of components.....94**
**5.10 Copyright notice.....94**

**Chapter 6 – Hybrid rhyolitic eruption at Big Glass Mountain, CA, USA.....97**
**Abstract.....97**
**6.1 Introduction.....98**

**6.2 Background.....99**
**6.3 Samples and analytical methods.....104**
6.3.1 Sample collection.....104
6.3.2 Analytical techniques .....105
6.3.3 Modeling volcanic degassing trends.....108
**6.4 Results.....110**
6.4.1 Field evidence for hybrid volcanism at BGM: key insights from recently active rhyolite volcanoes.....110
*6.4.1.1 Ballistic bomb fields.....111*
*6.4.1.2 Pyroclastic ridges.....111*
*6.4.1.3 Pyroclastic air-fall lava mantles.....113*
6.4.2 Hydrous geochemical signature of degassing: $H_2O$-δD measurements.....117
6.4.3 Modeling BGM degassing with VolcDeGas.....118
**6.5 Discussion.....121**
6.5.1 Physical evidence for simultaneous pyroclastic and effusive activity at Big Glass Mountain .....121
6.5.2 Degassing during pyroclastic and effusive activity: the H-isotopic record.....122
6.5.3 Divining eruptive activity from hydrous geochemical trends and field relations.....126
**6.6 Conclusions.....126**
**6.7 Acknowledgements.....127**
**6.8 Author contributions.....127**
**6.9 Data availability.....127**
**6.10 Copyright notice.....127**

**Chapter 7 – Hydrous geochemical evolution of the Lipari rhyolites during multi-vent, hybrid volcanic activity.....131**
**Abstract.....131**
**7.1 Introduction.....132**
**7.2 Background.....133**
**7.3 Geological Setting.....136**
**7.4 Samples and analytical methods.....138**
7.4.1 Sample collection.....138
*7.4.1.1 Forgia Vecchia sample site characteristics.....139*
*7.4.1.2 Lami sample site characteristics.....139*
*7.4.1.3 Rocche Rosse sample site characteristics.....140*
7.4.2 Analytical techniques .....140
7.4.3 Modeling degassing paths.....143

**7.5 Results……144**
7.5.1 Textural evidence ……144
7.5.2 FTIR measurements and results……148
7.5.3 TCEA/MS measurements ……151
7.5.4 Degassing modeling results……153
**7.6 Discussion……157**
7.6.1 Evidence for co-eruptive vents and hybrid rhyolitic volcanism on Lipari ……157
**7.7 Conclusion……161**
**7.8 Acknowledgements……161**
**7.9 Supplementary Material ……161**
**7.10 Author contributions ……162**

**Chapter 8 – Boron as a tracer for rhyolitic degassing……165**
**8.1 Preface……165**
**8.2 Introduction……165**
**8.3 Samples and analytical methods……166**
**8.4 Modeling boron degassing trends with VolcDeGas……167**
**8.5 Results……168**
8.5.1 Re-analysis of published boron data from Long Valley……169
8.5.2 Results of Big Glass Mountain boron measurements……172
8.5.3 Theoretical degassing models based on natural parameter……175
**8.6 Discussion……176**
8.6.1 Long Valley data re-evaluation……177
8.6.2 Big Glass Mountain boron data and correlation to hydrogen isotopes……178
8.6.3 Constraints on boron degassing: from theory to natural systems……179
**8.7 Conclusion……181**
**8.8 Manual (boron)……182**
8.8.1 Code overview……182
8.8.2 Usage instructions and input……183

**Chapter 9 – Conclusions and outlook……187**
**9.1 Numerical approach to degassing systems……187**
9.1.1 Implications ……189
**9.2 Hybrid eruptions, cryptic fragmentation and regassing……189**
9.2.1 Implications ……190
**9.3 Co-eruptivity of Lipari, Sicily……191**
9.3.1 Implications ……191

**9.4 Boron isotopic system ……..192**
9.4.1 Implications ……..192
**9.5 Future scientific questions……...193**

**References..……..197**
**Appendix: Supplementary Material of Chapter 7……213**
**Acknowledgements ……219**

# List of tables

**Table 6.1:** δD and bulk $H_2O$ content of obsidians from Big Glass Mountain, CA, USA…….107

**Table 7.1:** δD, bulk water content and water speciation of pyroclastic and effusive obsidians from the Lipari eruptions, Silicy, Italy……...149

**Table 8.1:** Boron concentration and $\delta^{11}B$ measurements obtained via SIMS for Big Glass Mountain obsidian samples……..173

# List of figures

**Figure 1.1:** Plot illustrating δD and $H_2O$ measurements in obsidian shards from the 1340 CE Mono Crater eruption……..…30

**Figure 1.2:** Plot of δD (in ‰) versus $H_2O$ (in wt.%), illustrating a closed-to-open system degassing trajectory, computed employing the VolcDeGas program……...30

**Figure 1.3:** Schematic representation of an ideal closed-degassing system……..31

**Figure 1.4:** Schematic illustration of an open-degassing system…….……32

**Figure 1.5:** Macroscopic image of a bomb from Rocche Rosse presenting tuffisite veins..…34

**Figure 1.6:** Schematic representation of the sintering process in rhyolitic melts……35

**Figure 2.1:** Graph portraying an idealized closed-degassing system model (δD in ‰ vs. $H_2O$ in wt.%), generated utilizing the VolcDeGas program…….44

**Figure 2.2:** Plot of δD (in ‰) versus $H_2O$ (in wt.%) of an idealized open-degassing system model, computed with the VolcDeGas program……...46

**Figure 2.3:** Graph presenting an idealized batched-degassing system (δD in ‰ vs. $H_2O$ in wt.%), simulated with the VolcDeGas program utilizing a 0.5 wt.% step size……..47

**Figure 5.1:** Qualitative trends of hydrogen isotope fractionation occurring during different degassing modes……..76

**Figure 5.2:** Comparison of estimates of alpha factor plotted against bulk $H_2O$ content (in wt.%) for the C.E. 1340 Mono Craters eruption……..85

**Figure 5.3:** δD vs. bulk $H_2O$ content (wt.%) for the C.E. 1340 Mono Crater eruption, comparing best-fit VolcDeGas simulations with published literature models..……..……..……....85

**Figure 5.4:** Plots displaying natural hydrous speciation data in obsidians (wt.% OH and $H_2O$) and calculated alpha factors from the Chaitén eruption (2008)…….87

**Figure 5.5:** Graphs displaying VolcDeGas models having fixed 0.001 wt.% and 0.5 wt.% $H_2O$ degassing steps in an open and batched system……88

**Figure 5.6:** Modeled, best-fit, single staged batched-system trend with variable step size for the 2008 Chaitén eruption products…..…….89

**Figure 5.7:** Two-stage, closed-to-batched system model fits to Chaitén pyroclastic obsidian and lava δD-$H_2O$ data……..90

**Figure 6.1:** Satellite image of the Big Glass Mountain (BGM) complex, northern California and picture of tephra outcrop where pyroclastic samples were collected……..……..……101

**Figure 6.2:** Satellite image of Big Glass Mountain and photographs presenting the texture of the breccia zones and deposits.....……..……..……114

**Figure 6.3:** Field photographs showing typical lava flow top morphology and texture on Big Glass Mountain, and some rare cases of pyroclastic mantle deposits on top lava flow....…...115

**Figure 6.4:** Optical light photomicrographs of breccia material sampled from the BGM lava flow……...116

**Figure 6.5:** δD–$H_2O$ (bulk) compositions of BGM and Chaitén rhyolites.……...119

**Figure 6.6:** Best-fit VolcDeGas degassing simulations of measured δD-$H_2O$ data from pyroclastic and effusive obsidians from Big Glass Mountain……120

**Figure 6.7:** Schematic showing possible eruptive events leading to the formation of juxtaposed explosive and effusive deposits at Big Glass Mountain……123

**Figure 7.1:** Satellite image of the northeastern part of Lipari, Silicia, showing sampling locations……..……133

**Figure 7.2:** Images of optical light microscope micrographs of FTIR samples and a hand sample photograph from the Lami eruption……..……..……147

**Figure 7.3:** Optical light microscope pictures of the Rocche Rosse FTIR samples and macroscopic image of a hand sample……..……147

**Figure 7.4:** Optical light micrographs of double-polished FTIR obsidian shards from the Forgia Vecchia eruption……..148

**Figure 7.5:** Figure exhibiting a qualitative 2-D FTIR map of sample FV-1a1 and a microscope image with an overlay graph of FTIR water contents measured along a transect……150

**Figure 7.6:** Graphs depicting water speciation data extrapolations and calculated alpha factors of the Lipari eruptions ……151

**Figure 7.7:** Plots of δD vs. water content (FTIR), δD vs. water content (TCEA), and FTIR vs. TCEA water contents for Lipari glass samples……..……153

**Figure 7.8:** Diagrams presenting δD versus $H_2O$ graphs of best-fit degassing calculations performed by the VolcDeGas program on Lipari samples……156

**Figure 7.9:** Schemata illustrating various stages of hybrid rhyolitic eruptions……..159

**Figure 8.1:** Photographic images of the two mounts incorporating the SIMS-measured Big Glass Mountain samples……..……166

**Figure 8.2:** Plots presenting $\delta^{11}B$ (‰) and boron concentration (ppm) data of Schmitt and Simon (2004) for individual eruptions at Long Valley……170

**Figure 8.3:** Best-fit VolcDeGas simulation on literature data from South Deadman Creek….171

**Figure 8.4:** Graph of $\delta^{11}B$ (‰) vs. boron concentration (ppm) for Big Glass Mountain obsidian samples..……174

**Figure 8.5:** Plot exhibiting boron concentration (ppm) versus water content (wt.%) for Big Glass Mountain samples……..174

**Figure 8.6:** Graph depicting $\delta^{11}B$ (‰) versus δD (‰) for Big Glass Mountain samples…..….175

**Figure 8.7:** Modeled graph portraying $\delta^{11}B$ (‰) versus boron concentration (ppm), revealing the maximum possible isotopic fractionation of boron during degassing in rhyolitic melts…..176

**Figure S1:** Photographs of tephra outcrops from the Forgia Vecchia, Lami, and Rocche Rosse eruptions ……..214

**Figure S2:** Figure presenting additional modeled degassing graphs of Rocche Rosse, Lami and Forgia Vecchia eruptions depicting δD versus $H_2O$ relations……...215

# Chapter 1
# Introduction

Silicic volcanic eruptions have played a critical role in shaping Earth`s environment and surface and embody one of the most significant natural threats to the ecosystem and life. These eruptions can create lethal conditions through the generation of pyroclastic flows, ballistic bombs, ash and lava. While pyroclastic flows—comprising hot ash, gas and coarser volcanic fragments—and lava flows can cause localized destruction, suspended ash can have more widespread and long-lasting effects. This ash can affect atmospheric conditions over a vast regions, covering the surface, diminishing sunlight, reducing air quality, threatening aviation (Black et al., 2016; Forte and Castro, 2019). Ash fall also impacts farming communities (Forte et al., 2018), which in turn complicates the efforts to develop long-term hazard assessments for areas far from silicic volcanoes. Although very large eruptions (>100 $km^3$) can have immense global effects, they are rare in Earth's history compared to medium-to-large sized eruptions (<1 $km^3$), which occur more frequently (every few years) and remain highly active (Alfano et al., 2011; Chiodini et al., 2016). Consequently, due to the potential massive impacts of rhyolitic eruptions, their study remains an area of vigorous ongoing research (e.g., Giachetti et al., 2020; Hudak et al., 2021; Pistolesi et al., 2021).

This thesis investigates the dynamics of medium-to-large (VEI 4-5) rhyolitic eruptions, as these are the most likely to pose an imminent threat to humanity and ecosystems. The primary aim is to study the behavior, progression, and timing of these eruptions. To elucidate these aspects, this thesis concentrates on the degassing processes by employing geochemical tracers (e.g., hydrogen and boron isotopes) measured in deposits, and by parallel iterative computations of theoretical degassing systems that serve as a framework for comparison between natural and theoretical data trends. Additionally, field relationships, textures, and structural features were analyzed, and the concentration and isotopic composition of water were measured in deposits and samples from the pre-historic eruptions of Big Glass Mountain (California) and Rocche Rosse, Forgia Vecchia, and Lami (Lipari, Sicily). These data were then compared to those from documented hybrid eruptions to spot potential similarities in their eruption processes. The numerous findings from this research could enhance the general understanding of rhyolitic eruptions and contribute to better hazards awareness in high silica volcanic systems.

## 1.1 Early studies on eruptions

Initial field studies on Holocene rhyolites (e.g., Heiken, 1978; Eichelberger and Westrich, 1981; Taylor et al., 1983; Newman et al., 1988) observed that tephra deposits from pyroclastic fall material were regularly covered by lava flows. The absence of tephra atop these flows suggested that a sequence exists with explosive pyroclastic material being initially deposited, before the effusive lava flow was emplaced to become perched atop the tephra. This lead to the hypothesis that these systems followed an “explosive-to-effusive” sequence in which the lavas emerge after the explosive phase ceased (e.g., Taylor et al., 1983; Miller, 1985; Newman et al., 1988). Thus, it was established that rhyolitic eruptions are initiated by an energetic explosive phase yielding pyroclastic products including bombs, lapilli, ash, and pyroclastic density currents before shifting into a less powerful effusive phase distinguished by extensive lava flows.

The trigger of eruption activity and the transition between eruptive styles were elucidated by Eichelberger (1975), who proposed that eruptions are initiated by magma injection and early pyroclastic venting with subsequent late-stage effusion of compositional mixed lavas. Such injections rapidly superheat the resident magma, inducing convection dynamics that facilitate extensive magma mixing (Sparks et al., 1977). These processes are regularly accompanied by elevated seismic activity, such as earthquakes. Several major volcanic eruptions have been linked to the magma injection process. Prominent examples include the eruptions of Vesuvius in 79 CE (Cioni et al., 1995), Big Glass Mountain in 1060 CE (Eichelberger, 1975; Donnelly-Nolan et al., 2016), Krakatau in 1883 (Self, 1992), and Eyjafjallajökull in 2010 (Sigmundsson et al., 2010).

Another significant factor was revealed by Eichelberger and Westrich (1981) on their study of the Medicine Lake Volcano complex (CA). They discovered that pyroclastic materials contained higher water contents (up to 1 wt.%), whereas lavas were nearly dry (~0.1 wt.% $H_2O$). These findings indicated that magma was stratified in its $H_2O$ content and the water acted as a driving force for explosive rhyolitic eruptions at Medicine Lake (Eichelberger and Westrich, 1981). Consequently, magma degasses (segregation of water from melt) over the course of the eruption whereas the explosive phase produces water-rich material while the effusive phase yields drier products. Later research postulated that the transition in eruptive styles depends on how efficiently magma could degas during its ascent which itself is a complicate trade-of between permeability and magma vesicularity (Eichelberger et al., 1986).

## 1.2 Degassing and hydrogen isotopic signature

Magmatic volatiles substantially affect the chemical and physical properties of magma and play a crucial role in numerous processes occurring within it. This section outlines the key volatile components, their behavior, their effects on magma, and, in particular their role in degassing. Volatiles are defined as “chemical species, which is in a gaseous or supercritical fluid phase at temperatures over 300 or 400 °C” (Holloway, 1981). A supercritical fluid is a substance above its critical temperature and pressure, where it exhibits properties of both liquid and gas.

The analyses of volatile contents in magmatic systems are routinely performed on eruptive products such as lava, obsidian, ash, and pumice by techniques like Fourier-Transform-Infrared-Spectroscopy (FTIR; Chapter 4.1) and Secondary Ion Mass Spectrometry (SIMS; Chapter 4.2.2). The primary magmatic volatiles dissolved in melts are carbon dioxide ($CO_2$) and water ($H_2O$), both of which can be present at concentrations of several weight percent (wt.%) in magmas (e.g., Eichelberger and Westrich, 1981; Holloway, 1981; Newman et al., 1988; Taylor, 1991; Blank et al., 1993; Carroll and Holloway, 1994; Sparks et al., 1994; Rust et al., 2004; Burgisser and Degruyter, 2015; Edmonds and Wallace, 2017; Giachetti et al., 2020). Notably $CO_2$ can also occur at concentrations in the lower parts-per-million (ppm) range, particularly in rhyolitic melts (e.g., Newman et al., 1988; Taylor, 1991; Blank et al., 1993; Carroll and Holloway, 1994; Rust et al., 2004). Due to its lower solubility, $CO_2$ exsolves at higher pressure and therefore at greater depths than $H_2O$, which dominates the vapor phase at shallower crustal levels (Blank et al., 1993; e.g., Edmonds and Wallace, 2017). The third most abundant volatile, sulfur, exists in the melt as the dissolved ions $S^{2-}$ and $SO_4^{2-}$, and occurs in lower concentrations (hundreds of ppm; e.g., Scaillet et al., 1998) than $H_2O$ and $CO_2$. Despite its lower abundance, sulfur strongly partitions into the vapor phase, then forming a mix of $SO_2$ and $H_2S$ (Edmonds and Wallace, 2017). This can lead to elevated sulfur concentrations in the eruptive plume during explosive activity (Scaillet et al., 1998; Edmonds and Wallace, 2017). Other volatiles, typically available in trace amounts (ppm) include halogens such as fluorine, chlorine, bromine, and iodine (Burgisser and Degruyter, 2015; Edmonds and Wallace, 2017), as well as boron (e.g., Schmitt and Simon, 2004; Wunder et al., 2005; see also Chapters 1.6 and 2.2).

Silicic melts can contain between 0 and 20 wt.% volatiles (Holloway, 1981), with water being the predominant one (Eichelberger et al., 1986; Allard et al., 1991; Blank et al., 1993; Burgisser and Degruyter, 2015; Ryan et al., 2015). In these melts, $H_2O$ concentrations commonly range from ~0.1 wt.% to several wt.% (e.g., Eichelberger et al., 1986; Newman et al., 1988; Taylor, 1991; Sparks et al., 1994; Castro et al., 2014; Forte and Castro, 2019; Giachetti et al., 2020),

and typically up to about 3 to 4 wt.%. The water originates from the magma storage region (Luhr, 2001; Castro and Dingwell, 2009; Castro et al., 2014), and it is a crucial factor controlling whether an eruption “blows or flows” (Dingwell, 1996); i.e., if it is explosive or effusive. Consequently, water is the primary driver of degassing within the magmatic system.

Degassing refers to the exsolution and transport of dissolved volatiles (e.g., $H_2O$) from the melt into a distinct volatile phase. Degassing is triggered by two mechanisms (e.g., Cashman, 1988; Anderson and Fink, 1989), decompression and/or crystallization (also termed “second boiling). The degree to which these mechanisms drive volatile exsolution is controlled by the solubility behavior of volatiles, especially $H_2O$. Only a limited amount of water can stay dissolved in the melt at a given pressure, temperature, and melt composition (e.g., Sparks, 1978; Silver et al., 1990; Zhang, 1999; Liu et al., 2005; Ryan et al., 2015). When this solubility limit is exceeded—either through the addition of water to the melt, or by reducing the solubility threshold—$H_2O$ exsolves from the melt.

Decompression-induced degassing is initiated by magma ascending in the conduit. The associated drop in pressure is accompanied by a reduced solubility of volatiles in the melt, prompting strong water exsolution (e.g., Sparks, 1978; Blank et al., 1993; Sparks et al., 1994; Zhang, 1999; Liu et al., 2005; Ryan et al., 2015). Because “water solubility in $H_2O$-saturated melts increases as the square root of pressure” (Sparks et al., 1994), even small pressure changes during ascent can lead to significant water release from the melt. In contrast, crystallization-driven degassing occurs during cooling and crystallization (second boiling) of minerals at depths under high-temperature and high-pressure conditions which produce large amounts of volatiles (e.g., $H_2O$, $CO_2$). Volatiles can be incompatible with the structure of certain minerals; that is, they are elements with an unsuitable size and/or charge preventing their incorporation into the mineral lattice, causing them to separate from minerals and being enriched in the melt. For water in particular, the crystallization of anhydrous minerals (e.g., olivine, pyroxene and garnet) results in oversaturation of the melt with water (Anderson and Fink, 1989). After the solubility limit of water in the melt is exceeded, water exsolves out of the melt.

Once degassing occurs, the exsolved water is transported through the melt via advection and diffusion, processes which frequently influence each other (e.g., Richter et al., 1998; Zhang and Gan, 2022). Advection describes the transport of chemical components (e.g., volatiles) and heat by a moving mass (e.g., melt), driven by heat, pressure or density differences. Diffusion, by contrast, portrays the arbitrary motions of particles and entities—such as hydrogen or water—through various media like glasses, melts, gases or fluids. In melts and

magmas diffusion is due to thermally excited random motion of atoms, ions, and clusters (Zhang, 1999; Zhang and Cherniak, 2010; Zhang and Gan, 2022). Additionally, the presence of a chemical potential gradient of the species of interest within the medium can also prompt diffusion (e.g., Zhang, 1999; Zhang and Cherniak, 2010). In such cases, the chemical species (e.g., $H_2O$) diffuses along the concentration gradient, moving from areas of higher to domains of lower concentrations.

Both transport mechanisms are significantly affected by melt viscosity, which can influence the efficiency of mass transfer within the melt (e.g., Dingwell, 1998; Giordano et al., 2004), and therefore also the speed of degassing. A high viscous melt provides more resistance to flow, thereby hindering the movement of material, subsequently inhibiting both diffusion and advection. Therefore, volatiles may not effectively migrate into the bubbles, reducing overall degassing efficiency and speed (Dingwell, 1996; Dingwell, 1998). Viscosity itself is influenced by a complex interplay of factors, such as temperature, pressure, and especially by the composition of the melt. For example, silicic-rich melts are generally more viscous than basaltic ones due to the polymerization (molecules forming chains) of silicates within the melt which increases the resistance to flow (e.g., Giordano et al., 2008; Hobiger et al., 2011; Romine and Whittington, 2015). Another crucial factor is water which depolymerizes the melt by breaking up the silicate chains. Thus, when water is lost from the melt, viscosity increases (Dingwell, 1996; e.g., Dingwell et al., 1996; Gardner et al., 2000).

The water exsolved via both degassing processes migrates through the melt by the two transport mechanisms, where it eventually accumulates into bubbles. This accumulation initiates widespread bubble nucleation and growth throughout the magma, forming the volatile phase. The size of these bubbles and their inner pressure is dependent on the diffusion rates of water in the melt, and melt's viscosity (e.g., Sparks, 1978; Gardner et al., 2000; Gonnermann, 2015). Specifically, high-viscosity melts exhibit lower diffusion rates and provide more resistance to bubble expansion, resulting in increased internal pressure within the bubbles (Sparks, 1978; Gardner et al., 2000).

As bubbles grow and accumulate in the magma, they may contribute to an increase in overpressure within the magma chamber and a decrease in density of the vesiculating magma rising in the conduit (Cashman, 1988). This, in turn, facilitates a buoyancy effect in which the magma may ascent (Eichelberger et al., 1986; Cashman, 1988; Anderson and Fink, 1989; Allard et al., 1991; Blank et al., 1993; Gonnermann and Manga, 2007; Gonnermann, 2015; Ryan et al., 2015). During ascent through the conduit, the magma experiences continuous decompression causing bubbles to become increasingly numerous and larger. Subjected to

factors such as magma porosity, permeability and magma ascent dynamics the magma may culminate in a violent fragmentation (e.g., Dingwell, 1996; Gonnermann and Manga, 2003, 2007).

Fragmentation refers to the process by which a continuous volume of molten rock breaks apart into individual pieces (fragments), creating pyroclastic debris mixed with gas (e.g., Alidibirov and Dingwell, 1996; Dingwell, 1996; Dingwell, 1998; Gonnermann and Manga, 2003, 2007; Gonnermann, 2015). This can occur when magma undergoes rapid decompression, inducing stress via a shockwave or “unloading wave” that propagates through the melt (Alidibirov and Dingwell, 1996; Gonnermann, 2015). If the tensile strength of the surrounding melt is exceeded, the bubbles rupture (Gonnermann and Manga, 2007), releasing their compressed gas content. This release amplifies the shockwave, fostering crack formation and the acceleration of melt fragments to the surface, which may ultimately result in explosive eruptions (Alidibirov and Dingwell, 1996; Dingwell, 1996; Dingwell, 1998; Gonnermann, 2015).

Effective outgassing, however, can mitigate the potential for violent fragmentation. If the bubbles interconnect to form a continuous vesicular network, a condition referred to as “permeable flow” (Eichelberger et al., 1986), overpressure can be reduced due to the increased porosity and permeability of the system. In such a case, the melt contains sufficient connected pore spaces to allow volatiles to efficiently escape from the system. These volatiles may escape via fracture and cracks in the conduit walls or directly through the magma column (e.g., Eichelberger et al., 1986; Anderson and Fink, 1989; Jaupart and Allègre, 1991; Gonnermann and Manga, 2003). The resulting decrease in internal overpressure reduces the likelihood of explosive fragmentation (e.g., Taylor et al., 1983; Eichelberger et al., 1986; Gonnermann and Manga, 2007; Gonnermann, 2015).

Research conducted on the mechanisms and processes described in this section reinforced the concept of a two-stage system with the eruption transitioning from explosive to effusive activity. It was postulated that after the explosive bursts caused by violent fragmentation, bubbly magma becomes highly permeable by the vesicles interconnecting, the ascent and shearing rates wane and magma overpressure declines during ascent (Jaupart and Allègre, 1991; Woods and Koyaguchi, 1994; Gonnermann and Manga, 2003, 2007). This in turn leads to effective and rapid gas-melt separation resulting in a finally dry magma capable of quiescent eruption (Eichelberger et al., 1986).

In addition to the water contents in eruptive products, hydrogen isotopic signatures have been extensively employed to trace degassing patterns and to elucidate the degassing mechanisms

responsible for gas release. This approach was applied in studies of past Holocene eruptions such as Inyo Domes, Mono Craters and Medicine, CA (e.g., Taylor et al., 1983; Newman et al., 1988; Dobson et al., 1989; Rust et al., 2004; Castro et al., 2014; Giachetti et al., 2020).

The hydrogen isotopic system contains three natural occurring isotopes—tritium ($^3$H—only found in trace amounts in nature), deuterium ($^2$H, with ~0.02% natural abundance) and protium (commonly referred to as hydrogen; $^1$H, with ~99.98% natural abundance). Because deuterium is the second most abundant stable isotope, and has twice the mass of hydrogen, the deuterium/hydrogen (D/H) ratio can be readily measured using mass spectrometry. The isotope content is commonly expressed as δD, being the D/H ratio normalized to the Standard Mean Ocean Water (SMOW) or the more modern Vienna Standard Mean Ocean Water (V-SMOW) standard, and demarcated as:

$$\delta D = \frac{\left(\frac{^2H}{^1H}\right)_{Sample} - \left(\frac{^2H}{^1H}\right)_{Standard}}{\left(\frac{^2H}{^1H}\right)_{Standard}} \times 1000\ ‰ \quad (1)$$

with $^2$H as deuterium, $^1$H as hydrogen and δD in ‰.

By plotting the hydrogen isotopic and water data on a δD vs. $H_2O$ graph, a degassing history can be tracked. For example, an important study conducted by Newman et al. (1988) measured H-isotopic compositions and water contents of Mono Craters' (1340 CE) pyroclastic and effusive obsidians, offering a model example for degassing related characteristics employing this tracer. Their work detected a distinctive pattern (Figure 1.1) whereby at higher water contents (e.g., >1 wt.%), δD showed minimal depletion from the initial value of -52 ‰ at ~2.6 wt.% $H_2O$. However, as water content decreases, δD values declined exponentially reaching as low as -123 ‰ together with low water contents of ~0.1 wt.% in lava samples. Such general trends have been widely recognized and confirmed by numerous past and recent studies on various rhyolitic eruptions (e.g., Taylor et al., 1983; Dobson et al., 1989; Rust et al., 2004; Castro et al., 2014; Giachetti et al., 2020; Hudak et al., 2021).

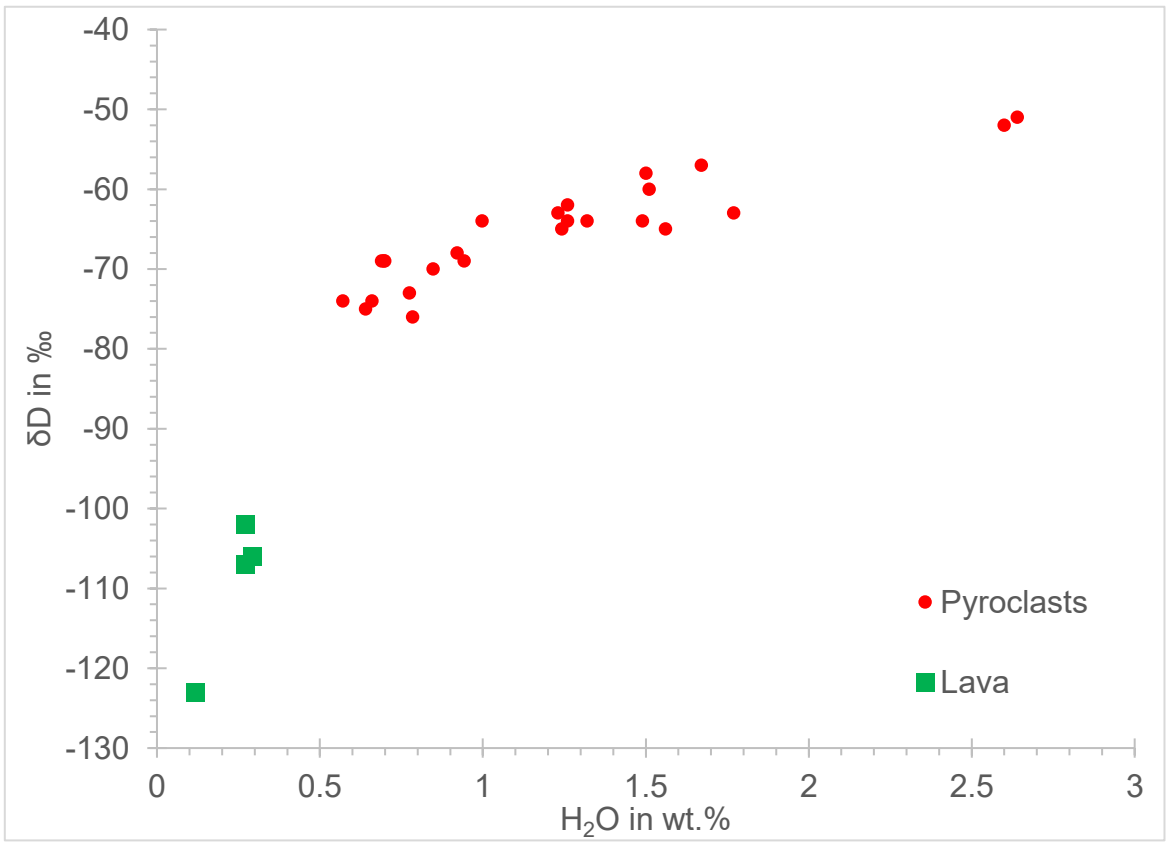


**Figure 1.1:** Plot illustrating δD and $H_2O$ measurements in obsidian shards from the 1340 CE Mono Crater eruption, based on Newman et al. (1988) data. Red dots represent pyroclastic samples, while green squares designate lava samples.

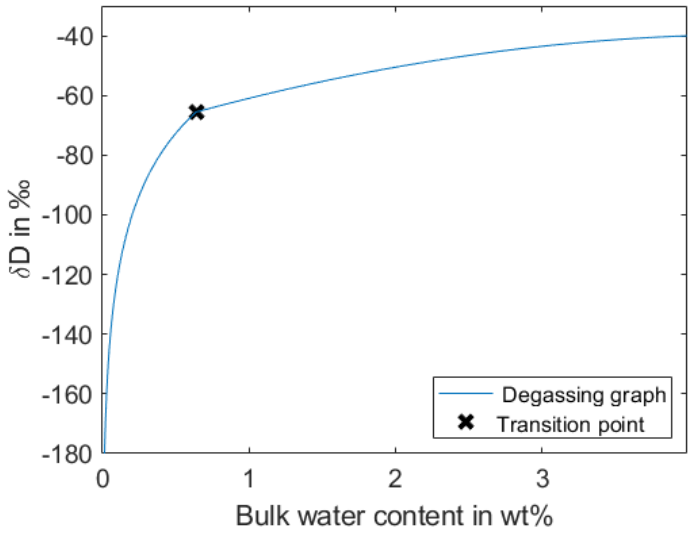


**Figure 1.2:** Plot of δD (in ‰) versus $H_2O$ (in wt.%), illustrating a closed-to-open system degassing trajectory, computed employing the VolcDeGas program (Chapter 5). Trends exemplified by water values above the transition point represent the closed system, while those below correspond to the open system. This idealized model initially follows a closed-system degassing path, characterized by a slight depletion of δD, until reaching a transition point (indicated by the black cross), where the system shifts to an open degassing regime. In the open system phase, deuterium depletion increases significantly, especially at lower water contents.

These geochemical patterns solidified the then-emerging concept of two distinct degassing regimes for the explosive and effusive phase, corresponding to closed and open chemical systems (Figure 1.2), respectively (e.g., Eichelberger et al., 1986; Newman et al., 1988; Dobson et al., 1989; Taylor, 1991). In the closed system, the melt and exsolved volatiles stay in contact and interact with each other, causing limited isotopic fractionation and depletion of δD (Figure 1.2). By contrast, the open system is characterized by efficient and instant volatile removable from the melt (Taylor et al., 1983; Eichelberger et al., 1986), resulting in greater fractionation and significant δD depletion (e.g., Newman et al., 1988; Dobson et al., 1989; Rust et al., 2004; Giachetti et al., 2020; Figure 1.2). The following two paragraphs summarize the behavior, mechanisms, and processes that distinguish closed and open degassing systems.

In a chemical closed system, equilibrium conditions emerge as hydrous magma remain intermingled with its exsolved volatiles (Figure 1.3) during rapid ascent in the conduit while increasing and expanding its bubbly state (Sparks, 1978). This process potentially triggers the fragmentation of the melt which leads to catastrophic gas expansion and release causing explosive events (e.g., Alidibirov and Dingwell, 1996; Dingwell, 1996; Gonnermann and Manga, 2003; Rust et al., 2004; Gonnermann and Manga, 2007). This explosive eruption phase ejects pyroclastic material with relatively high water contents (e.g., ~1 wt.%) and δD values (e.g., > -60 ‰).

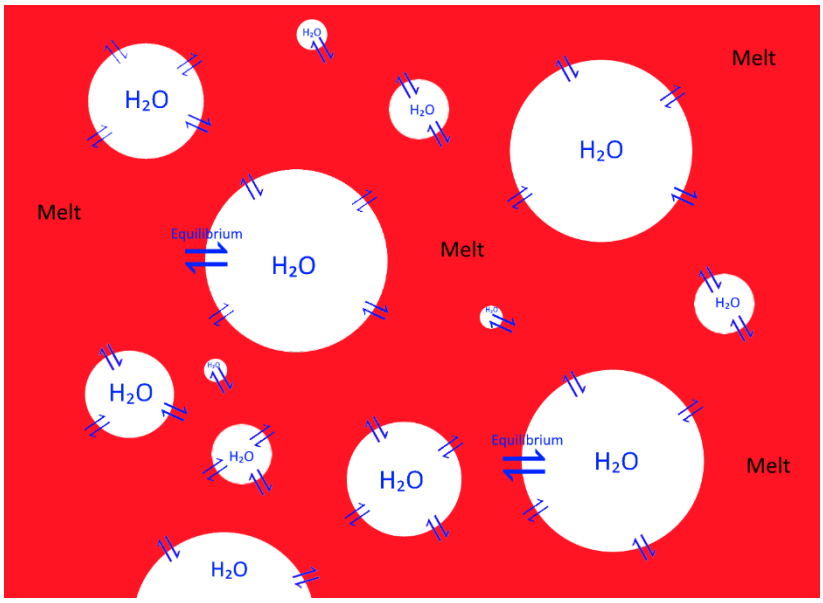


**Figure 1.3:** Schematic representation of an ideal closed-degassing system. White ovals indicate bubbles containing exsolved water, while the red areas represent the surrounding rhyolitic melt. The bidirectional equilibrium arrows indicate chemical equilibrium between exsolved water in the bubbles and dissolved $H_2O$ in the melt.

According to prevailing theories (e.g., Eichelberger et al., 1986), after the explosive stage, an open-system emerges, characterized by strong isotopic fractionation through disequilibrium conditions caused by volatiles being immediately and effectively removed from the melt (Figure 1.4). This separation is thought to occur via interconnected vesicles that allows for continuous outgassing as the magma evolves into a coherent, frothy state which then collapse upon extrusion creating lava flows (Taylor et al., 1983; Eichelberger et al., 1986). These flows yield low water contents (~0.1 wt.%) and highly depleted hydrogen signatures of under -100 ‰ (e.g., Newman et al., 1988; Dobson et al., 1989; Castro et al., 2014; Giachetti et al., 2020). Notably, the onset of this interconnected or “permeable foam” (Eichelberger et al., 1986) state has been linked to a porosity threshold of ~65% (e.g., Eichelberger et al., 1986; Giachetti et al., 2020).

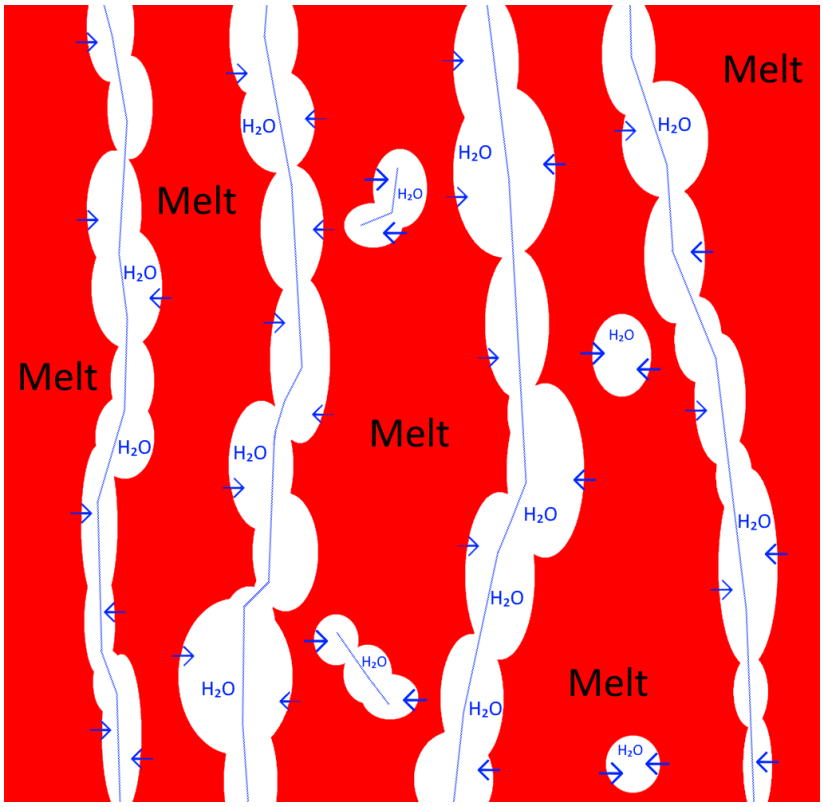


**Figure 1.4:** Schematic illustration of an open-degassing system. White domains represent interconnected bubbles incorporating exsolved water, while red areas denote the rhyolitic melt. Blue arrows indicate chemical disequilibrium between the exsolved water and the dissolved $H_2O$ in the melt. The dashed blue line marks the upwards transport of volatiles illustrating the removal of water from the whole system through outgassing.

### 1.2.1 Introduction into degassing simulations

Numerical modeling of single-, or two-stage chemical systems (e.g., Figure 1.2) is commonly employed to simulate degassing trends (e.g., Newman et al., 1988; Dobson et al., 1989; Giachetti et al., 2020). Such a model relies on the fact that hydrogen isotopes fractionate during degassing, whereas deuterium preferentially enriches into the vapor phase (Taylor et al.,

1983), leaving the residual melts progressively isotopic lighter as water is lost from the melt throughout the degassing process (Taylor et al., 1983).

The computations of the different degassing models involve formulae for chemical closed- and open-systems (see Chapter 2.1). Furthermore, all models require the hydrogen isotope fractionation factor between vapor and melt in rhyolitic melts, alpha ($\alpha_{v\text{-}m}$). This factor was often empirically determined (e.g., Taylor et al., 1983; Newman et al., 1988; Dobson et al., 1989) and some early studies simplified the model by employing a constant fractionation factor (e.g., Taylor et al., 1983).

Research revealed that magmatic water consists of two species, hydroxyl group ($OH^-$) and molecular water ($H_2O_m$). The relative amounts of these species are controlled by bulk water content and temperature (Stolper, 1982) with $H_2O_m$ dominating at high water contents while $OH^-$ becomes increasingly prevalent as bulk water content falls (Newman et al., 1988; Zhang et al., 1991; Zhang, 1999). This is because molecular water is the species that diffuses from the melt into bubbles during degassing (Zhang et al., 1991). Finally, each water species utilizes its own fractionation factor, which, in combination with the relative amount of the distinct species in the melt, is a function of the bulk alpha factor (Newman et al., 1988; Holloway and Blank, 1994) and therefore $\alpha_{v\text{-}m}$ changes during degassing. For detailed equations, models, and calculation methods, see “Chapter 2.1 Degassing modeling”.

### 1.3 Hybrid eruptions

The traditional models of silicic eruptions commonly interpreted the closed-to-open degassing behavior, illustrated by an explosive-to-effusive transition, as a rather linear and unidirectional process, largely due to limited direct observations of eruptions. However, this simplistic view changed when firsthand observations of eruptions at Chaitén (2008) and Cordón Caulle (2011), Chile, emerged (Castro and Dingwell, 2009; Lara, 2009; Alfano et al., 2011; Schipper et al., 2013; Castro et al., 2014). These eruptions revealed novel patterns that are inconsistent with the previously accepted eruption behaviors and degassing models.

The monitored Chilean eruptions initiated with a week-long Plinian stage comprising intense sustained explosive activity, followed shortly thereafter by a hybrid phase characterized by simultaneous explosive and effusive activity. This hybrid activity created explosive and effusive products including pyroclastic flows, thin air-fall deposits, and lava flows, all of which originated from the same vent and occurred concurrently (Schipper et al., 2013; Castro et al., 2014; Castro et al., 2016). After several months to a year of hybrid activity, the eruptions culminated

in completely effusive activity (dome building) that persisted for several months (Lara, 2009; Castro et al., 2013; Schipper et al., 2013; Tuffen et al., 2013).

Studies conducted on the deposits formed during the hybrid phases of Chaitén and Cordón Caulle unveiled unique geochemical and textural features, including intimate mixtures of pyroclastic and effusive material. For example, pyroclastic deposits such as tephra cones were sometimes found to have been transported by the lava flow which flattened the existing fragmental structures into welded tuff-like features (Pallister et al., 2013; Schipper et al., 2013). Furthermore, large tephra ridges or mixed breccias were detected within the interiors of the lava flow rather than at their rims, conflicting with patterns typically seen in explosive-to-effusive eruptions (Tuffen et al., 2013; Castro et al., 2014). The Chilean eruptions also produced glassy to pumiceous bombs exhibiting great textural diversity (e.g., brecciation, vesiculation) over small length scales (Castro et al., 2014; Schipper et al., 2021). Additionally, incoherent to dense, welded pyroclastic fall deposits overlying the lava have been identified (Castro et al., 2014). Such textures indicate that the pyroclastic material was still hot when it was emplaced on the hot effusing lava flow, which is consistent with simultaneous explosive-effusive activity.

**Figure 1.5:** Macroscopic image of a bomb from Rocche Rosse (Chapter 7). In the lower part of the sample, a tuffisite vein transects the entire bomb horizontally, incorporating a significant amount of ash and some small-to-medium sized obsidian fragments (black shards). In the central part of the sample another tuffisite is visible containing similar material. This tuffisite additionally shows fracturing of the surrounding obsidian during tuffisite formation.

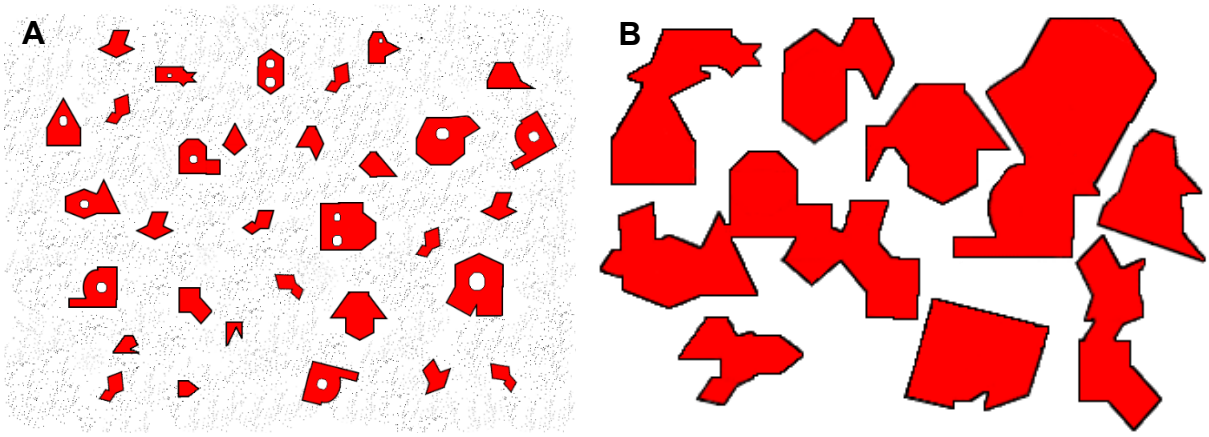


**Figure 1.6:** Schematic representation of the sintering process in rhyolitic melts. Red structures represent larger magma fragments, black dots symbolize smaller particles like ash, and white areas depict the melt or bubbles. Frame [A] displays the initial stage of sintering, where magma fragments stay largely separate as sintering has not yet occurred. Frame [B] presents the onset of sintering, with several fragments beginning to coalesce, leading to gradual compaction of the material into dense obsidian [C]. The sintering process occurs at shallower depths along tuffisites veins or conduits walls, where temperature and pressure conditions permit sintering. Since small particle sinter rapidly, they are integrated into the larger fragments early in the process. Frame [C] illustrates an advanced state of repeated sintering, where porosity between the fragments is significantly reduced, with only small vesicles left in the now densely compacted fragments.

Another significant feature produced in the Chilean events are tuffisites (Figure 1.5)—ash-, and clast-filled partially sintered veins—within the deposits (Tuffen et al., 2003; Tuffen and Dingwell, 2005; Castro et al., 2012; Castro et al., 2014). These veins act as pathways for exsolved gases, allowing volatiles to escape from other, deeper conduit regions. This process is assumed to be of explosive nature if the veins are clogged and enough volatiles accumulated before release (e.g., Tuffen et al., 2003; Castro et al., 2014; Gardner et al., 2018). However, tuffisite veins are transient, as sintering processes can rapidly reseal them within minutes, re-establishing closed-system conditions (Gardner et al., 2018).

Sintering is a process which compacts fragments (see Chapter 1.2) like residual ash through heat and pressure without melting it (Figure 1.6). The process can operate across a range of scales, from microscale within millimeter-thick tuffisites, to the macroscale, along meter-thick conduit walls. Sintering is often a dynamic episodic process, involving several cycles that progressively reduce porosity (Figure 1.6B, C), eventually forming solid material like obsidian

fragments or dense lava (Gardner et al., 2017; Gardner et al., 2018; Wadsworth et al., 2020; Wadsworth et al., 2022; Figure 1.6C). The timescale for solidification via sintering is highly controlled by temperature, pressure and size of the particles. Higher temperature and pressure, as well as small particles (e.g., ash) significantly accelerate the sintering process (Gardner et al., 2018).

### 1.3.1 Dynamics of batched degassing

The numerous textural and eruption observations made at the two Chilean volcanoes challenged traditional two-stage degassing models which treated explosive and effusive processes independently. The recognition of hybrid eruptive phases demanded a new degassing system to designate the underlying geochemical dynamics. Perusal of the published literature reveals indeed an alternative hypothesis and degassing mechanism to describe eruption dynamics at the Inyo Domes: Batched degassing (Taylor, 1991).

A pivotal investigation by Castro et al. (2014) offers a proof-of-concept that batched degassing was likely operating during the Chaitén and Cordón Caulle events. These workers employed hydrogen isotope analyses and field observations to examine geochemical and textural patterns—specifically of tuffisites—of the hybrid activity at Chaitén and Cordón Caulle. This study was the first at the site to link field observations with geochemical evidence, in particular hydrogen isotopic signatures, both of which have been successfully linked to hybrid eruptive activity and a "batched" degassing system. The batched degassing system, originally described as the "multi-step open/closed" system, was first developed by Taylor (1991) for modeling rhyolitic eruptions at the Inyo Domes, CA, 650–550 years B.P. (Miller, 1985). It involves the gradual accumulation of gas within the melt under closed-system conditions, followed by periodic interruptions manifested as explosive venting of volatile batches to the surface. As gas is successively lost during these frequent release events, the bulk $H_2O$ of the remaining melt drops, leading to a nonlinear decrease in δD values that is especially pronounced at low water levels. This process thereby creates a "quasi-open state" (Castro et al., 2014) in the system. It has been postulated that tuffisites play a fundamental role in facilitating this batched degassing process (e.g., Castro et al., 2014). Indeed, these pyroclastic channels are the prime candidates to periodically release batches of volatiles in explosive events from within effusing lava until they reseal (Tuffen et al., 2003; Castro et al., 2014; Saubin et al., 2016; Schipper et al., 2021) through processes such as sintering (Gardner et al., 2018). This cyclic sealing enables repetitive gas accumulation under closed-system conditions (Castro et al., 2014). By including the batched degassing system, the isotope systematics during degassing can now be modeled by three different systems (closed, open, batched)

linked to three eruption styles (explosive, effusive, hybrid), all of which portray distinctive geochemical mechanisms in the melt.

Following the discovery of hybrid activity and its geochemical and textural patterns, later and more recent studies have begun to investigate if these processes are recorded in pre-historic silicic eruptions. For instance, Black et al. (2016) identified tuffisites as pyroclastic degassing veins (e.g., Tuffen et al., 2003; Tuffen and Dingwell, 2005; Castro et al., 2014; Gardner et al., 2018) in the Panum Dome rhyolite (CA). They interpreted tuffisites in Panum as evidence of explosive ash venting throughout that obsidian dome's emplacement. Additionally, the Black et al. (2016) study emphasized the potential hazard posed by long-lasting ash venting during rhyolitic eruptions, specifically for air traffic (Black et al., 2016). This hazard highlights the importance of studying archaic deposits to better understand hybrid eruptive behavior.

### 1.4 Cryptic fragmentation model

Recent research (Gonnermann and Manga, 2003; Tuffen et al., 2003) has raised the question as to what role fragmentation and rewelding/sintering—as observed in, e.g., tuffisites—plays in assembling coherent magma bodies and lava, and their possible relation to simultaneous eruption style (Watkins et al., 2017; Gardner et al., 2018; Giachetti et al., 2020; Schipper et al., 2021). A promising mechanism possibly solving this dilemma is the cryptic fragmentation model, herein referred to as the fragmentation and sintering model, as described in studies such as Gardner et al. (2017); Wadsworth et al. (2020); Wadsworth et al. (2022).

This model proposes that hybrid activity originates from magma fragmentation at deeper regions, producing ash particles and other clasts or fragments that repeatedly sinter at shallower levels along the conduit walls, where temperature and pressure settings permit sintering (e.g., Gardner et al., 2017; e.g., Gardner et al., 2018; Wadsworth et al., 2020; Schipper et al., 2021; Farquharson et al., 2022; Foster et al., 2024). These sintered fragments increasingly seal the conduit (Schipper et al., 2021), resulting in pressure buildup driving closed-system conditions. Eventually, dense pyroclasts are produced and effusive dense lava emerges from the sintered magma parts (Wadsworth et al., 2020; Wadsworth et al., 2022; Foster et al., 2024). The consequences of the occluded system are explosive pulses resulting from temporary pressure releases, ejecting sintered material which blocked the pathways and releasing large batches of volatiles (Castro et al., 2016). These emitted sintered products represent different evolutional stages of the degassed magmas. This recurring process, the closure and reopening of the conduit, mirrors a "quasi" large-scale or "supersized tuffisite" (Schipper et al., 2021) which could geochemically align with the batched degassing system.

These discoveries raise the critical question on how frequently these hybrid eruptions occur and of their manifestation in pre-historic silicic eruptions. This dissertation aims to address this issue by exploring evidence for hybrid activity in the Big Glass Mountain (CA), 1060 CE, eruption and the Forgia Vecchia, Rocche Rosse and Lami eruptions at Lipari (Sicily), collectively erupting ~1250 CE (Pistolesi et al., 2021). By analyzing textures, water content, isotopic signatures, deposits, and employing numerical modeling, this thesis investigates the prevalence of hybrid activity in rhyolitic eruptions.

### 1.5 Rehydration

While the hydrogen isotope system is a highly effective tracer for magmatic degassing, it is susceptible to alteration by e.g., external water sources (e.g., ground water). Meteoric and hydrothermal waters can interact with eruption deposits, possibly overprinting both magmatic water content and H-isotopic signature, which complicates the interpretation of natural $H_2O$-δD datasets. Indeed, the chemical effects of hydration have been described in works such as DeGroat-Nelson et al. (2001); Seligman et al. (2016); Seligman et al. (2018); Giachetti et al. (2020), all of which investigated pyroclastic and effusive deposits from several silicic volcanoes.

A study conducted by DeGroat-Nelson et al. (2001) analyzed δD and water contents in samples of varying porosity (e.g., dense obsidian, lava flows, and pumice) from the Little Glass (Medicine Lake, CA), Big Glass Mountain (Medicine Lake, CA) and Obsidian Dome (CA) eruptions. Their findings revealed that "$H_2O$ is proportional to porosity" (DeGroat-Nelson et al., 2001); that is, that more vesicular samples contain higher water contents than their denser counterparts. Similarly, the hydrogen isotopic signature of lava flow samples exhibited, that dense obsidian contained lower δD values (depleted) than the most pumiceous samples, which were enriched in δD. In another study, Seligman et al. (2018) analyzed fresh near-surface pumice samples from Mount St. Helens. The results indicated an increase of ~15‰ in δD and 0.1 - 0.2 wt.% in water content compared to pumices collected from the same location in 1980. These differences were attributed to years of rehydration via δD enriched waters degassing from hot underlying deposits. A more recent study by Giachetti et al. (2020), uncovered that dense pyroclasts and flow samples from the 1060 CE Big Glass Mountain eruption were largely unaffected by meteoric rehydration, while their porous counterparts gained up to 1 wt.% of these waters.

In each of these studies, the alteration of hydrogen isotopic composition in the samples was directly tied to the isotopic signature of the water source that the deposit interacted with. For

instance, when the source is local meteoric water, the δD value varies regionally (e.g., Taylor et al., 1983; Seligman et al., 2016; Seligman et al., 2018). The data of the listed studies confirm that dense obsidians are less prone to rehydration due to their low permeability, and thus require longer timescales to undergo significant alteration at surface conditions (~1-10 µm/1000yrs; e.g., Anovitz et al., 2004) compared to porous pyroclasts (e.g., Friedman and Smith, 1958; Taylor et al., 1983; Taylor, 1991; Anovitz et al., 2004).

### 1.5.1 Rehydration prevention

The water and hydrogen alterations highlight the necessity for methods which allow to detect non-magmatic waters to ensure accurate determination of the “true” magmatic water content. Previous studies have provided different approaches to address this issue. One of the most effective strategies is to select dense glass samples for measurement as these can track a more complete degassing history while not being subjected to substantial alterations owing to their high density, which prevents significant diffusion of external water into the glass over large timescales (e.g., Friedman and Smith, 1958; Taylor et al., 1983; Taylor, 1991). Furthermore, in the case of highly altered dense glass these parts can be detected by being transformed into perlite (Friedman and Smith, 1958; Taylor et al., 1983; Taylor, 1991; Anovitz et al., 2004). This approach also has been implemented in this thesis.

In contrast to dense glass, if the samples are vesicular (e.g., pumice, ash, vesicular pyroclasts) it is essential to identify and account for external waters. This can be achieved by analyzing the $H_2O$ speciation values of the sample. Elevated levels of molecular water, especially at low bulk contents, are indicative of secondary hydration. This occurs since molecular water, which constitutes meteoric water, shows significantly higher diffusivity than OH-groups, which are regarded as an “essential immobile” species (e.g., Zhang et al., 1991; Giachetti et al., 2020). Additionally, these altered samples often portray offset data in δD vs. $H_2O$ plots, where water uptake increases bulk water content while modifying the δD value according to the hydrogen signature of the external source. Depending on the external source’s isotopic values, deviations of δD maybe be positive or negative with respect to the magmatic values.

To prevent interference from loosely bound adsorbed water (e.g., air moisture on ground powder), it is good practice to heat the powdered samples under vacuum at 130°C overnight. While this procedure is a useful initial step, it is insufficient to remove secondary water embedded in the glass matrix (Giachetti et al., 2020). A more effective and efficient method is step-heating, which further minimizes the measurement of meteoric water contamination and altered hydrogen isotopic signatures. This approach has been described in works such as

Eichelberger and Westrich (1981), DeGroat-Nelson et al. (2001), Giachetti et al. (2015), and Giachetti et al. (2020). This method involves sequential heating steps during mass spectrometry analysis. External waters, which are less strongly bound, are released at lower temperatures up to 400°C, while primary magmatic water is emitted at higher temperatures of 1100–1200°C (Giachetti et al., 2015; Shields et al., 2016; Giachetti et al., 2020).

### 1.6 Boron isotopic system overview

The alterations in the hydrogen isotopic system (δD and $H_2O$) by external waters raise the question whether an alternative isotopic system could act as an additional tracer for degassing related systematics. Such a system could at least verify existing hydrogen degassing patterns and, in case where alteration of the hydrogen isotopic signature or water content is significant, possibly replace hydrogen as the primary tracer, or provide further insights into degassing phenomena.

A promising alternative is the boron isotopic system, which consists of the two natural occurring boron isotopes, $^{11}B$ and $^{10}B$, present in a 4 to 1 ratio in terrestrial materials, and differing in mass by ~10%. Like the hydrogen system, boron isotopes are expressed using the δ notation, where $\delta^{11}B$ (or δB) is calculated as the ratio of the heavier to lighter isotope relative to a standard. The calculation follows the same formula detailed in Chapter 1.2 (Equation 1), with appropriate substitutions: $\delta^{11}B$ for δD, $^{11}B$ for $^{2}H$, and $^{10}B$ for $^{1}H$.

Boron demonstrates distinct characteristics in various hydrous solutions like solubility, partitioning and fractionation differences. This makes Boron concentration and isotopic signature valuable as geochemical tracers for both high- and low-temperature geochemical processes (Foster et al., 2018). Consequently, the boron isotopic system has been successfully applied to diverse fields. For instance, it is employed for studying hydrothermal environments (Spivack and Edmond, 1987), the investigation of crust-mantle dynamics (Tonarini et al., 2003), for characterizing fluid sources or reservoirs the fluids have interacted with (Pennisi et al., 2000; Savov et al., 2009), and to trace subduction-related processes, such as determining the depth of subducting slabs or to identify mass transfer in subduction settings (Rosner et al., 2003).

In hydrous solutions, and to a lesser extent, in silicic melts, boron exhibits high compatibility and solubility, leading to its enrichment therein (Dutrow and Henry, 2011; Konstantinos, 2017). In contrast, boron is incompatible in most rock-forming minerals, except for minerals such as mica and tourmaline (e.g., Anovitz and Grew, 1996; Palmer and Swihart, 1996; Marschall et al., 2017; Maner and London, 2018; Marschall and Foster, 2018; Trumbull and Slack, 2018).

As an incompatible lithophile element, boron is transported by granitic melts and hydrous fluids to shallower depths. As a result, it becomes concentrated in crustal rocks relative to the unmelted residuals such as the mantle, which is depleted in boron (Chaussidon and Libourel, 1993; Dutrow and Henry, 2011; Marschall et al., 2017; Marschall and Foster, 2018). While there has been limited research (e.g., Schmitt and Simon, 2004) on the application of boron isotopes and concentrations as a tracer for degassing related processes, the system nevertheless exhibits promising characteristics for this purpose. Specifically, boron and its isotope $^{11}B$ partition from the melt into the hydrous phase during degassing, resulting in depletion of the melt in both (Hervig et al., 2002; Maner and London, 2018). Chapter 2.2 provides a more detailed overview of the boron system, describing its behavior in different materials, its partitioning and isotopic fractionation processes, and its role in degassing, with the primary aim of assessing whether boron isotopes could theoretically serve as an alternative tracer to hydrogen in rhyolite systems.

# Chapter 2
# Background

## 2.1 Degassing modeling

The following sections provide an in-depth look at closed, open, and batched degassing systems, highlighting their chemical definitions and respective formulae for calculating geochemical trends. Furthermore, the specific eruptive conditions associated with each system, along with the volcanic domains in which they occur, are described.

### 2.1.1 Closed-system degassing

The closed degassing system may best represent the initial process of degassing of volatiles from the melt, likely driven by volatile oversaturation, that is, overstepping of the melt's $H_2O$ (and other components) solubility limit at depth (see also Chapter 1.2). The result of volatile supersaturation is of course the nucleation and growth of vapor phase bubbles (Anderson and Fink, 1989). These conditions probably occur in the magma chamber and could persist to shallow levels, i.e., some hundreds of meters below the surface within the feeder conduit. If permeability is low or nonexistent, and bubbles stay separated, closed-system bubble growth may lead to excessive overpressure and explosive fragmentation (e.g., Eichelberger et al., 1986; Newman et al., 1988; Dingwell, 1996; Gonnermann and Manga, 2003, 2007). These closed-system conditions persist until a vesiculation threshold is reached (e.g., ~ 65%, Eichelberger et al., 1986; Giachetti et al., 2020) at which point the magma reaches a "bubbly" state where the vesicles interconnect. This in turn results in the establishment of permeable gas flow conditions, allowing for effective gas-melt separation (Eichelberger et al., 1986), initiating open-system degassing behavior.

Degassing calculations of a closed-system, as conducted by numerous studies (e.g., Newman et al., 1988; Dobson et al., 1989; Rust et al., 2004; Giachetti et al., 2020), assume an idealized scenario, in which bubbles stay separate and melt and exsolved volatiles remain in permanent contact, preserving perfect compositional equilibrium conditions between these phases. For instance, this system presumes that bubbles grow fast enough to remain in equilibrium with the melt. However, such conditions are sometimes not met in the presence of a highly viscous melt (Navon and Lyakhovsky, 1998; Gardner et al., 1999; Gardner, 2007). In such melts,

volatile diffusion, bubble nucleation and growth are inhibited, leading to a buildup of internal pressure within bubbles (Sparks, 1978; Gardner et al., 2000; see also Chapter 1.2).

The ideal closed-system is described as a mass conservative system, where no material is added or removed from the melt. Consequently, the hydrogen isotopic configuration of the melt is a strong function of that in the bubbles in the vapor phase. As water solubility is closely tied to pressure conditions (e.g. Sparks, 1978; Gardner et al., 2000; see also Chapter 1.2), the external pressure controls the amount of $H_2O$ exsolved from the melt and consequently the extent of hydrogen isotopic fractionation, creating an "equilibrium-buffered state".

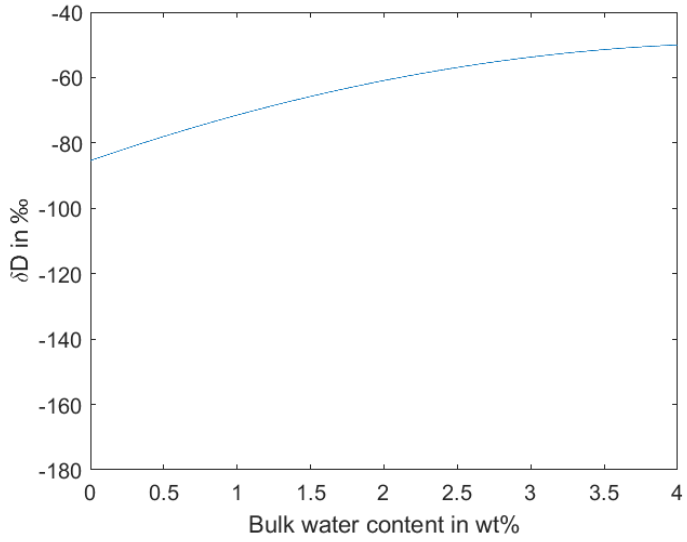


**Figure 2.1:** Graph portraying an idealized closed-degassing system model (δD in ‰ vs. $H_2O$ in wt.%), generated utilizing the VolcDeGas program (Chapter 5). This system exhibits minimal hydrogen isotopic fractionation effects resulting in a slightly curved trajectory.

The isotopic fractionation in a closed system can be exemplified using mass balance equation (Taylor et al., 1983):

$$\delta D_f = \delta D_i - (1 - F) \times 10^3 \times \ln(\alpha_{v-m}) \quad (2)$$

with $\delta D_f$ being the final δD value of the melt (in ‰) and $\delta D_i$ the initial δD of the melt (in ‰). $\alpha_{v-m}$ describes the fractionation factor alpha between vapor and melt at a given temperature and pressure, and F is the fraction of water remaining dissolved in the melt calculated as a ratio of final $H_2O$ ($H_2O_f$) in the melt divided by initial $H_2O$ ($H_2O_i$) in melt ($H_2O_f/H_2O_i$). Here $H_2O_i$ describes the original water content at the start of the process and $H_2O_f$ denotes the water content in the melt at the end of the process. In this context, a process is defined as a simulated degassing step, during which a distinctive amount of $H_2O$ is released, reducing the melt's

overall water budget. Degassing modeling typically involves multiple such steps, each accounting for progressive volatile exsolution.

In a closed system, the initial bulk water content and initial isotopic value remain constant throughout the entire degassing process, with each step causing only minor isotopic fractionations. This is illustrated by a near-linear trend on a δD vs. $H_2O$ graph (Figure 2.1), showing a slight decrease in δD (by a few tens of ‰) over a substantial decrease in water content (several wt.% of $H_2O$).

### 2.1.2 Open-system degassing

The open degassing system describes an degassing regime in which volatiles are exsolved from the melt into bubbles, and near-instantly removed entirely from the degassing system through pathways such as might exist in permeable magmatic foams, cracks, fractures, or brecciated conduit walls (Eichelberger et al., 1986; Gonnermann and Manga, 2003). Under these conditions, the volatiles are rapidly removed from the melt which suppresses chemical equilibration between melt and gas, in turn leading to continual and stark geochemical adjustment of the melt to the removal of gas. The factors facilitating these conditions are high magma porosity (e.g., 65%, Eichelberger et al., 1986; Giachetti et al., 2020) and permeability, enabled by interconnected vesicles, promoting efficient melt-gas separation (Eichelberger et al., 1986).

The isotopic fractionation in open systems is modeled utilizing the Rayleigh fractionation formula (Taylor, 1991):

$$\delta D_f = (\delta D_i + 1000) - (F^{\alpha_{v-m}-1}) - 1000 \quad (3)$$

where $\delta D_f$ represents the final δD value of the melt when the process ends and $\delta D_i$ is the initial δD value (in ‰) at the start of the process. F is the fraction of water left dissolved in the melt, which is calculated by the final $H_2O$ ($H_2O_f$) at the end of process divided by the initial $H_2O$ ($H_2O_i$) from the beginning of the process ($H_2O_f/H_2O_i$). $\alpha_{v-m}$ illustrates the fractionation factor alpha between vapor and melt at specific temperature and pressure conditions.

In contrast to the closed system, the open system does not maintain fixed initial values ($H_2O_i$, $\delta D_i$), as aliquots of water are continuously removed from the system during each degassing step. Therefore, $\delta D_i$ and $H_2O_i$ are constantly updated to reflect the progressively lower values of the preceding step. The step size directly influences the trajectory of δD decrease and the

final δD value, as the water loss of each step is derived from the successively δD-depleted depleted hydrous reservoir.

Open-system degassing results in significant isotopic fractionation, with δD depleting by several tens of ‰ (e.g., >150 ‰; Figure 2.2). In this system an initially moderate decrease in deuterium is observed, followed by an exponential reduction in δD at the late degassing stage (Figure 2.2), marked by low water contents. Such strongly depleted δD trends are the signature of open-system behavior, and have often been implicated in the formation of obsidian lavas exhibiting low δD and water contents (e.g., Taylor et al., 1983; Newman et al., 1988; Dobson et al., 1989; Giachetti et al., 2020).

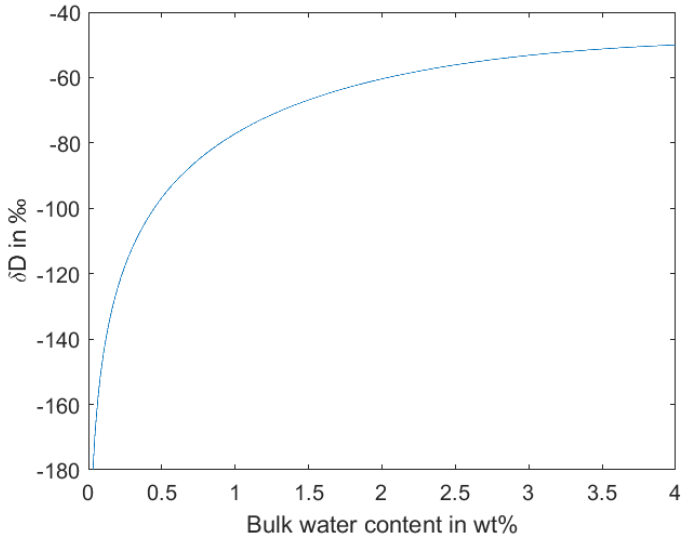


**Figure 2.2:** Plot of δD (in ‰) versus $H_2O$ (in wt.%) of an idealized open-degassing system model, computed with the VolcDeGas program (Chapter 5). This model depicts significant and exponential δD depletion during degassing, which maximizes at low water contents.

### 2.1.3 Batched-system degassing

The batched degassing system, or "multi-step open/closed" system, developed by Taylor (1991), effectively represents a hybrid between closed- and open-system behaviors. In this model, aliquots of volatiles continually accumulate in a temporarily sealed system under closed-system conditions, e.g., within bubbles, cracks, tuffisites (Castro et al., 2012; Castro et al., 2014), or entrapped between grains produced during fragmentation and sintering (Gardner et al., 2017; Wadsworth et al., 2020; Wadsworth et al., 2022), before being released to the surroundings in batches during episodic outgassing events. This periodic gas release is thought to correspond to many hundreds of explosive eruptions observed in natural systems (Schipper et al., 2013; Castro et al., 2014). Batched degassing is also thought to operate on larger scales, for example in a sealed volcanic conduit that might act as a super-sized tuffisite

(Schipper et al., 2021). Because the physical requirements of batched degassing closely match the ephemeral nature of gas storage and release structures in the natural system (Castro et al., 2012), this mechanism is probably the most realistic, and therefore widely applicable to explaining geochemical patterns throughout the whole eruption cycles at rhyolite volcanoes (see Chapters 5 – 7, and Sections 1.3 and 1.4).

The modeling of the batched system requires both closed- and open-system systematics. Initially, volatiles accumulate and become entrapped within a temporary closed system, where equilibrium conditions dominate. Periodically, the system opens, releasing the accumulated gas. The process then repeats, constituting a degassing cycle. Isotopic variations and water content in this cyclic process is calculated by firstly employing the closed system formula (Equation 2) to model an extracted gas aliquot, and, after gas release, adjustment of δD and $H_2O$, using initial δD and initial water contents (established in the F factor by $H_2O_f/H_2O_i$) that are adjusted after each step to account for the depletion happening in the previous step. In this way, through updating δD and water after each step, the batched system models some elements similar to the open system. For example, relatively strong δD depletions are possible under this degassing regime. The recurring gas accumulation and release continues until the system becomes water-depleted or the condition within the magma change, preventing further batched-system behavior.

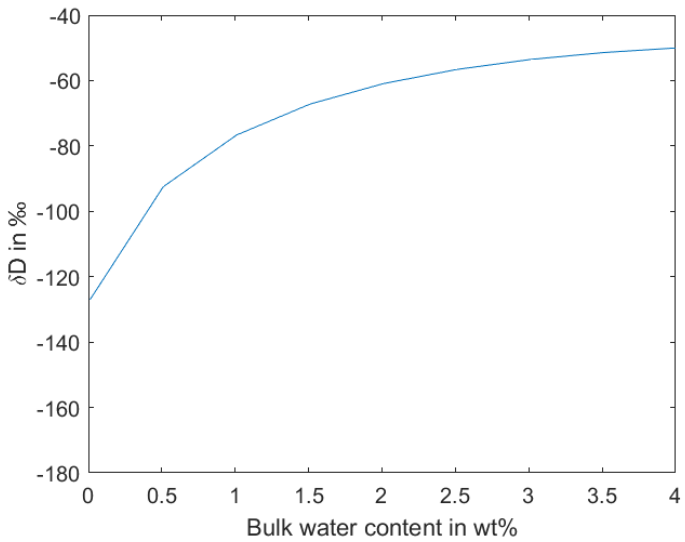


**Figure 2.3:** Graph presenting an idealized batched-degassing system (δD in ‰ vs. $H_2O$ in wt.%), simulated with the VolcDeGas program utilizing a 0.5 wt.% step size. The batched system displays mixed characteristics of closed- and open degassing systems.

This mixed degassing system can mimic characteristics of both closed- and open-system dynamics, with the extent of depletion being highly sensitive to step size (Figure 2.3). Due to

its flexibility, this system has been successfully applied to model hydrogen isotopic fractionation of samples from the 2008 Chaitén eruption (Castro and Dingwell, 2009), as demonstrated by Castro et al. (2014).

### 2.1.4 Buffered-system degassing

The buffered degassing system, developed by Rust et al. (2004), represents a specific variant of an open-degassing system. In this model permeable, brecciated magma remains in continuous equilibrium with a vapor flux of fixed composition. This differs from the traditional open-degassing system, where the melt does not interact with another phase (e.g., volatile phase), and the system is believed to be under complete disequilibrium conditions (Section 2.1.2). The interpretation of this alternative system was based on microtextural analyses, as well as measurements of $CO_2$, $H_2O$ and δD in pyroclastic obsidian samples of several Holocene eruptions in Oregon and California (Rust et al., 2004).

In these obsidians the researchers detected xenoliths, sheared bands of lithic powder, and textures consistent with magma autobrecciation (Rust et al., 2004). Based on the microtextural observations Rust et al. (2004) proposed that pyroclastic obsidians primarily form adjacent to conduit margins where the magma undergoes repeated brecciation and annealing. Within this environment, a continuous vapor flux, which flows through the permeable, fractured magma, controls the $H_2O$ and $CO_2$ composition of the melt (Rust et al., 2004). The geochemical description of these processes in the buffered-degassing system is that it behaves like an open system, with volatiles continuously lost near or at the conduit walls (Rust et al., 2004). However, unlike classical open systems, the melt is buffered by a vapor flux of constant composition, continuously re-equilibrating with that flux (Rust et al., 2004).

Building upon the buffered-degassing model, Rust et al. (2004) proposed that a “melt undergoing progressive volatile exsolution in equilibrium with a vapor of fixed $CO_2$ and $H_2O$ follows an isopleth”. They calculated several isopleths, each corresponding to different vapor flux compositions. This model successfully reproduced the observed $CO_2/H_2O$ ratios from the 1340 CE Mono Craters eruption in California—ratios that conventional closed or open system models could not explain (Rust et al., 2004). In non-buffered open systems, $CO_2$ decreases too rapidly relative to $H_2O$ to match the observed ratios, while closed systems require very large $CO_2$ contents in the parental magma and fail to account for the very low vesicularity of obsidian (Rust et al., 2004). In contrast, the buffered open system is consistent with both the $CO_2/H_2O$ ratios and the low vesicular obsidians observed in natural samples. Thus, the

buffered model provides a coherent explanation for the detected geochemical and textural patterns confirming its validity.

To further evaluate the buffered degassing model, Rust et al. (2004) applied hydrogen isotopic simulations using the open-system equation (Section 2.1.2; Equation 3), with a crucial modification. That is that the initial water content and δD are assumed as fixed values, as these parameters are constantly reset to the values of the buffering vapor flux. While the use of fixed initial δD and $H_2O$ resembles a closed system modeling approach (Section 2.1.1), the system itself remains open. Notably, unlike in the closed system, these fixed values do not represent the initial composition of the melt, but rather that of the interacting volatile flux. This buffered system was successfully applied to model the $H_2O$-δD data of pyroclastic obsidian from Little Glass Mountain (Medicine Lake, California), and Mono Craters, California. However the model could not account for the strongly depleted δD values detected in obsidian dome samples, which require non-buffered open-system calculations (Rust et al., 2004).

### 2.1.5 Alpha-factor and water speciation

The bulk water fractionation factor ($\alpha_{v-m}$) between vapor and melt in rhyolitic systems (hereby referred to as “alpha factor”) is used in all degassing models (closed, open, batched). This alpha factor is composition dependent and thus, evolves as progressively more water is lost during degassing (Newman et al., 1988). The specific formula is derived from the traditional fractionation factor for isotopic systems:

$$\alpha_{v-m} = \frac{(D/H)_{vapor}}{(D/H)_{melt}} = \frac{1000+\delta D_{vapor}}{1000+\delta D_{melt}} \quad (4)$$

Here, $(D/H)_{vapour}$ and $(D/H)_{melt}$ are the deuterium-to-hydrogen ratios in the vapor and melt phases, respectively, and δD is defined in either the vapor or melt phase and is derived from Equation 1.

As asserted by Newman et al. (1988), the alpha factor is sensitive to changes in water speciation and therefore depends on the two water species present in the melt: the hydroxyl group ($OH^-$) and molecular water ($H_2O_m$). In addition, Holloway and Blank (1994) postulated, that the alpha factor changes as the ratio of the water species evolves during degassing, in other words, during a drop in the bulk water in the system (Stolper, 1982). As aliquots of water degas, the proportion of $OH^-$ increases and this drives significant D/H fractionation with the water vapor, causing the bulk alpha factor to increase as degassing progresses.

Indeed, the proportions of the two hydrous species in the melt depend on temperature and total water content (Stolper, 1982; Dobson et al., 1989; Stolper, 1989), and experimentally determined calibrations of these effects on speciation are available (Stolper, 1982, 1989). Additionally, empirical determinations of bulk alpha factors as a function of temperature have been conducted in works such as of Dobson et al. (1989).

Thus, in order to account for variation in hydrous speciation, each water species is assigned its own alpha factor, which is calculated independently and referred to as $\alpha_{\mathrm{v-m\,(OH)}}$ for the OH-group and $\alpha_{\mathrm{v-m\,(H_2O)}}$ for the molecular water. The formula to calculate these factors is derived from Equation 4, but instead of considering the bulk water system, each individual species is accounted for, with appropriate tags (e.g., $H_2O_m$ or OH) attached to the factors. For instance, the bulk fractionation factor $\alpha_{\mathrm{v-m}}$ becomes $\alpha_{\mathrm{v-m\,(H_2O)}}$ when referring specifically to the molecular water component. Likewise, $\delta D_{\mathrm{vapor}}$ in Equation 4 would be replaced by $\delta D_{\mathrm{vapor(H_2O)}}$, to indicate that it refers to the δD of the vapor phase specifically in the form of molecular water.

Once the alpha factors for each species are determined, the bulk alpha factor can be calculated by employing the following equation (Taylor, 1991; Rust et al., 2004):

$$\ln\left(\alpha_{(\mathrm{v-m})\mathrm{bulk}}\right) = \mathrm{X} \times \ln\left(\alpha_{\mathrm{v-m\,(H_2O)}}\right) + (1-\mathrm{X}) \times \ln\left(\alpha_{\mathrm{v-m\,(OH)}}\right) \quad (5)$$

where X is the atomic fraction of hydrogen included as molecular $H_2O$ dissolved in the melt and (1-X) is the atomic fraction of hydrogen partitioned into OH-groups dissolved in the melt.

The formula can be refined to integrate the weight fractions of each water species, which can be derived from weight percentages (wt.%). These concentration units are commonly employed in geological studies and are measured by techniques such as Fourier-Transform-Infrared-Spectroscopy (FTIR). The acquired weight percentages of each species can be curve fitted and extrapolated to estimate $H_2O_m$ or OH values beyond the observed range enabling representation of each degassing step. These extrapolated speciation values, are then included in Equation 6 (presented at the end of this paragraph) to calculate the corresponding alpha values for each degassing step, as applied in studies like Newman et al. (1988). In instances where direct speciation measurements are unavailable, predictive models for water speciation exist. Prominent examples include the “Sil/Hol” or “regular solution” model, initially developed by Stolper (1989) and later modified by Silver et al. (1990). A numerical implementation of this model was provided by Holloway and Blank (1994), offering calculated speciation values and plots of bulk wt.% $H_2O$ versus wt.% molecular $H_2O$ by empirical factors.

The most recent and updated formula for calculating the bulk water fractionation factor that also accounts for the weight fractions of the water species is as follows (Taylor, 1991; Rust et al., 2004):

$$\alpha_{(\mathrm{v-m})\mathrm{bulk}} = \mathrm{H_2O_{m,frac}} \times \alpha_{\mathrm{v-m\,(H_2O)}} + \mathrm{OH_{frac}} \times \alpha_{\mathrm{v-m\,(OH)}} \quad (6)$$

Here, $\alpha_{\mathrm{v-m\,(H_2O)}}$ and $\alpha_{\mathrm{v-m\,(OH)}}$ are fixed fractionation factors, the values of which can be obtained from works such as Rust et al. (2004). $\mathrm{H_2O_{m,frac}}$ represents the weight fraction of molecular water in relation to the total water content, while $\mathrm{OH_{frac}}$ is the weight fraction of hydroxyl groups relative to the total water content. Both weight fractions can be calculated from the determined wt.% of each species using the following equation for hydroxyl groups (e.g., DeGroat, 1997) (a similar equation applies for molecular water):

$$\mathrm{OH_{frac}} = \frac{(\mathrm{OH_{wt.\%}}/100)}{(\mathrm{OH_{wt.\%}}/100) + (\mathrm{H_2O_{m,wt.\%}}/100)} \quad (7)$$

With all variables being defined as above.

### 2.2 Boron system information

While Section 1.6, “Boron isotopic system overview”, briefly summarized the boron isotopic system and its degassing theory, this chapter provides a more comprehensive description, specifically addressing why the boron system could theoretically serve as an additional tracer for degassing patterns in rhyolite magma.

To understand how boron acts in magmatic systems, it is crucial to examine the natural variations in boron concentrations and $\delta^{11}B$ values across Earth materials. This is especially important as boron occurs in trace amounts (ppm levels) in rocks and is susceptible to alteration by external boron sources or reservoirs. Thus, the following overview, which is derived from multiple studies (e.g., Palmer and Swihart, 1996; Rosner et al., 2003; Wunder et al., 2005; Dutrow and Henry, 2011; Deegan et al., 2016; Konstantinos, 2017; Trumbull and Slack, 2018), summarizes boron concentrations, isotopic ranges, and relevant processes influencing boron production.

The upper mantle and MORB exhibit low boron contents (< 1 ppm) and $\delta^{11}B$ values of approximately -7 ‰ (Chaussidon and Libourel, 1993; Dutrow and Henry, 2011; Marschall and Foster, 2018). These low boron contents are due to boron’s incompatibility in most rock-forming minerals and its preferential partitioning into silicic melts and hydrous fluids. The interaction of

the melt and fluid with the MORB or upper mantle—especially by partial melting (Chaussidon and Libourel, 1993)—deplete both in boron (Maner and London, 2018; Marschall and Foster, 2018). The negative $\delta^{11}B$ of MORB and upper mantle reflects isotopic fractionation, where the heavier isotope $^{11}B$ is preferentially incorporated in the melt and hydrous fluid phase, leaving the MORB and upper mantle isotopically lighter (Hervig et al., 2002; Marschall et al., 2017; Marschall and Foster, 2018). In contrast, the crust is slightly more enriched in boron, containing 2-17 ppm, but exhibits marginally lower $\delta^{11}B$ values of ~-9 ‰ (Dutrow and Henry, 2011; Marschall and Foster, 2018). This negative boron isotopic value in the crust is attributed to the "exsolution of water from granitic melt during ascent and crystallization" (Hervig et al., 2002; Maner and London, 2018) and to "loss of the heavier boron isotope to water during devolatilization of metamorphic rocks with increasing metamorphic grade" (Kasemann et al., 2001; Wunder et al., 2005; Maner and London, 2018). Shallow slab-derived fluids act as a significant boron source, as they are highly enriched in boron and its heavier isotope. This is because the subducting slab continually loses the immobile elements, including boron, during the subduction process (e.g., Noll et al., 1996; Savov et al., 2009; Pabst et al., 2012). Seawater, another boron reservoir, yields high $\delta^{11}B$ values of ~40 ‰ but low boron concentrations of ~4.4 ppm due to significant dilution within the vast seawater reservoir.

Boron concentrations in silicic igneous rocks exhibit extensive variability, ranging from 5 to 1900 ppm (Dutrow and Henry, 2011; Konstantinos, 2017). This is due to the compatibility of boron in silicic melts and hydrous fluids. These two boron "carriers" not only facilitate the upward transport of boron from deeper regions like the upper mantle, but also contribute to its enrichment in igneous rocks, which form from boron-bearing melts (Dutrow and Henry, 2011; Marschall and Foster, 2018). Silicic melts exhibit boron concentrations which can exceed 60 ppm and $\delta^{11}B$ values ranging between ~-25 and ~+15 ‰, particularly if the melts are associated with volcanic arc settings (e.g., Wunder et al., 2005; Deegan et al., 2016; Marschall and Foster, 2018). Among minerals, tourmaline yield the highest boron content, comprising up to 3 wt.% (Anovitz and Grew, 1996; Trumbull and Slack, 2018) with $\delta^{11}B$ values between 0 ‰ and -20 ‰ for magmatic tourmalines (Palmer and Swihart, 1996). Mica group minerals, which are more abundant than tourmaline (Maner and London, 2018), can contain up to 269 ppm of boron preferentially integrating the lighter $^{10}B$ isotope (Domanik et al., 1993; Wunder et al., 2005). Consequently, these two minerals are extensively examined in boron-related studies (e.g., Gonfiantini et al., 2003; Marschall et al., 2007; Trumbull and Slack, 2018). Abundant mica is the primary host of boron in felsic crystalline rocks (Trumbull and Slack, 2018), while in felsic volcanic rocks containing glassy groundmasses, the glass phase may host the highest boron concentrations (Schmitt and Simon, 2004; Trumbull and Slack, 2018). In regards to magma types, S-type magmas which are derived from sedimentary sources contain an average $\delta^{11}B$

value of ~-11.1 ‰, while I-type magmas, derived from igneous sources, yield a typical $\delta^{11}B$ value of -2.8 ‰ (Trumbull and Slack, 2018).

### 2.2.1 Boron degassing theory

With knowledge of boron sources and their reservoirs, the theory of isotopic fractionation and partitioning of boron during eruptive progression can now be explored.

Boron is highly soluble in hydrous solutions, and in magmatic systems in general, water and boron exist in a supercritical state, that is that each behaves simultaneously as a fluid and gas (Spivack et al., 1990; Kowalski and Wunder, 2018). The two relevant boron species dissolved in water, $B(OH)_3$ and $B(OH)_4^-$ (Barth, 1993), are thus "carried" by the fluid phase, exsolving out of the melt with other components in a separate low density hydrous fluid. This process in turn results in the partitioning of boron and the fractionation of its heavier isotope $^{11}B$ into the hydrous phase, with the consequence of boron depletion in the melt (e.g., Hervig et al., 2002; Maner and London, 2018). As degassing progresses, isotopically heavy, boron-enriched fluids are created and segregated from the melt.

Several studies have investigated the behavior of boron between melt and fluid phases (e.g., Hervig et al., 2002; Maner and London, 2018). Hervig et al. (2002) performed experiments to determine boron partitioning and fractionation between melts of rhyolitic and basaltic composition and hydrous fluids, while Maner and London (2018) focused their experiments on rhyolitic melts. The experiments were conducted with a high water concentration in the starting material and over long durations; i.e., 7 wt.% $H_2O$ and 30 days (Maner and London, 2018). After melting and quenching, boron concentrations and isotopic signatures ($^{11}B/^{10}B$) were measured in the quenched glass and the starting material, to back-calculate the boron composition of the hydrous phase. In the following paragraphs the results of the measurements, conclusions as well as implications are summarized.

These experiments answered a key question regarding whether boron primarily partitions into the hydrous fluid or into the melt. This difference determines whether boron behaves similarly to the hydrogen isotopic system, i.e., if degassing progresses from higher to lower concentration or conversely. This in turn has important implications for interpreting boron's isotopic data. Hervig et al. (2002) reported that the fluid/melt partition coefficient for basaltic melts is less than 1, indicating a boron compatibility in basaltic melts. In contrast, the partition coefficient exceeds 1 in rhyolitic melts, implying that boron preferentially concentrates in the

hydrous fluid phase, thereby depleting the silicate melt of boron (Hervig et al., 2002). Thus, in rhyolitic melts, boron degassing proceeds from high to low concentration.

The boron isotopic data from these experiments ($^{11}B/^{10}B$; $\delta^{11}B$) were inputted in Equation 4 (Section 2.1.5) to calculate the boron fractionation factor between fluid and melt ($\alpha_{f-m}$), under specified pressure and temperature conditions (Hervig et al., 2002; Maner and London, 2018). To apply the equation to the boron isotopic system, the formulae was updated by replacing D/H with $^{11}B/^{10}B$ and $\alpha_{v-m}$ with $\alpha_{f-m}$. Both studies found, that during degassing melts are depleted in $^{11}B$ whereas the coexisting fluid becomes enriched (Hervig et al., 2002; Maner and London, 2018). Furthermore, Hervig et al. (2002) concluded that boron fractionation is independent of melt composition (e.g., basaltic, rhyolitic).

Hervig et al. (2002) attributed the observed fractionation to differences in boron coordination between melt and fluid. In silicate melts, boron primarily exists in tetragonal coordination ($B(OH)_4^-$) which predominantly incorporates $^{10}B$ (Hervig et al., 2002; Maner and London, 2018). In contrast, hydrous fluids at magmatic temperatures favor trigonal ($B(OH)_3$) coordination (Schmidt et al., 2005), mainly integrating $^{11}B$ (Hervig et al., 2002; Maner and London, 2018). The distinctive coordination in each phase (e.g., melt and fluid) therefore results in fractionation between these phases at a given temperature and pressure (Wunder et al., 2005; Meyer et al., 2008). Because there is no substantial fractionation between vapor and liquid phases (Spivack and Edmond, 1987; Spivack et al., 1990) and boron is highly soluble in water, the boron fractionation factor for the melt/liquid systems (Maner and London, 2018) can be leveraged to model degassing sequences (Spivack et al., 1990; Hervig et al., 2002). Consequently, liquid and vapor demonstrate similar behavior in the boron system. Notably, Hervig et al. (2002) observed that the fractionation factor is inversely proportional to temperature (1/T). This temperature dependance was later confirmed by Maner and London (2018), who furthermore expanded on this factor by developing an empirical formula to describe the temperature dependence of $\alpha_{m-f}$ (see next Section 2.2).

The degassing process is significantly influenced by diffusion (see Chapter 1.2), as it plays a substantial role in controlling how volatiles move within the melt and escape during degassing. A study by Spallanzani et al. (2022) explored the diffusivity of boron and its isotopes in rhyolitic melts through experiments involving synthesized rhyolitic glass containing enriched and depleted endmembers to produce a chemical (concentration) gradient. The results demonstrated limited and slow diffusion of boron through the glass, with a diffusion coefficient of $2.4 \times 10^{-14} \pm 3 \times 10^{-15}$ $m^2/s$ at 1000°C (Spallanzani et al., 2022) which is more than four orders of magnitude lower than that of lithium, which yields a diffusion coefficient of $9.46 \times 10^{-}$

$^{10}$ ± 2 × $10^{-10}$ $m^2/s$ at 1050°C (Spallanzani et al., 2022). Although a minor depletion in $^{11}$B was measured in the low concentration endmember, no clear isotopic fractionation ($^{11}$B to $^{10}$B) during diffusion was detected within the experimental timeframe (20 hours). The authors noted that the "boron isotope results are very difficult to interpret, possibly because of the more complex structural incorporation of boron in the silicate melt." (Spallanzani et al., 2022). Based on the diffusion coefficients, the study also calculated an approximate timeframe for complete homogenization (at 1000°C) of boron and lithium in the melt during magmatic degassing. Boron may homogenize within a few days in a water-rich environment (4.2 wt.%) with a high decompression rate of 10 $m^2/s$, but requires 100 years for homogenization in a dry environment with a low decompression rate of 0.001 $m^2/s$ (Spallanzani et al., 2022). In contrast, lithium with its significantly higher diffusivity requires only ~10 seconds to ~25 minutes to homogenize under the same respective conditions (Spallanzani et al., 2022). As these calculations account for decompression rate-dependent bubble distribution and sizes, which provides an approximate path length for boron diffusion into the volatile phase (from melt into the bubble), the timeframe also symbolizes exsolution rates.

In a more field-based context, Schmitt and Simon (2004) examined boron isotopic values in melt inclusions and volcanic glasses from multiple eruptions of Long Valley, California. Trends were evaluated considering several factors such as degassing, which makes it the biggest case study on boron degassing systematics at the time. They concluded that possible degassing related isotopic fractionation variations are insignificant, and portrayed trends could be attributed to processes such as assimilation of hydrothermally altered rocks subsequent to injection of fresh magma into the reservoir. However, their methodology combined multiple differently timed and separate eruptions into a single analysis, which may obscure eruption-specific degassing trends.

To assess the usage of the boron isotopic system as a possible additional degassing tracer, this thesis analyses boron isotopic signatures and concentrations in samples from the Big Glass Mountain (1060 CE) eruption, California. The boron data are then paired with their specific water contents and hydrogen isotopic signatures, to investigate boron degassing systematics (Chapter 8). Furthermore, trends of individual eruptions at Long Valley (Schmitt and Simon, 2004) are evaluated using an updated version of the "VolcDeGas" program (Chapter 8).

### 2.2.2 Boron degassing modeling

The boron system employs the same formulae for closed, open, and batched degassing as the hydrogen system, which is exhaustively described in Chapter “2.1, Degassing modeling". The only difference lies in the replacement of variables whereas δD designations are substituted with $\delta^{11}B$ (or δB), and the water content ($H_2O$) is swapped with the boron content. However, the calculation of the boron fractionation factor between fluid and melt ($\alpha_{f-m}$) diverges from that of hydrogen. For boron, alpha is experimentally determined for low boron concentrations utilizing the equation by Maner and London (2018):

$$1000 * \ln(\alpha_{m-f}) = 0.6962 \times \left(\frac{1000}{T}\right) - 7.5821 \quad (8)$$

Where T is the temperature in Kelvin.

The alpha factors for magmatic temperatures derived from Maner and London (2018) are less than one and pertain to the fluid rather than the melt. To correlate these values to the melt, they must be recalculated using the equation:

$$\alpha_{f-m} = \frac{1}{\alpha_{m-f}} \quad (9)$$

This approach aligns with the fact that the melt is depleted in the heavier isotope (e.g., Hervig et al., 2002; Maner and London, 2018). It is generally recognized that an alpha factor (see also Equation 4) greater than 1 leads to the depletion of the heavier isotope in the phase of the denominator (here melt), whereas an alpha factor less than 1 results in its enrichment. Finally, the alpha factor is independent of the boron concentration, making temperature the only variable in this calculation (Maner and London, 2018).

## 2.3 Numerical modeling

As part of this thesis a program titled VolcDeGas was developed utilizing MatLab. It features a user-friendly program employing a graphical user interface (GUI) and is designed to iteratively calculate large amounts of degassing histories for isotopic systems based on inputs such as initial concentration values, step size, optional speciation values, initial δ range, and natural data.

The program detects the best-fitting degassing trends for each system to natural data by minimum Root-Mean-Square-Error (RMSE), and it visualizes the results in δ vs. concentration

graphs. Additional button functionalities include layout customization of the graphs and data export to Excel.

The hydrogen system employment of VolcDeGas, which is described Chapter 5 and published in Walter and Castro (2020), serves as the foundation for the program. Subsequently, the boron system was integrated into VolcDeGas and applied in Chapter 8 as a second standalone part. A comprehensive summary of the program, its theoretical approach, results, and conclusions is provided in Chapters 5 and 9.1.

# Chapter 3

# Thesis outline

## 3.1 Thesis aims

The aim of this thesis is to expand our knowledge of rhyolite magma's eruptive mechanism, chronology, and origins of eruption transitions through the investigation of degassing in rhyolitic melts. In addition, this work aims to document and analyze obsidian textures within deposits formed during explosive and effusive activity. Special attention is given to isotopic tracers of degassing, specifically in the form of the established hydrogen isotopic system, and their numerical modeling employing the self-written VolcDeGas program.

The findings highlight that hybrid eruption styles—recently observed in two Chilean volcanoes—are more common than previously recognized, which has crucial implications for hazard assessments. The thesis further suggests that hybrid activity is linked to the batched-degassing system, the fragmentation and sintering mechanism, and regassing. Furthermore, it was determined that the boron isotopic system is not a reliable tracer for degassing related studies in natural systems, as degassing appears to be inhibited, resulting in the signature being obscured by other stronger geochemical processes and factors.

## 3.2 Chapters outline

**Chapter 4** describes the analytical techniques utilized to evaluate natural samples in this thesis.

**Chapter 5** published as Walter and Castro (2020), presents the VolcDeGas program, which was designed to iteratively model degassing histories of rhyolitic eruptions. The program additionally objectively identifies the best-fit degassing systems to natural data. Its functionality is validated using historical natural datasets and previously published models. Moreover, the program is employed to investigate the theoretical degassing behavior of closed, open and batched systems. The results reveal that the program can be employed for degassing modeling and best-fit analyses. Furthermore, it was discovered that batched degassing systems are highly sensitive to the amount of water loss at each simulated degassing interval/step, allowing them to replicate both closed- and open-system behaviors. This insight directed the development of an enhanced system within the program, incorporating a batched model with

"variable step size". This system considerably improves the ability of the program to replicate natural degassing systematics, especially those observed in hybrid eruption systems, such as the simultaneous explosive and effusive activity of Chaitén (2008) and Cordón Caulle (2011), both in Chile.

**Chapter 6** published as Castro and Walter (2021), applies VolcDeGas to study the pre-historic 1060 CE Big Glass Mountain eruption in California, USA. Textural and geochemical evidence of pyroclastic and effusive deposits indicate a hybrid activity similar to that observed at Chaitén in 2008, and Cordón Caulle in 2011. Furthermore, hydrogen isotopic data, analyzed using VolcDeGas, reveal that a batched system with variable step size best represents this hybrid activity. These findings suggest that hybrid activity may have been more common in pre-historic eruptions than previously recognized, and therefore could also occur in future eruptions. Misinterpreting the start of lava effusion as the termination of explosive activity, rather than recognizing the possibility of simultaneous explosive and effusive activity, could lead to a significant underestimation of associated risks to ecosystems, human life and air traffic.

**Chapter 7** explores three rhyolite eruptions at Lipari, Sicily, around 1250 CE (e.g., Pistolesi et al., 2021) regarding their texture, hydrogen isotopic signature and concentration. Here, the same approach as for the previous chapter is applied. The first-ever δD measurements of obsidian in explosive and effusive deposits from these eruption centers were made, as well as textural analyses and past research support the notion of co-eruptive activity and the underlying eruption sequence being that of a joint hybrid activity. The study also proposes linking the mechanism responsible for hybrid activity, the cryptic fragmentation, to the batched-degassing system, and to regassing. These insights are an important addition to the hazard assessment in Lipari and emphasize the broader consequences of hybrid eruptions. This chapter is based on a manuscript submitted to the *Bulletin of Volcanology*, which is currently under review.

**Chapter 8** evaluates the boron isotopic system as a potential tracer of degassing in rhyolitic melts. Boron concentrations and isotopic compositions were measured in obsidian samples from the 1060 CE Big Glass Mountain eruption (California, USA) and compared with their respective water contents and hydrogen isotopic values. Literature data from different eruptions at Long Valley (Schmitt and Simon, 2004) were also analyzed using the same methodology. The results show that the boron isotopic data do not display a noticeable degassing trend, and no correlation exists between the two systems, indicating that degassing has little effect on the boron system. Theoretical degassing models generated with VolcDeGas further suggest that degassing-induced fractionation in natural boron systems is minimal and

likely obscured by other processes. A key factor that may explain these findings is the slow diffusion rates of boron in rhyolitic melts, which could inhibit efficient outgassing and isotopic fractionation. This work concludes that boron isotopes are not suitable to trace degassing in rhyolitic systems.

**Chapter 9** summarizes and concludes the key findings of this thesis together with the implications for understanding eruptive processes and degassing dynamics. Future research questions arising from this work are also outlined.

### 3.3 Authors contributions

**Chapter 5** VolcDeGas: A program for modelling hydrogen isotope fractionation during degassing of rhyolitic melts - Sebastian C. Walter (SCW), Jonathan M. Castro (JMC), 2020: SCW developed, tested, and utilized the VolcDeGas program, interpreted data, and wrote the initial version of the manuscript. JMC helped to conceive the project, assisted with data interpretation and revised and rewrote the manuscript.

**Chapter 6** Hybrid rhyolitic eruption at Big Glass Mountain, CA, USA - Jonathan M. Castro (JMC), Sebastian C. Walter (SCW), 2021: SCW prepared samples, performed FTIR analysis, applied VolcDeGas, and co-wrote the manuscript. JMC collected the samples, co-authored the manuscript, guided the FTIR analysis and provided project funding. Both Authors contributed equally to reviewing and editing.

**Chapter 7** Hydrous geochemical evolution of the Lipari rhyolites during multi-vent, hybrid volcanic activity (under review) - Sebastian C. Walter (SCW), Jonathan M. Castro (JMC), Ilya N. Bindeman (INB): SCW prepared samples, conducted FTIR measurements, analyzed data using VolcDeGas and wrote the initial manuscript, while JMC provided project funding and co-wrote the manuscript. JMC and SCW collected the samples and INB measured the samples via TCEA-MS. All authors reviewed and edited the manuscript prior to submission, and assisted with data interpretation.

### 3.4 Software

This thesis was written utilizing Microsoft Word 365 for Enterprise version 2411. MatLab 2018b was used to develop the VolcDeGas program which was then employed to generate degassing graphs. Graphs were also created and edited with ImageJ (version 1.54f) with integrated Fiji bundle (version 2.16.0) and Microsoft Excel 365 for Enterprise version 2411. Figure editing and schematic drawings were primarily performed using Paint.Net (version 5.1.8) and Microsoft Paint (version 11.2504.551.0).

# Chapter 4

# Analytical techniques

### 4.1 FTIR spectroscopy

Fourier-Transform Infrared (FTIR) spectroscopy is a widely adapted analytical technique in Geoscience, and is detailed in works like Cherniak et al. (2010); Aulock et al. (2014); Della Ventura et al. (2014). The major principles and procedures of FTIR spectroscopy are summarized below.

FTIR is used for both qualitative and quantitative analysis of chemical species and molecules in solids, liquids, and gases. It is based on the vibrational motion of molecules or clusters, which are excited by infrared (IR) irradiation. This interaction results in absorption of IR light at specific wavelengths, with the absorbance being characteristic for each substance (e.g., $OH^-$, molecular water). FTIR uses electromagnetic radiation in the IR-region ($\lambda$ ~ 0.75–100 μm), which has a longer wavelength than visible light ($\lambda$ ~ 400–750 nm). FTIR spectra are typically represented in terms of wavenumber ($cm^{-1}$), the number of waves per unit length.

The FTIR apparatus contains an IR light source that emits a beam, which is collimated and directed through a Michelson interferometer. Inside the interferometer, the beam encounters a beam splitter (e.g., KBr in this study), which allows part of the beam to be transmitted and another part to be reflected. The transmitted beam is then reflected by a moving mirror, while the other portion of the beam is directed to a fixed mirror. As the moving mirror changes position, it alters the optical path length. Both beams then recombine at the splitter, where they interfere with each other, and the resulting beam is focused on the sample. Upon interacting with the sample, specific wavelengths of IR radiation are absorbed. The remaining light reaches the detector, generating an interferogram that records light intensity as a function of the moving mirror's position—an effect known as retardation. Finally, Fourier transformation computations convert the interferogram into a complete spectrum across the IR range.

As the FTIR machine is usually not evacuated, the beam traverses ambient air and therefore a background or blank measurement is necessary to account for absorption by atmospheric components such as $H_2O$ and $CO_2$. The practice of data analysis involves regular background scans and measuring the peak high (absorbance) of the targeted species. For quantitative analysis, absorbance (A) is incorporated into the Beer-Lambert Law as:

$$A = \epsilon \, l \, c \tag{10}$$

Where absorbance (A) is dimensionless, $l$ is the path distance of the beam through the sample material in cm, $\epsilon$ is the molar absorptivity (or absorption coefficient) of the sample in L * $mol^{-1}$ * $cm^{-1}$ and $c$ is the molar concentration in mol $l^{-1}$.

In earth science mass fractions (W) of the absorber are frequently utilized (kg/kg) which can be converted to wt.% through multiplying W by 100. Incorporating this element, the Beer-Lambert equation is updated as follows (Aulock et al., 2014):

$$W = \frac{A \; M}{\epsilon \; l \; \rho} \tag{11}$$

Here, the same labeling as in Equation 10 is applied. In addition, M is the molar mass in g/mol of the absorber species, and $\rho$ is the density of the sample in kg $m^{-3}$.

In transmission FTIR spectroscopy, silicate glass samples can be measured, as applied in this thesis. In this FTIR mode, the path length ($l$) is obtained by thickness of the prepared wafer, while the sample density ($\rho$) can be attained via established methods such as the Archimedean approach as utilized in works like Richet et al. (2000). The molar absorption coefficient of each species ($\epsilon$) is related to bulk chemistry and is required for every individual sample material. For common samples of similar compositions (e.g., silicic glass), predetermined values exist in the form of lists such as shown in Table 1 of Aulock et al. (2014).

FTIR sample preparation is usually the most time-consuming process. Samples for volcanological studies can be prepared as KBr pellets (sample powders mixed with KBr and pressed into disks) for bulk composition analysis of materials such as ash, or as double polished wafers (e.g., glass, minerals) for spatially resolved quantitative analyses. The wafer production process demands precise polishing on both sides of the sample to achieve a flat surface and a consistent thickness that aligns with the estimated concentration of the pursued species. It is common practice to manufacture wafer thicknesses ranging between tens to hundreds of micrometers. For samples containing low concentrations of the species of interest, thicker wafers may be prepared to generate a higher signal-to-noise ratio. This in turn has the additional advantage of enhancing sample durability and minimizing the risk of breakage, which is more likely to happen with very thin wafers. Establishing the ideal thickness requires careful pre-estimations, balancing factors like species concentration, crystal content, sample opacity, and absorbance-to-background ratio. Therefore, samples preparation must be

conducted with precision and accuracy as it is the most important step to produce compelling and interpretable FTIR data. Detailed guidelines for FTIR sample preparation, specifically in relation to the volcanological context, are outlined in Aulock et al. (2014).

The FTIR method presents several benefits, including non-destructive analysis, rapid and high-precision quantitative measurements over the entire IR-range, spatial resolution down to 3 µm, and cost-effectiveness. However, the main disadvantage of this method is the time-intensive and demanding sample preparation process which must be performed diligently to ensure high-quality results. Additionally, extinction coefficients for the material of interest must be available for precise quantitative data or need to be derived from calibrations employing other techniques.

For this thesis, FTIR spectroscopy was employed in transmission mode to quantify hydrous species concentrations (OH-groups and molecular water) as well as bulk water content in dense glass samples (pyroclasts and lavas) from deposits associated with three eruptions on Lipari (Rocche Rosse, Lami, Forgia Vecchia; ~1250 CE: Pistolesi et al., 2021), Sicily, and the Big Glass Mountain eruption (1060 CE) at Medicine Lake, California. Information on the sample collection for these locations, and the FTIR procedures applied to the samples, is provided in Chapters 6 and 7, while a summary of the measurement technique is outlined below.

All samples were prepared according to the techniques described earlier, at the Johannes Gutenberg-University (JGU) in Mainz, Germany. Measurements were conducted at the JGU, employing a Thermo-Nicolet FTIR Bench with attached Continuum microscope. The system includes a nitrogen-liquid-cooled mercury cadmium telluride (MCT) detector and a KBr beamsplitter, allowing for detection across a broad spectral range (~6000 $cm^{-1}$ to <1000 $cm^{-1}$). Measurements were performed in transmission mode on ~50 µm spots of clean, dense obsidian, each scan being an average of 265 individual measurements per spot. The spectral resolution was set to 4 $cm^{-1}$, and sample thicknesses were determined using a Mitutoyo digital micrometer with an accuracy of ~5 µm. Sample-free background scans were conducted at least every 30 minutes to account for variations in ambient air composition (e.g., $CO_2$, $H_2O$).

Peak heights were measured relative to the baseline and incorporated into Equation 11, along with sample thickness, density, and other required parameters, to obtain quantitative results. The analyzed peaks included the 4500 $cm^{-1}$ (OH), 5200 $cm^{-1}$ ($H_2O_m$) bands, mainly for wetter samples, and the 3550 $cm^{-1}$ (OH) peak for dry samples (<0.1 wt.% $H_2O$). Rhyolitic absorption coefficients of Ihinger et al. (1994) were utilized for the 4500 $cm^{-1}$ and 5200 $cm^{-1}$ peaks, and of Okumura (2005) for the 3550 $cm^{-1}$ peak.

## 4.2 Isotope-ratio mass spectrometry

Mass Spectrometers (MS) are broadly used to detect the mass-to-charge ratios of charged particles (ions), with a mass spectrum as the output. These instruments can be employed to detect elemental or isotopic signatures, to determine the masses of particles and molecules, and to uncover the chemical identity or structure of molecules and other chemical compounds. Various types of mass spectrometers exist, utilizing different geometry, separation methods or acceleration techniques.

An Isotope-Ratio Mass Spectrometer (IRMS), as employed in this thesis, is used to measure isotope ratios of diverse isotopic systems. In this device, the sample is ionized and accelerated by a high voltage (e.g., 10 kV), generating a stream of ions that are separated based on their mass-to-charge ratios. This separation is accomplished by a magnetic field, bending the ion beams where lighter ions follow smaller-radius trajectories, and heavier ions track larger-radius paths. The distinctive ion beams then reach Faraday cups or electron-multiplier detectors, which convert the ion currents into electrical signals producing a mass spectrum that can be used to determine isotopic ratios.

### 4.2.1 TCEA-MS

The Temperature Conversion Elemental Analyzer also referred to as TC/EA or TCEA operates in tandem with a Mass Spectrometer, specifically an IRMS as employed in this thesis. It is a device that converts liquid or solid samples into gaseous form, which is then injected into and analyzed by a Mass Spectrometer. The core component of the TCEA is the reactor chamber, where bulk material is heated to temperatures typically exceeding 1400 °C in a reducing environment. The resulting gases are then transferred to an isothermal gas chromatograph, where the target gas is separated from other components before introduction into the IRMS. There, the gas of interest is ionized, separated by mass-to-charge ratio, and measured. This technique is commonly used to analyze isotope systems such as those of hydrogen, carbon, nitrogen, and oxygen.

Isotope ratios are expressed in delta notation (e.g., δD), as outlined in Chapter 1.2, and calculated by Equation 1. They are measured relative to an international standard material, which establishes the isotopic measurement scale of each isotopic system. Additional standards can be measured, and their data utilized alongside predetermined calibration curves, to calibrate e.g., total δD and water data.

The solid sample preparation for TCEA typically involves grinding the substance into a powder which is then sieved to achieve suitable grain sizes (e.g., 75-150 µm) for an efficient heating process. This powder is weighed with at least 5-digit precision (typically a few milligrams, depending on water content), packed into silver foil and sealed shut to prevent leaks. For hydrogen isotope analysis, it is advantageous to heat powdered samples under vacuum at 130 °C for an extended period before measurement to remove loosely bound absorbed water (see also Chapter 1.5). Examples and instructions for optimal preparation are provided in studies such as Giachetti et al. (2020).

The TCEA/MS technique is particular suitable for measuring isotope ratios and can also be employed to acquire concentration values. Furthermore, the preparation times are relatively short. However, disadvantages include the high operation costs, the time-consuming measurements, the need for accurate weighing and packing, the possible leaks in the silver foil package, and the limited different isotopic systems which can be analyzed.

Over the course of this study, TCEA-MS preparations on obsidian samples were performed at two institutions: the Johann Wolfgang Goethe-University in Frankfurt and the Johannes Gutenberg-University (JGU) in Mainz. Preparations for the Lipari obsidian samples were solely carried out at the JGU, while those for the Big Glass Mountain (BGM) samples were conducted at both JGU and the Goethe University. At each location, the previously described preparation methods were applied.

Measurements of BGM samples were conducted at the Johann Wolfgang Goethe-University in Frankfurt under the supervision of Jens Fiebig, and samples of Lipari were analyzed at the Stable Isotope Laboratory at the University of Oregon by Ilya Bindeman. At both facilities, δD and water contents were measured employing a Thermo Finnegan TCEA-MAT 253 IRMS system, in relation to the V-SMOW standard. In Frankfurt, standard glasses NBS-30, NBS-22, and CH7, and in Oregon standards USGS57 (biotite) and USGS58 (muscovite) were employed to calibrate total δD and $H_2O$ data as well as rhyolitic glass UOR1 and low-δD mica BUD. Further details on sample preparations and measurements are presented in Chapters 6 and 7.

### 4.2.2 SIMS

Secondary Ion Mass Spectrometry (SIMS), also known as ion microprobe analysis, is a microanalytical technique that utilizes a focused primary ion beam with energy levels of several KeV. This beam impacts the sample surface, sputtering atoms from the uppermost layer (tens

of nanometers deep) which produces secondary particles. The ions among these secondary particles are accelerated by a strong electric field forming a secondary ion beam that is analyzed by a mass spectrometer (see Section 4.2).

SIMS can measure almost all elements of the Periodic Table, except noble gases, but is specifically well-suited for isotope ratio and trace element analyses. This method can achieve spatial resolutions of ~10 µm for horizontal scans. Due to the sputtering effect, the primary beam can incrementally abrade the surface, allowing for limited depth profile analyses, a capability which has been demonstrated in studies such as Cherniak et al. (2010). Similar to the TCEA-MS, in the case of isotopic measurements, their ratios are expressed by δ and are measured relative to a specific standard.

The sample preparation technique for solid samples involves the mounting of the material (e.g., glass) into epoxy and polishing the surface, which is subject to the measurement, flat. Additionally, gold coating is required to prevent surface charging. Samples are typically dried in an oven prior to analyses to minimize alteration by loosely bound external substances.

The key advantage of SIMS is the ability to analyze nearly all elements, measure isotope ratios and trace elements, and that only a small amount of sample material is required for successful measurements. Another benefit is the high spatial resolution. Although this method is not completely destruction-free, SIMS only creates nanometer-sized craters on the sample surface which can also be used for depth profiling by focusing the beam on a spot for a longer time. The main shortcomings are its very high operational costs and the time-consuming nature of the measurements.

In this study, SIMS was utilized to analyze the boron content and isotopic composition of BGM samples. The sample preparations and measurements were performed at the GeoForschungsZentrum (GFZ) in Potsdam by Alexander Rocholl/Michael Wiedenbeck employing a CAMECA 1280-HR SIMS system, measured relative to standard glass Rocc-3. The reference glass StHs6 was additionally employed for quality control. Three to five spot analyses were performed on each sample to determine average sample values.

# Chapter 5

# VolcDeGas: A program for modeling hydrogen isotope fractionation during degassing of rhyolitic melts[1]

**Keywords: Obsidian; Rhyolite; Explosive-effusive eruption; H-isotopes; Fractionation; Modeling**

**Abstract**

Magma degassing mechanisms are key determinants of explosive and effusive eruption styles. Paired measurements of $H_2O$ content and hydrogen isotopic ratios (e.g., δD) in pyroclastic and effusive products can elucidate endmember degassing mechanisms (e.g., closed and open system) during eruption. Here we present "VolcDeGas", a MatLab program that models δD-$H_2O$ degassing trajectories of rhyolitic magma. Operating within an intuitive GUI, VolcDeGas calculates degassing paths based on: initial δD (in ‰), the $H_2O$ content of the melt (wt.%), degassing step size, and temperature. VolcDeGas also calculates hydrous speciation based on either empirical models or analytical data, and incorporates this effect in simulations. VolcDeGas solves open-, closed-, and batched-system fractionation equations, and also combines these into multi-stage (e.g. closed-to-open) degassing paths. Tests show that degassing is highly sensitive to step size, and multi-stage scenarios involving progressively declining steps (e.g., a closed- to batched-system) provide the best statistical fit to pyroclastic and effusive obsidian geochemical datasets.

[1] This chapter is published as Walter, S., Castro, J., 2020. VolcDeGas: A program for modelling hydrogen isotope fractionation during degassing of rhyolitic melts. Volcanica 3 (1), 155–168, doi: 10.30909/vol.03.01.155168

## 5.1 Introduction

### 5.1.1 Natural context: rhyolitic volcanism

Much volcanological research over the last decades has been focused on understanding the mechanisms driving silica-rich rhyolite eruptions (e.g., Melson and Saenz, 1973; Wilson, 1976; Ninkovich et al., 1978; Castro and Dingwell, 2009; Alfano et al., 2011; Ogburn et al., 2015). Moderately sized rhyolite eruptions (<1 $km^3$), while rarely directly observed, often start with an explosive phase that involves fragmentation and the formation of pyroclastic columns (Castro and Dingwell, 2009). Sometime later the eruption transitions to an effusive phase whereby lava is emitted (Castro et al., 2012; Castro et al., 2013; Tuffen et al., 2013). This sequence is termed an “explosive-to-effusive” eruption. Specifically how the transition between eruption styles occurs—e.g., how long it lasts and what triggers it—has long been a target of investigations (Eichelberger et al., 1986), as it bears on the way hazards are understood and eventually mitigated. Prior to the first direct observations of rhyolite activity (e.g., Castro and Dingwell, 2009), it was assumed that these eruptions transitioned rapidly from explosive to effusive behavior, this interpretation being based on the conformable superposition of obsidian lavas on co-eruptive pyroclastic fall deposits (e.g., Taylor et al., 1983; Newman et al., 1988). Hydrous geochemical patterns (i.e., δD vs. $H_2O$ trajectories) measured in the deposits of pre-historic eruptions were interpreted to reflect a two-staged degassing sequence comprising initial closed- and later open-system degassing (e.g., Eichelberger et al., 1986; Newman et al., 1988; Dobson et al., 1989) and corresponding to the purported pyroclastic to effusive activity. Thus, the phrase “explosive-to-effusive transition” was meant to encapsulate both the physical and geochemical aspects of an eruption sequence, even though these eruptions remained unobserved. Detailed observations and geochemical measurements of the 2008 eruption of Chaitén, Chile (Castro et al., 2014) showed that rhyolite eruptions may not follow the previously accepted explosive-to-effusive paradigm. Notably, this eruption lacked a sharp explosive-to-effusive transition and was instead characterized by “hybrid” activity—simultaneous pyroclast and lava venting—during most of its duration (e.g., see also Castro et al., 2013). The hydrous geochemical signature of Chaitén’s deposits, is furthermore, consistent with a one-staged degassing mechanism that lacked a transition (to be discussed in further detail in Subsection 5.1.3). In this work we present VolcDeGas, a tool that can model both one- and two-staged degassing paths so as to account for the variety of measured hydrous geochemical patterns in eruption deposits.

Explosive and effusive eruption styles are influenced by the budget and behavior of volatile components in the melt, which are dominantly $H_2O$ originating from the magma storage region

(e.g., Luhr, 2001; Castro and Dingwell, 2009; Castro et al., 2014). Due to the strong dependence of $H_2O$ solubility on pressure, $H_2O$-rich bubbles will grow in the magma as it decompresses during ascent (e.g., Eichelberger et al., 1986; Allard et al., 1991; Blank et al., 1993; Ryan et al., 2015). Depending on many complicated trade-offs between magma porosity and permeability, and magma ascent dynamics, the magma may begin to violently fragment (Gonnermann and Manga, 2007). Experimental and analytical evidence suggests that high initial magmatic $H_2O$ contents lead to explosive fragmentation and lower initial magmatic $H_2O$ contents prompt coherent lava flows (Forte and Castro, 2019). Other variables such as temperature and decompression rate are also important for how degassing takes place (e.g., Gonnermann and Manga, 2007; Forte and Castro, 2019). In our model, we address a range of $H_2O$ and temperature conditions on resultant degassing paths in rhyolite magma.

Hydrogen isotope ratios (e.g., the deuterium/hydrogen ratio), generally cast in terms of the variable δD, is calculated as the difference between ratio of the measured H-isotopes, D/H, in the unknown sample and a standard (e.g., Standard Mean Oceanic Water: SMOW) normalized by the D/H ratio of a standard:

$$\delta D = \frac{(\frac{^2H}{^1H})_{Sample} - (\frac{^2H}{^1H})_{Standard}}{(\frac{^2H}{^1H})_{Standard}} \times 1000‰ \quad (12)$$

Such isotopic ratios are routinely measured in concert with magmatic $H_2O$ to synoptically track degassing processes that give rise to pyroclastic-effusive sequences (Taylor et al., 1983). Traditionally, δD's are plotted against the bulk-$H_2O$ content measured on obsidians, and the resulting plots or "degassing trends" interpreted in terms of end-member degassing mechanisms (Figure 5.1).

Because deuterium fractionates preferably into volatile phase (Taylor et al., 1983) magmatic degassing results in isotopic "lightening" of the residual melt, leading to trends pyroclastic sample arrays that are characterized by subtle to sharp decreases in δD with decreasing $H_2O$ concentration (e.g., Taylor, 1991; Castro et al., 2014). Degassing trends will reach a minimum at the most-degassed levels, and often, lava samples' δD demarcate a strong final downturn in the degassing path (Figure 5.1). This pattern has been observed at numerous rhyolite systems and has been widely interpreted as a signature "open-system" degassing (e.g., Taylor et al., 1983; Eichelberger et al., 1986; Newman et al., 1988; Castro et al., 2014).

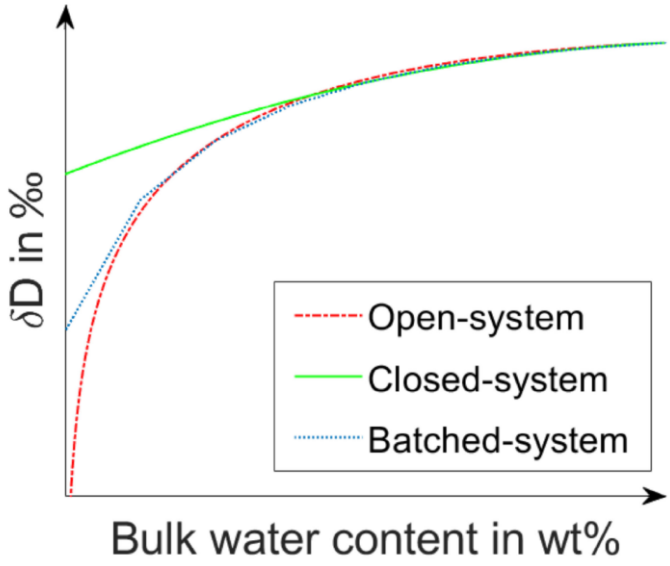


**Figure 5.1:** Qualitative trends of hydrogen isotope fractionation occurring during different degassing modes. In each case, the effect of degassing—i.e., progressive separation of $H_2O$ from melt—results in a decrease δD. [A] Closed-system degassing results in a relatively subtle near-linear drop in δD. [B] Open-system degassing (Rayleigh fractionation) results in a non-linear yet significant depletion in δD at low $H_2O$ contents. [C] Batched-degassing, a hybrid mechanism comprising both closed and open-system elements, involves repetitive degassing "steps", the size of which dictate the ultimate degree of δD decrease as degassing progresses to low $H_2O$ contents.

### 5.1.2 $H_2O$ speciation in rhyolitic melts

$H_2O$ in silicate melt exists as hydroxyl groups ($OH^-$) and molecular water ($H_2O$), with the relative amounts of these hydrous species being controlled by the bulk $H_2O$ content and temperature (Stolper, 1982). Although these two species exist, it is the molecular $H_2O$ that diffuses out of the melt and into bubbles (Zhang et al., 1991). Since deuterium is preferentially fractionated into the vapor, the degree of fractionation (and path of δD) depends on how the species ratios change with falling $H_2O$ concentration. A hydrogen isotope fractionation factor between vapor and melt in rhyolitic melts, alpha ($\alpha_{v-m}$), accounts for this speciation dependence on bulk $H_2O$ content in modeling degassing trends (Newman et al., 1988). Thus, to completely retrace the degassing history several variables need to be known or estimated: $\alpha_{v-m}$, temperature of the melt, initial bulk $H_2O$ content and initial δD. Early studies performed hydrogen fractionation calculations with a constant $\alpha_{v-m}$ factor (Taylor et al., 1983); these factors were experimentally determined (Taylor et al., 1983; Newman et al., 1988; Dobson et al., 1989). However, as the hydrous speciation of the melt (i.e., the relative proportions of $OH^-$ and $H_2O$ species) is dependent on both the total $H_2O$ content and temperature, both of which may change during an eruption, alpha factors are not likely to be constant. Accordingly, later studies used hydrous-speciation dependent $\alpha_{v-m}$ factors.

In addition to syn-eruptive degassing, the uptake of externally derived meteoric water during rehydration of obsidian may alter the hydrogen isotopic signature of eruption products (e.g., DeGroat-Nelson et al., 2001; Seligman et al., 2018). While the degree to which original magmatic isotope signatures are altered depends on both time and the isotopic composition of the external water, significant departures of δD-$H_2O$ from idealized magmatic degassing trends have been observed (e.g., Giachetti and Gonnermann, 2013; Bindeman and Lowenstern, 2016; Seligman et al., 2018). This warrants independent control on the magmatic versus meteoric signature of the isotopic and bulk $H_2O$ signatures of eruption deposits.

### 5.1.3 Observations of rhyolitic eruptions

The 2008 eruption of Chaitén volcano, Chile (Castro and Dingwell, 2009; Alfano et al., 2011) provided many new insights into the degassing systematics and eruption mechanisms of rhyolitic systems. This was the first opportunity to see how the actual “explosive-to-effusive” sequence came about, and given close observations (Lara, 2009) it became clear that the previously assumed temporally sharp changeover of explosive-to-effusive activity (e.g., Eichelberger et al., 1986) was not the case (Castro et al., 2012). Instead, after a period of about two weeks of purely explosive activity, a simultaneous lava and pyroclastic eruption occurred and lasted several months before solely lava effusion closed out the eruptive episode. This simultaneous, or "hybrid" eruption style (e.g., Castro et al., 2013), involved intermittent pyroclastic explosions from several vents stationed within the effusing lava itself (Schipper et al., 2013). As observations of the Chaitén event may shed new light on how other pre-historic eruptions like Mono Craters, Big Glass Mountain, (USA) and Big Obsidian Flow (USA) may have behaved (Rust and Cashman, 2007; Castro et al., 2014), here we aim to use geochemical characteristics of the eruption deposits of Chaitén and Mono Craters to model aspects of rhyolite eruption systematics. This work presents a new program that can be used to investigate how eruption styles relate to degassing mechanisms (Figure. 5.1) with particular emphasis on H-isotope and $H_2O$ content systematics in eruption deposits.

### 5.1.4 Modeling theory and degassing path calculations

Hydrogen-isotope fractionation patterns in rhyolitic magmatic systems have been explained in a relatively small number of ways (Figure 5.1): 1) by a closed system; a simple conservative mass balance between melt and vapor, 2), by an open system involving Rayleigh fractionation, and 3) as a batched-system (Taylor, 1991) comprising combinations of closed- and open-system degassing. Modeling these isotopic and degassing patterns assumes that the outgassed part of the volatile system was in equilibrium with the remaining parts of the system

(i.e., the quenched silicate glass). Analysis of eruption deposits, therefore, track the remaining mass of $H_2O$ and H-isotopic composition of the glassy pyroclasts rather than the once-present vapor. Additionally, in all model systems, the step size—defined as a fixed amount or the percentage of bulk water loss at each degassing interval—is an initial condition and is required for calculating each point in the degassing history. In the following sections we describe each system in detail including their respective H-isotopic fractionation equations.

#### 5.1.4.1 Closed-system degassing

Closed-system degassing takes place when volatile components begin to exsolve into vapor bubbles (e.g., Anderson and Fink, 1989; DeGroat, 1997) and may continue to shallow (hundreds of meters) levels in a feeder conduit, potentially driving explosive fragmentation (e.g., Eichelberger et al., 1986; Newman et al., 1988). In these scenarios, melt and fluid and/or vapor stay in contact and it is assumed that compositional equilibrium is maintained between these phases. As no material is added or released from the magmatic system, these conditions comprise a mass-conservative system, and consequently the isotopic composition of hydrogen in the melt is a strong function of that in the bubbles. This "equilibrium buffered state" whereby the ambient pressure controls the amount of $H_2O$ exsolution—and therefore the hydrogen fractionation degree—is not to be confused with buffered states within an open-system, whereby the gas-rock ratio is so high that equilibrium is maintained between melt and the permeating gas (e.g., Rust et al., 2004). Closed-system conditions can however give way to open-system degassing when a magma reaches the critical vesicularity to stimulate effective melt-gas separation via permeable gas flow (Eichelberger et al., 1986).

Isotopic fractionation in the closed-system is modeled by the mass balance equation (Taylor et al., 1983):

$$\delta D_f = \delta D_i - (1 - F) \times 10^3 \times \ln(\alpha_{v-m}) \quad (13)$$

Where $\delta D_f$ is the final δD value (in ‰) in the melt, $\delta D_i$ is the initial δD value of the melt, F is the fraction of $H_2O$ remaining dissolved in the melt, calculated as final $H_2O$ at the end of the process divided by the initial $H_2O$ content in the melt at the start of the process ($H_2O_f$ / $H_2O_i$), and $\alpha_{v-m}$ is the bulk H-isotope fractionation factor between vapor and melt at specific temperature and pressure conditions. Here, a “process” is defined as a cycle or a discrete degassing “step” which releases a fixed aliquot (e.g., a percent of total $H_2O$ budget) of vapor from the melt. Furthermore, in terms of modeling the closed system, the initial δD and initial bulk $H_2O$ content are thought to be constant through the process.

The isotopic shift in a perfectly closed system follows a nearly linear trend in wt.% $H_2O$-δD space and is relatively subtle in terms of the amount of fractionation that occurs with degassing. In other words, a large drop in bulk $H_2O$ content (several wt.%) results in only slight (few tens of ‰) decrease in δD.

### 5.1.4.2 Open-system degassing

During open-system degassing, volatiles are continually exsolved from melt into bubbles and, due to high magma porosity and permeability, these volatiles are immediately removed from the bubbly melt through pathways (e.g., magmatic foam, cracks, or the brecciated conduit walls; Eichelberger et al., 1986; Gonnermann and Manga, 2003). This highly effective degassing mechanism drives very strong isotopic fractionation, as equilibration between dissolved and exsolved $H_2O$ is prevented by the constant removal of gas. Open system isotope fractionation is described by the Rayleigh fractionation formula (Taylor, 1991):

$$\delta D_f = (\delta D_i + 1000) - (F^{\alpha_{v-m}-1}) - 1000 \quad (14)$$

Where $\delta D_f$ is the final δD value (in ‰) in the melt at the end of the process, $\delta D_i$ is the initial δD value of the melt at the beginning of the process, F is the fraction of $H_2O$ remaining dissolved in the melt, calculated as the final $H_2O$ at the end of the process divided by the initial $H_2O$ content in the melt at the start of the process ($H_2O_f$ / $H_2O_i$), and $\alpha_{v-m}$ is the bulk H-isotope fractionation factor between vapor and melt at specific temperature and pressure conditions.

Here, in contrast to the closed-system case, the initial δD ($\delta D_i$) as well as initial bulk $H_2O$ content ($H_2O_i$) are not constant because $H_2O$ vapor gets continually removed and consequently, the initial δD and $H_2O$ must be accordingly adjusted to lower values after each degassing step. In addition, degassing step size has an influence on the calculated δD value in the open system case because each successive "new" degassing aliquot must derive from an increasingly depleted hydrous reservoir. Therefore, calculations (in the open system) result in quite large isotopic fractionation (several tens of ‰) at low $H_2O$ content. Thus, $H_2O$-poor and strongly D-depleted lavas have been interpreted to be indicators of open-system degassing (e.g., Taylor et al., 1983).

### 5.1.4.3 Batched-system degassing

In batched-system or “multi-step open/closed” degassing (Taylor, 1991) batches of exsolved gases are held resident in the magma for periods of time (e.g., in bubbles or cracks; Castro et

al., 2012), and then get episodically released from the system in outgassing pulses. These successive gas-release events could, in principle, correspond to real explosions or blasts observed during activity (Schipper et al., 2013; Castro et al., 2014).

To simulate a batched-system, both open-, and closed-system degassing elements are required; collectively these two essential steps constitute a hybrid degassing cycle. That is, the initial exsolution stage takes place in a finite closed system step (using the appropriate mass-balance Equation 13) with gas staying trapped in contact with melt. This closed-system is then disrupted during a subsequent opening of this system, which then removes that aliquot of exsolved gas. The hybrid degassing cycle then repeats—all the while simultaneously accounting for the updated and incrementally lower $H_2O$ budget and δD values—until the point that the system eventually becomes highly depleted in deuterium at low total $H_2O$ contents. As Castro et al. (2014) showed, this gas release mechanism best explains large H-isotopic fractionation they measured on a suite of pyroclastic and effusive products from the 2008 rhyolite eruption of Chaitén volcano (Castro and Dingwell, 2009).

To simulate batched degassing, the formula of the closed system is used in a series of degassing increments, but the initial $H_2O$ content ($\mathrm{H_2O_i}$) which is established in the F-factor ($\mathrm{F} = \frac{\mathrm{H_2O_f}}{\mathrm{H_2O_i}}$) and $\delta\mathrm{D_i}$ get continually updated at the beginning of each step. As will be shown, the degree of fractionation during batched process is heavily influenced by the step size. Furthermore, this system can be simulated with variable step sizes (e.g., by implementing a percentage rather than fixed amount of water loss at each step), to mimic the observation of variably sized explosions during hybrid activity (e.g., Schipper et al., 2013).

#### 5.1.4.4 $\alpha_{\mathrm{v-m}}$ factor and speciation of $H_2O$ in rhyolitic melts

Regardless of the degassing system at hand (closed, open, or batched), variations of the alpha fractionation factor that occur during progressive $H_2O$ loss from the melt must be calculated (e.g., Newman et al., 1988). The bulk $H_2O$ hydrogen fractionation factor—hereafter referred to as "alpha factor"—between vapor and melt ($\alpha_{\mathrm{v-m}}$) in rhyolitic melts, is defined as:

$$\alpha_{\mathrm{v-m}} = \frac{\left(\frac{\mathrm{D}}{\mathrm{H}}\right)_{\mathrm{vapour}}}{\left(\frac{\mathrm{D}}{\mathrm{H}}\right)_{\mathrm{melt}}} = \frac{1000 + \delta\mathrm{D_{vapour}}}{1000 + \delta\mathrm{D_{melt}}} \quad (15)$$

Where all variables above are defined as before.

The influence of the hydrous species ratio on the $\alpha_{v-m}$ factor was first examined by Newman et al. (1988). They determined that since $H_2O$ is present in the glasses (Stolper, 1982) as both hydroxyl groups ($OH^-$) and molecular $H_2O$, the $\alpha_{v-m}$ factor should also change when the proportions of those two species change with decreasing bulk $H_2O$ content. Similarly, Holloway and Blank (1994) postulated that as the relative proportions of dissolved hydrous species change when the total amount of $H_2O$ is declining, the proportion of $OH^-$ (which has a large D/H fractionation with water vapor) increases as degassing progresses. Consequently, the bulk fractionation factor between the melt and vapor will increase as magma degasses. Moreover, the greatest change in isotopic composition of the melt resulting from degassing will occur at low total dissolved $H_2O$ content. Experimental calibrations of the effects of temperature and total $H_2O$ content on hydrous speciation are available in empirical studies (Stolper, 1982, 1989).

In order to calculate the $\alpha_{v-m}$ factor while accounting for its dependency on hydrous speciation, Newman et al. (1988) used polynomial curve fits to plots of "total wt.% $H_2O$" versus "wt.% as molecular $H_2O$", which were in turn based on their own measurements of hydrous speciation in obsidians. Alternatively, another way of determining the hydrous species in the melt and $\alpha_{v-m}$, is the "Sil/Hol" model, which was originally developed by Stolper (1989) and later modified by Silver et al. (1990). This "regular solution model" is implemented in a program by Holloway and Blank (1994) that numerically determines permissible values of speciation, output as "total wt.% $H_2O$" versus "wt.% as molecular $H_2O$" plots using empirical parameters.

To keep the variables needed to calculate degassing paths in VolcDeGas to a minimum, the following equations were used, deriving from the ideal mixing model of Stolper (1989). This model considers that the thermodynamic properties of the solution are analogous to those of a mixture of ideal gases. Firstly, the proportions of hydroxyl groups and the molecular $H_2O$ are governed by the equilibrium speciation equation with associated constant, K:

$$H_2O_m(melt) + O(melt) = 2OH \tag{16a}$$

$$K = \frac{[OH]^2}{[H_2O_m][O]} \tag{16b}$$

Where square brackets refer to the mole fraction of hydrous species in the melt on a single oxygen basis and O denotes anhydrous oxygen. The K factor is dependent on temperature and has been experimentally determined (Ihinger et al., 1999; Zhang, 1999), whereas the temperature (T) dependent K models of Zhang (1999) and Ihinger et al. (1999) produce nearly the same results. The model of Zhang (1999) has been utilized in this work:

$$\ln(K) = 1.89 - \left(\frac{3120}{T}\right) \quad (17)$$

Where T is in kelvin.

VolcDeGas models the hydrous silicate melt as an ideal mixture of $H_2O$ molecules, hydroxyl groups and oxygen atoms, as proposed by Silver and Stolper (1985). The following formula is used to calculate the mole fraction of $OH^-$ ($XOH_m$) (Silver and Stolper, 1985):

$$XOH_m = \frac{\frac{1}{2} - \left(\frac{1}{4} - \left(\frac{K-4}{K}\right) \times \left(X_{bulk} - {X_{bulk}}^2\right)\right)^{0.5}}{\frac{K-4}{2K}} \quad (18)$$

Where $X_{bulk}$ is the mole fraction of total $H_2O$ in the melt and can be calculated by (Silver and Stolper, 1985):

$$X_{bulk} = \frac{\left(\frac{wt.\%\ H_2O}{18.015}\right)}{\left(\frac{wt.\%\ H_2O}{18.015}\right) + \left(\frac{100 - wt.\%\ H_2O}{W}\right)} \quad (19)$$

Where W is the molecular weight of anhydrous silicate melt on a single oxygen basis (= 30.04 g $mol^{-1}$, based on the molecular weight of $SiO_2$, 60.08 g $mol^{-1}$), calculated by dividing the molecular weight of the substance by the number of oxygen atoms in the substance.

Each hydrous species ($OH^-$, $H_2O$) possesses its own alpha fractionation factor and is calculated independently, for example, the alpha factor for molecular $H_2O$ ($\alpha_{(v-m)H_2O}$) is determined as such:

$$\alpha_{(v-m)H_2O} = \frac{\left(\frac{D}{H}\right)_{vapor}}{\left(\frac{D}{H}\right)_{H2O-melt}} = \frac{1000 + \delta D_{vapor}}{1000 + \delta D_{H2O-melt}} \quad (20)$$

Here δD represent values of molecular water in the melt phase. “Vapor” refers to the gas phase. The hydroxyl group fractionation factor also employs a similar formula.

Once the alpha factors of each hydrous species are determined, VolcDeGas calculates the bulk fractionation factor with the following equation (Taylor, 1991; Rust et al., 2004):

$$\ln\left(\alpha_{(v-m)bulk}\right) = X \times \ln\left(\alpha_{(v-m)H_2O}\right) + (1 - X) \times \ln\left(\alpha_{(v-m)OH}\right) \quad (21)$$

Where X is the atomic fraction of hydrogen incorporated as molecular $H_2O$ dissolved in the melt and (1-X) is the atomic fraction of hydrogen as $OH^-$ in the melt. However, if $H_2O$ speciation data is available (e.g., from Fourier-transform infrared spectroscopy—FTIR—measurements), the following formula can be applied:

$$\alpha_{(v-m)bulk} = H_2O_{m,frac} \times \alpha_{(v-m)H_2O} + OH_{g,frac} \times \alpha_{(v-m)OH} \quad (22)$$

Where $H_2O_{m,frac}$ is the weight fraction of molecular $H_2O$ in relation to the total $H_2O$ content and $OH_{g,frac}$ is the weight fraction of the hydroxyl groups. In this case, the speciation-specific alpha factors, $\alpha_{(v-m)H_2O}$ and $\alpha_{(v-m)OH}$ are fixed values (0.9896 and 1.0415, respectively), after Rust et al. (2004).

## 5.2 Results

### 5.2.1 Program functionality and verification

The program VolcDeGas was written in MatLab and uses the formulae described in the previous sections to calculate entire degassing histories (i.e., spanning a range of high- to low-$H_2O$ content). Degassing paths may be modeled as either one-stage or two-stage, and may comprise open-, closed-, and batched system segments, as well as combinations thereof. The program is ideally suited for rhyolitic eruptions, whose glassy eruptive products have been routinely measured to yield δD vs. bulk $H_2O$ content relations, therefore providing a natural degassing trend to simulate with VolcDeGas.

VolcDeGas is operated by way of a user-friendly GUI in which the required input parameters (e.g., temperature, initial δD, initial bulk $H_2O$ content, step size, degassing mechanism transition point, speciation data), and plot layouts can be easily set (Supplementary Information[i], Figure A1-A2). Each parameter's input location in the GUI is indicated by a series of clearly defined labels that appear by hovering the mouse over them, allowing the user to understand which functions the buttons/parameters carry out. Once these parameters are loaded, VolcDeGas automatically calculates and displays the best-fit degassing paths to natural, user-input δD-$H_2O$ data (e.g., based on lowest Root-Mean-Square-Error (RMSE), and highest $R^2$; Supplementary Information[i]). Owing to the underlying Matlab code, which is thoroughly described in the dialog window in the program interface, the user can perform literally thousands of calculations per minute, a feat not possible by employing standard spreadsheet and graphing programs (e.g., Castro et al., 2014). An in-depth description of the

[i] Supplementary Information download: https://www.jvolcanica.org/ojs/index.php/volcanica/article/view/62/81

code can be found in the code comments and the program manual (Supplementary Information[i]).

In order to test the modeling capabilities of VolcDeGas, we used published bulk $H_2O$ and H-isotopic data from the 1340 C.E. Mono Craters, CA eruption as a basis for model simulations (Newman et al., 1988; Dobson et al., 1989). In addition, we also applied VolcDeGas to data from the 2008 Chaitén eruption; those tests are discussed at the end of this section.

Our approach with respect to the Mono Crater's eruption was to compare our model fits to natural data with the degassing paths fit by Dobson et al. (1989). The initial magmatic values for $H_2O$ content and δD are from Newman et al. (1988): δD of -51 ‰, and bulk $H_2O$ content of 2.64 wt.%. These are based on the most $H_2O$-rich obsidian clast found in the eruption deposits. We investigated temperatures of 600˚C (Figure 5.2) and 800°C (Figure 5.3), as well as closed- to open-system degassing paths. One model calculation uses temperature-dependent hydrous speciation values with formulae based on the ideal mixing model (e.g., Silver and Stolper, 1985) and an empirically determined equilibrium constant K (Zhang, 1999; Figure 5.2A, 5.3A), while the other simulation uses alpha factors based on the measured hydrous speciation values of Barnes et al. (2014) and Newman et al. (1988) (Figure 5.2B, 5.3B). Both Mono Craters simulations are shown in relation to the original data and associated fit curves from Dobson et al. (1989) (Figure 5.3C).

#### 5.2.1.1 Relation between bulk $H_2O$ and alpha factors

Figure 5.2 displays the relationship between bulk $H_2O$ content and alpha factor between vapor and melt ($\alpha_{v\text{-}m}$). The alpha relations are calculated at 600°C and incorporate simulated speciation values (in Figure 5.2A), and real speciation measurements (in Figure 5.2B; Barnes et al., 2014). Figure 5.2C is reproduced from DeGroat (1997) to demonstrate the differences between values computed with a modified version of the "Sil/Hol" Program (Silver et al., 1990; Holloway and Blank, 1994) and using natural speciation data of Newman et al. (1988). According to Figure 5.2, the primary difference between alpha factor simulations (Figure 5.2A) and literature-derived data fits (Figure 5.2B, C) is the curved versus linear projections of alpha factor. Despite this difference, the alpha values are relatively similar, even though the offsets grow larger as the $H_2O$ increases. As we show below, despite some alpha factors inequalities, models will result in just few per mil difference in the final calculations of δD.

[i] Supplementary Information download: https://www.jvolcanica.org/ojs/index.php/volcanica/article/view/62/81

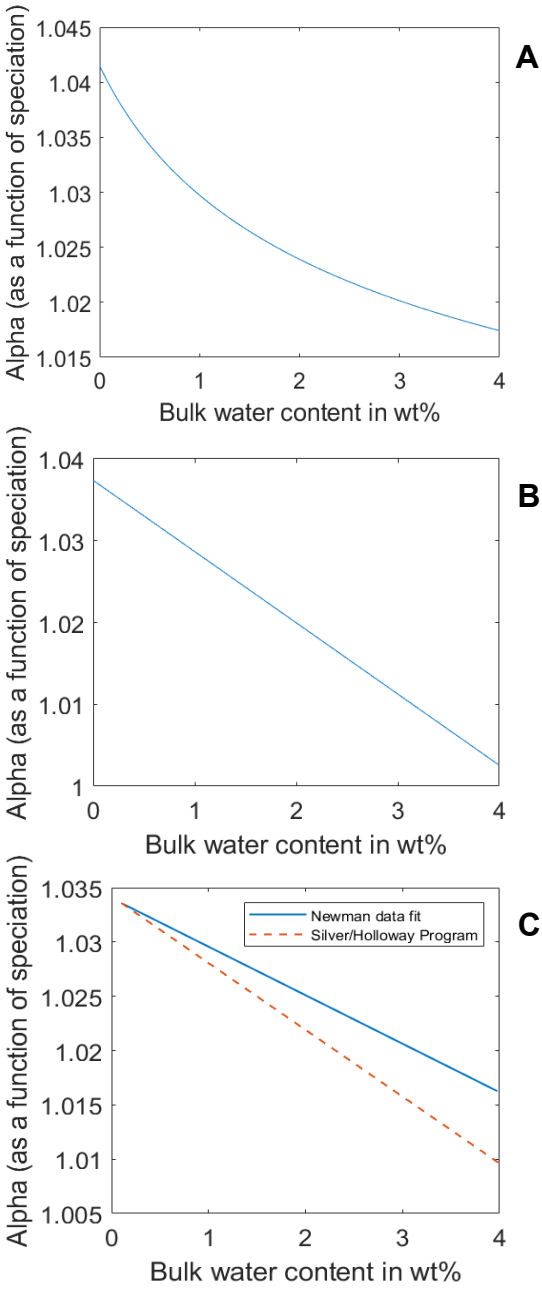


**Figure 5.2:** Comparison of estimates of alpha factor plotted against bulk $H_2O$ content (in wt.%) for the C.E. 1340 Mono Craters eruption. The hydrous speciation and bulk $H_2O$ data values are from Dobson et al. (1989) and Newman et al. (1988). Panel [A] and [B] present the VolcDeGas-simulated (by way of the ideal mixing model) and extrapolated alpha factors based on speciation data (Barnes et al., 2014), respectively. In [C] the linear fits to speciation values of Newman et al. (1988) and of the Silver/Holloway Program (Silver et al., 1990; Holloway and Blank, 1994) are compared.

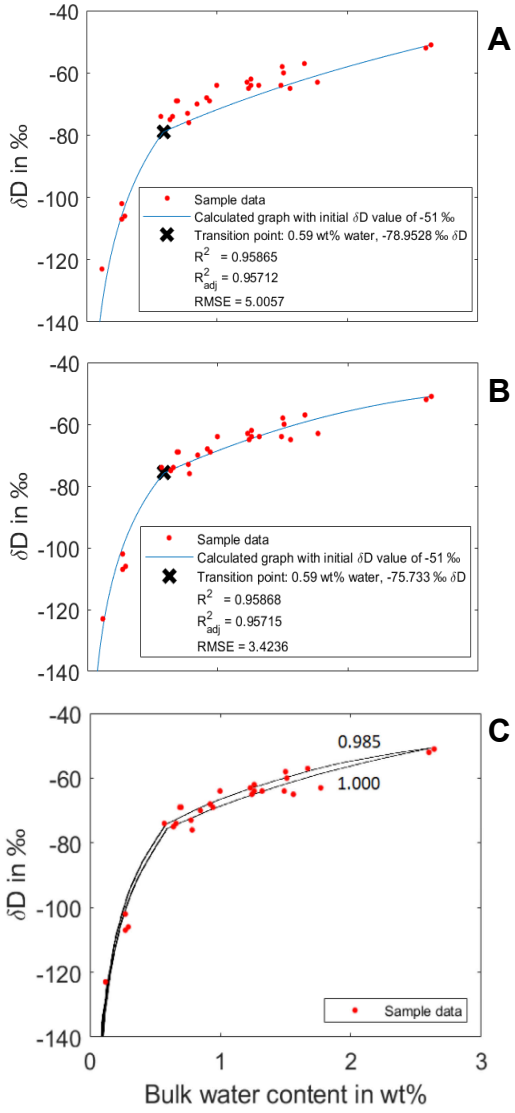


**Figure 5.3:** Diagrams illustrating δD values vs. bulk $H_2O$ content (in wt.%) of the C.E. 1340 Mono Crater eruption based on the sample data and initial values from Dobson et al. (1989) and Newman et al. (1988). [A] and [B] show the computed values by VolcDeGas. The blue line displays the VolcDeGas simulated closed-, to open- system degassing graph, the red dots the sample data and the black cross shows the transition where the degassing system changes. [C] presents a published model fits to data from the literature (Dobson et al., 1989), with red dots being the sample data (Newman et al., 1988). Numbers on two plots in [C] indicate the alpha factor values used by Dobson et al. (1989). The two VolcDeGas plots ([A], [B]) illustrate different fits arising from the contrasting $\alpha_{v-molecularwater}$ values utilized. The alpha factor in [A] is based on speciation values which were calculated by the program (see Figure 5.2A), and in [B] on measured speciation values from Barnes et al. (2014) (see also Figure 5.2B).

### 5.2.1.2 Modeling pyroclastic $H_2O$-δD patterns in the Mono Craters 1340 C.E. eruption

Figure 5.3A and 5.3B show the results of VolcDeGas calculations of $H_2O$-δD trends for the Mono Craters system comprising an inferred closed- to open-system degassing history (Dobson et al., 1989) and using the previously determined alpha factors (e.g., Figure 5.2A, B). Here, the same parameters (e.g., starting $H_2O$ and δD values) as previously described are applied, with the exception of temperature, which is set to 800°C. The results demonstrate that the computations of the degassing history that utilize natural speciation data are the best match to the natural data (Figure 5.3B) and those analogous calculations from literature (Figure 5.3C; Dobson et al., 1989). A lower quality fit to data arises from using the purely simulated hydrous speciation (Figure 5.3A), illustrating that it is preferable to use available natural speciation data for the simulations. Such variations of δD between Figure 5.3A and Figure 5.3B, C only ranges up to 3.3 ‰ in the closed-system stage, and up to 8 ‰ in the open-system stage (Figure 5.3).

In the next section, we demonstrate how VolcDeGas can be used to calculate permissible degassing paths and resolve best-fit magmatic degassing parameters in another natural rhyolitic system, Chaitén volcano (Chile).

### 5.2.1.3 Modeling pyroclastic $H_2O$-δD patterns in the Chaitén 2008 eruption

In this section, we demonstrate a case study involving a rhyolitic volcanic eruption that was directly observed and therefore provides essential information about the style of explosive and effusive activity that was responsible for the samples that have been measured for their H-isotopic and $H_2O$ contents (e.g., Castro et al., 2014). Our main goal is to illustrate how, using the Chaitén dataset, a user would be able to produce a best-fit degassing trend to measured data, which in turn, serves to demonstrate the effectiveness and versatility of the program. It is not the goal however to interpret the volcanological underpinnings of the dataset, as was done earlier by Castro et al. (2014).

Degassing simulations were performed using FTIR-based bulk $H_2O$ and hydrous speciation data of pyroclastic obsidians from the 2008 Chaitén eruption (Lara, 2009; Castro et al., 2012; Castro et al., 2014, Figure 5.4A). We first used VolcDeGas to test for effects of external hydration (e.g., meteoric water sourced) then computed $\alpha_{v-m}$ based on species-specific alpha factors $\alpha_{(v-m)H_2O}$ and $\alpha_{(v-m)OH}$ from Rust et al. (2004), and the non-hydrated speciation data. VolcDeGas makes speciation extrapolations via polynomial fitting (Figure 5.4).

Testing for hydration involved first generating hydrous speciation graphs with the program, which are polynomial curve fits to natural speciation and bulk $H_2O$ content data (Figure 5.4). The fitted natural speciation data which are derived from Castro et al. (2012), allowed for extrapolation of OH/$H_2O$ values, the trends of which comprise a clear envelope corresponding to a high-temperature "magmatic" array (Figure 5.4A). Hydration is recognized in samples that contain too much molecular $H_2O$ with respect to the curves, which is a hallmark of late-stage alteration of hydrothermal fluids (Figure 5.4A). Data points that fall off the speciation fits (by ~0.3 wt.%) are suspect and filtered out as they are not suitable for the best-fit alpha-factor calculations. This is important because altered speciation values may lead to alpha factor values under 1. In such cases, VolcDeGas will return an error, as the degassing trend would lead to more highly enriched δD with falling bulk $H_2O$ content, instead of the depleted δD values typical of magmatic degassing.

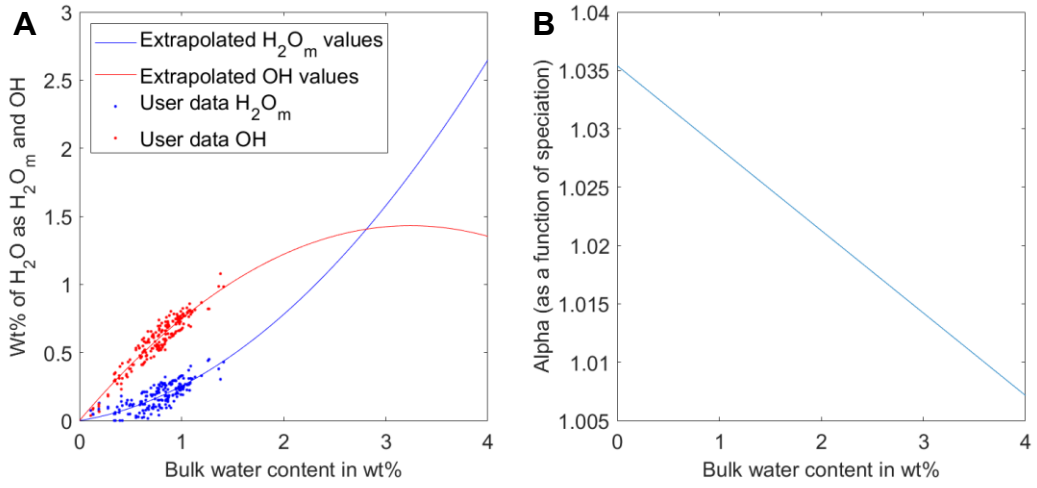


**Figure 5.4:** [A] Plots displaying natural hydrous speciation data (red and blue dots) in obsidians (wt.% OH and $H_2O$) from the Chaitén eruption, 2008 (Castro et al., 2014; Forte and Castro, 2019) in relation to bulk $H_2O$ content. Curves are 2nd degree polynomial fits to each species. [B] The graph shows the calculated alpha factor trend, which is based on hydrous speciation extrapolations shown in [A].

Figure 5.5A and 5.5B show degassing paths calculated for variable step sizes in open- and batched-degassing systems. As can be seen in Figure 5.5A, although the step size in the open-system is changed substantially, (from 0.5 wt.% down to 0.001 wt.% steps) the influence on the δD value is relatively negligible across all degassing intervals. These step size changes result in δD differences of only 3 ‰ at 0.5 wt.% bulk $H_2O$ and of 4.9 ‰ at 0.001 wt.% $H_2O$. Furthermore, the open-system plot resolution for bigger step sizes is lower as less points are calculated. It consequently appears as if there is a strong fractionation in δD over the last 0.5 wt.% $H_2O$. In reality, this is only an optical effect as the space between the steps are connected (interpolated) by a line which has no calculated intermediate values.

In contrast to the open system, the batched-degassing system **(**Figure 5.5B) is highly sensitive to step size variations. In particular, δD differences at variable step sizes sum up to over 7 ‰ at 0.5 wt.% bulk $H_2O$ content and reach ~170 ‰ at 0.001 wt.% $H_2O$. These extreme fractionation differences occurring at the lowest of $H_2O$ contents (0.001 wt.%) are meant to demonstrate the theoretical maximum disparity in the step-size effect. In natural magmatic systems, melts rarely degas to values lower than about 0.05 wt.%, however, even at these values small modeled steps may still result in large δD offsets (~70-100 ‰; Figure 5.5B). This observation highlights the importance of step size during the end-stages of degassing.

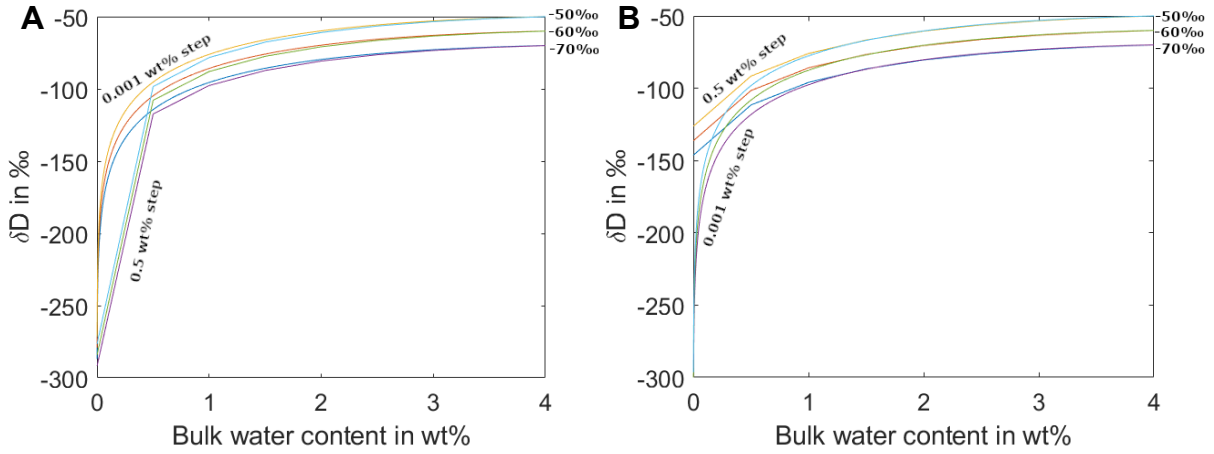


**Figure 5.5:** Graphs displaying VolcDeGas models having fixed 0.001 wt.% and 0.5 wt.% $H_2O$ degassing steps in an [A] open system and [B] batched system. The initial values are: 4 wt.% bulk $H_2O$ content and -70 to -50 ‰ δD. It is clear that having a small step size in either open or batched systems yields smooth trends and, in the case of the batched system, results in slightly stronger δD depletion. As seen in both cases, a larger 0.5 wt.% step size will result in dramatically different degassing paths topologies, characterized by a kinked trend. Notably, large degassing steps results in a very strong late-stage δD depletion in the open system at low $H_2O$ [A].

Figure 5.5B as well as other calculations included in the Supplementary Information[i] support the idea that simulated batched magma degassing can mimic either open-, or predominantly closed-system behavior by mere selection of the appropriate step sizes. A large step size contributes to a closed-system trend (i.e., less overall δD depletion), whereas a smaller step size produces what may resemble an open-system trend. Moreover, in comparison to a truly open system—known to generate highly depleted δD values (e.g., up to -289 ‰; Figure 5.5A)—a small step size of 0.001 wt.% in the batched system (Figure 5.5B) produces even stronger fractionation, with negative δD values as low as -316 ‰ (Figure 5.5B; Supplementary Information[i]).

Thus, VolcDeGas runs of the batched system, in which a percentage of $H_2O$ is lost at each step, may best approximate the natural system (e.g., Castro et al., 2014). To better illustrate this point, Figure 5.6 shows a batched system calculation with an initial δD value of -61 ‰, and

[i] Supplementary Information download: https://www.jvolcanica.org/ojs/index.php/volcanica/article/view/62/81

a variable step size, implemented by setting an $H_2O$ loss of 40% at each step (see Supplementary Information[i] for additional conditions). Goodness-of-fit for this simulation is reasonable, as evidenced by the adjusted coefficient of determination ($_{adj}R^2$) and $R^2$, as well as the RMSE (Figure 5.6).

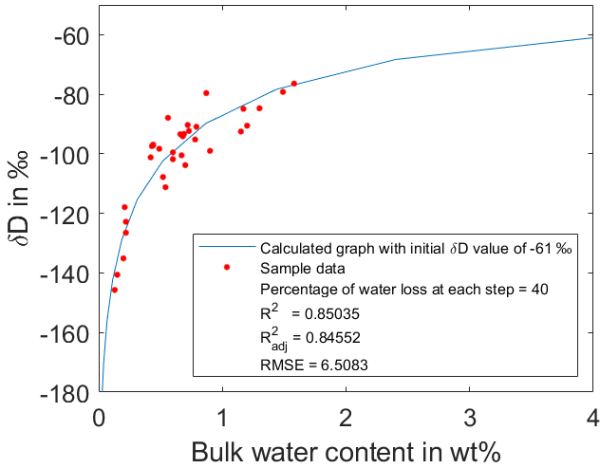


**Figure 5.6:** Modeled, best-fit, single staged batched-system trend with variable step size for the 2008 Chaitén eruption products. Simulations performed at an assumed eruption temperature of 800˚C (Castro and Dingwell, 2009). Data from Castro et al. (2014) are shown as red dots. Here each step invokes initial closed- and later open-system release of 40% of the $H_2O$ budget. The fit is particularly good at low $H_2O$ contents, in materials that have undergone the most degassing.

In Figure 5.7, we investigate the possibility of a two-stage history for the Chaitén eruption, one involving early closed-system degassing followed by batch degassing (both at a presumed eruption T of 800˚C; Castro and Dingwell, 2009). This scenario may for example mimic degassing across an entire eruptive sequence, from high-energy, pulsating Plinian activity (e.g., purely closed-system dynamics; e.g., Newman et al., 1988) to later hybrid activity involving both rhyolite pyroclast and lava eruption (e.g., batched degassing; Castro et al., 2013; Castro et al., 2014). Of the two-stage best-fit models (Figure 5.7A, B), the closed-, to batched-system with a small, fixed step size (0.001 wt.% $H_2O$) exhibits slightly better results (Figure 5.7A), as reflected by calculated goodness-of-fit ($R^2$ and RMSE). However, both batched-system models exhibit similar fit statistics, suggesting that either is a good choice to model the Chaitén sequence (Figure. 5.7B).

Another factor that affects goodness-of-fit and therefore must be taken in to account in order to model a two-stage system, is the transition point, defined as the $H_2O$ content at which the closed-system gives way to the batched-system. Transitions can also be generally defined as changeovers between any other combination of degassing styles (e.g., closed- to open-system degassing). In the previously modeled closed-to-batched system with the constant step size (Figure 5.7A), the best-fit transition point is at 0.5 wt.% $H_2O$, whilst in the system with variable

[i] Supplementary Information download: https://www.jvolcanica.org/ojs/index.php/volcanica/article/view/62/81

step size (Figure 5.7B), the transition occurred at 0.6 wt.% $H_2O$. These transition points may seem very similar but the differences are significant and exemplify the sensitivity of VolcDeGas' fitting process, which entails an iterative determination of the "most likely" transition point through statistical minimization of RMSE values (Supplementary Information[i]). This objective way of determining a transition point could offer an advantage over previous manual transition point placement methods (e.g., Dobson et al., 1989).

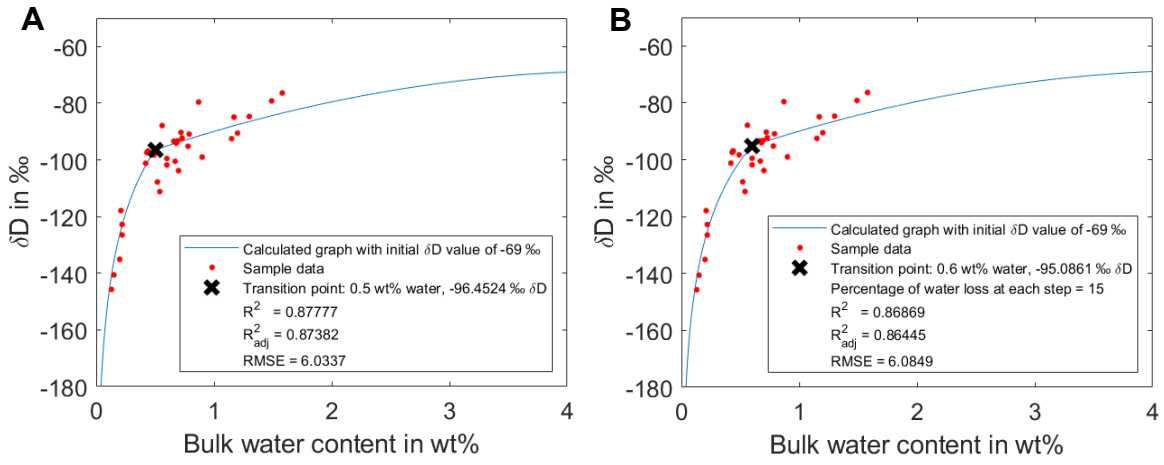


**Figure 5.7:** Two-stage, closed-to-batched system model fits to Chaitén pyroclastic obsidian and lava δD-$H_2O$ data (Castro et al., 2014) showing transition points (black x's) at [A] 0.5 and [B] 0.6 wt.% $H_2O$. Step sizes differ from [A] a small fixed step size 0.001 wt.%, to [B] a variable one comprising 15% $H_2O$ loss at each step. Despite these differences, model fits to data are virtually identical. In addition, the goodness-of-fit of these two-stage systems is better than observed in the single-stage batched system with variable step size (Figure 5.6). All simulations were performed at a presumed eruption temperature of 800˚C (Castro and Dingwell, 2009).

In summary, two-stage degassing systems (Figure 5.7) fit the sample data significantly better than the previously analyzed one-stage model (Figure 5.6). In particular, the relevant RMSE-value is around 0.5 lower, whereas the $R^2$ is ~0.3 higher. As a result, two-stage closed-, to batched-system degassing paths can be viewed as the best-fit for the available data points. In the following discussion section, batched systems with constant-, and with variable-step sizes are discussed and compared based on available literature data as well as observations from the eruptions themselves, to identify the most probable system of the two.

## 5.3 Discussion

The VolcDeGas program is a useful tool to investigate feasible degassing histories of rhyolitic magmatic systems, provided the appropriate D/H isotopic and bulk $H_2O$ content data are available. Because the program integrates all of the required parameters in degassing calculations—e.g., real and extrapolated hydrous speciation, alpha factors, temperature, and

[i] Supplementary Information download: https://www.jvolcanica.org/ojs/index.php/volcanica/article/view/62/81

degassing step size (both fixed and variable)—the user can investigate the influence of these variables on one-, and two-stage degassing systems in an objective manner. The program is furthermore not a “black box” insofar as it provides an intuitive GUI for entering the data, setting key parameters and visualizing output in a variety of multi-axis plots. A view of the code itself (see VolcDeGas.m) shows a detailed description of how the program functions. As a result, after a short familiarization with this program, the user can quickly calculate the different kinds of degassing systems, while being able to comprehend how the program executes these calculations.

Of the many initial conditions that influence isotopic fractionation calculations, the partitioning of deuterium and hydrogen between vapor and melt, encapsulated in the alpha factor, $\alpha_{v\text{-}m}$, imparts a strong influence on degassing trends. This is because the alpha factor is a function of hydrous speciation in the melt, which in turn varies as degassing progresses. That VolcDeGas is able to calculate and update the alpha factor according to real or modeled speciation values during a simulation is a major advantage that requires relatively little user intervention, however, the user can also use this functionality to spot potential sources of error in the simulation that stem from natural processes (e.g., hydration). For example, after loading hydrous speciation data, the user can inspect the data and associated VolcDeGas speciation curve fits identify anomalous values (Figure 5.4). Altered samples (e.g., those with high molecular $H_2O$) will change the speciation graph extrapolations significantly, and in turn calculated alpha factors may be less than 1. VolcDeGas will flag these instances and output an error message and stop the simulation, thereby precluding counterintuitive, positively sloping degassing trends. Finally, as some degassing paths yielding very good fits to natural data were calculated utilizing alpha factors (Figure 5.3B) that are based on natural hydrous speciation values, we recommend wherever possible, to use available natural speciation-based calculation of alpha factors, instead of the temperature-dependent ideal mixing model species calculations.

Test models show that in addition to alpha factors, the step size—the amount of $H_2O$ lost during each interval—is also hugely important in the form of degassing trends and yielding good fits to natural data (e.g., Figure 5.5). Batched-degassing simulations exhibit particularly strong sensitivity to this variable (Figure 5.5B). In the most extreme case, δD differences between moderate (0.5 wt.%) versus small steps (0.001 wt.%) amount to more than 100 ‰ variation in the small window of degassing from about 0.5 wt.% to 0.1 wt.% (e.g., Figure 5.5B). This clearly shows that in the low-$H_2O$ content interval, δD in a magma responds sensitively to each progressive degassing step, with the implication that extreme deuterium-depletion in lavas could portend many repetitive small steps rather than large pulses in the waning stages of an

eruption. Indeed, VolcDeGas models of the Chaitén pyroclastic and lava data set support this conclusion (Figure 5.6, 5.7B), and exemplify how progressively decreasing step sizes may provide an excellent fit to natural products. The Chaitén simulation, shown in Figure 5.6, employs a degassing step that removes 40% of the remaining $H_2O$ at each interval, which is tantamount to having variable, diminishing step sizes. The result is a relatively smooth trend and good fit for a one-stage system to natural data (see also e.g., Castro et al., 2014), which provides good evidence for a repetitive degassing process having been operant in the natural eruption.

In addition to single-stage (e.g., closed, open, or batched) degassing trajectories, VolcDeGas is capable of calculating two-step degassing paths with good precision, and with a relatively small number of parameters required as initial inputs. Especially relevant is the capacity of VolcDeGas to find the best "transition point" whereby the degassing mechanism changes from one mode to another (e.g., purely closed to open). Traditional closed-to-open, two-stage degassing interpretations of natural data (e.g., Newman et al., 1988; Rust et al., 2004) are based in part on evidence in the $H_2O$ contents of melt inclusions, which may contain several wt.% $H_2O$, and pyroclastic obsidians, which can be significantly degassed (down to a few tenths of a wt.% $H_2O$), together suggesting that initial Plinian activity must be fueled by vigorous closed-system degassing involving fragmentation as the main mechanism to liberate volatiles. Eventually a "transition point" is reached, marking an abrupt change in the degassing mode (i.e., to an open system). The modeled trends should therefore be "kinked". This is indeed well depicted by VolcDeGas' closed-to-open system degassing simulation of the D/H-$H_2O$ data for the Mono Craters (Figure 5.3). These calculations yield plots that are very good matches to the δD and $H_2O$ values in Mono Craters pyroclasts and lavas, and even reproduce the transition points and fits to these data from the published literature (Newman et al., 1988; Dobson et al., 1989). This good correspondence verifies this program's ability to reproduce and confirm previously published model trends.

Two-step degassing simulations may also comprise closed- to batched-system degassing sequences, as was done for example for Chaitén D/H-$H_2O$ data (Figure 5.7). In this simulation (Figure 5.7) the initial closed-system degassing trend can be representative of the first explosive eruption(s) that must have liberated large quantities of $H_2O$. Following this, the progression gives way to a batched system, demarcated by a kink in the graph and corresponding to the best-fit transition point (Figure 5.7). The batched system with the variable step size (Figure 5.7B) is able to explain the degassing data after the closed-system phase and could represent hybrid explosive-effusive activity characterized by declining explosive

energy with time, which in turn releases fewer volatiles from each successive batched degassing step.

## 5.4 Summary and conclusions

In summary, the VolcDeGas program is effective at modeling degassing paths as well as being a tool for fitting and interpreting natural data that can lead to new insights into magmatic processes. Our understanding of rhyolite eruptions can in turn be more quantitatively based, ultimately fostering a better connection between observations of activity and measured geochemical degassing proxies (e.g., $H_2O$ and D/H). Establishing how step size variations modeled in VolcDeGas may scale to actual volcanic eruption processes—in particular the repetitive blast events that characterize hybrid activity (Castro et al., 2014; Saubin et al., 2016)—is one goal that may improve coupling natural field observations to analysis of eruption products. For example, it is currently unknown how big the individual blasts are and to what extent each blast “bleeds” off vapor pressure from the underlying magma body. Therefore, future field and analytical studies could profitably focus on obtaining estimates of degassing amounts during repetitive volcanic blasts. Linking these data with VolcDeGas could pave the way to understanding how degassing proceeds in a temporal context and deliver the root causes of different eruption stages.

## 5.5 Acknowledgements

This work was supported by the VAMOS research center University of Mainz. The authors are grateful for the review comments of Thomas Giachetti and Fabian Wadsworth, which greatly improved the manuscript.

## 5.6 Author Contributions

S. Walter wrote and tested the program and co-wrote the manuscript. J.M. Castro conceived of the project and co-wrote the manuscript.

## 5.7 Data availability

The program VolcDeGas was created by Sebastian Carl Walter of the University of Mainz and written in MatLab 2018a/b. Access to code: The files VolcDeGas.m, VolcDeGas.fig, VolcDeGasoptions.m, VolcDeGasoptions.fig should be placed into a folder MatLab can access (e.g. MatLab folder). The program is invoked by typing VolcDeGas into the MatLab workspace.

Another way to start the program is by running the VolcDeGas VolcDeGasinstall.exe which installs the compiled version of the program by downloading all required MatLab assets (only Windows systems). All files are available as Supplementary Material alongside the online version of this article at: https://www.jvolcanica.org/ojs/index.php/volcanica/article/view/62.

### 5.8 Software requirements

MatLab with Signal Processing, as well as the Statistics and Machine Learning Toolbox. The program has been tested to be downwards compatible with at least MatLab R2012a.

### 5.9 Size of components

300 kilobytes for the .fig and .m files. 3.8 megabytes for VolcDeGasinstall.exe as well as around 1 Gigabyte for the installed program and the required MatLab assets.

### 5.10 Copyright notice

# Chapter 6

# Hybrid rhyolitic eruption at Big Glass Mountain, CA, USA[2]

**Keywords: Big Glass Mountain; Rhyolite; Obsidian; Pyroclasts; Batched degassing; Hydrogen isotopes; Explosive-effusive eruption**

**Abstract**

Eruptive dynamics of the 1060 CE eruption of rhyolite from Big Glass Mountain (BGM) are investigated with field observations, hydrogen isotope, and $H_2O$ content analysis of pyroclastic obsidian chips and lavas. Field relations at BGM reveal evidence for hybrid eruption, defined as synchronous explosive venting and effusive emplacement of vast obsidian lava flows. This activity is particularly well manifested by extensive breccia zones implanted within BGM's obsidian lavas, which may represent rafted tephra cones, in addition to remnants of air-fall tephra on the lava. Rhyolitic obsidians collected from a 2.5-m-thick fall deposit and co-eruptive lava flow were studied by FTIR and TCEA methods to elucidate the eruption's degassing history. The data, along with VolcDeGas program simulations, demonstrate a correlation between $H_2O$ content and H-isotopic composition (δD) reflecting ever-increasing amounts of volatile and deuterium loss to the vapor phase. VolcDeGas simulations suggest a best-fit degassing mechanism comprised of repetitive, variably sized closed-system steps, which is termed "batched degassing". This degassing mechanism, along with the field evidence at BGM, implies an eruptive sequence that is devoid of a sharp break and entirely consistent with observed Chilean rhyolite eruptions: initial explosive venting transitioning to a hybrid style of activity. Collectively, the $H_2O$-δD patterns and field characteristics of BGM's eruption deposits lend credence to the idea that hybrid venting is common during rhyolite eruptions and should be accounted for in future eruption hazards assessments.

[2] This chapter is published as Castro, J., Walter, S.C., 2021. Hybrid rhyolitic eruption at Big Glass Mountain, CA, USA. Volcanica 4 (2), 257–277, doi: 10.30909/vol.04.02.257277

## 6.1 Introduction

Studying silicic volcanism, particularly rhyolite eruptions, is critical to assessing volcanic threat (e.g., Eichelberger, 1995; Castro and Dingwell, 2009; Watt et al., 2009). A first order question in the context of volcanic hazards mitigation is, How will an eruption progress once underway? Early work on Holocene rhyolites—a rare yet physically impactful form of volcanism—recognized that these systems are both “explosive and effusive” in nature, this assessment being drawn from field observations of obsidian lava flows perched atop pyroclastic fall deposits (e.g., Heiken, 1978; Eichelberger and Westrich, 1981; Taylor et al., 1983). The lack of preserved tephra on top of the lavas lead to the logical conclusion that the eruptions followed an explosive-to-effusive sequence, with lavas emerging after the explosive eruptions ceased (e.g., Miller, 1985; Donnelly-Nolan et al., 2016). Disparate eruption styles were explained by the different magmatic $H_2O$ contents in pyroclasts and lavas, which showed that the former still had significant quantities of primary $H_2O$, while the latter were nearly completely degassed (Eichelberger and Westrich, 1981; Taylor et al., 1983). A uni-directional shift from explosive to effusive behavior, it was argued, depended on how efficiently the magma could degas during ascent, itself a complicated function of intrinsic magma vesicularity and permeability (Eichelberger et al., 1986). Modeling studies reinforced the notion of bifurcating eruption behavior, even predicting sharp “explosive-to-effusive” transitions as bubbly magma becomes highly permeable, ascent and shearing rates wane, and magma chamber overpressure declines during magma rise (Jaupart and Allègre, 1991; Woods and Koyaguchi, 1994; Gonnermann and Manga, 2003, 2007).

Despite many insightful studies on rhyolites, it came as a surprise then when eruptions in Chile were first observed (Lara, 2009; Alfano et al., 2011; Castro et al., 2013; Schipper et al., 2013; Castro et al., 2014), as these events showed that rhyolite eruptions may actually progress differently than previously thought. After initial week-long explosive episodes, eruptions at both Chaitén (2008) and Cordón Caulle (2011), Chile, exhibited rarely seen “hybrid” activity, comprising simultaneous pyroclastic fountains (100’s to 1000’s m) and lava eruptions from the same vents (Schipper et al., 2013; Castro et al., 2014; Castro et al., 2016). Such activity had only once been reported on once before in regards to 1960 rhyodacitic fissure eruption at Cordón Caulle (e.g., Katsui and Katz, 1967; Lara et al., 2004). The eruptions concluded with purely effusive activity (Pallister et al., 2013; Tuffen et al., 2013).

The hybrid eruption phases, which were the most protracted (i.e., months-long) and lasted until a majority of the lava fields were emplaced, started with lava emerging directly from one or more tephra cones (e.g., Castro et al., 2014; Castro et al., 2016). The lavas occasionally

bulldozed these fragmental edifices, causing the pyroclastic deposits to be rafted away by the flows (Pallister et al., 2013; Schipper et al., 2013, Supplementary Information[ii]). The result of such effusive and explosive co-eruption can be readily seen in the mixing of breccia, or tephra ridges within the lava fields at both Chaitén and Cordón Caulle (Figure 6.1; Tuffen et al., 2013; Castro et al., 2014).

A particularly important question is, Just how common was hybrid activity in the many pre-historic (late Holocene) obsidian producing events? Evidence for long-lasting hybrid ash and lava venting at other well studied pre-historic rhyolite systems has begun to emerge. Black et al. (2016) discovered pyroclastic degassing structures, so-called tuffisites, on Panum Dome rhyolite (CA) that they interpret as evidence of explosive ash venting during the emplacement of an obsidian dome. Black et al. (2016) concluded that persistent ash venting would be a significant threat to air traffic, thereby underscoring the importance of studying pre-historic rhyolites in order to clarify how these systems may have erupted in the past, and how they may possibly erupt in the future.

In order to improve our understanding of how pre-historical rhyolites may have erupted, we have investigated field and geochemical characteristics of the 1060 CE eruption of Big Glass Mountain, CA (BGM) (e.g., Anderson, 1933; Chesterman, 1955; Donnelly-Nolan et al., 2007; Donnelly-Nolan et al., 2008). This explosive and effusive event produced about 0.1 $km^3$ of rhyolitic tephra and the most voluminous rhyolitic obsidian flow (~ 1 $km^3$) in Cascades volcanic province (Heiken, 1978). Existing literature purports that BGM's effusive phase began after explosions had ceased (e.g., Donnelly-Nolan et al., 2016). However, as we show, BGM erupted simultaneously in explosive and effusive modes, this evidenced by physical depositional features and by hydrous geochemical trends in deposits that are strikingly similar to features observed in previously monitored Chilean eruptions (e.g., Lara, 2009; Castro et al., 2013). Our data show that hybrid explosive-effusive activity was important during Big Glass Mountain's most recent eruption and such eruptive activity may be more common than previously recognized.

## 6.2 Background

In this section we review important aspects of the Big Glass Mountain eruption, including its salient deposit characteristics and hydrous geochemical patterns thereof that served as the earliest basis for models of explosive-effusive rhyolite eruptions. We then summarize the hydrous geochemical patterns observed in pyroclastic and effusive deposits of different pre-historic (including BGM) and recently active rhyolite systems, and convey how these published

[ii] Supplementary Information download: https://www.jvolcanica.org/ojs/index.php/volcanica/article/view/121/137

data have shaped theories of how rhyolite magma degasses during explosive and effusive eruption modes.

Big Glass Mountain is a late-Holocene dacitic to rhyolitic volcanic complex located near the summit of Medicine Lake Volcano (MLV), northern California (e.g., Donnelly-Nolan et al., 2008). The latest activity of MLV, about 950 years ago (Donnelly-Nolan et al., 2007), formed Big Glass Mountain, a broad (~5 km diameter) silicic landform comprising pyroclastic fall deposits, near-vent breccia and tephra cones, and a voluminous obsidian flow. Although some andesitic material is found in BGM's most recent eruption deposits, and is probably co-eruptive, the majority of the complex ranges from dacite to rhyolite in composition (Donnelly-Nolan et al., 2016). The youngest eruption deposits, originating from a ~6 km NW-SE trending fissure, comprise some 0.1 $km^3$ rhyolitic tephra and ~1 $km^3$ of rhyodacite to rhyolite obsidian lava flows and domes (Heiken, 1978; Donnelly-Nolan et al., 2016). Numerous studies have elucidated the general progression of the eruption, including its trigger via magma injection (Eichelberger, 1975) and ensuing eruptive activity, which presumably began with early pyroclastic venting followed by late-stage effusion of compositionally mixed silicic lava (e.g., Heiken, 1978; Eichelberger and Westrich, 1981). Heiken (1978) suggested that the volumetric dominance of lava over tephra (~9:1 at BGM), is characteristic of moderate-volume rhyolite eruptions, including the Little Glass Mountain complex on Medicine Lake Volcano, the Inyo Domes (Heiken, 1978; Castro and Gardner, 2008), and the Rock Mesa and Devils Hill rhyolites on South Sister Volcano, Oregon (e.g., Scott, 1987).

The pyroclastic and effusive deposits at BGM contain abundant rhyolitic obsidian (Figure 6.1); these glasses were some of the first ever to be analyzed to constrain volatile contents in rhyolite magmas. In their landmark study, (Eichelberger and Westrich, 1981) demonstrated that BGM (and Little Glass Mountain) obsidians contain a range of remnant (0.1 to ~1.0 wt.%) magmatic $H_2O$ (and minor $CO_2$). This $H_2O$ range reflects values measured on effusive (the minimum values) and pyroclastic obsidians (upper range in $H_2O$). Eichelberger and Westrich (1981) interpreted this water to be the primary driver for explosive rhyolite eruptions at Medicine Lake. Their measurements also showed that obsidian lavas are nearly completely depleted in $H_2O$ (~0.1 wt.%), which—together with the relatively more hydrous pyroclast data –suggested that the magma body feeding explosive and effusive eruptions was stratified in $H_2O$. Thus, the primary implication was that eruption style is dictated by how much $H_2O$ is in the magma, with the explosive-to-effusive transition being triggered by $H_2O$-rich magma being exhausted and positioned "abruptly" atop drier magma that would later erupt effusively.

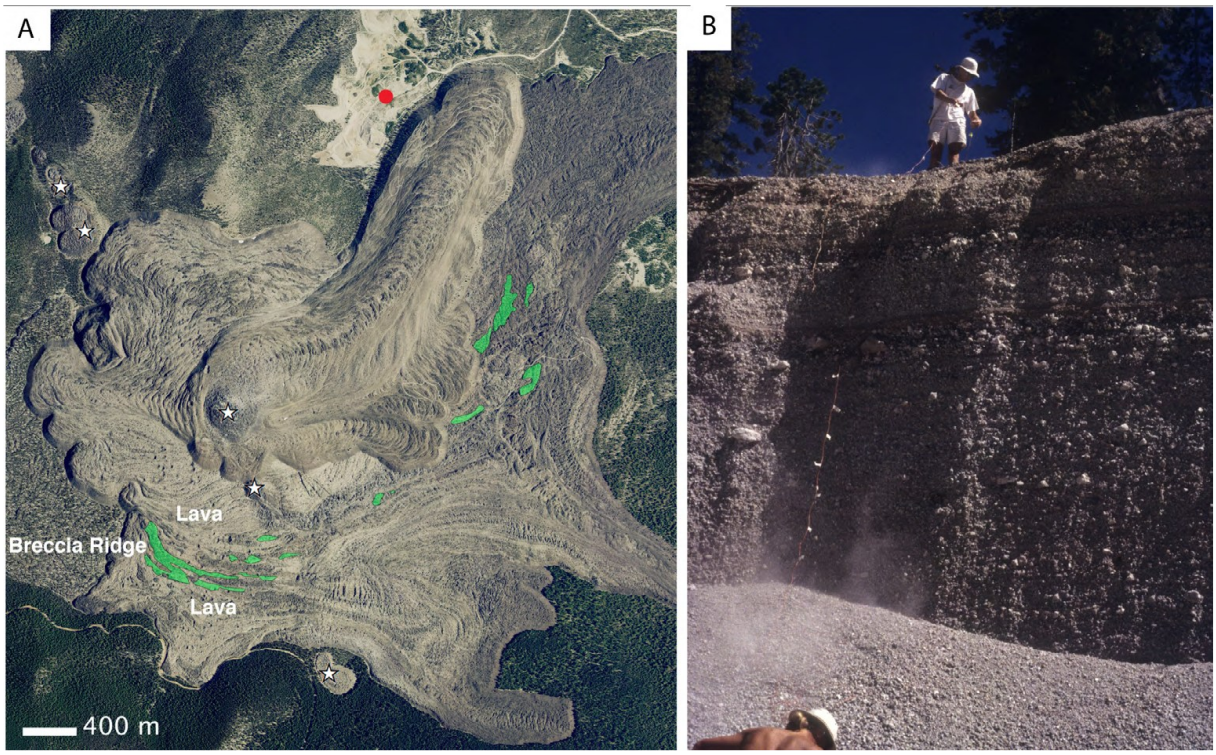


**Figure 6.1:** [A] Satellite image of the Big Glass Mountain (BGM) complex, northern California. North direction is up in image. Imagery dates from 29 June 2017 and is provided by the National Agricultural Imagery Program (NAIP/USDA-FSA). Obsidian lava of the BGM occupies most of the field of view, however co-eruptive air-fall deposits are apparent in vegetated land and in the quarry to the NW of the BGM flow. White stars show the approximate locations of vents within the flow and on the extension of the presumed fissure system (e.g., Eichelberger, 1975). The red dot shows the approximate location of our pyroclastic samples, collected in 1997. Green areas superimposed on the flow demarcate breccia ridges, which host significantly more vegetation than the normal flow top lava. Breccia ridges are particularly well exposed and positioned *inboard* of the southern and westernmost flow fronts, indicating that they were incorporated into the flow at some point after the onset of effusive activity. [B] Close-up view of the ~2.5 m tall outcrop of pumice and obsidian fall. We sampled this section at 15 cm intervals (shown by white tape markings on section line). Mapping by Chesterman (1955) suggests the total fallout section thickness is 3.6 m at this location.

In addition to the absolute $H_2O$ contents of eruption products, the H-isotopic signatures of pyroclastic and effusive obsidians at Medicine Lake and other Holocene systems (e.g., Inyo Domes and Mono Craters, CA) have been used to elucidate specific degassing mechanisms responsible for syn-eruptive gas release (e.g., Taylor et al., 1983; Newman et al., 1988; Dobson et al., 1989). As studies have shown, hydrogen isotopic measurements on pyroclastic and effusive obsidians trace relatively consistent patterns of initial subtle decline in δD in relatively hydrous pyroclasts (e.g., from ~4 to 1 wt.% $H_2O$; Newman et al., 1988), and later extreme isotopic fractionation (i.e., deuterium depletion) comprising a sharp exponential decrease in δD for the last several tenths of a wt.% of $H_2O$ found in obsidian lavas. These trends have been interpreted as evidence for initial “closed-system” degassing related to explosive processes (i.e., corresponding to hydrous pyroclasts; Taylor et al., 1983), and later “open-

system" degassing in obsidian-flow producing phases. Eichelberger et al. (1986) purport that the open-system signatures of obsidian lavas reflect the inevitable transition of rising bubbly magma to a highly permeable state, which in turn induces effective and immediate gas-melt separation that will result in dry magma capable of erupting "quiescently" (Eichelberger et al., 1986).

Most recently, Giachetti et al. (2020), performed detailed hydrous geochemical ($H_2O$ and δD) and paired porosity measurements of pyroclastic and effusive obsidians and pumices from Big Glass Mountain's 1060 CE eruption. Similar to previous interpretations (e.g., Eichelberger et al., 1986; Newman et al., 1988), this study contends that the BGM eruption progressed from early closed to open-system degassing, the shift being caused by bubbly magma reaching a threshold ~65% porosity. Like the Eichelberger et al. (1986) model, the main mechanism bringing about this changes is magma reaching a permeability threshold, beyond which open system degassing takes over and quiescent effusion occurs.

In contrast to the aforementioned studies that treat rhyolite eruptions as two-stage, closed-to-open systems Taylor (1991) proposed "batched degassing", a multi-stage, repetitive degassing mechanism for late-Holocene explosive-effusive rhyolite eruptions at the Inyo Domes, Ca (Miller, 1985). According to this model—termed "multi-step open/closed"—hydrous magma outgasses in repetitive closed-system "batches" that are periodically released by explosions that vent exsolved gas to the surface. The repetitive closed system batches may get progressively smaller with time as the hydrous magmatic component declines with successive eruptions. The net effect of Taylor (1991) model is the progressive depletion of the magma's $H_2O$ budget, which enhances "quasi-open" system behavior with each degassing step.

Taylor's multi-step model fit to the Inyo Domes isotopic data yields isotopic shifts and δD-$H_2O$ trends that are excellent fits to both the initial subtle decrease in pyroclastic obsidian δD, and the later extreme deuterium depletion observed in lavas. The repetitive nature of the degassing process, Taylor (1991) contends, is manifested in the physical character of pyroclastic deposits themselves, which exhibit stratified heterogeneous distributions of obsidian-and pumice-rich layers (Figure 6.1). Although not explicitly stated in Taylor (1991) work, the multi-step, batched-degassing model represents a *single* repetitive mechanism that geochemically links explosive to effusive products. In other words, the model does not entail a distinct shift in degassing mechanism nor does it require that eruptive activity change as the aforementioned two-stage models do (e.g., Newman et al., 1988; Giachetti et al., 2020).

Castro et al. (2014) applied Taylor (1991) batched-degassing approach to model δD-$H_2O$ measurements on explosive and effusive products from the first scientifically observed rhyolite eruption, that of Chaitén volcano, Chile (Castro and Dingwell, 2009; Castro et al., 2012). Because this event was well monitored, the $H_2O$ and isotopic measurements and modeling thereof could be directly linked to the observed eruptive behavior. Castro et al. (2014) found that a multi-step, batched-degassing mechanism could fit the δD-$H_2O$ data from *the entire* eruptive complement: early-erupted Plinian pumice and obsidian lapilli, Vulcanian bombs, and lavas. In addition, the multi-step degassing mechanism was entirely consistent with and correlative to the observed eruption behavior, in particular Chaitén's hybrid activity (simultaneous bomb blast and pyroclastic venting alongside effusion) that commenced shortly after the eruption had started.

The simultaneous explosive and effusive eruption of Chaitén involved persistent ash venting and repetitive explosions, much like those seen at Cordón Caulle a few years later (Castro et al., 2013; Schipper et al., 2013; Schipper et al., 2021). The ubiquitous explosions that occur during effusion (e.g., Schipper et al., 2013) are manifestations of the periodic build up and release of pressure on conduit-spanning fractures and pyroclastic degassing channels known as tuffisites, whose time-dependent porosity and permeability (Black et al., 2016; Saubin et al., 2016; Heap et al., 2019; Schipper et al., 2021) lead to intermittent bomb blast and ash venting activity (Castro et al., 2012; Castro et al., 2014; Black et al., 2016). Collectively, the eruption observational information, geochemical signatures, and textural features of Chaitén and Cordón Caulle argue for a degassing mechanism that could operate relatively unchanged across the whole eruptive sequence, including initial Plinian explosions and later synchronous, hybrid venting of pyroclasts and lava.

In summary, rhyolitic obsidian eruptions have historically been viewed as "explosive OR effusive", and accordingly ascribed to a two-stage degassing history (e.g., Cabrera et al., 2015). Indeed, the overwhelmingly dominant interpretation of hydrous geochemical data and physical textures in eruption products is one indicating a sharp "transition" in eruptive style, coinciding with the degassing regime shift from closed to open-system (e.g., Taylor et al., 1983; Eichelberger et al., 1986; Newman et al., 1988; Eichelberger, 1995). Testing whether this interpretation is valid is clearly important for accurately assessing the hazards of these and future events, especially considering that the two observed Chilean rhyolite eruptions did not behave according to current paradigms. In other words, because the hybrid form of activity is temporally dominant (lasting months to more than a year) in the observed events, very different hazards are implied than would be considering the prevailing "explosive OR effusive" paradigm (e.g., Castro et al., 2014; Saubin et al., 2016; Forte and Castro, 2019).

Aside from the work of Castro et al. (2014), no previous study has linked both field and geochemical evidence of degassing to hybrid eruptive activity in a rhyolite system. Thus, our goal is to find hallmarks of this behavior in the geochemical and physical nature deposits at BGM. Our results show that hybrid activity probably played a dominant role in the pre-historic rhyolite eruption of BGM.

## 6.3 Samples and analytical methods

### 6.3.1 Sample collection

We collected tephra samples in September, 1997, from a freshly exposed, 2.5 m-tall vertical outcrop of airfall tephra in a pumice quarry (“Fouch pumice pit”; Chesterman, 1955) on the north side of the Big Glass Mountain obsidian flow (Figure 6.1). This sample location was selected in part based on field mapping by Heiken (1978), whose own tephra sections and isopach maps reveal a maximum deposit thickness ranging from ~3-6 m in the quarry we sampled from. The bottom of the air-fall tephra was not encountered during our sampling but it could have extended up to 1 m beneath our lowest sample owing to an earlier published estimated total deposit thickness at this location of about 3.6 m (Chesterman, 1955). At the time of our sampling, exposures in the quarry could be continuously traced to the contact they made with the northern obsidian flow lobe. This confirmed that the location of our sampling corresponds to a conformable stratigraphic (and co-eruptive) pyroclastic fall linked to the overlying effusive lava (Figure 6.1).

We sectioned pyroclastic samples in bulk with a small trowel at 15 cm intervals over the entire 2.5 m exposed section. Samples were placed into air- and watertight bags in amounts of about one kilogram. As talus obscured the base of the fall deposit, it is unclear where the tephra fall section ended. However, the sampled section does represent a majority of the upper part (~70%) of the fall deposit at this location (i.e., 2.5 m of a total 3.6 m; Chesterman, 1955). Although we cannot establish the relative age of the tephra deposit with respect to the neighboring lava—i.e., if they erupted simultaneously—these pyroclastic samples collected at a high sampling interval (about every 15 cm) do contain an important record of the explosive phase at BGM and, in the event that it did temporally overlap with effusive activity, could reveal hydrous geochemical signatures evolve during hybrid activity (Castro et al., 2014).

The pyroclastic samples analyzed in this study are labeled from deposit top to bottom as 2a through 15a and comprise rhyolite pumice, obsidian chips, and grey lithic fragments (Table 6.1). Because the pumice samples, comprising 1-5 cm sized lapilli fragments, are in all

likelihood hydrated by meteoric waters (Eichelberger and Westrich, 1981; DeGroat-Nelson et al., 2001; Giachetti et al., 2020), we did not analyze them. We instead focused analyses on obsidian fragments (~0.5-2 cm in diameter). We separated 35 glass chips from the bulk pyroclast samples, and set them aside for geochemical analysis. The possibility that these obsidian clasts were hydrated can be discounted on the basis of their relatively young age (~$10^3$ yrs), low (<5 vol.%) to negligible porosity, and the exceptionally slow rates of glass hydration at surface conditions (~1-10 μm $kyr^{-1}$; e.g., Anovitz et al., 2004). For example, recent hydration modeling of natural fulgurite glasses shows that significant uptake of meteoric water in dense silicate glass requires thousands to hundreds of thousands of years (Castro et al., 2020). Based on this evidence, it is unlikely that BGM pyroclastic and effusive obsidians have undergone appreciable hydration since their eruption.

We also collected dense obsidian lava samples from the northeastern and southern lobes of Big Glass Mountain obsidian flow; these samples were also analyzed for their $H_2O$ contents by FTIR using well established techniques (e.g., Castro et al., 2005), and were found to be very $H_2O$ depleted (~0.13 wt.%). However, isotopic (TCEA) analyses (see Section 6.3.2) of these same samples were problematic in that $H_2O$ contents were erroneously high, perhaps due to clogging of the reaction chamber in the instrument. Hence isotopic and $H_2O$ content data of these samples have been discarded in favor of published data on BGM effusive obsidians from DeGroat-Nelson et al. (2001). The inclusion of these data shall induce no uncertainty stemming from the types or locations of these obsidians because one of the authors of the present study (Castro) assisted in sampling campaign of DeGroat-Nelson et al. (2001).

### 6.3.2 Analytical techniques

Measurements of the deuterium ($^2H$) to hydrogen ($^1H$) ratio (=δD) on 74 pyroclastic obsidian clasts (Table 6.1) were carried out at the Johann Wolfgang Goethe-University in Frankfurt using TCEA-MS (Thermal Conversion Element Analyzer-Mass Spectrometer). δD is assessed with respect to Standard Mean Ocean Water (SMOW) and is defined as follows:

$$\delta D = \frac{(\frac{^2H}{^1H})_{Sample} - (\frac{^2H}{^1H})_{Standard}}{(\frac{^2H}{^1H})_{Standard}} * 1000\ ‰ \quad (23)$$

Standard glasses (NBS-30, NBS-22, CH7) were measured during the analysis session to verify instrument accuracy.

We followed the sample preparation techniques outlined in Nolan and Bindeman (2013) and Castro et al. (2014), which are briefly summarized here. After selecting fresh ~1 cm diameter obsidian chips for analysis, the materials were cleaned in an ultrasonic bath and individual pyroclasts where then split by breaking them into coarse fragments with a steel mortar and pestle whereupon a large (~3 mm) fragment was set aside for FTIR analysis. In doing a replicate FTIR measurement on the same material as would be measured by TCEA-MS, we could compare (and independently check) $H_2O$ content assessments. The remaining fragments of the broken clast were dedicated to TCEA-MS analyses, and thusly, ground in an agate mortar to a grain size of about 150 μm, constrained by passing the powdered samples through sieves. The powders were then packed into silver cups and folded shut before weighing on an analytical balance with 6 digit precision. The mass of material analyzed (~3-10 mg) was determined in part by the anticipated range of $H_2O$ in the samples (e.g., Bindeman et al., 2012; Nolan and Bindeman, 2013). The hydrogen isotopic analyses were performed on a Thermo Finnegan TCEA-MAT 253 system, which yields $\delta D_{smow} = ([(^2H/^1H)_{sample} /(^2H/^1H)] - 1) \times 10^3$. Measurements have a precision of $\pm$ 3 ‰ for δD. In some cases (e.g., very dry obsidian) more sample material was needed leading to a larger capsule, which in turn had poor positioning within the TCEA's reactor chamber. The adjusted precision is estimated to be 3-6 ‰ for these samples.

Analytical problems were encountered when measuring the driest obsidian samples, i.e., the effusive obsidians, by TCEA. The reason for this was that given the low total $H_2O$ (and hydrogen concentrations), significant material (>10 mg) had to be loaded into the furnace, which resulted in clogging and failure of the TCEA's reaction chamber furnace. Consequently, the data on BGM obsidian lava were anomalous and unusable. We therefore supplemented our pyroclastic obsidian data set with published hydrogen isotopic data of DeGroat-Nelson et al. (2001), who made their measurements via step-heating and whole rock fusion methods on BGM effusive obsidians located near the outcrops sampled in this study.

Even though it has been reported that the TCEA-MS procedure returns an $H_2O$ content for the bulk sample with an accuracy of $\pm$0.01 wt.% (Bindeman et al., 2012), no inter-laboratory standards for $H_2O$ quantification via TCEA exist; furthermore, a thorough $H_2O$-measurement error analysis on the instrument at the University of Frankfurt has not been made. Consequently, we sought an independent assessment of bulk $H_2O$ content and hydrous speciation through the FTIR method (e.g., Castro et al., 2012). The bulk $H_2O$, along with the

**Table 6.1:** δD and bulk $H_2O$ content of pyroclastic and effusive obsidians from Big Glass Mountain, CA, USA. S.D. = standard deviation; n.d. = not determined.

| Sample Name | Type (position) | δD (‰) | S.D. (‰) | $H_2O$ by FTIR (wt.%) | $H_2O$ molec. (wt.%) | OH (wt.%) |
|---|---|---|---|---|---|---|
| Mz_VTS0_2a3 (n=2) | Pyroclastic (30 cm) | -104.6 | 1.6 | 0.40 | 0.10 | 0.30 |
| Mz_VTS0_2a4 (n=2) | Pyroclastic (30 cm) | -90.7 | 3.0 | 0.76 | 0.14 | 0.63 |
| Mz_VTS0_2a5 (n=2) | Pyroclastic (30 cm) | -99.3 | 0.5 | 0.57 | 0.09 | 0.49 |
| Mz_VTS0_2b1 (n=2) | Pyroclastic (45 cm) | -92.5 | 1.0 | 0.79 | 0.16 | 0.64 |
| Mz_VTS0_2b2 (n=2) | Pyroclastic (45 cm) | -95.0 | 0.2 | 0.75 | 0.14 | 0.61 |
| Mz_VTS0_2b4 (n=2) | Pyroclastic (45 cm) | -95.7 | 1.2 | 0.52 | 0.08 | 0.45 |
| Mz_VTS0_3a2 (n=2) | Pyroclastic (60 cm) | -115.4 | 1.7 | 0.24 | 0.03 | 0.21 |
| Mz_VTS0_3a3 (n=2) | Pyroclastic (60 cm) | -90.9 | 1.9 | 0.74 | 0.10 | 0.64 |
| Mz_VTS0_3a4 (n=2) | Pyroclastic (60 cm) | -100.4 | 5.0 | 0.53 | 0.12 | 0.41 |
| Mz_VTS0_3b3 (n=2) | Pyroclastic (75 cm) | -90.2 | 2.2 | 0.80 | 0.17 | 0.63 |
| Mz_VTS0_3b4 (n=2) | Pyroclastic (75 cm) | -105.6 | 2.9 | 0.43 | 0.08 | 0.35 |
| Mz_VTS0_4b1 (n=1) | Pyroclastic (90 cm) | -88.2 | - | 0.76 | 0.12 | 0.64 |
| Mz_VTS0_4b3 (n=2) | Pyroclastic (90 cm) | -98.4 | 4.7 | 0.51 | 0.05 | 0.46 |
| Mz_VTS0_5a2 (n=2) | Pyroclastic (105 cm) | -97.7 | 3.8 | 0.56 | 0.07 | 0.49 |
| Mz_VTS0_5a3 (n=2) | Pyroclastic (105 cm) | -96.8 | 0.3 | 0.49 | 0.07 | 0.42 |
| Mz_VTS0_5b3 (n=2) | Pyroclastic (120 cm) | -91.1 | 4.6 | 0.87 | 0.18 | 0.70 |
| Mz_VTS0_5b5 (n=2) | Pyroclastic (120 cm) | -89.7 | 2.3 | 0.78 | 0.14 | 0.65 |
| Mz_VTS0_6a1 (n=2) | Pyroclastic (135 cm) | -101.3 | 1.2 | 0.39 | 0.02 | 0.37 |
| Mz_VTS0_6a2 (n=2) | Pyroclastic (135 cm) | -109.8 | 1.1 | 0.29 | 0.02 | 0.27 |
| Mz_VTS0_6b1 (n=2) | Pyroclastic (150 cm) | -101.4 | 0.4 | 0.44 | 0.06 | 0.38 |
| Mz_VTS0_6b3 (n=2) | Pyroclastic (150 cm) | -99.5 | 0.7 | 0.49 | 0.07 | 0.42 |
| Mz_VTS0_6b4 (n=2) | Pyroclastic (150 cm) | -106.4 | 0.1 | 0.38 | 0.02 | 0.36 |
| Mz_VTS0_7A1 (n=2) | Pyroclastic (165 cm) | -90.7 | 0.4 | 0.77 | 0.12 | 0.64 |
| Mz_VTS0_7A2 (n=2) | Pyroclastic (165 cm) | -104.8 | 2.8 | 0.30 | 0.02 | 0.28 |
| Mz_VTS0_7b2 (n=1)† | Pyroclastic (180 cm) | -99.1 | - | 0.56 | n.d. | n.d. |
| Mz_VTS0_7b5 (n=2)† | Pyroclastic (180 cm) | -100 | 1.5 | 0.48 | n.d. | n.d. |
| Mz_VTS0_8a1 (n=2) | Pyroclastic (195 cm) | -99.2 | 3.5 | 0.46 | 0.05 | 0.41 |
| Mz_VTS0_8a2 (n=1) | Pyroclastic (195 cm) | -108 | - | 0.36 | 0.04 | 0.32 |
| Mz_VTS0_8a5 (n=2) | Pyroclastic (210 cm) | -100 | 0.1 | 0.56 | 0.06 | 0.5 |
| Mz_VTS0_10b2 (n=1) | Pyroclastic (225 cm) | -97.2 | - | 0.66 | n.d. | n.d. |
| Mz_VTS0_15a1 (n=2) | Pyroclastic (245 cm) | -102.8 | 0.1 | 0.50 | n.d. | n.d. |
| GM94-10 (n=1)* | Lava | -152.2 | - | 0.14 | n.d. | n.d. |
| GM94-11 (n=1)* | Lava | -146.5 | - | 0.13 | n.d. | n.d. |
| GM95-02 (n=1)* | Lava | -120 | - | 0.13 | n.d. | n.d. |
| GM95-06 (n=1)* | Lava | -117.1 | - | 0.14 | n.d. | n.d. |
| GM95-07 (n=1)* | Lava | -126.3 | - | 0.10 | n.d. | n.d. |
| GM95-11 (n=1)* | Lava | -142.9 | - | 0.12 | n.d. | n.d. |
| GM95-15 (n=1)* | Lava | -138.1 | - | 0.11 | n.d. | n.d. |
| GM97-01 (n=1)* | Lava | -139.1 | - | 0.06 | n.d. | n.d. |
| GM97-02 (n=1)* | Lava | -139.4 | - | 0.07 | n.d. | n.d. |
| GM97-03A (n=1)* | Lava | -131.9 | - | 0.10 | n.d. | n.d. |
| GM97-03B (n=1)* | Lava | -143.5 | - | 0.10 | n.d. | n.d. |

*Measurements from DeGroat-Nelson et al. (2001)

†$H_2O$ contents from TCEA

$H_2O$ and OH-group species in splits of TCEA-MS measured obsidian glasses were quantified using a Thermo-Nicolet FTIR Bench with attached Continuum microscope at the Johannes Gutenberg University in Mainz. Doubly polished pyroclastic obsidians, sectioned from pyroclast interiors so as to avoid surface alteration, and ranging in thickness (~160-500 μm) were analyzed on spots (~50 μm) in transmission mode at a spectral resolution of 4 $cm^{-1}$, using 256 scans and a sample-free-path background spectra collected every 30 minutes. Sample thicknesses were determined to an accuracy of $\pm$ 5 μm with a Mitutoyo digital micrometer. A KBr beamsplitter, and liquid-$N_2$ cooled MCT detector were configured on the FTIR system to yield maximum signal strengths over a broad bandwidth (~6000 $cm^{-1}$ to <1000 $cm^{-1}$ spectral range). The relatively thick samples were required because of the need to resolve the hydrous species peaks at 4500 $cm^{-1}$ and 5200 $cm^{-1}$, which correspond to OH and $H_2O$ molecular groups, respectively. In addition, some samples with rather low bulk $H_2O$ contents (<0.1 wt.%) exhibited good quantifiable mid-IR absorbance peaks at 3550 $cm^{-1}$. We used a linear baseline to measure the different peaks' heights, and, these absorbance values would then be input into Beer's Law. As Beer's law also requires a glass density and extinction coefficient values, we calculated glass densities using the approach of Lange and Carmichael (1990) and used extinction coefficients for rhyolite glass from Ihinger et al. (1994). Finally, we estimated detection limits of ~0.005 wt.% $H_2O$ based on the analysis of multiple spots yielding the 3550 $cm^{-1}$ peak and observing its topological change as we collected unknown spectra at various scan rates.

### 6.3.3 Modeling volcanic degassing trends

The analytical measurements yield $H_2O$ bulk concentration (wt.%) and corresponding δD (in ‰) values of pyroclastic obsidians (Table 6.1). We plotted these two parameters against one another to investigate "degassing trends", particularly by fitting them with various idealized degassing models, including: closed-system, open-system, and batched degassing (e.g., Newman et al., 1988; Taylor, 1991; Rust et al., 2004). As single-stage model fits were not sufficient to match the data, we additionally investigated "two-staged" paths, specifically, closed-to-open and closed-to-batched, both of which simulate the magma becoming progressively more open as degassing proceeds (e.g., Eichelberger et al., 1986).

All model simulations were performed with the Matlab program "VolcDeGas" (Walter, 2017; Walter and Castro, 2020; Castro and Walter, 2021, Supplementary Material[ii]), which allows users to input various magmatic conditions to investigate different degassing mechanisms in hydrous rhyolite melts. VolcDeGas outputs comprise plots of δD vs. $H_2O$ superimposed on, and statistically fit to the original analytical data. The program's input parameters include: 1)

[ii] Supplementary Material download: https://www.jvolcanica.org/ojs/index.php/volcanica/article/view/121/137

the initial and final $H_2O$ content, 2) the initial δD of the melt, 3) the hydrous speciation (determined by FTIR and confirmed and extrapolated to other higher-than-observed $H_2O$ contents by the program), 4) the temperature (when hydrous speciation data are unavailable), and 5) the speciation-dependent fractionation factors (also computed by VolcDeGas based on measured $H_2O$ speciation). VolcDeGas calculates solutions to simple closed-system (mass conservative), open- (Rayleigh distillation), and batched system equations by mass balance for each degassing step (e.g., Taylor, 1991; Castro et al., 2014).

Batched systems were modeled by using sequential closed-system steps, similar to the approaches of Taylor (1991) and Castro et al. (2014). Each step is treated as a “vapor reservoir” filling event, whereby the reservoir is imaginary but could represent cracks or bubbles. During the initial filling calculation, VolcDeGas iteratively determines the equilibrium composition of δD in both the vapor and melt for a given amount of $H_2O$ loss into the reservoir. When the filling reaches the step-size determined value of $H_2O$ decrease, the vapor is then instantaneously removed from the system. The result of this calculation procedure is a slightly curved line corresponding to a single closed system step (e.g., Dobson et al., 1989; Walter and Castro, 2020).

In all degassing systems, the step size must be specified, which is the fractional amount of $H_2O$ exsolved and lost from the initial magmatic $H_2O$ budget during each step. In a simple closed system, this amount of $H_2O$ loss is fixed because the vapor is forced to stay in isotopic equilibrium with the initial $H_2O$ budget. However, in batched- and open-system cases, because the amount of “residual” $H_2O$ is continually updated with each step, and decreases, a fractional amount of this residual $H_2O$ produces variable step sizes that will get incrementally smaller as the bulk $H_2O$ budget diminishes with each degassing step (Walter and Castro, 2020).

We assessed the most permissible degassing scenario for the BGM eruption based on VolcDeGas’ internal goodness-of-fit to data assessment routine (Walter and Castro, 2020). More specifically, the best-fit trend for each degassing system is the result of hundreds of separate computed degassing trends, each taking into account the user input data and degassing intervals (e.g., step size). The best-fit is then selected by VolcDeGas on the basis of its own determination of the minimum Root Mean Square Error (RMSE), which indicates the standard deviation between predicted δD-$H_2O$ values and the observed natural data (Walter and Castro, 2020). Two-stage degassing models, furthermore, have a transition point corresponding to the changeover from closed-system process and the onset of a new mechanism, be it batched or open-system degassing. These transition points were objectively chosen by VolcDeGas, which finds the best-fit transition with an iterative approach in which it

firstly calculates the initial best-fit closed-system degassing segment via the aforementioned calculation-intensive procedure. Next, the program tests different transition point positions along the previously calculated closed-system segment by adjusting both the input parameters and the resultant second stage degassing trend. VolcDeGas automatically adjusts the transition point to achieve the maximum coefficient of determination ($R^2$) and minimum RMSE values. Additional information on how VolcDeGas operates including its validation with case study data can be found in Walter and Castro (2020).

## 6.4 Results

### 6.4.1 Field evidence for hybrid volcanism at BGM: key insights from recently active rhyolite volcanoes

Recent eruptions at Chaitén and Cordón Caulle provided evidence of how rhyolite events can progress, showing in a clear and unprecedented manner that transitions from explosive to effusive activity may be exceptionally drawn-out (months long), rather than sharp (e.g., Eichelberger, 1975; Giachetti et al., 2020). At both volcanoes, hybrid effusive-pyroclastic venting lasted until the lavas were nearly completely emplaced, meaning that the initial purely explosive and final effusive phases were short (weeks-long), effectively "bookending" activity dominated by this hybrid style. Both Chaitén and Cordón Caulle exhibited hybrid venting for months to upwards of a year (Castro et al., 2013; Pallister et al., 2013, Supplementary Material[ii]). We contend that field evidence for simultaneous venting of pyroclasts and lavas should be present in older systems that erupted this way, yet were not observed. We therefore firstly describe the depositional record at Chaitén and Cordón Caulle to establish a framework to interpret features indicative of hybrid activity in and on BGM's lava flow. These features, for all intents and purposes, argue for a drawn-out transition from initial explosive to effusive of activity during the eruption of BGM. As we have no firm constraints on temporal scale for activity at BGM, we can only speculate that if eruption rates at BGM resembled those of the Chilean events (~tens of $m^3s^{-1}$; Pallister et al., 2013), the similarity in effusive eruption deposit volumes (~1 $km^3$) may imply similar months-long hybrid activity at BGM.

The salient depositional features formed during Chaitén and Cordón Caulle's hybrid eruptions comprise mixtures of pyroclastic and effusive materials, ranging from very large-scale depositional structures to microscopic textures. The key deposits include: 1) glassy to pumiceous ballistic bombs comprised of various textural components (e.g., breccia: Schipper et al., 2021) and deposited in vent-proximal locations (e.g., Castro et al., 2014); 2) expansive (100s m long) pyroclastic ridges positioned in middle of the lava field (e.g., Tuffen et al., 2013;

[ii] Supplementary Material download: https://www.jvolcanica.org/ojs/index.php/volcanica/article/view/121/137

Castro et al., 2014); 3) unconsolidated to well welded pyroclastic fall deposits mantling the tops of lava; 4) interspersed mixtures of pyroclasts and coherent obsidian lava that occur in joint-like channel structures—so-called tuffisite veins—that crosscut massive lava bodies (Tuffen et al., 2003; Wadsworth et al., 2018). With the clear physical evidence for hybrid eruption at Chaitén and Cordón Caulle in hand, in the following passages, we describe evidence for three of the four features that indicate significant hybrid activity at BGM.

#### 6.4.1.1 Ballistic bomb fields

Ballistic bomb activity characterized the early transition from purely explosive activity to hybrid venting at both Chaitén and Cordón Caulle volcanoes (Schipper et al., 2013; Castro et al., 2014). The bomb fields at both Chaitén and Cordón Caulle are well preserved due to the topography and emplacement patterns of the lavas, which precluded burial of the bombs by advancing lava. In both locations, ballistic bombs ranging from decimeters to a couple meters in size litter the near-vent region, but can also be found cratering the landscape several km from the vent.

At BGM, the lava fields are so extensive that most vent regions are obscured by lava. Our field work, which focused on the south-central flow fields and tephra fall deposit (Figure 6.1), did not reveal the presence of a bomb field at BGM. However, because the BGM eruption occurred along a fissure, and the north end of this fissure was not overtopped by lava, (Anderson, 1933; Donnelly-Nolan et al., 2016), abundant ballistic bombs can be found resting on tephra aprons and the many satellite domes at these locations (Donnelly-Nolan et al., 2016; personal communication). We suggest that the lack of bombs at BGM in more central fissure locations may be due to the overrunning of the bomb field by the expansive BGM lava flows.

#### 6.4.1.2 Pyroclastic ridges

Pyroclastic ridges at BGM are conspicuous accumulations of reddish brecciated material that have distinct surface texture (e.g., an abundance of fine ash and lapilli sized particles) and componentry that is atypical of rhyolite lava, which comprises coarse (decimeter to meter sized) blocky lava with varying vesicularity (Figure 6.1, 6.2, 6.3A, B). Anderson (1933) suggested that these ridges are evidence of how lavas at BGM effused and destroyed a very large pumice cones and that remnants of these accumulations—now present as pyroclastic ridges—are now exposed in the southern part of the flow (Figures 6.1 and 6.2). Eichelberger (1975) recognized these distinct breccia zones too, and noted that their arcuate shape and topographic relief conform to the inferred flow emplacement mechanism and sequence.

However, based on a lack of pumice bombs, as is seen in the tephra cones to the north of BGM, Eichelberger (1975) argued that these ridges were not rafted pyroclastic cones but rather lava bodies that had brecciated in place and were subsequently hydrothermally altered to clay.

The breccia ridges are distributed at BGM in a radial pattern with respect to the central vent of the flow, which is the highest point from which they may have been sourced (Figure 6.1). Ridges comprise large (tens of m in width by several hundreds of m in length) curved zones that outcrop predominantly in the SW flow interior (Figures 6.1 and 6.2), however fragments of ridges are also present in the NE and SE flow sections (Figure 6.1). The ridges are distinctly pinkish-red and highly vegetated in contrast to the barren grey and black lava that surrounds them (Figure 6.3A, B).

Close up examination of the components and textures of breccia zones (Figure 6.2) reveals that Eichelberger (1975) hypothesis positing *in situ* auto-brecciation of lava could not have been the case. Specifically, the breccia zones do in fact contain all of the components of tephra cones (Donnelly-Nolan et al., 2008), including pristine pumice bombs, highly vesicular pumices, dense obsidian, and polymictic breccia, comprising clasts ranging from ash to block-size (~1 mm to 1 m; Figure 6.2). The breccia zones, furthermore, have undergone varying degrees of welding, as evidenced by zones of vitrophyric textured lava, observable on both mesoscopic and microscopic scales (Figure 6.2E - G, 6.4). Welding would not be expected if these zones formed solely by superficial brecciation of relatively cool and blocky surface crust (Figure 6.3).

Breccia zones are rich in fine red ash, which forms a supporting matrix to larger clasts (Figure 6.2D, Figure 6.4). The clasts within the breccia range from dense glassy to vesicular grains with internal frothy zones mantled by outer glassy selvages (Figure 6.2F). Such textures are indicative of fragmentation of initially low vesicularity material followed by later frothing of $H_2O$-saturated melt. Similar textures and structures are abundant in bombs from Chaitén, whose origin was directly linked to hybrid activity from Chaitén's tephra cone (Castro et al., 2012).

The aforementioned field observations and textural and lithological features of BGM's breccia zones indicate that these features must be of pyroclastic origin. Unlike the typical flow-top lava, which lacks a matrix component, and comprises large (decimeter to meter scale) coherent, separable and movable blocks (Figure 6.3A, B), the breccia is much more cohesive at the outcrop scale and lacks evidence of hydrothermal alteration (e.g., clay mineralization, perlite, etched glass; Eichelberger, 1975). The welded areas within breccia zones, furthermore, have

ignimbrite-like foliated textures (Figure 6.2E-G), suggesting that these pyroclastic materials were hot when they were incorporated into the lava. Thin sections of welded breccia reveal partially to completely sintered pyroclasts, some of which retain their original outlines and are moderately to severely stretched into a eutaxitic foliation (Figure 6.4). Some larger clasts (~5 cm) appear to have re-expanded after some time in the flow, in turn resulting in distortion of the foliation. Foliated and revesiculated structures are absent in the "normal" lava flow flow top breccias.

The textures of the breccia zones are consistent with the production of their inherent pyroclasts from a venting cone, wherein the thermal energy and $H_2O$ remaining in freshly erupted fragments would foster deformation, welding, bubble nucleation and growth (Castro et al., 2005). These characteristics, along with the macroscopic form and structure of the ridges, in turn require that the pyroclastic materials now making up the breccia ridges were swept away by a moving mass of lava shortly after they were freshly lain down. Breccia ridges found embedded within the vast Cordón Caulle lava flow formed exactly in this manner (Tuffen et al., 2013; Castro et al., 2014, Supplementary Material[ii]), and thus, provide a model of how this could have transpired at BGM.

#### 6.4.1.3 Pyroclastic air-fall lava mantles

Evidence for pyroclastic fallout during lava emplacement is difficult to find on obsidian flows. This is due in part to the pervasive fracturing that the lava surface undergoes as it deforms and cools. Unconsolidated pyroclastic material deposited on that dynamically deforming and brecciated surface may be ingested by the flow itself as cracks provide space for clasts to fall into. This behavior was observed at both Cordón Caulle and Chaitén, where newly effused near-vent lava was initially covered with falling pyroclastic debris, but then quickly ingested that thin mantle as the flow moved from the vent (Supplementary Material[ii]; see also Figure 1 in Castro et al., 2014).

At BGM, however, some sections of lava remain draped with thin pyroclastic units (Figure 6.3C, D). These rare, meter-thick exposures consist of poorly sorted, unconsolidated pumice and obsidian blocks that grade downward into poorly welded pumice and ash deposits. The pumice lapilli then grade into moderately well welded breccia whose foliation is parallel to the flow surface. In a similar context to the breccia ridges, we interpret these deposits as products of hot pyroclastic deposition—likely by proximal air fall—and incipient welding of the pyroclasts as they accumulated on a hot flow surface.

[ii] Supplementary Material download: https://www.jvolcanica.org/ojs/index.php/volcanica/article/view/121/137

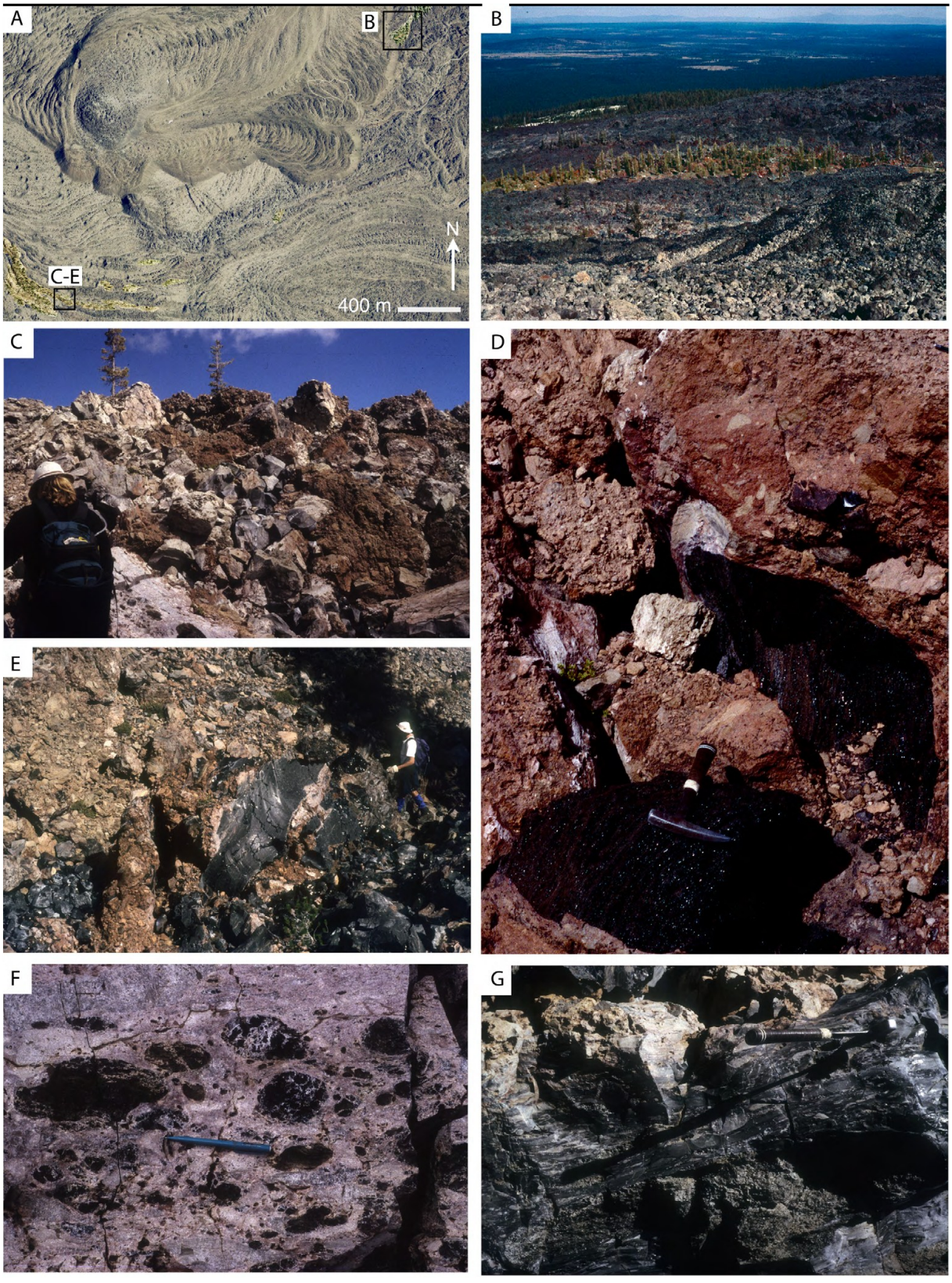


**Figure 6.2:** [Caption on next page]

**Figure 6.2:** [A] NAIP (National Agriculture Imagery Program) satellite image of Big Glass Mountain. Breccia zones are highlighted by color enhancement in the lower left and upper right to distinguish them from "normal" flow top lava textures. Frames [B] and [C-E], correspond to field photographs of the boxed in areas in frame [A]. These views show breccia zones [C] comprising meter-scale massive red breccia, pumice and obsidian bombs [D], and ash-rich polymictic breccia fragments [D]. Some breccia zones contain massive obsidian blocks interwoven with channels containing unconsolidated pyroclasts [E]. Such features may represent mega-tuffisites that were actively venting as lava effused from the vent (e.g., Castro et al., 2014). Frames [F] and [G] show representative welding textures in breccia blocks that most likely underwent intense shear deformation during emplacement of the lava flow. That fragments as small as a centimeter are re-expanded through vesiculation (see rounded clasts in frame [F]) and also densely welded [G] indicates that pyroclasts retained significant heat and $H_2O$ during the process of post-fragmentation welding. In the most densely welded case, breccia has a eutaxitic foliation like that found in welded tuffs. Such textures—not found in "normal" flow top breccia—indicate that little if any time elapsed between the explosive activity that made the breccias and lava emplacement that swept them away.

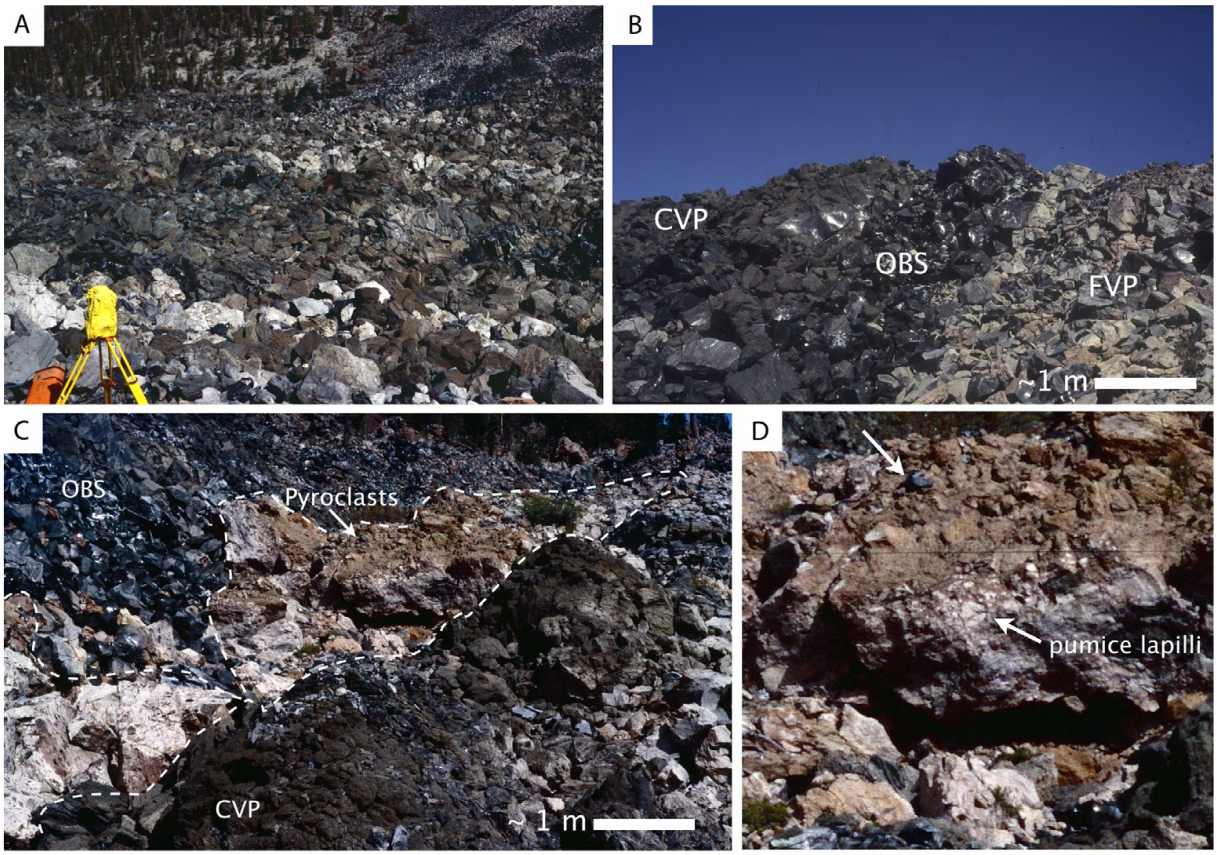


**Figure 6.3:** [A] – [B] Field photographs showing typical lava flow top morphology and texture on Big Glass Mountain. Lava comprises meter-sized angular blocks of finely and coarsely vesicular pumice (FVP and CVP) and dense black obsidian (OBS). Frames [C] and [D] show rare exposures of pyroclastic mantle deposits on normal obsidian lava flow top. In frame [C], pyroclastic deposits are confined to a small swale (enclosed in white dashed lines) in the flow, which corresponds to a valley formed during folding of the flow top. These pyroclasts are shown in magnified view in frame [D]. Like pyroclastic material in the breccia zones, these deposits have a reddish hue that contrasts sharply from the surrounding lava. The overall grain size is highly variable, ranging from lapilli to bomb size fragments, and grading from blocky pyroclastic material on top to progressively denser partially welded pyroclasts in contact with the lava at its base. The presence of pumice lapilli and unconsolidated obsidian blocks suggest these materials were deposited from the air on an actively effusing lava (see also equivalent features at Cordón Caulle in the Supplemental Material[ii]).

[ii] Supplementary Material download: https://www.jvolcanica.org/ojs/index.php/volcanica/article/view/121/137

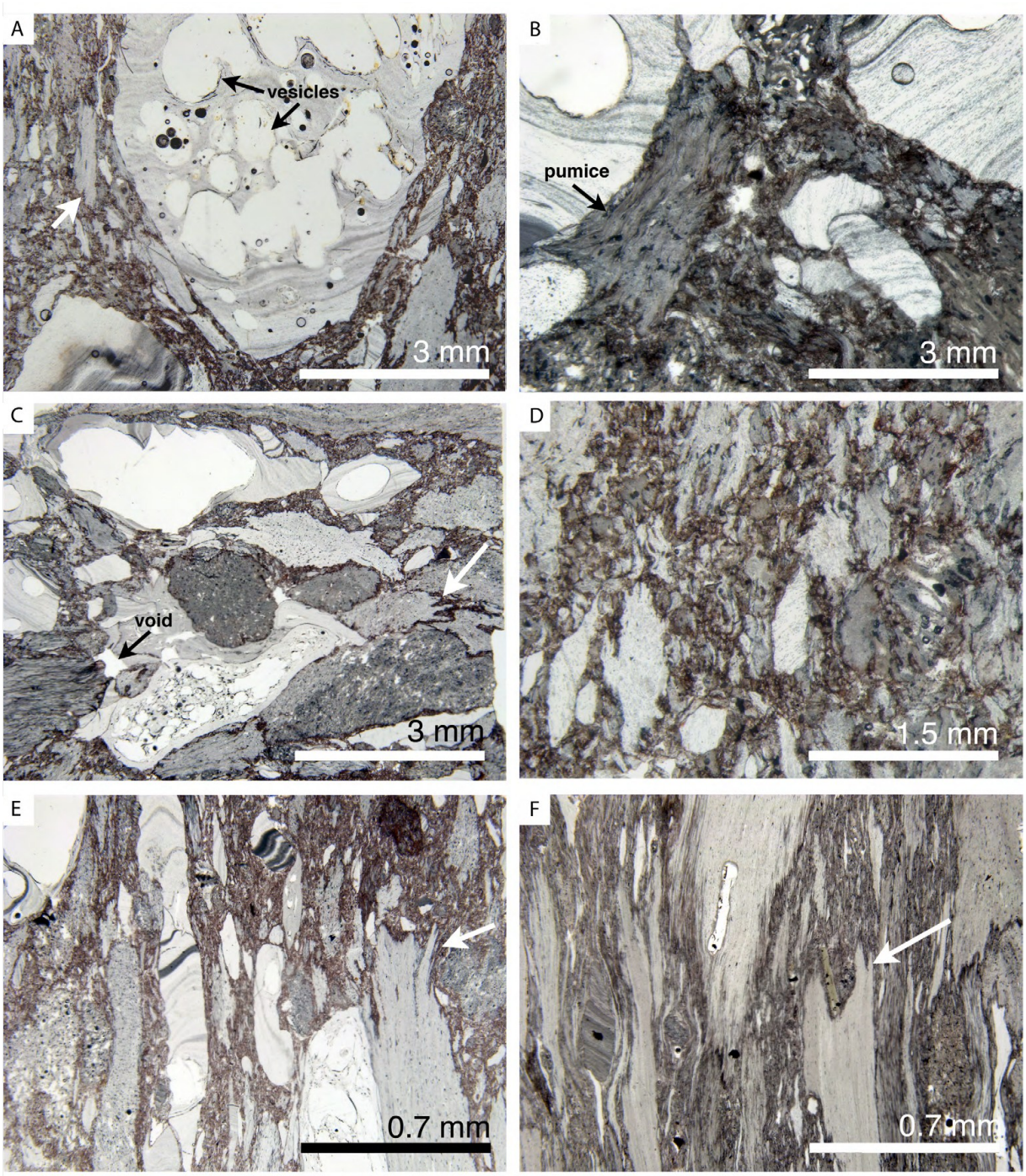


**Figure 6.4:** Optical light photomicrographs of breccia material sampled from the BGM lava flow. In thin section, the breccia comprises variable amounts of fine ash matrix and lapilli-sized clasts. The fragments themselves consist of dense, often flow banded glass, to moderately vesicular pumice [A], [B]. Frames [A] and [B] show relatively outsized flow banded obsidian clasts that underwent secondary vesiculation that disrupts flow banding. Such evidence, along with prevalent fiamme structures (white arrows in frames [A], [B], [C], and [F]) indicates that post-fragmentation welding and expansion occurred while material was pyroclasts were still hot, relatively hydrous, and above the glass transition point (~740˚C; Castro et al., 2005). Frame [C] shows the abundance of diverse clasts with sutured grain boundaries and some remnant pore space (void). Frames [D] through [F] indicate the progression of increasing welding intensity in dense sintered ash, from moderate [D] to extreme [F].

Nearly identical pyroclastic veneers are found on the distal parts of the Cordón Caulle lava, corresponding to products that were effused early in the eruption when simultaneous pyroclastic venting was elevated in energy (Supplementary Material[ii]; Figure S1). Like at BGM, these deposits are thin (~1 m), spatially constrained (2-5 $m^2$), and exhibit the same sequence of coarse to fine pyroclasts overlying incipiently welded tuffs on the flow surface (Supplementary Material[ii]; Figure S1). The striking similarity between field relations of these airfall deposits, along with the observed mode of formation at Cordón Caulle, strongly supports the field evidence for simultaneous effusive-explosive activity at BGM.

### 6.4.2 Hydrous geochemical signature of degassing: $H_2O$-δD measurements

Figure 6.5 shows the results of $H_2O$ (via FTIR) and hydrogen isotopic measurements (TCEA) on BGM pyroclastic obsidians. Also shown for reference are $H_2O$-δD data from BGM lavas analyzed by DeGroat-Nelson et al. (2001); these are included because they extend the range in data to lower $H_2O$ contents, thereby providing a more complete picture of degassing history (e.g., see also Giachetti et al., 2020, who use data from DeGroat-Nelson et al., 2001). The collective trend in δD is at first subtle (Figure 6.5) followed by a very pronounced drop in δD quite similar to those of other rhyolite systems (e.g., Inyo Domes, Taylor, 1991; Chaitén, Castro et al., 2014).

The distribution of $H_2O$ contents of pyroclastic and lava samples shows a range of $H_2O$ (~1.1 to ~0.1 wt.%), which are similar to, and within the range of values observed at other rhyolite systems, including Chaitén (Castro and Mercer, 2004; Castro et al., 2012; Forte and Castro, 2019, Figure 6.5). We interpret these hydrous data to represent the true "magmatic $H_2O$" component and contend that BGMs pyroclasts have not suffered any post-depositional $H_2O$ loss due to, for example, hot deposition and slow cooling of clasts within the pyroclastic pile. Drawing on the work of Castro et al. (2012), who performed diffusive $H_2O$ outgassing calculations of 1-cm-sized spherical obsidian fragments at 625˚C, we note that particles of this size require exceedingly long timescales (~340 days) to diffusively release just a minor amount of $H_2O$ (~0.2 wt.% in the interval 0.8 - 0.6 wt.% $H_2O$; Castro et al., 2012). As it seems untenable that a pyroclast could stay hot for upwards of a year within a deposit, notwithstanding the potential for significant cooling during that pyroclast's flight, we believe that the $H_2O$ contents measured on pyroclastic (and effusive) obsidians are robust records of hydrous geochemical processes during eruption.

As shown in Figure 6.5, the δD's of obsidians measured in this study (Table 6.1) range from -88.1 ‰ at high-$H_2O$ to -116.6 ‰ at the low-$H_2O$ limit. However, effusive obsidian data of

[ii] Supplementary Material download: https://www.jvolcanica.org/ojs/index.php/volcanica/article/view/121/137

DeGroat-Nelson et al. (2001) extend the range of BGM values to extremely deuterium-depleted values (~-152 ‰) at low bulk-$H_2O$ contents. Finally, we found no systematic variation in either $H_2O$ or δD with stratigraphic position in the pyroclastic deposit (Table 6.1). This corroborates the results of Giachetti et al. (2020), whose own $H_2O$-δD data also lack a vertical trend in these variables. The lack of pattern may stem from the eruption of BGM along a fissure, and the possibility that pyroclastic lobes sourced from different fissure vents might overlap with one another (C. Dan Miller, 2007, personal communication), thereby colluding potential systematic variation in hydrous component values.

### 6.4.3 Modeling BGM degassing with VolcDeGas

In order to investigate potential degassing mechanisms that could have given rise to this geochemical trend, we used VolcDeGas, a Matlab-based utility for modeling degassing trajectories (Walter and Castro, 2020). VolcDeGas allows the user to determine the statistically best-fit degassing paths to natural δD–$H_2O$ data by simulating single and multi-staged degassing paths (e.g., closed-to-open system). The accuracy of these model paths is objectively determined by the program through an iterative data-fitting algorithm (further details in Walter and Castro, 2020).

Modeling potential BGM degassing paths required that initial pre-eruptive conditions (e.g., $H_2O$ content and δD) of the magma be established as starting points for VolcDeGas simulations. Waters et al. (2015) and Waters and Lange (2016) determined the storage conditions of BGM rhyolite based on phase petrology experiments and plagioclase hygrometry. Their results suggest a range of possible pre-eruptive *P-T* conditions (T= ~850-930˚C; P= ~25-80 MPa), that collectively imply an initial volatile budget of ~2-4 wt.% $H_2O$. We have chosen to run models based on the average of these estimates, i.e., a pre-eruptive water content on the order of 3 wt.% $H_2O$, consistent with an intermediate pressure. As $CO_2$ went undetected in all measured obsidians (e.g., see also Giachetti et al., 2020), we proceeded with modeling under pure $H_2O$-saturated conditions. The initial δD of the magma is not known *a priori*, however, for modeling degassing paths this parameter is varied iteratively over a set range of possible starting conditions by the program that lead to a best fit to data (e.g., Castro et al., 2014; Giachetti et al., 2020). In particular, the best fit models described below (e.g., two-staged closed-to-open and batched) were achieved with initial δD's of -68 ‰, which corresponds well with values measured on similarly aged hydrous rhyolitic obsidians (~3.1 wt.% $H_2O$) from Little Glass Mountain (Taylor et al., 1983).

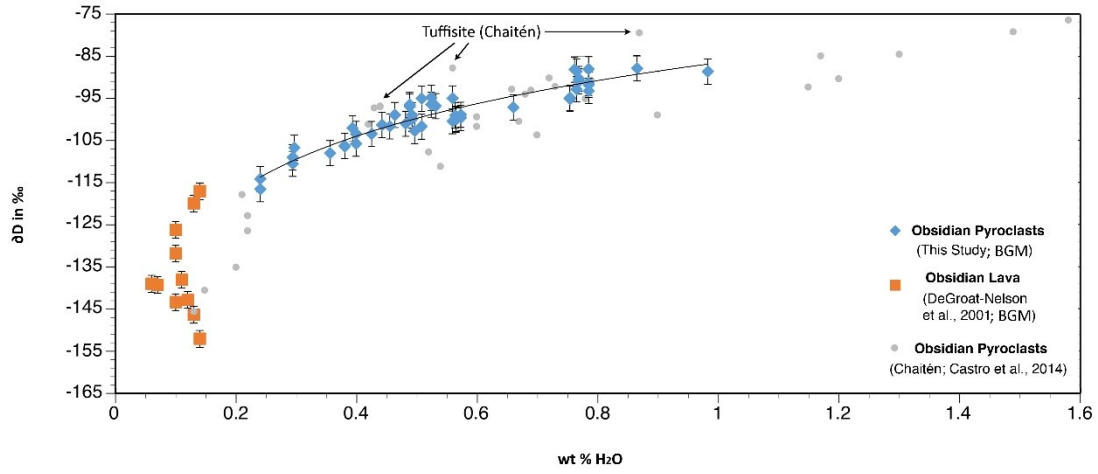


**Figure 6.5:** δD–$H_2O$ (bulk) compositions of Big Glass Mountain rhyolite. Blue diamonds are obsidian pyroclasts analyzed in this study whereas orange squares are data collected by DeGroat-Nelson et al. (2001) on flow margin obsidian lavas. Grey circles are data derived from pyroclasts sampled from Chaitén volcano by Castro et al. (2014). Error bars demarcate the measurement uncertainty for the TCEA-method applied in this study (isotopic error is ±3 ‰, whereas the DeGroat-Nelson et al. (2001) data carry a ±2 ‰ error. Measurement uncertainty in $H_2O$ contents (determined by FTIR; ~0.01 wt.%) are well within the breadth of the symbols. The curve fit ($R_2$ = 0.88) to the pyroclastic obsidian data is a logarithmic expression of form: y = 17.6 ln(x) - 87.7; meant for statistical representation of trend and not as a degassing model.

Figure. 6.6A, B shows VolcDeGas model fits to natural data assuming a single-staged (either closed- or open-system) degassing mechanism. In general and perhaps unsurprisingly, single-staged models do not fit the complete range of data. In particular, the closed-system degassing path from an initial δD of -70 ‰ fits only the first segment of data ranging from approximately 1.0 to 0.5 wt.% $H_2O$, resulting in poor RMSE and $R^2$ values (>14.7, 0.8, respectively). Open-system degassing starting at a δD of -53 ‰ provides a better fit to the data than closed-system model (Figure 6.6B), however this model does not match the $H_2O$-rich samples at the start of the trend, which in part arises from the relatively high initial δD required to ensure that final degassing steps yield the very δD-depleted values at low-$H_2O$ content (effusive obsidians). Overall, the open system (with a small degassing step ~0.001 wt.%) yields moderately improved fit parameters (RMSE=8.5, $R^2$=0.89) over the closed-system case, but still leaves much of the data not adequately fit.

The poor-fits of single-stage models to the data (Figure 6.6A, B) imply that a two-staged, open-to-closed system model would globally fit the natural isotopic observations better (e.g., Taylor et al., 1983; Eichelberger et al., 1986; Newman et al., 1988; Giachetti et al., 2020). Thus, in Figure 6.6C we show the results of a two-stage, closed-to-open system path using an initial δD of -68 ‰. The transition point (0.4 wt.%) from closed- to open-system degassing was determined by VolcDeGas iterative fitting process (e.g., see Walter and Castro, 2020), and

signifies the best-fit change in degassing mechanism based on data. It is important to note that this transition point is purely empirical and does not implicate a sharp physical shift in eruptive activity in nature. As we can see in Figure 6.6C, the two-stage model conforms nicely to the data, yielding RMSE of ~6.7 and an $R^2$ of 0.87, a considerably better fit than the single-stage systems.

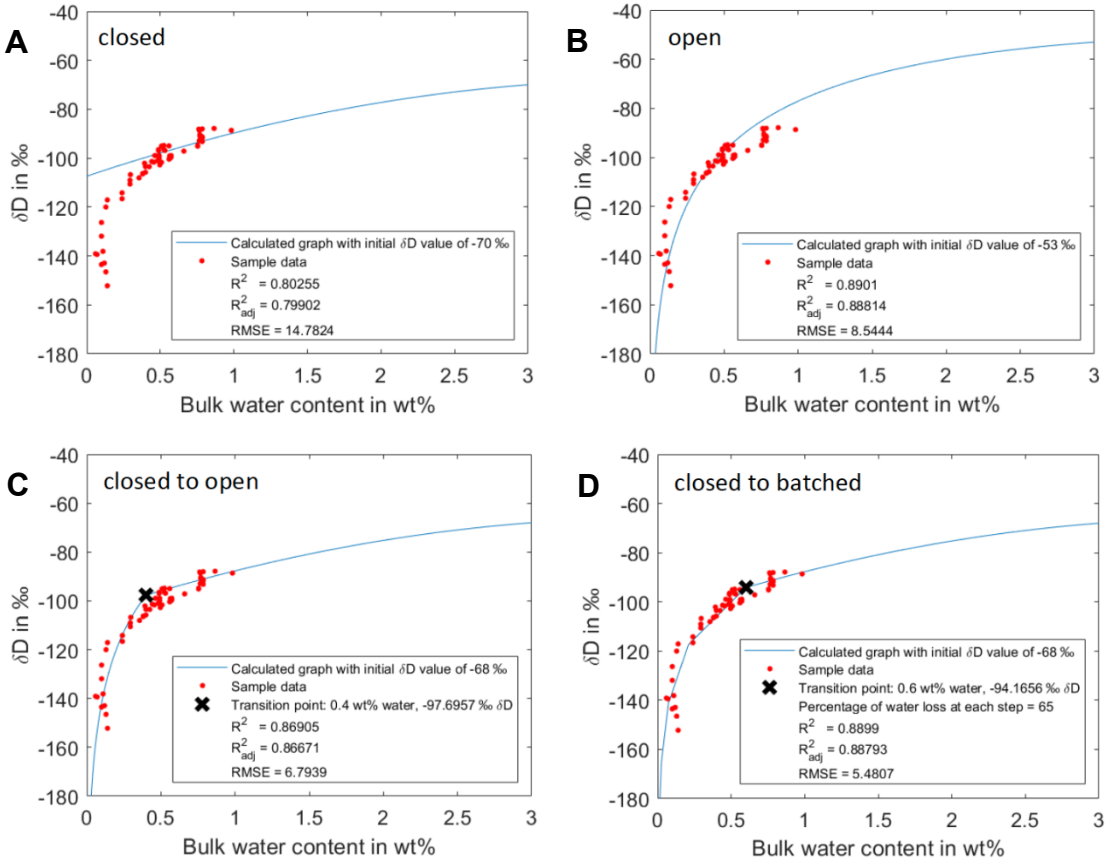


**Figure 6.6:** Best-fit VolcDeGas degassing simulations (blue curves) of measured δD–$H_2O$ data (dots) from pyroclastic and effusive obsidians from Big Glass Mountain. VolcDeGas iteratively determines the best-fit path based on initial δD (in ‰) and $H_2O$ content, hydrous speciation calculations, variable degassing step size, and a degassing mode transition point (in the case of two-stage and batched degassing, frames [C] and [D], respectively). The best-fit parameters are shown in the figure insets along with statistical model errors. All simulations start at 3.0 wt.% $H_2O$. Lava data points (at lowest $H_2O$, <0.2 wt.%) are measurements made by DeGroat-Nelson et al. (2001). Frames [A] and [B] show single-stage, end-member closed- and open-system degassing paths, which appear to only partially fit the high- and low- $H_2O$ content segments of data, whereas frames [C] and [D] indicate best fit models involving two-staged, closed-to-open system and batched-system degassing respectively (e.g., Taylor, 1991).

Another type of degassing mechanism is a batched system, whereby an initial closed-system step is followed by many smaller closed-system steps of ever-decreasing size (batches). Taylor (1991) and Castro et al. (2014) both employed similar models to explain degassing of the Inyo and Chaitén eruptions, respectively, and found good correspondence between models

and data across all types of eruptive products. Accordingly, Figure 6.6D shows a batched degassing model applied to the BGM data, involving a large initial closed-system step, followed by multiple repetitive batches of decreasing size (65% $H_2O$ drop at each step).

As before, the degassing step size is determined by iterative best fitting in VolcDeGas. The variable, ever-diminishing batched steps result in strong δD decrease at the end of degassing, and could mirror the tendency for an erupting magmatic system to "dry out" with time. Consequently, as the $H_2O$ budget decreases, there is less energy to supply plumes and explosive degassing (e.g., Schipper et al., 2013). The result of this batched model (Figure 6.6D) shows a good statistical fit to the natural data. In comparison to the closed-to-open system (Figure 6.6C), the batched system yields a slightly better fit as determined by both $R^2$ and RMSE values (Figure 6.6D).

In summary, the best fits to BGM $H_2O$-δD data are those that involve either a two-stage degassing model, mimicking a progression from an early closed-system to an open-system, or a batched system with successively smaller batched-system steps that alleviate the volatile budget (Figure 6.6).

## 6.5 Discussion

### 6.5.1 Physical evidence for simultaneous pyroclastic and effusive activity at Big Glass Mountain

Field relations, in addition to geochemical data, all suggest that hybrid explosive and effusive activity occurred at BGM. To our knowledge, only scant physical evidence for this eruptive behavior has been previously recognized in the tuffisite structures of Panum Dome (Black et al., 2016), which nonetheless link that eruption to hybrid activity. At BGM, the close spatial association of coherent (effusive) and pyroclastic deposits suggest that explosive and effusive activity were closely overlapping in space and time. In this discussion we link BGM's salient field depositional relations and structures to possible eruption modes and evolution thereof.

Early in the eruption, one or more active tephra cones vented pyroclastic material, producing thick, overlapping airfall deposits (Figure 6.7; C. Dan Miller, personal communication 2005). Given clear contact depositional relations, these vents were in close proximity to, and likely sourced, the voluminous obsidian lava flow as it effused. This interpretation corroborates previous work (Anderson, 1933; Eichelberger, 1975) indicating that the BGM lava flow was emitted from three separate vents, along an ~1.5 km NNW trending fissure, each erupting at

different initial stages, but also simultaneously later in the eruption (Figure 6.7). In such a multi-vent eruption scenario, the conditions for pyroclast deposition on co-eruptive flows would have been met (e.g., Lara et al., 2004). Indeed, the presence of pyroclastic deposits laying conformably atop BGM lava (Figure 6.3; Supplementary Material[ii]) speaks to this, and indicates that pyroclastic venting had not stopped when effusion started.

Further evidence for simultaneous explosive-effusive activity is provided by numerous pyroclastic ridges positioned *within* the flow, and not at the flow's margins (Figure 6.1). Pyroclastic deposits positioned at the flow's edge—were they to exist—would imply a sharp, unidirectional explosive-to-effusive eruption sequence. However, we have found no flow-bounding pyroclastic ridges, making this scenario implausible in light of the actual positioning of pristine lavas *outboard* of the pyroclastic units, particularly in the SW flow (Figure 6.1). Thus, the observed arrangement of lava → breccia ridge → lava (Figure 6.1) found in the SW flow requires that some of the lava was firstly emplaced unhindered to the SW before the inboard pyroclastic units—at the time comprising actively venting cones—were rafted away. Later, as the pyroclastic cones were disrupted by lava sourced from different vents and transported, the breccia deposits became buttressed by both the early and later-erupted lava (Figure 6.7). The lava that rafted the pyroclasts would have been sourced from a different vent than the SW cone and accordingly must have been somewhere to the north along the fissure (Figure 6.7). That the form of the ridges is conformable with the large scale flow ridges indicates significant deformation of the pyroclastic cones and that integration of the pyroclasts in lava must have occurred well before the flow reached its final position.

Collectively, the formation of both the flow-top pyroclastic mantles and internal pyroclastic ridges require initial unhindered lava effusion from an actively venting pyroclastic cone or cones (Figure 6.7). Simultaneous eruption of lava away from the pyroclastic source would allow the first unhindered lava to come to rest without significant impediment of earlier built pyroclastic cones. We therefore envision at least early emission of lava from multiple horseshoe-shaped cones whereby lava could flow out from one side of the structure, as was observed at Cordón Caulle in 2011 (Castro et al., 2014, Supplementary material[ii]).

### 6.5.2 Degassing during pyroclastic and effusive activity: the H-isotopic record

Hydrous geochemical measurements comprising δD and bulk $H_2O$ content on eruption products provide clues into the mechanism(s) of degassing that drove the most recent explosive and effusive activity at BGM (e.g., Eichelberger and Westrich, 1981; Newman et al., 1988; Taylor, 1991; Rust et al., 2004; Giachetti et al., 2020). The data from this system—like

[ii] Supplementary Material download: https://www.jvolcanica.org/ojs/index.php/volcanica/article/view/121/137

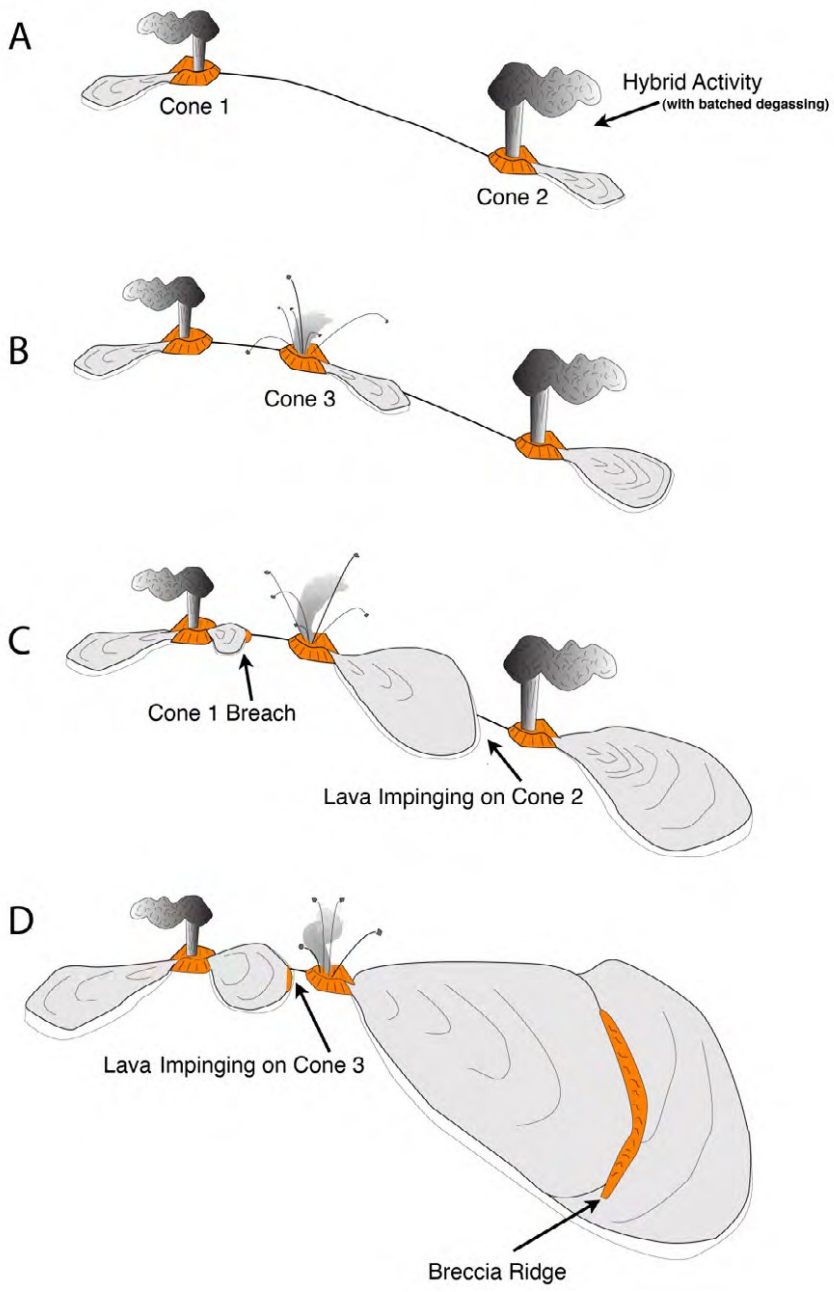


**Figure 6.7:** Schematic showing possible eruptive events leading to the formation of juxtaposed explosive and effusive deposits at Big Glass Mountain. Multiple eruptive vents were aligned along a NNW trending fissure (bold diagonal line), as shown in this perspective view from the southwest (see also Chesterman, 1955; Eichelberger, 1975). [A] Initial pyroclastic eruptions occurred from northern and southernmost vents (Cones 1 and 2) along the main fissure (Eichelberger, 1975). [B]-[C] A third, middle vent (Cone 3) probably formed later, and may have been initially explosively active with later synchronous hybrid venting with the other two vents (Eichelberger, 1975). [D] The advancing lava from the Cone 3 vent would have eventually destroyed the southern most pyroclastic cone leading to its entrapment in the lava the observed pattern of Lava-Breccia Ridge-Lava on the SW flow front. Lava emitted from Cone 1 could have also breached its southern wall, leading to impingement of this flow on Cone 3 (Frame [D]), ultimately causing the destruction and rafting of Cone 3 and incorporation as a breccia ridge into the final flow field. The intense welding, vesiculation, and deformation of pyroclasts within the breccia zones (Figure 6.4) shows that little time passed between pyroclastic venting and subsequent disruption and rafting of cones by lava.

those observed in other young rhyolite systems—shows an initial slight decline in δD over an extensive drop in $H_2O$ from high low values, followed by a sharp drop in δD in the low-$H_2O$ content realm (Figures 6.5 and 6.6). This geochemical pattern reflects an enhancement in fractionation of deuterium into the vapor phase, which is strengthened in the latest stages by both the shift in hydrous speciation (to more OH-rich composition) and consequent change of the melt vapor fractionation factor (e.g., Walter and Castro, 2020). Typically, the sharp drop in δD is attributed to late-staged opening of the system to gas loss (e.g., Newman et al., 1988).

As we showed in Section 6.4.3, batched degassing, involving an initial large closed-system step followed by repetitive and progressively smaller batched-system steps (Figure 6.6; e.g., Taylor, 1991) provided the best fit to natural δD-$H_2O$ data. This good fit suggests that a repetitive degassing mechanism involving numerous outgassing pulses was important following what may have been an initial purely explosive Plinian stage at Big Glass Mountain.

Batched degassing behavior as described above was also identified in the δD-$H_2O$ data of pyroclasts and lavas from Chaitén, and linked to the action of tuffisites during its 2008 hybrid eruption (Castro et al., 2014). This recently active system provides a working model for how BGM's δD-$H_2O$ data may have arisen from physical eruption processes. In particular, the ballistic-bomb hosted tuffisite veins at Chaitén were found to alternately act as mass conservative and mass liberating systems, both storing pyroclasts and gas for short periods (10s of minutes) and then explosively releasing them (c.f., Fig. 7 in Castro et al., 2014). In this sense, Chaitén's tuffisites behaved like valves, enabling "batched" degassing cycles comprising closed-system filling (e.g., via vesiculation and gas percolation into a crack) and explosive draining of volatile "aliquots". All the while that tuffisites were active, lava poured out from the same vent, its own degassed state an outcome of vigorous pyroclastic degassing through tuffisites. The outcome of this physical behavior is manifested in Chaitén's H-isotopic array, which shows clear geochemical continuity between early Plinian pyroclasts and later erupted lava (Castro et al., 2014; Figure 6.5).

It is also important to note that the pyroclastic fill in some of Chaitén's tuffisites (Castro et al., 2012; Castro et al., 2014)—comprising densely sintered fine ash and obsidian lapilli—exhibits markedly heavier H-isotopic signatures than the dense obsidian hosts that contain them. Castro et al. (2014) interpreted this as evidence that tuffisite veins accessed deep portions of the conduit where they tapped into more primitive, deuterium-rich gas and pyroclasts, before conveying them to the surface and leading to some local pyroclast and lava buffering (e.g., Rust et al., 2004). Tuffisites are, in this context and somewhat paradoxically, the physical hallmarks of "open-system" behavior—the deep conveyance of material reflects this—but at

the same time, such pyroclastic material lacks the classical geochemical signature of open-system degassing, that is, the extreme deuterium depletion stemming from Rayleigh fractionation. Unlike δD-depleted obsidian lavas from Chaitén, the previously described tuffisites remain δD-enriched despite being relatively poor in $H_2O$. Thus, owing to these complexities, which collectively demonstrate that tuffisite structures may cycle through various different degassing modes (e.g., closed, batched, open, buffered; see Fig. 7 in Castro et al., 2014), a simple two-stage, unidirectional shift in degassing mode (e.g., closed-to-open) does not sufficiently explain Chaitén's hydrous geochemical array while also remaining consistent with the physical eruption events causing that data array.

We view the remarkable similarity in δD-$H_2O$ systematics between eruption products from BGM and Chaitén's (Figure 6.5), along with field relations pointing towards hybrid activity at BGM (e.g., breccia ridges), as strong evidence that the eruptive underpinnings of the degassing history at BGM were similar to those at Chaitén. While we have yet to find and analyze tuffisites from BGM, we contend that the conduit(s) at BGM could very well have undergone periods of shifting degassing mode as its degree of openness changed during hybrid activity. In other words, the conduits at BGM, acting like a scaled-up tuffisite, would have experienced episodes of gas and pyroclast storage and transmittance, all of which could have been governed by fine-scale conduit processes involving cycles of fragmentation and re-healing of material (e.g., Schipper et al., 2013; Wadsworth et al., 2018; Kolzenburg et al., 2019; Schipper et al., 2021) Indeed, Schipper et al. (2021) showed that brecciated rhyolite bombs repeatedly cast from the conduit at Cordón Caulle behaved like "supersized" tuffisites, the internal structures of these bombs indicating alternating modes of vesiculation, fragmentation and sintering that led to densification of degassed magma that was in turn periodically forcefully ejected from the conduit during hybrid explosive-effusive activity (Castro et al., 2016).

Finally, it is also important to note that a two-staged, closed-to-open system model also fits the data rather well (Figure 6.6C). Despite similar goodness of fit to natural data, this closed-to-open model is physically different than the batched-system model in that it requires a sharp unidirectional change in degassing *and* eruption mechanism, something that is not consistent with previously described field relations, degassing mechanisms and requisite geochemical patterns, or observations of active systems (e.g., Castro et al., 2013). Future work should aim to sample and measure the hydrous signatures of bomb-hosted tuffisites at BGM to confirm the proposed geochemical and physical eruptive parallels between this and other active rhyolite systems. We recognize however that a geochemical dataset alone (i.e., in the absence physical eruption deposit evidence and/or real-time eruption observations) cannot implicate a particular eruption style or sequence.

### 6.5.3 Divining eruptive activity from hydrous geochemical trends and field relations

In terms of how the eruption may have physically transpired, the batched-degassing path is consistent with both an early purely explosive phase of activity (closed-system degassing)—as evidenced by thick pumice fall deposits—and later hybrid eruptive behavior, involving repetitive blast and simultaneous lava effusion activity (e.g., Schipper et al., 2013; Castro et al., 2014). The initial closed-system, and effectively large degassing amounts that mark the beginning of the sequence, could have come about from initial magma rise and attendant volatile exsolution into closed bubbles that remained in contact with the melt. The start of the eruption (the Plinian phase) would therefore have marked a massive closed-system, explosive release of these early exsolved volatiles. This interpretation has been validated by historically active subaerial rhyolites where the degassing pattern and eruption mechanism were found to be consistent across a wide range of samples (Chaitén and Cordón Caulle; e.g., Castro et al., 2014). Most importantly, instead of sharply distinct degassing and eruption mechanisms—closed first then open, and first explosive then effusive—the Chilean eruptions exhibited pulsed, batched degassing, with explosive outbursts declining in intensity during prolonged effusive activity (Schipper et al., 2013).

On the whole, our hydrous geochemical data provide evidence of the nature of degassing that accompanied hybrid volcanism during the most recent explosive-effusive eruption of BGM. This geochemical evidence points to a repetitive degassing process that physically coincides with distinctive, intercalated effusive and explosive deposits. This geochemical and physical evidence places the BGM eruption squarely in the behavioral class of Chaitén and Cordón Caulle eruptions. Thus, as concerns potential future rhyolite eruptions and hazards either at Medicine Lake or other potentially active systems, we would envision extensive hybrid activity with month-long periods of ash production alongside effusive activity and extensive pyroclastic flows (e.g., Schipper et al., 2013).

## 6.6 Conclusions

Detailed analyses of field relations, microtextures and hydrous geochemical signatures preserved in pyroclastic and effusive obsidians at BGM suggest that the most recent BGM eruption followed an hybrid eruptive course, one very much like the recent rhyolite events at Chaitén and Cordón Caulle. There was not likely a sharp shift in activity from explosive to effusive behavior, but rather a gradual shift from early intense Plinian explosions to long, drawn-out repetitive explosive venting accompanied by lava effusion. That the effusive lavas are so voluminous suggests that BGM would been explosively active for a very long time,

perhaps months to years. Such activity would have produced ash clouds while the voluminous obsidian flow was emplaced (e.g., Black et al., 2016; Forte and Castro, 2019). Clearly, were such persistent ash venting and lava effusion to happen again today, this would present a most critical threat to air traffic, the local farming economy and regional volcanic threat (Forte et al., 2018).

Our work on BGM adds to the growing evidence that effusive rhyolitic volcanism is inextricably linked to explosive eruption (Black et al., 2016) and thusly calls for reassessment of prior models involving temporally abrupt change-overs in activity linked to thresholds in magmatic properties, such as bulk permeability (e.g., Eichelberger et al., 1986; Newman et al., 1988; Giachetti et al., 2020). New models that incorporate cycles of volatile exsolution, melt fracturing, explosive outburst and release, followed by re-sintering of fragmental magma will contribute to better hazard assessments of the impacts of rhyolite events (Schipper et al., 2021).

### 6.7 Acknowledgements

The authors would like to thank Benjamin A. Black, Juliet Ryan-Davis, and Kayla Iacovino (editor) for insightful comments that helped improve the quality of this work. Jens Fiebig provided essential analytical support while Nick Joslin and Brian Olmsted made fieldwork tractable and fun. We thank the University of Mainz's VAMOS research center for support of laboratory and analytical costs.

### 6.8 Author contributions

Both authors contributed equally to this study.

### 6.9 Data availability

All data in this manuscript are available as Supplementary Material alongside this article: https://www.jvolcanica.org/ojs/index.php/volcanica/article/view/121/137.

### 6.10 Copyright notice

the source, provide a link to the Creative Commons license, and indicate if changes were made.

# Chapter 7

# Hydrous geochemical evolution of the Lipari rhyolites during multi-vent, hybrid volcanic activity[3]

**Keywords: Lipari; Rocche Rosse; Forgia Vecchia; Lami; Rhyolite; Batched degassing; Hydrogen signature; Hybrid eruption; Co-eruptivity**

**Abstract**

Eruptions of rhyolite magma have occurred infrequently but have nevertheless resulted in significant changes to the Earth's landscape and human society. Some of the most recent silicic eruptions in Europe occurred approximately 800 years ago from three craters on the island of Lipari, Sicily. The Lipari eruptions produced ash and lava deposits that share many of the physical and chemical traits known to exist in hybrid explosive-effusive volcanic systems like the Mono Craters and Medicine Lake (USA), in addition to recently active rhyolite volcanoes at Chaitén and Cordón Caulle (Chile). Here we present a study of the microtextures and hydrous geochemical characteristics of pyroclastic and effusive deposits of three rhyolite eruptions on Lipari (Lami, Forgia Vecchia, and Rocche Rosse). Textural features of obsidian pyroclasts are, within our parameters of analysis, identical amongst the three centers. The three vents furthermore display overlapping bulk $H_2O$ concentrations (0.08 – 1.22 wt.%) that are in turn similar to previous studies on Lipari and other systems. Hydrogen isotope geochemical data indicate that all erupted products degassed along a single trend, which is consistent with a manner of eruption that would have involved repetitive and simultaneous explosive and effusive emission of isotopically heterogenous gas from a single source. Collectively, the geochemical trends point to hybrid activity characterized by simultaneous lava and pyroclast emission. Finally, these findings support previous ideas that Lipari's three youngest rhyolitic centers were co-eruptive, which implies that more than half of the island would have been affected by direct impacts of a rhyolitic fissure event.

[3] This chapter was submitted by Walter, S.C; Castro, J.M.; Bindeman, I.N. and is currently *under review* for publication in *Bulletin of Volcanology*

## 7.1 Introduction

Volcanic eruptions pose significant threats to humans, infrastructure, and can invoke rapid environmental change. The ejection of ash, gas, bombs, pyroclastic flows, and lava can cause extensive damage across wide surface environments and may also affect the atmosphere. Eruptions of rhyolitic magma are particularly impactful in this regard because they have been known to generate copious amounts of ash over very long durations (Black et al., 2016; Forte and Castro, 2019), making hazards forecasting difficult and more importantly maintaining a functioning society and economy during ongoing long-lasting volcanic events.

Large (VEI 4-5) rhyolite eruptions that have been directly observed and monitored amount to just two events: Chaitén (2008) and Cordón Caulle (2011), both in Chile. However, despite the paucity of historical records, we have learned a lot about how rhyolite eruptions start, progress, and how they end. Both Chilean events were surprises in that they did not conform to the earlier paradigms of how “silicic volcanism” operates (e.g., Eichelberger et al., 1986; Fink et al., 1992). Specifically, neither event showed a sharp transition or change over from explosive to effusive behavior (e.g., Castro et al., 2013; Schipper et al., 2013). Instead, these eruptions were dominantly “hybrid” eruptions, meaning, after a short purely explosive phase, they swiftly progressed to simultaneous outpouring of lava and tephra (e.g., Lara, 2009; Black et al., 2016; Walter and Castro, 2020). This hybrid activity posed long duration (several months to a year) hazards at proximal and distal location due to persistent bomb and ash venting activity near the vent, and widespread ash fall many kilometers from the vent, respectively. Both events then concluded with slow effusion of lava.

Now that we know *how* rhyolites may erupt, and importantly, that they can be very explosive for months on end, it is useful to turn to other recently active rhyolite systems to look for signs that these too may have behaved in a similar manner. In this work, we address this very problem in the Lipari Isles, the site of Europe’s most recent rhyolite activity (Figure 7.1). Lipari is an island built of multiple rhyolitic centers, the youngest of which were active in historic times (e.g., Forni et al., 2013; Pistolesi et al., 2021). It is on these most recently active centers (Figure 7.1) that we have conducted textural analyses and geochemical measurements of the pyroclastic and effusive eruptive deposits. Our analyses highlight commonalities among the features in the young Lipari rhyolites and in turn demonstrate that there could have been hybrid activity (e.g., Castro et al., 2013), in addition to the three vents erupting at the same time. These findings have implications for hazards assessments of eruptions on Lipari.


**Figure 7.1:** Satellite image of the northeastern part of Lipari, Silicia, created using Google Earth/Maps, showing sampling locations. The positions are tagged in the picture on each symbol. Red symbols represent the Forgia Vecchia sites, blue the Lami sites and green the Rocche Rosse sites.

## 7.2 Background

The question of how eruptions of silicic magma initiate and progress has been extensively explored in prior works (e.g., Eichelberger, 1975; Heiken, 1978; Eichelberger and Westrich, 1981; Eichelberger, 1995) and remains an active area of research (e.g., Castro and Dingwell, 2009; Watt et al., 2009). In particular, as regards rhyolites, it was established early on that eruptions begin with a vigorous explosive phase, yielding copious ash, bombs, and pyroclastic flows, before transitioning into less forceful effusions of obsidian lava. This sequence, termed an "explosive-to-effusive" eruption, was initially inferred from stratigraphic observations of obsidian lavas overlaying co-eruptive pyroclastic fall deposits (e.g., Heiken, 1978; Eichelberger and Westrich, 1981; Taylor et al., 1983; Newman et al., 1988). A study by Eichelberger and Westrich (1981) further elucidated the characteristics of obsidians from various eruptions of Medicine Lake Volcano (MLV; CA), revealing a large range of magmatic water content (~0.1 to >1 wt.%). Notably, obsidian lavas have the lowest contents, whereas pyroclasts occupy the middle to higher end of the range. From these discoveries, it was inferred that magmatic water

is the primary driver of explosive rhyolitic eruptions, fueling the initial explosions and, as this fuel is depleted during the course of the eruption, yielding obsidian lavas to become the dominant eruption mode. Subsequent investigations have corroborated the findings at MLV (e.g., at the Inyo Domes and Newberry Volcano; Taylor, 1991; Rust and Cashman, 2007), in that they too show consistently higher water contents in pyroclasts compared to lavas at several different eruption sites.

In addition to bulk water concentration analyses, measurements of hydrogen isotope concentrations in obsidian pyroclasts and lavas can yield additional insights into the degassing mechanisms of rhyolite eruptions (e.g., Castro et al., 2014). When coupled with magmatic water measurements, the H-isotopic data often show an early, more hydrous section of subtle deuterium depletion followed by a rather sharp decline when bulk water decreases to a minimum (e.g., Taylor et al., 1983). These patterns—observed at many different rhyolite centers—correspond to the pyroclastic and effusive materials from which they are measured and thus, have been widely interpreted as a two-stage, closed to open-system degassing path (e.g., Newman et al., 1988) that underpins the explosive and effusive phases. Indeed, a recent study by Giachetti et al. (2020) purports that the 1060 CE eruption of Big Glass Mountain (BGM), CA operated this way, progressing from early closed-, to later open-system degassing, with a sharp transition/shift that would have been triggered by the magma achieving a highly vesicular state (~65%; e.g., Eichelberger et al., 1986).

Owing to a lack of directly chronicled rhyolite eruptions, it was for a long time impossible to test the aforementioned ideas on how rhyolitic systems progress and degas through eruptions. As mentioned before, the deposits of many eruptions have been geochemically interrogated, but the measured materials could not be linked to a time in the eruption sequence. This all changed dramatically however with the eruption of two closely monitored volcanoes: Chaitén (2008-2009) and Cordón Caulle (2011-2012), Chile (Lara, 2009; Alfano et al., 2011; Castro et al., 2013; Schipper et al., 2013; Castro et al., 2014). Both events offered complete records of how rhyolites erupt from start to finish, along with fresh unaltered pyroclastic and effusive materials to measure, allowing linkages of hydrous geochemistry to the concurrent eruption modes to be made (Castro et al., 2014). What stood out in both events, was the lack a sharp “explosive-to-effusive” transition in the sense that was previously defined (e.g., Eichelberger et al., 1986) and supported (Giachetti et al., 2020). Instead, following a rather abbreviated (one-week-long) purely explosive phase, both events exhibited an hybrid eruption mode comprising simultaneous pyroclastic fountains and effusing lava flows from the same vents (Lara, 2009; Schipper et al., 2013; Castro et al., 2014; Castro et al., 2016). Eventually, after months of

hybrid venting, both eruption centers gave way to purely effusive emission (Pallister et al., 2013; Tuffen et al., 2013).

Despite the fact that neither Chaitén nor Cordón Caulle displayed sharply delineated explosive and effusive eruption modes, their hydrous geochemical characteristics (Castro et al., 2014) were found to be very much like those measured at Californian rhyolite centers, including the Inyo Domes (e.g., Taylor, 1991) and at MLV's Big Glass Mountain (BGM; Castro and Walter, 2021). Specifically, both Chaitén and Cordón Caulle exhibit similar ranges of magmatic water concentration (~0.1 – 2.0 wt. %), and very similar isotopic shifts, or deuterium depletions with declining water content as other rhyolite systems (Castro et al., 2014; Walter and Castro, 2020; Castro and Walter, 2021). These geochemical commonalities among many independent rhyolite eruptions are suggestive of a universal degassing mechanism that operates across multiple rhyolite systems. Furthermore, and equally important, in the space of a single eruption cycle, it appears that the degassing mode need no change during the eruption; a single mechanism—implied by the dominant and long-duration hybrid venting—is wholly sufficient to link early explosive activity to effusive activity (i.e., not a two-staged event) by way of hybrid activity (Castro et al., 2014).

Indeed, analytical and modeling studies of both Chaitén and BGM show that a singular degassing mechanism may be the best explanation of hybrid rhyolitic activity. More specifically, a "batched" degassing system mimics both closed and open-system behaviors that combine to generate a well-fitting (to natural data) degassing path (Castro et al., 2014; Walter and Castro, 2020). This "batched" system was first proposed by Taylor (1991) as a "multi-stage repetitive degassing mechanism" for late-Holocene explosive-effusive rhyolitic eruptions at Inyo Dome, Ca (Miller, 1985). In this "multi-step open/closed" model, magma accumulates in a closed-system in repetitive steps whereas these volatiles (specifically $H_2O$) are then removed by explosions that vent exsolved gases in "batches" to the surface. Castro et al. (2014) envisioned that these batches get released during observed pulsatory Vulcanian activity, in turn actuated by pyroclastic vents known as tuffisites (Tuffen et al., 2003); the scale of tuffisites may range from mm's to approaching the size of the whole conduit (Schipper et al., 2021). Over time these "batches" may get progressively smaller in volume as the total volatile budget decreases. This system therefore creates a "quasi-open" system behavior by successive depletion of the magma's $H_2O$ amount with each degassing step.

These findings from pre-historic rhyolites and the two observed Chilean events suggest that hybrid activity may be more common than previously recognized. Determining how frequent these hybrid events really are in pre-historic rhyolitic eruptions will require examining other

systems for evidence of this activity. This may in turn help us assess more accurately the true hazard posed by silicic eruptions and warrants further investigation.

Thus, in this study, we examine three rhyolite centers on the isle of Lipari, Sicily—Rocche Rosse, Forgia Vecchia, and Lami—all of which erupted around 1250 CE (Pistolesi et al., 2021) for their probable modes of eruption. We specifically combine textural and geochemical observations of deposits to draw parallels with the materials erupted from known hybrid volcanic events. After our detailed analyses, we will compare the results with features observed in other hybrid eruptions. Our findings suggest that the three centers are likely connected and were co-eruptive. Moreover, these centers and their products also share similarities with the eruptions of BGM, Chaitén, and Cordón Caulle, thereby indicating hybrid activity.

### 7.3 Geological Setting

The island of Lipari, situated off the northeastern coast of Sicily, represents the largest atoll within the Aeolian archipelago and represents the culmination of an extensive submerged, mostly silicic volcanic complex. Lipari occupies the central portion of the Vulcano–Lipari–Salina volcanic belt. This volcanic belt, which traverses the arched structure of the archipelago`s central sector, is affiliated with the major NNW–SSE strike-slip Tindari–Letojanni fault system, which is thought to govern magma ascent, eruption, and vent localization and alignment (Barberi et al., 1994; Mazzuoli et al., 1995; Lanzafame and Bousquet, 1997; Billi et al., 2006; Ventura, 2013; Ruch et al., 2016). Compositional analyses reveal a diverse range of rock types on Lipari, ranging from calc-alkaline affinity basaltic andesites to rhyolites, with silicic rocks dominating in more recent eruptions over the past 43 ka (Forni et al., 2013; Albert et al., 2017).

The volcanic activity within this region commenced at ~267 ka, and has persisted through historical times culminating in multiple rhyolite events, which comprise the Forgia Vecchia, Rocche Rosse and Lami episodes around 1250 CE (e.g., Cortese et al., 1986). The primary eruption deposits of these three events are situated in the northeastern region of Lipari (Figure 7.1). Despite these three events being clearly the youngest on the island based on geomorphic and cross-cutting relations, accurate age dating as well as relative chronostratigraphic correlations between these eruptions and deposits are inconsistent and remain unresolved (e.g., Bigazzi and Bonadonna, 1973; Cortese et al., 1986; Davì et al., 2009; Davì et al., 2011; Forni et al., 2013; Pistolesi et al., 2021).

Recent studies, especially the work of Pistolesi et al. (2021), resolved some of the uncertainties surrounding the age and eruptive characteristics of the Rocche Rosse and Lami eruptions,

showing that they may have been co-eruptive in nature, with a probable age of around 1250 CE. These two eruption centers are situated in close proximity to each other (Figure 7.1), and exhibit distinct depositional features. Rocche Rosse is demarcated by a long (ca. 2.5 km) and slender obsidian flow sourced from and associated with explosive pyroclastic deposits within the Monte Pilato crater. By contrast, Lami`s activity created a small volume pyroclastic cone near the village of Lami on Monte Pilato´s southern flank (e.g., Cortese et al., 1986; Forni et al., 2013; Pistolesi et al., 2021).

Approximately 1.3 km SE from the Lami center and collinear with both it and the Rocche Rosse vent, lies the Forgia Vecchia vent (Fig. 7.1). The Forgia Vecchia eruption, whose explosive and effusive deposits are located just to the west of the village of Canneto (Figure 7.1), has been the subject of debate regarding its age. Earlier studies have suggested an eruption age of 1.6 ka, based on fission track analysis (Bigazzi and Bonadonna, 1973), while others have proposed a co-eruptive relation to the Monte Pilato eruption in CE 776, that being based on stratigraphic evidence (Cortese et al., 1986; Keller, 2002; Forni et al., 2013). Recent research, however, has provided a more restricted and recent age estimation by utilizing paleomagnetic dating of Forgia Vecchia's lava flow, indicating a timeframe of 1242-1306 CE, in addition to radiocarbon analyses of carbonized material, which independently suggests a permissible age of 1160-1260 CE (Pistolesi et al., 2021). These age estimates align well with historical reports and archeological data (Bernabò, 1978; Pistolesi et al., 2021), and further imply that Forgia Vecchia could have been co-eruptive with the Rocche Rosse and Lami events (Pistolesi et al., 2021).

Indeed, Pistolesi et al. (2021) postulated that the Forgia Vecchia lava may have been still hot and flowing when the pyroclastic falls from Rocche Rosse partially covered it. They cite vent-proximal, welded flow-top breccias on the Forgia Vecchia lavas as evidence of co-eruptivity, the idea being that as pyroclastics from Rocche Rosse fell, remnant heat from the freshly emplaced Forgia Vecchia obsidian flow promoted their welding. Castro and Walter (2021) found similar welded flow-top breccias at BGM, whose own multi-vent rhyolite eruption involved simultaneous explosive and effusive activity, and came to the conclusion that such veneers could have only formed during hybrid activity (see also Walter and Castro, 2020).

While the total duration of the three Lipari eruptions is unknown, including the sequence in which vents opened and evolved through different styles of activity, some details have been resolved as regards magmatic degassing of the potentially co-eruptive rhyolite magmas. For example, previous work revealed that the magmatic water contents of Rocche Rosse`s explosive and effusive products were comparatively low across different deposits (i.e.,

pyroclastic and effusive), ranging from just 0.08–0.41 wt.% $H_2O$ (Cabrera et al., 2015; Shields et al., 2016). Lami`s deposits exhibited similar yet somewhat higher water contents from 0.2 to 0.9 wt.% $H_2O$ (Cabrera et al., 2015). To our knowledge, no previous study has examined the water content distribution of Forgia Vecchia's pyroclastic and effusive deposits. Part of the goal of our work is to confirm and expand these values to include Forgia Vecchia, as they seem much lower than many previously documented rhyolite eruptions in other locations (e.g., Castro et al., 2012; Castro et al., 2014).

Textural analyses of Rocche Rosse deposits have revealed the presence of ubiquitous tuffisite veins, in addition to healed fractures and highly vesicular domains within otherwise dense obsidian bombs (e.g., Tuffen et al., 2013; Cabrera et al., 2015; Shields et al., 2016). These textural features have also been observed in Lami´s products (Cabrera et al., 2015) and are well documented in recent Chilean rhyolites (e.g., Castro et al., 2014). Finally, investigations into the composition of tephra from all three eruptions (Pistolesi et al., 2021) have revealed strong similarities in major and trace element glass composition throughout all three deposits.

## 7.4 Samples and analytical methods

### 7.4.1 Sample collection

We collected samples on the isle of Lipari, from the Forgia Vecchia, Rocche Rosse, and Lami eruption centers (Figure 7.1) between 17$^{th}$ and 21$^{st}$ of May, 2023. Our sampling sites were determined by the degree of accessibility of the deposits, and those locations in turn being guided by maps provided by Forni et al. (2013) and Pistolesi et al. (2021). Each sample, whether it be granular tephra clasts or dense obsidian lava fragments, was stored in a watertight bag and uniquely marked with a sample number. Additionally, detailed photographic documentation of the outcrops and samples was conducted, and GPS data were recorded for each sample to ensure accurate spatial referencing.

Obsidian samples—either lava or pyroclasts—were specifically targeted for analysis due to their reduced susceptibility to hydration by meteoric water, unlike pumice samples (e.g., DeGroat-Nelson et al., 2001), which, despite their relatively young age of under 1000 years, may be subject to significant secondary water uptake (e.g., Eichelberger and Westrich, 1981; Seligman et al., 2016; Castro et al., 2020; Giachetti et al., 2020). However, it should be noted that some obsidians exhibited small vesicular domains that could be characterized as pumiceous. In such cases, efforts were made to break up and isolate dense, bubble-free portions of the obsidian glass for analysis, specifically the Thermal Conversion Element

Analyzer-Mass Spectroscopy (TCEA-MS) measurements that analyze bulk powdered material (more methodological details are provided below). The issue of potentially measuring secondarily hydrated glass did not arise during Fourier Transform Infrared Spectroscopy (FTIR) measurements, as it was easy to pick analysis points far away from hydrated vesicle walls, features that were confirmed to exist in the study of hydration in Rocche Rosse obsidians by Shields et al. (2016). Lastly, thin-sections of selected lava (Rocche Rosse) and some bomb obsidians (Lami cone) that were collected on previous field trips (2004 and 2016) were also utilized for textural analyses of Rocche Rosse and Lami deposits. Here, one bomb from Lami was also exploited for some TCEA and FTIR measurements. Specific details of our sampling methods and locations are briefly summarized in the following sections.

#### 7.4.1.1 Forgia Vecchia sample site characteristics

On May 17th, 2023, glassy obsidian flow samples from Forgia Vecchia were collected a few meters downslope from the observation point at the flow's summit, which is located approximately 700 meters due west of the village of Canneto (Figure 7.1). Several lava fragments of varying sizes (3-10 cm) from a two-meter-high lava spine were taken. Two days later, on May 19th, bulk pyroclastic fall samples thought to be from the same eruption (e.g., Pistolesi et al., 2021) were collected from an exposed vertical outcrop approximately 2.5 meters tall (Supplementary Material; Figure S1A), situated along a pathway leading to a quarry on the hill about 500 m north of the village of Pirrera (Figure 7.1). Samples were obtained as bulk grain mixes from three distinct layers of the tephra deposit spaced out in roughly 20 cm intervals along a vertical line. Each layer was sampled in duplicate, with one bag filled with bulk material comprising pumice, obsidian chips, and lithic fragments, while a second bag from the same layer was filled exclusively with hand-picked obsidian shards. The lava flow samples were labeled as FV-23, while pyroclastic samples were named as FV-1a to FV-1c, corresponding to their position within the deposit from top to bottom.

#### 7.4.1.2 Lami sample site characteristics

The samples of the Lami eruption were collected on May 18th, 2023, from a small quarry within the village of Lami (Figure 7.1). Here, various sized vesicular and glassy tephra clasts (3-15 cm) from each of three, greyish lapilli-and-ash dominated layers from the exposed 1.5- meter-high outcrop (Supplementary Material; Figure S1B) were collected. Additionally, obsidian shards (1 cm) from each layer were separately collected and stored in distinct bags. Furthermore, a large, approximately 30 cm diameter bomb with breadcrusted texture was extracted from the site, along with another bomb collected during the previous campaign (in

2016); all materials would be subjected to FTIR/TCEA measurements. Pyroclastic samples were labeled L-1a to L-1c, indicating their position within the deposit from top to bottom, while the bomb samples were labeled as L-1cB (from the current campaign) and L-B45 for the previously collected bomb.

#### 7.4.1.3 Rocche Rosse sample site characteristics

Rocche Rosse`s pyroclastic samples were collected on 18th May, 2023, at the edge of the large quarry on the eastern flank of the Monte Pilato crater (Figure 7.1). At this site, the pyroclastic fall deposits comprise very coarse to fine grained, poorly sorted, decimeter-scale layers amounting to a maximum of about 5 meters in total thickness. The deposit thins rapidly towards the east, where erosion has clearly removed some of the top layers of the deposit. We collected samples from two distinctive layers of an approximately 2-meter high exposure (Supplementary Material; Figure S1C) where it appeared that the entire deposit was intact. As done before at other localities, samples were taken in duplicate, with a bag for bulk mixed material and a bag for obsidians shards only. We also located and sampled two bombs in the vicinity of this site. Lava flow samples were then taken on the 21th May on top the Rocche Rosse lava flow, near its point of emission at the Monte Pilato crater's north western rim, just south of the village of Acquacalda (Figure 7.1). The flow samples were taken near a small footpath at different spots, and then stored in individual water-tight bags. Pyroclastic samples were labeled RR-1a to RR-1c, corresponding with their stratigraphic position from the deposit top to bottom. Lava flow samples were labeled as RR-flow or RR-F and bombs were labeled as RR-B.

### 7.4.2 Analytical techniques

Isotope measurements were performed in order to quantify the deuterium ($^2H$) to hydrogen ($^1H$) ratio in 30 different Lipari obsidian clasts at the Stable Isotope Laboratory at the University of Oregon. This lab employs a TCEA (Thermal Conversion Element Analyzer) coupled to a MAT253 isotope ratio mass spectrometer (hereafter referred to as TCEA/MS; these instruments were run by Dr. Ilya Bindeman). This system also concurrently measures the bulk $H_2O$ in the sample, providing an accurate and independent assessment of magmatic water (Bindeman et al., 2021). Briefly, several milligrams of hydrous sample are dropped into a glassy carbon furnace held at 1450°C, and the released water is instantaneously pyrolyzed into $H_2$ and CO gas that is getting put through a Gas Chromatograph, open split by a Helium flow and then analyzed on a large radius mass spectrometer MAT253. The use of 10 KV MAT253 allowed us to measure samples that have 4 times smaller water concentration (and 4 times

smaller samples) than is typically done on a more common 3 kV Delta-TCEA systems (Martin et al., 2017). The δD values are determined with a precision on the order of 1-3 ‰ and are expressed relative to the Standard Mean Ocean Water (SMOW) or its modern counterpart, the V-SMOW standard, which is demarcated as:

$$\delta D = \frac{(\frac{^2H}{^1H})_{Sample} - (\frac{^2H}{^1H})_{Standard}}{(\frac{^2H}{^1H})_{Standard}} * 1000‰ \quad (24)$$

Bulk $H_2O$ measurements carry a precision of better than ± 0.04 wt.% (Bindeman et al., 2021), and the amount of water are based on areas of $H_2$ and HD on a spectrogram, normalized to concurrently run solid standards and TCEA conditions. Standards USGS57 (biotite) and USGS58 (muscovite), both described in Qi et al. (2017), were measured several times as standards in order to calibrate $H_2O$ and δD, as well as rhyolitic glass UOR1 (Bindeman et al., 2021) and low-δD mica BUD (Martin et al., 2017).

The samples for isotope analyses were prepared according to techniques outlined by Castro et al. (2014) and Giachetti et al. (2020), whereas techniques described by Aulock et al. (2014) were followed for the FTIR measurements. These methods and specific sample details are briefly summarized below:

For the Rocche Rosse sites, seven obsidian shards of each of the two pyroclastic layers, two fragments from each of the three flow samples, two obsidian fragments from bomb RR-B1, and three pieces from bomb RR-B2 were analyzed, amounting to twenty-five different samples. All of these samples were measured by FTIR, and of these, ten smaller sub-samples were extracted for further analysis by TCEA/MS. The Lami samples included six obsidian pieces from each of the three pyroclastic layers, one clast from bomb L-B45 and two clasts from bomb L-1cB, yielding a total of twenty-one unique samples which were analyzed by FTIR; we subsampled nine smaller fragments from FTIR materials for TCEA/MS measurements. Forgia Vecchia samples consisted of eight obsidian glasses from layer FV-1a, six from layer FV-1b and five from layer FV-1c, two clasts from each of the three lava flow samples (FV-F1, FV-F2, FV-F3), and one for sample FV-F4, totaling twenty-six distinctive samples all of which were examined by FTIR. Eleven subsamples of these were prepared and measured by TCEA/MS.

All samples were cleaned in an ultrasonic bath to remove soil and debris. For TCEA/MS measurements, dense obsidian fragments were scrutinized for their textures to ensure they were bubble-free in order to minimize meteoric water influence on isotopic signature. The subsampled obsidians were then further cleaned in an ultrasonic bath with ethanol, dried, and

then pulverized inside a hardened steel mortar, and sieved between 75 and 150 μm grain size for optimal TCEA/MS results (Martin et al., 2017). This powder was placed inside labeled vials, and the grinding equipment was intensively cleaned between each sample to prevent contamination. After powdering and sieving, the samples were weighed by 5-digit precision analytical balance, in amounts (3.1-10.8 mg) based on their water content as determined by concurrent FTIR measurements (described below); this procedure ensures that the proper target masses would be reached for TCEA/MS measurements (Castro et al., 2014). These powders were packed into silver foil cups, sealed by folding, weighed again, and observed under a microscope for possible tears or holes. We prepared duplicates for samples with a higher water content and triplicates for those with a very low water content (~0.1 wt.%). The samples were then sent to the University of Oregon Isotope Lab, where they were dried overnight at 130 ˚C in a vacuum oven to remove any adsorbed water. There, the final hydrogen isotope measurements were performed on a Thermo Finnegan TCEA-MAT 253 system on the 5$^{th}$ December, 2023.

For the FTIR analyses, one or more shards per sample were embedded in two-part epoxy, cured, and sectioned into wafers that were then doubly-polished to a thickness ranging between 270 and 755 μm. Thickness was measured with a Mitutoyo digital micrometer with accuracy of $\pm$2 μm. Some of these samples, particularly the dense obsidian fragments, also represent “splits” off of sample masses used for TCEA/MS measurements.

Bulk $H_2O$, together with hydrous species (OH-groups and molecular water $H_2O_m$) were measured utilizing a Thermo-Nicolet FTIR Bench with attached Continuum microscope at the Johannes Gutenberg University in Mainz, Germany. Our FTIR setup includes a nitrogen-liquid-cooled MCT detector and a KBr beamsplitter, configured to allow maximum signal strength over a broad spectral range of ~6000 cm$^{-1}$ to <1000 cm$^{-1}$. The measurements were made in transmission mode, conducted on ~50 μm spots of dense obsidian glass to avoid contamination or hydration. The Lipari obsidians are largely crystal-free, thus corrections to the path length (sample thickness) for the presence of crystals were not necessary. Spectral resolution was set to 4 cm$^{-1}$ with each analysis being the average of 256 scans. Background scans comprising a measurement of a sample-free path were performed every 30 minutes to account for changes in temperature, moisture or $CO_2$ content. Magmatic $CO_2$ was nevertheless not detected in any of our samples. The prepared wafer thicknesses allowed for good resolution of the water species peaks at 4500 cm$^{-1}$ and 5200 cm$^{-1}$ (corresponding to OH and $H_2O_m$) and for a quantifiable mid-IR absorbance peak at 3550 cm$^{-1}$ for dry obsidians (<0.1 wt.%). Peak heights were measured with respect to a linear baseline, and resulting absorbance values were inserted in the Beer’s Law formula that returns a weight concentration of hydrous

species (OH and $H_2O$) for known values of the path length, extinction coefficients for rhyolite glass (e.g., Ihinger et al., 1994), and sample density. Density values were based on the measured Lipari obsidian compositions of published works (e.g., Gottsmann and Dingwell, 2001; Cabrera et al., 2015). The estimated detection limit of our FTIR instrument is about 0.005 wt.% $H_2O$, while measurement error is generally lower than ±0.01 wt.% $H_2O$ (Castro et al., 2013).

Finally, all petrographic observations and microtextural descriptions were based on standard thin sections and polished wafers of pyroclastic and effusive obsidians. We did these analyses with a Zeiss Axiolab petrographic microscope in transmitted light mode. The sectioned obsidian fragments, including those with tuffisite vein structures, flow banding, vesicular areas, and dense glass domains, were in many cases the same materials that were later measured with both FTIR and TCEA/MS methods, which allowed us to link geochemical patterns to physical microstructures and textures.

### 7.4.3 Modeling degassing paths

The hydrous component and H-isotopic data, when plotted as δD vs. $H_2O$ graphs often show trends of falling δD as bulk water decreases, manifesting a volcanic system's degassing history and mode (e.g., Castro and Walter, 2021). The hydrous geochemical data that we measured were accordingly used as a basis for modeling the potential degassing paths of the Lipari pyroclastic and effusive deposits. We used the program VolcDeGas (Walter and Castro, 2020) to perform the modeling. Several formulae—built into VolcDeGas—are required to model degassing history, expressions of which account for degassing-sensitive variables such as hydrous speciation in the melt, which influences the vapor-melt fractionation factor (alpha), in addition to degassing step size, and different modes (e.g., closed, open, batched). To visualize these degassing histories, model runs are plotted as δD vs. $H_2O$ graphs corresponding to a range of several user-defined variables. This program is described in detail in our previous work (Walter and Castro, 2020), where it was also verified to function as intended (see also Castro and Walter, 2021; Hudak et al., 2021).

VolcDeGas determines the best-fit degassing trends (closed, open, batched, two-stage systems) based on the minimum RMSE between numerous simulated trends and the actual data. The program's input variables were:

1. The initial water content of 3.5 wt.% based on rhyolitic melt inclusions (Shields et al., 2016).

2. A range of initial δD (-100 ‰ to 0 ‰ with 1 ‰ steps).
3. The fractionation factor, alpha, between vapor and melt for rhyolites, computed based on speciation-dependent alpha factors. The speciation data is either
   a) based on FTIR speciation measurements, with VolcDeGas extrapolated high-$H_2O$ content values (we found this option the best) or
   b) by temperature, with specific speciation values experimentally determined by Zhang (1999), producing a less precise degassing history.
4. The degassing step-size, set as 0.001 wt.% $H_2O$ to allow for high resolution and smooth simulation graphs.
5. The measured δD vs. $H_2O$ data provided in a prepared excel sheet, allowing the program to emulate the best-fit degassing histories.
6. Optionally, in the case that two-staged degassing is modeled, e.g., closed-to-open system, an estimated transition point is set at 0.5 wt.% $H_2O$ (including outliers) and 0.8 wt.% $H_2O$ (excluding outliers) to demarcate the shift in degassing mode.

## 7.5 Results

### 7.5.1 Textural evidence

Microscope images and hand samples from the three eruptions reveal several key textural features that demonstrate magmatic-process commonalities among the three eruption sites. In the following paragraphs, the general textural characteristics of the samples are described and notable features highlighted. These features are compared across the three centers in order to tie them to one another, and aid in comparisons of similar entities found in other systems that have already been documented in the literature and that had endured hybrid eruption processes.

The vesicularity for Rocche Rosse's deposits has been reported in previous works, indicating great heterogeneity of bubble-porosity (Cabrera et al., 2015; Shields et al., 2016) on scales ranging from millimeters to decimeters. We observed similarly diverse vesicularity patterns in Forgia Vecchia lavas and tephra. By contrast, vesicularity for the Lami eruption is generally high (Davì et al., 2011) even though dense, nearly vesicle-free glass pyroclasts are found in the deposits. We classify the lava and pyroclasts on the basis of their vesicularity as proposed by (Shields et al., 2016):

- **Type 1: Glassy** - Dense glass with low vesicularity.
- **Type 2: Frothy Glass** - A mix of dense and vesicular glass with some larger vesicles.

- **Type 3: Pumiceous** - Highly vesicular and low-density glass with variable-sized vesicles and high degrees of vesicle connectivity.
- **Type 4: Shear banded** - Low-to-medium vesicular glass with coalescent and flattened vesicles interpreted to have undergone shearing.

All types of volcanic material were identified in each of the three eruptions' deposits. Dense glass (Type 1) is exemplified best microscopically by the Lami sample L-1b3 (Figure 7.2A), Forgia Vecchia sample FV-1a1 (Figure 7.5) and macroscopically in the hand sample of Lami Bomb L-B45 (Figure 7.2E), which contains black glassy bands traversing the middle of the sample. The overall texture of the glass samples ranges from clear, pristine and crystal free, to domains that are relatively rich in oxides, and tabular feldspar and needle-shaped pyroxene microlites (e.g., Figure 7.2A, C, Figure 7.4B). The pyroxene needles are sometimes aligned, while the tabular microlites in samples from all sites (e.g., Figure 7.2B, Figure 7.4C), exhibit varying development of swallow-tail terminations, potentially a sign of rapid decompression (Hammer and Rutherford, 2002).

The Type 2 frothy glass frequently mingles with the dense glass (Type 1) as well as pumiceous glass (Type 3), and it is often localized to specific domains within the sample (Figure 7.2). Lami Bomb L-B45 (Figure 7.2E) provides a good example of pumiceous glass (Type 3), that is intercalated with transecting dense glass domains. The appearance of the vesicular domains is very much foam-like. The general textural trend among samples from all three eruptive centers is one of diversity; particularly we find that several degrees (from sparse to high) of vesicularity frequently coexist within a single sample's domain.

Banding by microlites, vesicles and tuffisites represent some key textural features detected across nearly all three eruptions (e.g., Figures 7.2-7.4). In this context, banding refers to differences in the concentrations of microlites or vesicles, across zones of differing glass colors or areas of incorporated materials like ash (Figure 7.2). Typically, these bands appear as layers, a few micrometers to several millimeters thick, that either transect entire samples or are discontinuous and confined to localized domains. Vesicular banding, a conspicuous characteristic that gives samples a striped appearance, is best demonstrated by sample L-1b12 (Figure 7.2C), where it transects large portions of the sample. We find macroscopic vesicular banding in sample RR-F1 (Figure 7.3C). However, these types of banding can also manifest on a smaller, more localized scale (few mm). Microlite bands, identifiable by their 'dirty' or 'dusty' appearance within the glass matrix, are most prominently represented by samples L-1b12 (Figure 7.2C) and L-1b3 (Figure 7.2A).

The Type 4, shear-banded obsidians, are defined by coalesced and flattened vesicles which underwent shearing (Rust et al., 2004). That shearing forces may have been affecting the samples is also evident at the macroscopic scale in hand sample RR-F1 (Figure 7.3C), where vesicular bands are offset by a fracture that shifts their alignment along the fracture axis. Type 4 glass is also visible in the microscopic images of RR-1b4 (Figure 7.3B) and FV-1b2 (Figure 7.4A). There is no compelling evidence indicating the presence of Type 4 glass in the Lami samples that we analyzed.

Another distinctive feature, which might be related to possible hybrid degassing mechanisms, are tuffisites (e.g., Tuffen et al., 2003; Castro et al., 2012; Castro et al., 2014). These are typically associated with clastic material, microlites and oxides transecting the sample, giving a band, or vein-like appearance. In this study, tuffisite bands exist in varying intensity from nearly clean bands with scarce microlites, oxides, and clasts, to highly clastic, ‘dusty’ bands. These parallel bands may incorporate dense accumulations of brown, ‘dusty’ clasts interspersed with oxides or cleaner white-to-brown glass fragments. Representative examples include L-1b3 (Figure 7.2A) and FV-1a1 (Figure 7.5), both of which are nearly identical in appearance. Rocche Rosse samples, such as RR-1b4 (Figure 7.3B), show less numerous clastic tuffisite bands, but these too resemble those of the Forgia Vecchia and Lami eruptions. The study conducted by Cabrera et al. (2015) on Rocche Rosse also highlights the presence of tuffisites in the Rocche Rosse pyroclastic deposits. This in turn reinforces our finding that similar banding/tuffisite features are present in all three eruptions.

Another notable feature among all eruption sites, are healed fractures, which are associated with oxidation and the sintering of ash particles within the fracture. These fractures sometimes display a distinctive form on their edges, producing a sharp contrast with the surrounding material, making these structures clearly distinguishable from the far-field matrix. As samples L-1c2 (Figure 7.2D), FV-1b2 (Figure 7.4A), RR-1a1 (Figure 7.3A), demonstrate, the fractures occur in varying sizes and degrees and occasionally exhibit a “fishbone”-like structure, as seen in sample L-1c2 (Figure 7.2D).

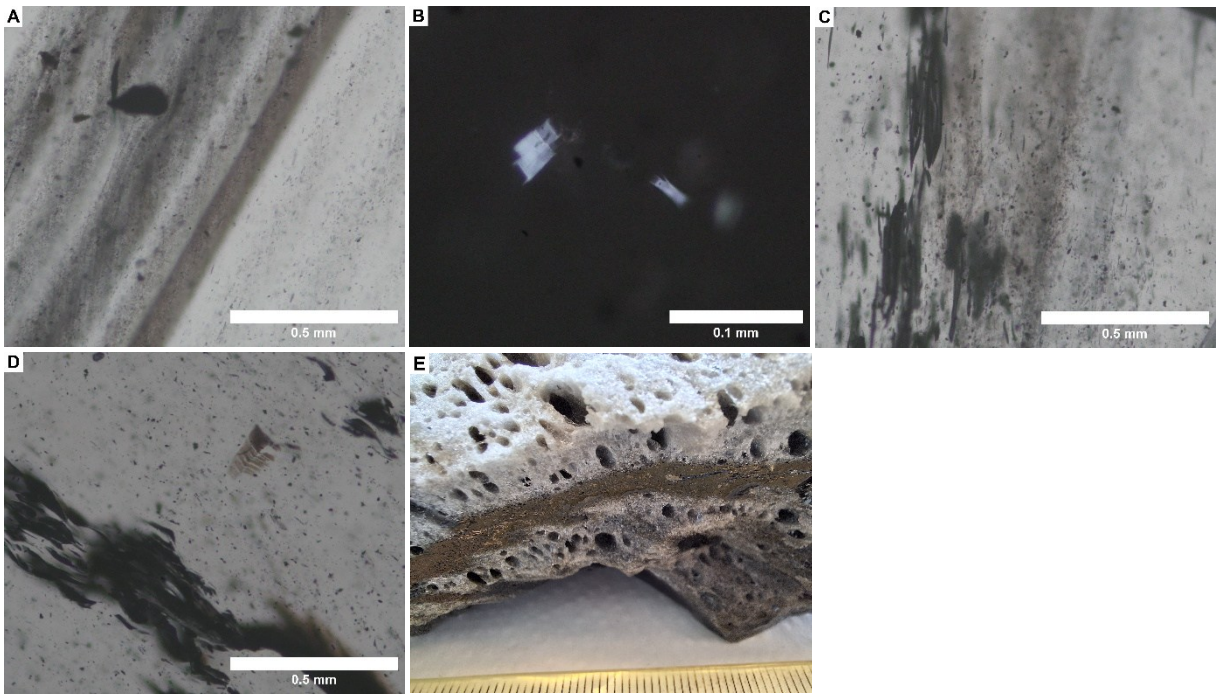


**Figure 7.2:** Images including optical light microscope micrographs of FTIR samples [A], [B], [C], [D] and photography of a hand sample [E] of the Lami eruption. [A] presents sample L-1b3 exhibiting prominent parallel brownish and greyish tuffisite bands. On the left side of the image a large oxide clast intersects two tuffisite bands, forming pressure shadows by oriented microlites, clasts, and oxides. The right side reveals pristine glass with smaller 'dusty' glass bands of microlites parallel to the tuffisites. Frame [B] focuses on sample L-1b10, showing two feldspar crystals (white) under crossed-polarized light with distinct swallow-tail terminations. [C] features sample L-1b12, with a relative clean glass matrix with few clasts on the far left and far right and diffuse white and 'dusty' brown tuffisite bands or veins in the middle. These bands or veins incorporate microlites, pyroxene and feldspar needles, and oxides. Bands of larger vesicles transect the obsidian on the left, creating a boundary between 'dusty' and clean glass. Image [D] depicts the sample L-1c2, containing a medium-dusty matrix composed of oxides, clasts, microlites, and pyroxene/feldspar needles. The left shows a large accumulation of elongate vesicles, while the central fishbone-like texture is a healed fracture filled with oxidized, sintered ash particles. The macro photography of the L-B45 bomb [E] illustrates highly vesicular white pumiceous glass (Type 3) on the top and bottom, separated by a dense black obsidian layer (Type 1) in the middle.

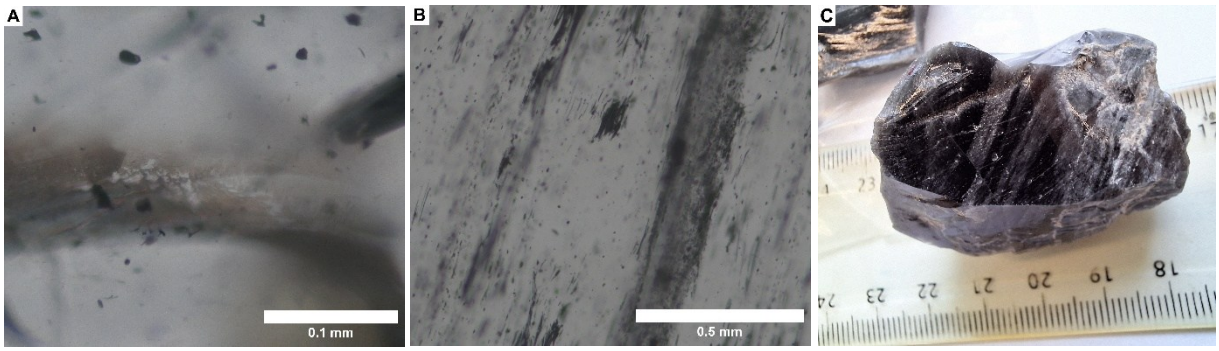


**Figure 7.3**: [Caption on next page]

**Figure 7.3:** Optical light microscope pictures of the Rocche Rosse FTIR samples. [A] shows sample RR-1a1, which features a clear glass matrix with some oxides and a central high-relief brown texture identified as a healed fracture filled with sintered and oxidized ash. Micrograph [B] displays sample RR-1b4 compromising clear glass with oxides and a thick grey tuffisite band containing clasts, oxides, and microlites, transecting the sample. Parallel to the band, numerous elongate, flattened vesicles typical of Type 4 (shear banded) are visible. [C] is a macroscopic image of hand sample RR-F1, highlighting vesicular (white) and dense (black) obsidian glass bands offset by a central fracture, which acts as evidence for shearing during the eruption.

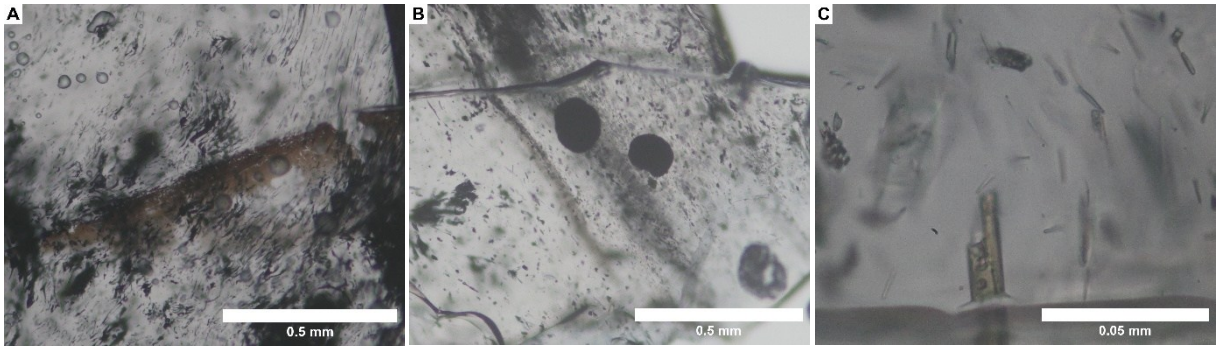


**Figure 7.4:** Optical light micrographs of double-polished FTIR obsidian shards from the Forgia Vecchia eruption in Lipari. [A] features the pyroclastic sample FV-1b2, exhibiting a clear glass matrix with prominent elongate and flattened vesicles typical of shear banded glass (Type 4). In the center of the image a brown distinctive structure represents a healed fracture filled with sintered ash particles displaying oxidation. Frame [B] illustrates the lava flow sample FV-23-21, which contains vesicles throughout the sample, becoming more orientated and elongate on the right side of the image. The center of the image shows dark-brown/black spherulites formed by radially oriented microlites as well as a large amount of 'dusty' glass consisting of microlites and pyroxene/feldspar needles, and a thick microlite-rich band that could be a diffuse tuffisite vein. Parallel to it, a reddish-brown tuffisite band with defined edges is observed, incorporating microlites and smaller clasts. In contrast, the left side of the image consists of more pristine glass with smaller amounts of microlites and needles. [C] presents a magnified view of sample FV-23-22, highlighting a greenish-brown feldspar needle with swallow-tail terminations and no noticeable compositional zoning.

### 7.5.2 FTIR measurements and results

In total, ninety-four shards were measured. Of these, four were excluded from analyses due to them having excessive vesicles, a lack of clear glass, or high opaque material content. Of the measured pyroclastic and effusive samples, bulk water contents varied, ranging from ~0.44 to 1.10 wt.% $H_2O$ for Lami, ~0.09 to 0.89 wt.% $H_2O$ for Forgia Vecchia and ~0.11 to 0.47 wt.% $H_2O$ for Rocche Rosse (Table 7.1). We did not observe a systematic trend of water content with stratigraphic height in the deposits, indicating that obsidian shards from different layers can and do display similar water contents. The water concentration range for Rocche Rosse is consistent with that reported in the literature (e.g., Cabrera et al., 2015; Shields et al., 2016). Lami's water content range is slightly extended beyond a previous maximum measured value (~0.90 wt.% $H_2O$; Cabrera et al., 2015) by about two tenths of a weight percent. While no previous $H_2O$ data exists for Forgia Vecchia, the relatively broad range of water content we

measured for this center (0.09 – 0.89 wt.%) brackets the values from the other two centers, suggesting that our measurements are representative and not outliers among all materials studied herein and in prior works.

**Table 7.1:** δD, bulk water content and water speciation of pyroclastic and effusive obsidians from the Lipari eruptions, Silicia, Italy. S.D. = standard deviation.

| Sample name | Location and type | δD (‰) | S.D. (‰) | $H_2O$ by TCEA* (wt.%) | $H_2O$ by FTIR ¥ (wt.%) | $H_2O$ molec. (wt.%) | OH (wt.%) |
|---|---|---|---|---|---|---|---|
| RR-1a1 (n=3) | Rocche Rosse Pyroclast | -76.42 | 0.63 | 0.21 | 0.12 | n.d. | n.d. |
| RR-1a2 (n=2) | Rocche Rosse Pyroclast | -96.40 | 0.02 | 0.20 | 0.19 | n.d. | n.d. |
| RR-1b4 (n=2) | Rocche Rosse Pyroclast | -90.43 | 5.09 | 0.27 | 0.24 | n.d. | n.d. |
| RR-1b12 (n=2) | Rocche Rosse Pyroclast | -85.59 | 3.51 | 0.40 | 0.39 | 0.04 | 0.35 |
| RR-F12 (n=3) | Rocche Rosse Lava | -98.10 | 4.67 | 0.11 | 0.11 | n.d. | n.d. |
| RR-F22 (n=2) | Rocche Rosse Lava | -89.43 | 1.75 | 0.22 | 0.34 | 0.10 | 0.24 |
| RR-F31 (n=2) | Rocche Rosse Lava | -90.77 | 24.54 | 0.33 | 0.30 | 0.11 | 0.19 |
| RR-B13 4 (n=2) | Rocche Rosse Bomb | -91.33 | 4.94 | 0.23 | 0.17 | n.d. | n.d. |
| RR-B13W (n=2) | Rocche Rosse Bomb | -86.49 | 7.09 | 0.29 | 0.17 | n.d. | n.d. |
| RR-B13T (n=2) | Rocche Rosse Bomb | -81.99 | 1.16 | 0.18 | 0.47 | 0.19 | 0.28 |
| L-1a1 (n=2) | Lami Pyroclast | -70.89 | 2.81 | 0.76 | 0.71 | 0.16 | 0.55 |
| L-1a3 (n=2) | Lami Pyroclast | -65.56 | 2.25 | 0.89 | 0.87 | 0.23 | 0.64 |
| L-1a10 (n=2) | Lami Pyroclast | -73.67 | 5.64 | 0.82 | 0.79 | 0.19 | 0.60 |
| L-1a11 (n=2) | Lami Pyroclast | -81.66 | 5.29 | 0.78 | 0.76 | 0.17 | 0.59 |
| L-1b2 (n=2) | Lami Pyroclast | -69.62 | 5.42 | 0.67 | 0.58 | n.d. | n.d. |
| L-1b12 (n=2) | Lami Pyroclast | -79.16 | 0.56 | 0.72 | 0.65 | 0.04 | 0.61 |
| L-1c2 (n=2) | Lami Pyroclast | -75.79 | 0.51 | 0.58 | 0.44 | 0.06 | 0.38 |
| L-1cB1 (n=2) | Lami Bomb | -77.97 | 5.21 | 0.55 | 0.49 | 0.08 | 0.42 |
| L-B45 (n=2) | Lami Bomb | -67.71 | 2.64 | 1.22 | 1.09 | 0.36 | 0.73 |
| FV-1a2 (n=2) | Forgia Vecchia Pyroclast | -76.30 | n.d. | 0.64 | 0.73 | 0.19 | 0.54 |
| FV-1a10 (n=2) | Forgia Vecchia Pyroclast | -98.14 | n.d. | 0.23 | 0.35 | 0.04 | 0.32 |
| FV-1a11 (n=2) | Forgia Vecchia Pyroclast | -73.17 | 5.79 | 0.66 | 0.55 | 0.08 | 0.47 |
| FV-1a12 (n=2) | Forgia Vecchia Pyroclast | -50.89 | 5.55 | 0.67 | 0.62 | 0.10 | 0.52 |
| FV-1b12 (n=2) | Forgia Vecchia Pyroclast | -86.53 | 4.41 | 0.61 | 0.47 | 0.04 | 0.42 |
| FV-1c10 (n=2) | Forgia Vecchia Pyroclast | -69.67 | n.d. | 0.75 | 0.78 | 0.15 | 0.63 |
| FV-1c12 (n=2) | Forgia Vecchia Pyroclast | -76.30 | 2.76 | 0.71 | 0.89 | 0.14 | 0.74 |
| FV-23-12 (n=3) | Forgia Vecchia Lava | -104.85 | 0.76 | 0.18 | 0.12 | n.d. | n.d. |
| FV-23-22 (n=3) | Forgia Vecchia Lava | -97.68 | 9.69 | 0.13 | 0.10 | n.d. | n.d. |
| FV-23-31 (n=3) | Forgia Vecchia Lava | -98.99 | n.d. | 0.19 | 0.15 | n.d. | n.d. |
| FV-23-42 (n=2) | Forgia Vecchia Lava | -89.68 | 2.67 | 0.15 | 0.09 | n.d. | n.d. |

* Typical reproducibility by applied TCEA technique = ±0.04 wt.% $H_2O$ (Bindeman et al., 2021)

¥ Measurement error = ±0.01 wt.% $H_2O$

Additionally, a 2D FTIR map, which traverses a banded domain in sample FV-1a1 was collected (Figure 7.5A). Within this 2D map, a water content line graph was extracted in order to illustrate the small but significant variations in water content that occur over hundreds of microns (Figure 7.5B). We do not see a systematic correlation between $H_2O$ content and band appearance—i.e., whether $H_2O$-enriched bands are dark or light—but we do recognize that $H_2O$ content undergoes inflection at and across glass domain boundaries (Figure 7.5B), which is consistent with the domains being relict glass fragments that were welded back together post fragmentation (Castro et al., 2014). The maximum difference in $H_2O$ between clear glass and thick bands is ~0.11 wt.% $H_2O$.

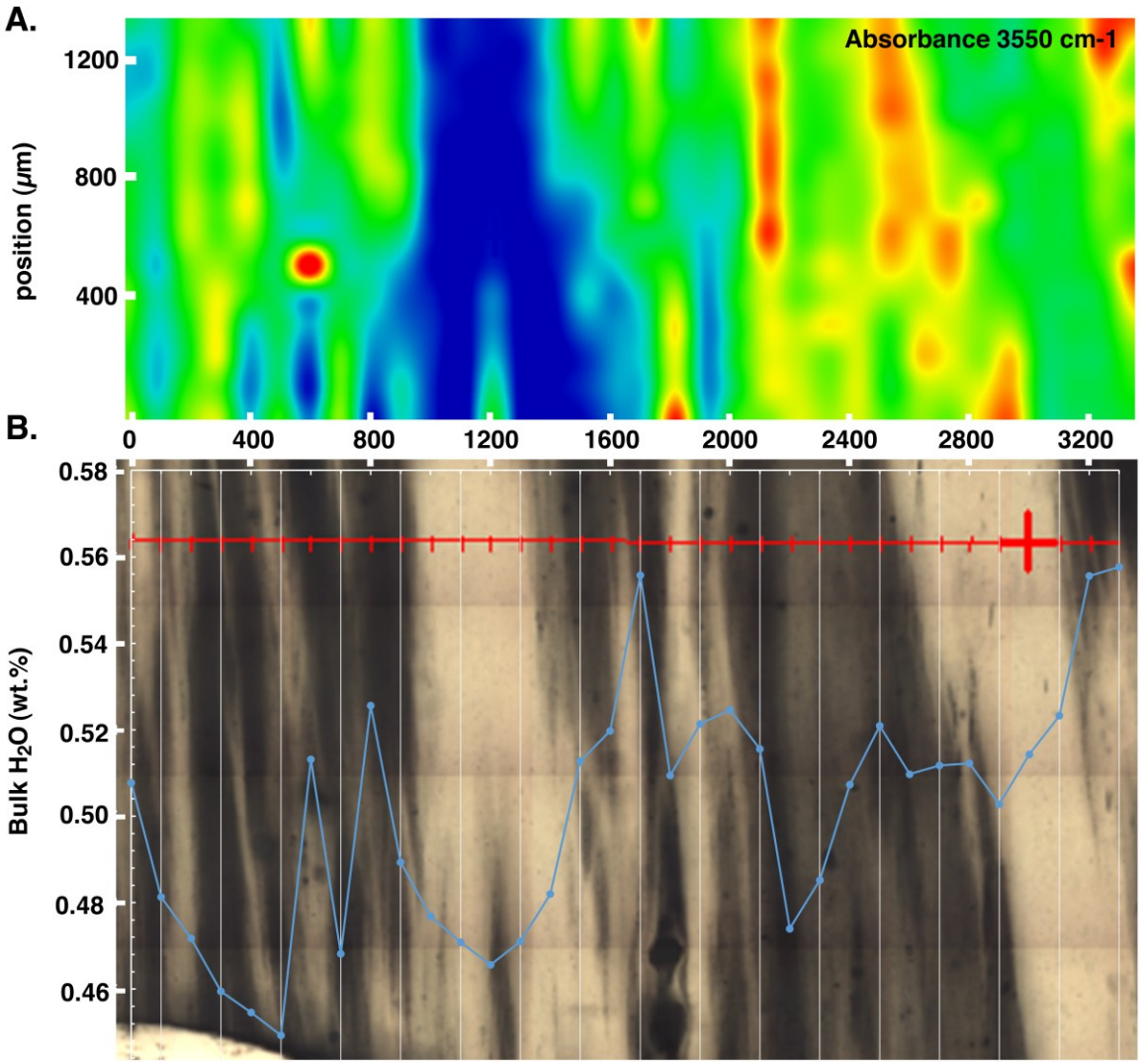


**Figure 7.5:** FTIR measurements of tuffisite banded obsidian sample FV-1a1. Frame [A] presents a qualitative 2D FTIR map displaying the intensity of the 3550 $cm^{-1}$ peak absorbance (blue for low and red for high). Panel [B] depicts a photomicrograph of the same area shown in [A], overlaid with a graph of quantitatively measured bulk $H_2O$ contents along a transect corresponding to the topmost edge of the 2D map in [A]. The x-axis (distance in micrometers) is displayed at the top, while the y-axis (bulk $H_2O$ in wt.%) is on the left. Vertical lines on the red transect line indicate the measured points, with corresponding water content values plotted below in the graph. The graph generally presents lower water contents in the dense glass regions and higher values in thick tuffisite bands, with mixed values in the medium density tuffisites.

Finally, the analyses of $H_2O$ speciation plot on speciation curves (Figure 7.6A) expected for purely magmatic water and in turn, the FTIR data do not show contamination from external sources, such as meteorological water as this would divert the speciation values away from ideal magmatic ratios. This is partly an outcome of our choice to measure only clear dense glass that is less susceptible to hydration over time compared to vesicular glass (DeGroat-Nelson et al., 2001). These speciation values were used as inputs in VolcDeGas to calculate the alpha factors at each bulk water content (e.g., Walter and Castro, 2020; Figure 7B).

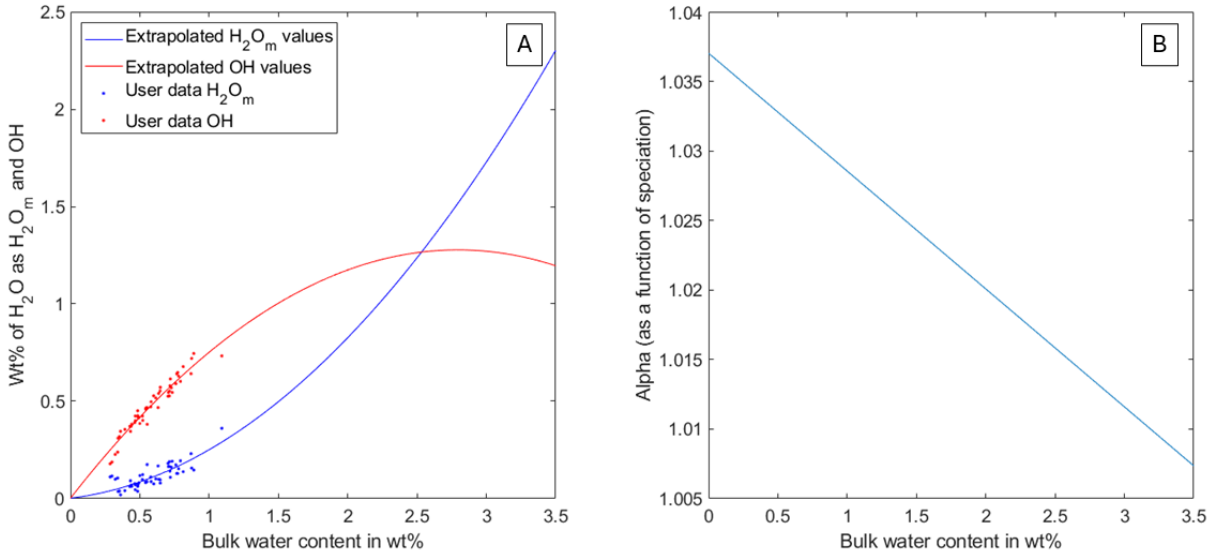


**Figure 7.6:** [A] Graph depicting the FTIR-measured water speciation values (wt.% $OH^-$ in red dots, wt.% $H_2O_m$ in blue dots) for Lipari samples. The data is fitted with 2nd degree polynomial trendlines and extrapolations for required further data (red lines for $OH^-$ and blue lines for $H_2O_m$). [B] presents the calculated hydrogen isotope fractionation factor (α) between vapour and melt in rhyolitic systems, derived from water speciation data of [A]. These graph and calculations were generated by the VolcDeGas program, as described in detail by Walter and Castro (2020).

### 7.5.3 TCEA/MS measurements

Dense glass samples for the hydrogen isotope measurements amount to 30 different samples, the δD data of which are presented along with corresponding $H_2O$ values in Table 7.1 and Figure 7.7. Even though five measurements failed due to a capsule rupture or material loss during transport to the lab, measurements were always conducted in either duplicate or triplicate, ensuring that results are indeed available for every sample. The bulk $H_2O$ concentrations determined from TCEA range from about 0.1 to 1.22 wt.%, mirroring the values returned by the FTIR method (0.1 – 1.1 wt.%; Table 7.1). Minor variations in both TCEA/MS and FTIR water contents could be due to the FTIR measurements being made on different, non-altered glassy spots, which in and of themselves are chemically heterogeneous over small length scales (Figure 7.5). Similarly, variability in TCEA/MS values could reflect that the bulk powders were somewhat heterogeneous, possibly stemming from glass fragments having small domains of vesicular glass, spherulites, or tuffisites, all of which might have induced $H_2O$ heterogeneities (e.g., Castro et al., 2005; Castro and Dingwell, 2009; Castro et al., 2014).

Despite the vast majority of data being relatively consistent, some duplicates did not return the same or similar $H_2O$ content values. To address this, we examined the samples with duplicates showing significantly different TCEA/MS-determined water contents and compared them to their counterpart FTIR measured water contents, which tended to be rather constant across

measurement points. In such cases, TCEA/MS water contents exhibiting big discrepancies (>0.5 wt.%) relative to FTIR values were excluded from later analysis (i.e., FV-1a2_2, FV-23-31_2, FV-1c10_1). Additionally, sample RR-F31, which contains numerous spherulites, exhibited rather large variations in both δD and water contents across its duplicate measurements. We attribute this to heterogeneous amounts of crystalline spherulite material in the powders. However, since the average TCEA/MS water content and δD (Figure 7.7A) align closely with FTIR water contents (Figure 7.7B), this sample's data were retained in the analysis. All other replicate analyses illustrate close correspondence of TCEA/MS water values to FTIR-determined values, confirming their accuracy (Table 7.1, Figure 7.7C; e.g., Bindeman et al., 2021).

The graph in Figure 7.7B exhibits the δD values plotted against $H_2O$ contents (by FTIR) of the pyroclastic and effusive samples from all three eruption centers. The δD values of the samples (Table 7.1) range from about -104.9 ‰ to -50.9 ‰, which combined with the water concentration range of 0.09 to 1.1 wt.%, provides for a robust dataset that traces out a degassing trend spanning the three centers (Figure 7.7). When observed collectively, there does not appear to be a systematic grouping of either δD or $H_2O$ as a function of eruption center, aside from the clear separation of Lami and Rocche Rosse data into distinct but co-linear groups. A clear trend emerges from the data, spanning over the entire range of water contents and characterized by a relatively constant decrease in δD followed by a later "flaring" of the range in δD at the lowest of $H_2O$ contents. The overall decreasing δD pattern with falling water is consistent with trends observed in numerous other rhyolitic systems (e.g., Newman et al., 1988; Dobson et al., 1989; Castro et al., 2014; Giachetti et al., 2020; Castro and Walter, 2021). Furthermore, the graph does not show any sharp kinks in δD as water is lost; the variations appear to be smooth.

An intriguing couple of anomalies in the δD-$H_2O$ dataset are represented by samples FV-1a12 and RR-1a1 (Figure 7.7, Table 7.1), which owing to their significantly higher δD values (up to +~20‰ for FV-1a12 and +~15‰ for RR-1a1) than other samples with similar water contents, plot as outliers above the trend. Such elevated δD values are not unique to this study or system; they have typically been seen in samples from other volcanoes where the obsidian or tuffisite samples were enriched in external magmatic vapor having a significantly different (i.e., isotopically heavier) δD (Giachetti et al., 2020). Indeed, Castro et al. (2014) observed similar δD enrichments in relatively degassed tuffisite-bearing obsidians and suggested these anomalous, isotopically heavy obsidians reflected the uptake (i.e., entrapment and redissolution) of deeper-derived exsolved magmatic fluids during explosive venting and lava effusion.

In summary, data from all three eruptions collectively build a trend, with the Lami samples plotting at higher water contents, the Forgia Vecchia eruption occupying intermediate to high values, and the Rocche Rosse samples occupying the drier end of the spectrum. Despite this apparent ordering of the three centers, there is however overlap in both $H_2O$ and δD amongst the different vents.

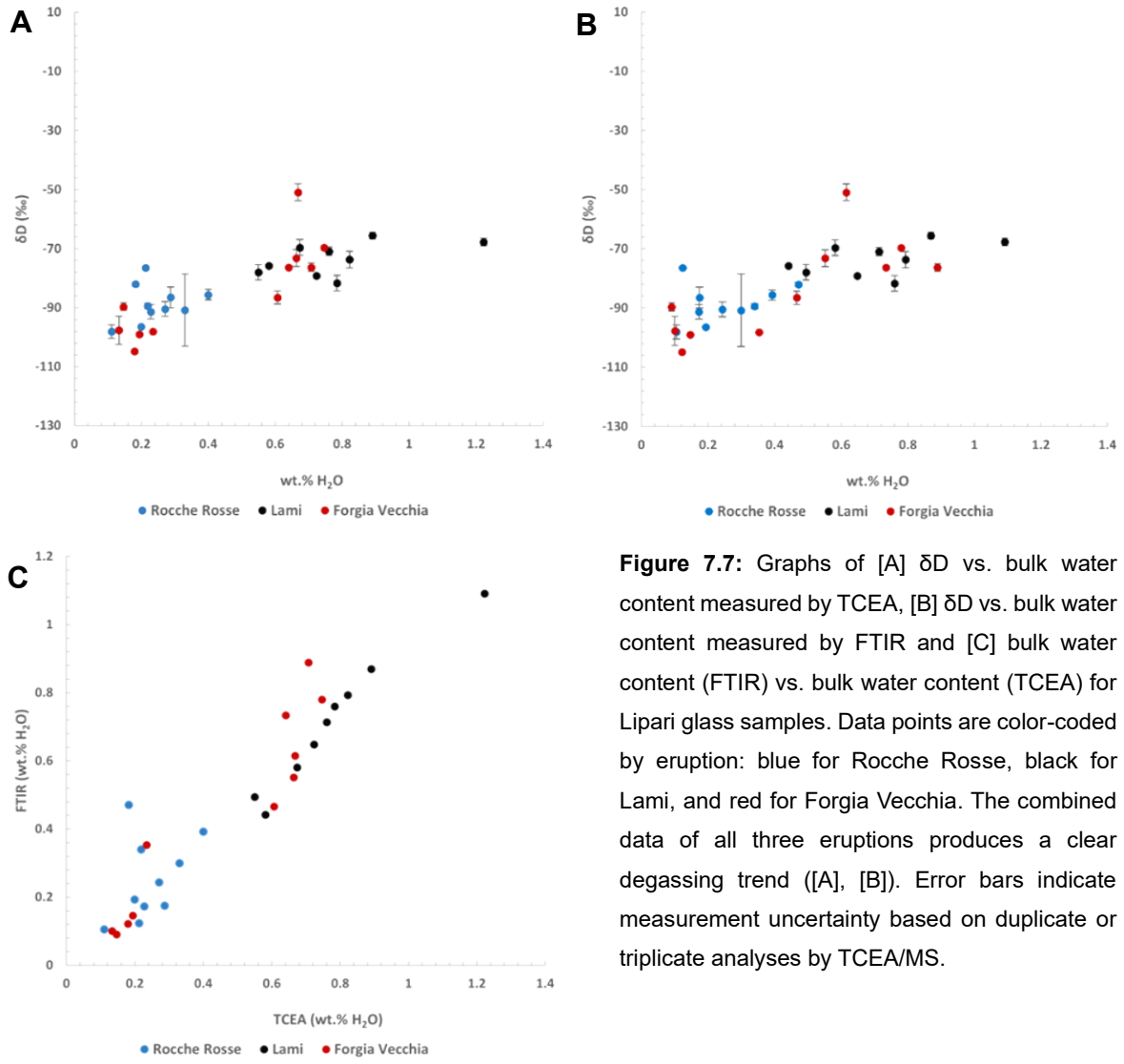


**Figure 7.7:** Graphs of [A] δD vs. bulk water content measured by TCEA, [B] δD vs. bulk water content measured by FTIR and [C] bulk water content (FTIR) vs. bulk water content (TCEA) for Lipari glass samples. Data points are color-coded by eruption: blue for Rocche Rosse, black for Lami, and red for Forgia Vecchia. The combined data of all three eruptions produces a clear degassing trend ([A], [B]). Error bars indicate measurement uncertainty based on duplicate or triplicate analyses by TCEA/MS.

### 7.5.4 Degassing modeling results

Here we are focused primarily on volatile *loss* during the Lipari eruptions in order to understand the system's degassing trajectory and eruptive behavior. By contrast, regassing, a process that, while potentially evidenced in the outliers within the δD-$H_2O$ dataset (e.g., Giachetti et al, 2020), cannot be simulated by our modeling software (VolcDeGas). Thusly, in the following section, we will omit the two anomalously isotopically heavy (in terms of δD) values from data that VolcDeGas models are compared to. However, for completeness, we have also included one VolcDeGas model trends fit to the complete δD-$H_2O$ data, incorporating the two heavy-δD

outliers, in Figure 7.8D. Additional model runs using the full data set can be found in the Supplementary Material (Figure S2).

Figure 7.8A - C presents best-fit results of our modeled degassing trends utilizing VolcDeGas on all data except for the two outliers, the incorporation of which would have altered the fits significantly (see Supplementary Material; Figure 7.8D). Consequently, the observed variation of δD has been adjusted to between -104.9 ‰ and -65.6 ‰. The parameters used for the modeling were previously described in the “Modelling degassing paths” section. The results of modeling cover various degassing scenarios, which comprise different system types (closed, open, batched), initial δD’s, and transition points in order to reach the best-fit simulation match to the δD-$H_2O$ data. VolcDeGas identified (by minimizing RMSE) the best-fit degassing scenarios as variable-step-size batched degassing systems, with either a single-stage batched (Figure 7.8A) or two-stage closed-to-batched system (Figure 7.8B). Both systems exhibit the lowest RMSE and highest $R^2$ of all modeled systems. The single-stage batched system (A) displays a slightly better fit with an RMSE of 5.8, compared to the two-stage system (B) which has an RMSE of 6.3. However, both systems achieve nearly identical $R^2$ values of 0.77 and 0.79, respectively. The best-fit initial δD value, determined iteratively, is about -47 to -48 ‰, and combined with an 85% water loss at each step, yields good fits for both degassing histories. In the two-stage closed-to-batched system the best-fit transition point occurs at about 0.6 wt.% $H_2O$.

It is not surprising that the batched system yields the best results, given that past studies (Castro et al., 2014; Walter and Castro, 2020; Castro and Walter, 2021) have also shown that this system is able to mimic simultaneous, multi-step closed and open system behavior through variation in degassing step size (see also Taylor, 1991). Indeed, the batched systems’ dependence on step size (Walter and Castro, 2020) means that with each successive degassing interval the batches of gas released get progressively smaller, leading to sensitive and smooth variations in δD that can very closely match the curved trajectories of natural data. Naturally, a batched system with its ever-decreasing steps could approximate successive smaller-scale explosive releases of volatiles that occur during hybrid activity, ultimately reflecting devolatilization of magma over time (e.g., Schipper et al., 2013; Castro et al., 2014). In contrast to the batched system, an open system produces a poor fit (Figure 7.8C). Even though the open system provides an acceptable fit for data below ~0.6 wt.% $H_2O$, it fails to adequately describe less degassed samples, collectively resulting in a very high RMSE (14.7), and an $R^2$ value of about 0.73. Furthermore, an open system would require a highly enriched initial δD value of -30 ‰ in comparison to the modest values inferred from batched system modeling. The closed system (Supplementary Material; Figure S2A) performs better than the

open system but still falls well short of the good fits produced by the aforementioned batched systems (Figure 7.8A, 7.8B). Lastly, the two-stage, closed-to-open system yields an RMSE of 7.9 and very poor $R^2$ of 0.58 (Supplementary Material; Figure S2C).

As regards the two outlier samples, their influence on the goodness-of-fit of a VolcDeGas single-stage batched degassing path is apparent in the batched system model presented Figure 7.8D. By including the two diverging data points, the model yields an elevated RMSE (compared to the cases without outliers) of approximately 8.2 and an $R^2$ of roughly 0.6 for the ideal one-stage batched system with variable step size (see e.g., Figure 7.8A vs. Figure 7.8D). This significant impact from just two data points underscores the importance of their exclusion in earlier model runs. The more extreme of the two outliers (in terms of δD separation from the main cloud of data; FV-1a12) exhibits a δD value (-51‰) that is close to the implied initial δD value (-48 ‰) at the degassing simulation starting point (3.5 wt.% $H_2O$). This sample's retention of high δD in spite of great $H_2O$ loss clearly signals negligible fractionation during water loss; why this occurred is an open question that cannot be addressed with the limited data in this work. This large deviation cannot however be attributed to measurement error and thus this datum along with the other outlier require a more complex degassing history than most of the samples that are well-fit by VolcDeGas models.

In summary, the VolcDeGas modeling results suggest a best-fit solution of a batched-degassing system for the Lipari rhyolites. These findings corroborate previous studies of other rhyolite eruptions that found batch systems yielded the best model fit to δD-$H_2O$ data sets (e.g., Walter and Castro, 2020; Castro and Walter, 2021). As discussed in the "Background" section, the batched system characteristics can be linked to hybrid eruption styles observed in other rhyolite eruptions (e.g., Chaitén and Cordón Caulle; Castro et al., 2014; Lara, 2009; Castro et al., 2013). Interestingly, the degassing trends—both the raw data and models—from the three different eruptions display considerable overlap with one another, collectively leading to a singular path that is well fit by batched degassing models. Such geochemical continuity amongst the different eruption centers provides indirect evidence that these three events may have been synchronous. We will address this possibility in depth in the following discussion section.

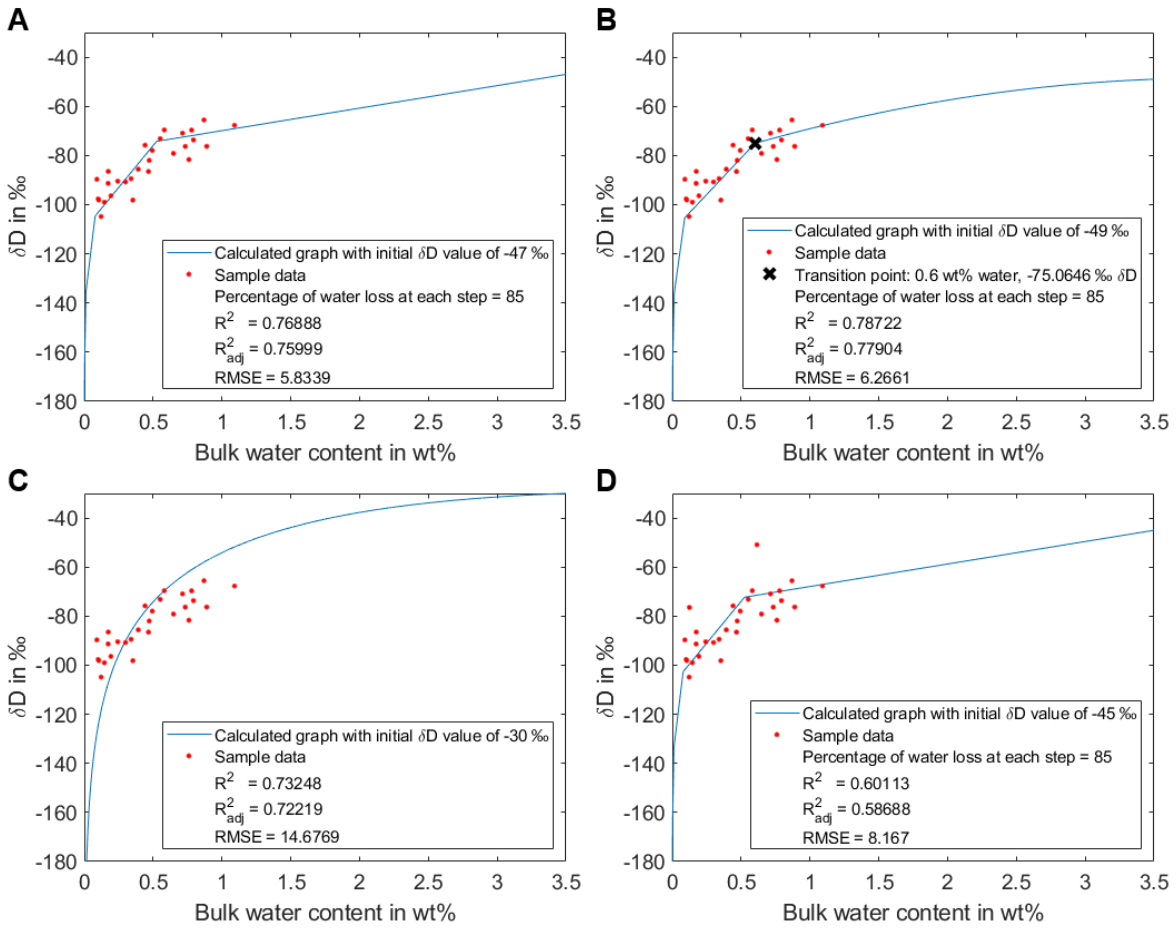


**Figure 7.8:** Diagrams presenting δD versus $H_2O$ graphs of best-fit degassing calculations performed by the VolcDeGas program (blue curve) utilizing the Lipari sample data (red dots) where graphs [A], [B], and [C] exclude the outlier samples FV-1a12 and RR-1a1, while graph [D] incorporates them. The VolcDeGas program identifies optimal fits through iterative calculations based on various parameters, including initial δD (in ‰), initial water content (in wt.%), hydrous speciation, and data from natural samples. These parameters are utilized to generate numerous simulated degassing curves and the best-fit for each system is distinguished by the lowest RMSE (Root Mean Square Error). Additional metrics, such as $R^2$ values, RMSE, the transition point in two-stage systems and the percentage of water loss, are provided in the information box on the lower right of each figure. All simulations assume an initial water content of 3.5 wt.% and employ a fixed step size of 0.001 wt.%. The modeled best-fit trends establish the expected initial subtle decline in δD at higher water contents, followed by a distinct exponential decrease at lower water contents during late-stage degassing. Frames [A] and [B] depict batched degassing systems with variable step sizes, with [A] representing a one-stage system and [B] a two-stage closed-to-batched system. Both show approximately identical results and their low RMSE values and high $R^2$ evidently make them the best-fit models. In contrast, the open-system model displayed in frame [C] exhibits a poor fit, with RMSE values more than double those of the batched models with variable step size, and shows significant deviations, particularly for data above ~0.6 wt.% $H_2O$. Frame [D] illustrates the best-fit single-stage batched model with variable step size when the two outlier samples are included. However, incorporating these outliers does significantly worsens the model's fit, as indicated by a noticeable increase in RMSE and a sharp decline in $R^2$, underscoring the reduced reliability of this scenario in capturing the ideal natural degassing trends.

## 7.6 Discussion

### 7.6.1 Evidence for co-eruptive vents and hybrid rhyolitic volcanism on Lipari

There is mounting evidence supporting co-eruptivity of the three Lipari vents in recently published works. For example, paleomagnetic and radiocarbon ($^{14}C$) age-dating by Pistolesi et al. (2021) suggests simultaneous eruption of Rocche Rosse, Lami and Forgia Vecchia at around 1250 CE. In addition, these workers presented field evidence in the form of lava-topping, Rocche-Rosse-sourced, welded pyroclastic material covering the Forgia Vecchia lava flow to substantiate their geochronological evidence of co-eruptive vents. Their interpretation of the overlapping fall deposits requires that the Forgia Vecchia lava was still hot, and possibly still being emplaced (Pistolesi et al., 2021) when the fall deposit from Rocche Rosse was lain down. The heat of the Forgia Vecchia lava, according to Pistolesi et al. (2021) contributed to the welded nature of the overlapping fall material. Our field research on Lipari, specifically on the vent area of the Forgia Vecchia flow, confirms the existence of these flow mantling breccias on the lava in this location. Furthermore, our own research on BGM has identified similar welded fall deposits in superposed contact with obsidian lava (Castro and Walter, 2021), lava that effused during a multi-vent hybrid rhyolite eruption. Thus, the outcome of vent-proximal tephra deposition during hybrid activity appears to leave a lithostratigraphic signature that is well expressed on Lipari, one that is indicative of simultaneously active explosive and effusive vents.

Qualitative descriptions of textural features in our study (e.g., vesicular bands, tuffisites, microlitic domains; Figures 7.2-7.5) illustrate commonalities in eruptive materials from the different eruption deposits, consistent with a co-eruptive relationship amongst the Lipari vents. In our samples, diverse vesicular banding structures can be observed in all three deposits as well as the presence of spherulites in the two effusive lavas. The groundmass glass derived from the three centers, is of uniformly low crystallinity, and contains distinctive pyroxene and feldspar microlite needles having swallow-tail structures (Figures 7.2B, Figure 7.4C). Furthermore, healed fractures containing oxidized material and sintered ash particles are present in all three deposits, further suggesting eruptive material consistency amongst the three vents. Though not a proof co-eruption, the consistent and excellent, unweathered preservation of these textural features across all eruption deposits supports co-eruptivity of the Lipari rhyolites.

Next, the occurrence of tuffisites within all eruption deposits adds to the evidence for co-eruptivity and hybrid eruption mode (Figure 7.2A, C, Figure 7.3B, Figure 7.4B, Figure 7.5; see also Cabrera et al., 2015). Tuffisites are known to foster magma outgassing by repetitive pyroclastic explosions through channels embedded within lava or crosscutting vent-plugging magma (Castro et al., 2012; Castro et al., 2014; Saubin et al., 2016). Tuffisites' cyclical buildup and release of gas and pyroclasts (Crozier et al., 2022) is the functional underpinning of a batched degassing system, as previously described in studies of hybrid eruptions (Castro et al., 2014; Walter and Castro, 2020; Castro and Walter, 2021). Just as previous works on Chilean rhyolites have done, our observations and sample suite establish a close association of tuffisites—both geochemically and physically—with pyroclastic and effusive rhyolite deposits. Unlike the case of the Chilean rhyolites, however, we do not have the benefit of real-time eruption observations and sampling of tuffisite-bearing obsidians from freshly lain deposits to directly link them to hybrid activity. Our inference of the Lipari tuffisites being a hallmark of hybrid activity is instead circumstantial, and based largely on geochemical degassing signatures discussed further below. Nevertheless, it stands to reason that these structures are consistent with simultaneous explosive and effusive activity.

In addition to textural and lithological evidence, hydrous geochemical aspects of the three eruption deposits offers additional support for a co-eruptive origin. The FTIR measurements indicate staggered, yet overlapping values amongst the vents (Figure 7.7). For example, the maximum water content observed in Rocche Rosse aligns closely with the minimum water content in the Lami samples, while the full range of water content exhibited by Forgia Vecchia encompasses the combined ranges of both Rocche Rosse and Lami eruptions. All of this is consistent with there having been a single batch of magma that was degassing to varying degrees and amounts during eruption from the three vents. Another aspect of hydrous speciation revealed by FTIR measurements is that there is no evidence for secondary hydration in any of the three deposits. This fact supports that all the eruption materials are uniformly young, and therefore have not yet been exposed sufficiently long to hydration at the Earth's surface. That all three sample suites share this trait is consistent with their co-eruptivity.

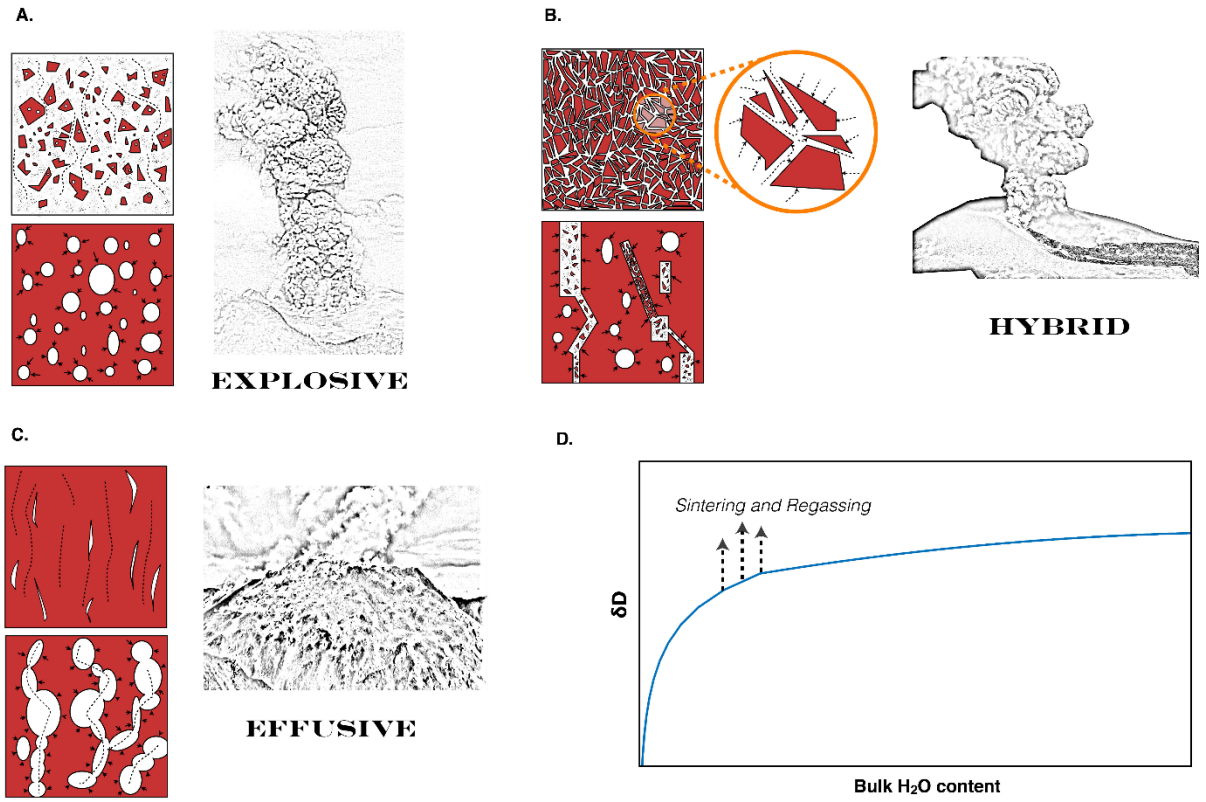


**Figure 7.9:** Schematic diagram showing various stages of hybrid rhyolitic eruptions including the initial explosive onset (frame A), the protracted hybrid phase (frame B), and conclusive effusive stage (frame C). Each of these eruption phases is driven by degassing mechanisms (red diagrams) characterized by differing amounts of gas exsolution and separation, comprising "batched degassing systematics". Unique to the hybrid phase is the potential for "regassing" promoted by annealing and re-dissolution of previously exsolved interstitial volatiles back into sintering melt (frame B). Such regassing would result in outlier isotopic signatures in geochemical trends, comprising anomalously deuterium-rich values (vertical arrows) in otherwise extensively degassed samples (frame D).

The collective $H_2O$-hydrogen isotopic trends and accompanying modeling of degassing histories of the Rocche Rosse, Lami and Forgia Vecchia eruptions also point to both co-eruptivity and hybrid explosive-effusive eruption style. The δD vs. $H_2O$ data—excluding the two outliers (Figure 7.8D, Supplementary Information; Figure S2)—comprise a single degassing trend with overlapping individual vent isotope values, observations of which support the co-eruptivity hypothesis. If the vents were to have erupted independent of one another in different episodes, a continuous geochemical trend might not be expected. Instead, the hydrous geochemical data of Forgia Vecchia, with their broad range in both δD and $H_2O$, appear to “stitch together” the two other data sets (Figure 7.8). Indeed, the wettest and most isotopically primitive of the Forgia Vecchia samples align closely with data from Lami, while the drier Forgia Vecchia samples match δD and $H_2O$ in Rocche Rosse`s obsidians. In a simultaneous, multi-vent eruption scenario, these overlapping and continuous trends could represent different fragmentation depths—manifested by bulk $H_2O$ pyroclast contents—or different fragmentation

conditions altogether, achieved at each vent through variations in magma ascent and vent dynamics (e.g., Rust et al., 2004; Rust and Cashman, 2007).

Part and parcel of the multi-vent, simultaneous eruption scenario are the results of VolcDeGas modelling, which identify a single batched degassing path as the best-fit system. This model, with its low RMSE and high $R^2$ values (Figure 7.8A), is one that simulates repetitive release of batches of outgassed vapor, tapped from a common, isotopically homogeneous source at depth. If indeed the three vents were simultaneously active and erupting from a common magma at depth, we might expect them to generate overlapping geochemical signatures—which they do—and, show continuous, undisrupted variations in δD-$H_2O$ space. If on the other hand, the three vents acted independently of one another, or were otherwise fed by different magma sources, we might expect to see offsets or step-function changes between vents, particularly with respect to their δD values. Such sharp variations in geochemistry among the three vents are not observed. Thus, collectively, these findings provide compelling evidence for the co-eruptivity of Lami, Forgia Vecchia, and Rocche Rosse, and support the hypothesis that all three vents tapped a common magmatic source.

Finally, one process that could have also occurred during degassing of the Lipari rhyolite is regassing, which is the uptake of already exsolved magmatic fluid by the melt (e.g., Watkins et al., 2012; Giachetti et al., 2020; Figure 7.9). If for example gas is trapped in pores within fragmental tuffisite, sintering of that material back to a coherent mass (e.g., Gardner et al., 2018) would necessitate re-incorporation of the fluid along with its magmatic geochemical signatures ($H_2O$ and δD) into the melt. Regassing of deuterium-enriched hydrous vapor originating from deeper, less evolved magma will shift the δD of the obsidian to higher values, as has been observed in some Chaitén tuffisites (Castro et al., 2014). Although our data is limited, we suggest that two outlier data points in the Lipari dataset (Figure 7.7B), which exhibit significantly higher δD values than the other samples of similar $H_2O$ content, may have been subject to regassing. If this were the case, the physical evidence of pyroclastic state is effectively erased, but the geochemical signature remains, entirely consistent with these obsidians being “cryptic fragmentation” masses (e.g., Wadsworth et al., 2022). Future in depth studies of anomalously deuterium enriched obsidians within pyroclastic and effusive sequence may help shed light on the cryptic processes that are known to occur in obsidian (e.g., Foster et al., 2024).

## 7.7 Conclusion

Our study of pyroclastic and effusive obsidians from the Rocche Rosse, Lami and Forgia Vecchia eruptions on Lipari reveal a multifaceted (i.e., explosive and effusive) eruptive history from multiple widely spaced vents, and highlights the potential interconnected nature of these three rhyolitic centers. Textural and geochemical evidence, including the first-ever hydrogen isotope analyses for these eruptions, strongly supports the recently established thesis of a co-eruptive origin (Pistolesi et al., 2021). Furthermore, our results suggest that the vents acted both collectively and singularly as a hybrid system that, instead of undergoing sharp shifts from purely explosive to effusive eruption, instead erupted in a hybrid manner, much like recent Chilean rhyolite eruptions at Chaitén and Cordón Caulle have (e.g., Castro et al., 2013). Like those Chilean events, the Lipari eruptions could have evolved from initial violent, high-intensity explosive outbursts to a long period of simultaneous explosive and effusive activity, before shifting into a predominantly effusive eruption. Identifying the hybrid nature of past eruptions like Lipari will improve our ability to understand and assess the danger of future rhyolite eruptions that may act in similar ways. The periodic explosive events that must accompany lava effusion are a particular threat, as are persistent ash plumes that emerge from the lavas themselves (Schipper et al., 2013). Future detailed geochemical and textural investigations into other rhyolite systems may help us avoid misinterpreting their classic eruption stratigraphy as the result of a sharp shift from purely explosive to effusive activity, as has been assumed to be the correct rhyolite eruption paradigm for decades (e.g., Eichelberger et al., 1986; Giachetti et al., 2020). This is to say that recognizing the potential for hybrid and overlapping vent activity, will undoubtedly lead to better assessments of volcanic risk, especially to air traffic, ecosystems and life (Black et al., 2016).

## 7.8 Acknowledgements

The authors thank the University of Mainz for a development grant (Forschungsförderung) that paid for the analytical and fields costs. INB thanks the Alexander von Humboldt foundation for the research award that enabled his visit to Mainz.

## 7.9 Supplementary Material

Supplementary Figures S1 and S2 can be found in the Appendix at the end of this thesis (page 213).

### 7.10 Author contributions

S.C. Walter prepared samples, conducted FTIR measurements, analyzed data using VolcDeGas and wrote the initial manuscript, while J.M. Castro provided project funding and co-wrote the manuscript. J.M. Castro and S.C. Walter collected the samples and I.N. Bindeman measured the samples via TCEA-MS. All authors reviewed and edited the manuscript, and assisted with data interpretation.

# Chapter 8

# Boron as a tracer for rhyolitic degassing

## 8.1 Preface

This chapter studies rhyolitic degassing processes using boron isotopic systematics, which are applied to glass samples from the 1060 CE Big Glass Mountain eruption, California, USA, and to published data (Schmitt and Simon, 2004). The goal here is to assess the applicability of boron isotopes for tracking rhyolitic degassing processes. In other words, is boron as effective as a degassing tracer as hydrogen isotopes? The chapter begins with a brief introduction summarizing key concepts of boron degassing behavior, followed by methodology sections describing the analyzed samples, analytical techniques, and novel boron modeling functionalities implemented in VolcDeGas. The results section presents a re-evaluation of Long Valley boron data, new measurements from the Big Glass Mountain eruption, and theoretical degassing models generated using VolcDeGas. This is followed by a discussion that critically evaluates the findings, with a focus on whether the boron isotopic system reliably traces the syn-eruptive degassing process. The conclusion then summarizes the key findings of this chapter. The final section presents an updated VolcDeGas manual along with the program`s code download link. This chapter`s work was supported by the VAMOS research center, University of Mainz.

## 8.2 Introduction

For comprehensive background information on the boron isotopic system and its potential application to degassing-related processes, readers are referred to Chapter 1.6 and 2.2. In summary, the boron isotopic system theoretically enables the tracking of degassing trends, as during degassing, boron and its heavy isotope ($^{11}B$) preferentially partition into the fluid/vapor phase (e.g., Hervig et al., 2002; Maner and London, 2018), which is primarily composed of $H_2O$. In this study, the VolcDeGas program (see Chapter 5) was updated to incorporate the boron isotopic system through the implementation of the relevant equations (Equations 8 and 9) described in Section 2.2.2.

## 8.3 Samples and analytical methods

Obsidian shards were extracted from bulk samples of tephra comprising rhyolitic pumice, lithic fragments and obsidian chips from the 1060 CE Big Glass Mountain (BGM) eruption, located at the Medicine Lake Volcano (California) which is part of the Cascade Range. These obsidian samples were originally collected from a pumice quarry northeast of BGM (Chapter 6; Castro and Walter, 2021) and were analyzed in regard to their boron concentration and boron isotopic signature. The same samples were already interpreted in a previous study (Chapter 6; Castro and Walter, 2021) in relation to their water content and δD value (Table 6.1). Readers are referred to Chapter 6, where additional descriptions of the site can be found.

Boron concentration and isotopic measurements were conducted by Alexander Rocholl/Michael Wiedenbeck at the GeoForschungsZentrum (GFZ) in Potsdam, employing Secondary Ionization Mass Spectrometry (SIMS; Section 4.2.2). Of the original sixteen shards, thirteen were successfully prepared through polishing, gold coating, and embedding into epoxy. These samples were then mounted onto the sample holder and analyzed in a CAMECA 1280-HR SIMS system.

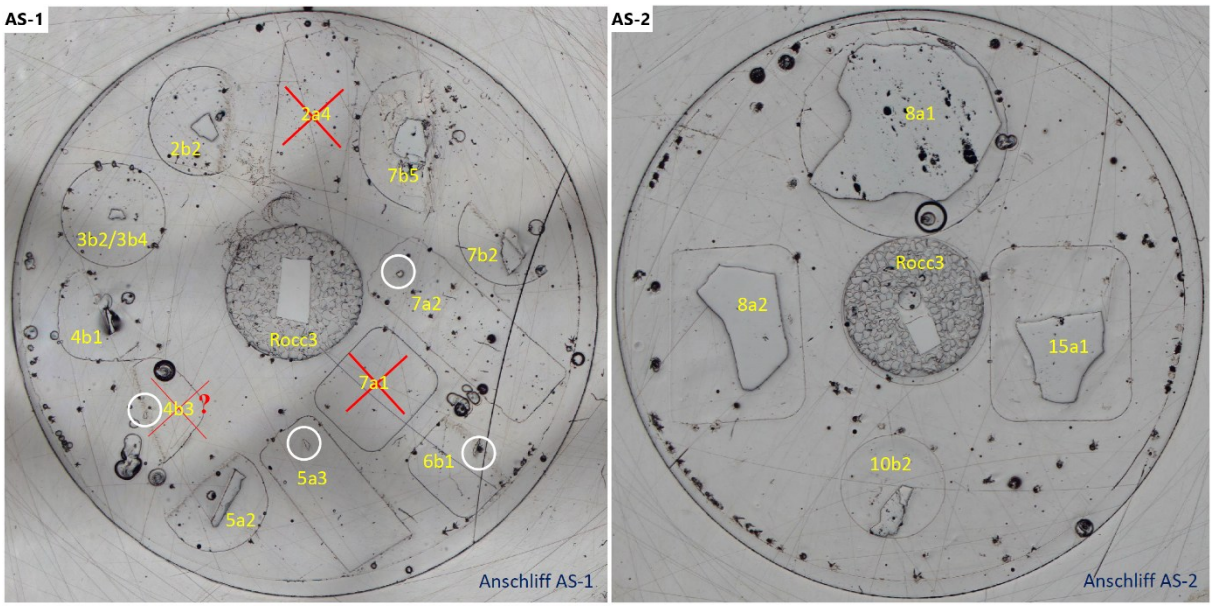


**Figure 8.1:** Photographic images of the mount [AS-2] containing sample 8a1, 8a2, 10b2 and 15a1 measured on the 15th and 16th February 2019. The other mount [AS-1] incorporates samples 2a4, 2b2, 3b2, 3b4, 4b1, 4b3, 5a2, 5a3, 6b1, 7a1, 7a2, 7b2 and 7b5 and was measured on the 19th and 20th February 2019. Crossed out samples represent those which were lost during preparation or did not contain obsidian shards.

Prior to analysis, test measurements produced count rates of 7000 counts per second, (cps) which translates to 15 minutes of analysis time per measurement to achieve a 1 per mil (1sd) uncertainty. All samples were stored in a dry oven before analyses and then mounted on one

of two sample holders, AS-1 and AS-2 (Figure 8.1): Mount AS-1, containing samples 2a4, 2b2, 3b2, 3b4, 4b1, 4b3, 5a2, 5a3, 6b1, 7a1, 7a2, 7b2 and 7b5, and mount AS-2, comprising samples 8a1, 8a2, 10b2 and 15a1. Measurements were taken at three spots for each AS-1 sample (Figure 8.1 AS-1), and five spots for each AS-2 sample (Figure 8.1 AS-2), targeting the homogeneous matrix of the obsidian glass to obtain averages for each shard. The analyses were carried out over two sessions (Figure 8.1): AS-2 samples were measured on the 15$^{th}$ and 16$^{th}$ February 2019, and AS-1 samples on the 19$^{th}$ and 20$^{th}$ February 2019. The sample identifiers used here are identical to those from the previously analyzed hydrogen isotopic system (see Chapter 6: Table 6.1), allowing for direct comparison between datasets. Samples which were lost during preparation or did not contain obsidian shards are crossed out in the pictures (Figure 8.1). As a calibration material, a rhyolitic glass (Rocc-3) from Roccastrada (Nord-Apennin, Italy) with a boron concentration of 561 ppm and a $\delta^{11}B$ of 5.9 ‰ ± 0.2 ‰ was utilized. This standard is from the same location and yields an identical $\delta^{11}B$ value as the standard GCA 67 published by Tonarini et al. (2003). Furthermore, the MPI-DING reference glass StHs6 (Jochum et al., 2006) was used to monitor analytical accuracy and potential systematic drift.

### 8.4 Modeling boron degassing trends with VolcDeGas

The simulations and resulting interpretations of best-fit degassing trends are based on the “VolcDeGas” program written in MatLab (Chapter 5) which has been validated for modeling of degassing in rhyolitic melts utilizing the hydrogen isotopic system (Chapter 5 - 7). For this work, the program has been updated as described in Section 2.2.2 to include the appropriate boron isotopic system formulae (Equation 8, 9). An in-depth description, a “how to use” guide, and a manual for the program´s original code can be found in the Chapter 5 and its Supplementary Material (use the download link). The modifications for the boron algorithm align closely with the existing hydrogen system workflows, diverging only in their terminology. Each button in the graphical user interface (GUI)—along with its clarifying tooltip displayed when hovering over it with the mouse—is intuitive and self-explanatory. A short summary of the updated program can also be found in the manual of this chapter (Section 8.8).

To operate the boron-specific part of the program, the user must first select $\delta^{11}B$ from the drop-down menu on the main Graphical User Interface (GUI) of “VolcDeGas.” Each button functions as described in the hydrogen system manual, except that there is no "speciation" button, and the temperature must be either known or estimated. For simulations based on the boron system, the user must input several key parameters, including:

- The initial boron concentration (= maximum boron concentration).
- Minimum and maximum boron concentrations and their interval (illustrating simulated degassing step size) over which the degassing trend has to be calculated.
- A range of initial $\delta^{11}B$ values (minimum, interval, maximum) to calculate different degassing trajectories (does not need to be known a priori).
- The temperature which must be specified based on available data or estimates.
- A preferred axis layout for graph visualization.
- A prepared excel sheet comprising boron concentrations and isotopic values for automatically best-fit calculations.

Natural data are inputted into the program via a prepared Excel sheet (refer to the manual in 8.8) containing boron concentration and isotopic data. Users are advised to adjust the most likely transition point (default: 55 ppm) to a value lower than the boron concentration of the most enriched sample if the automatic calculation mode is selected. VolcDeGas is then able to calculate several degassing histories and automatically determines the best-fit systems employing a minimum Root-Mean-Square-Error (RMSE), which quantifies the deviation between predicted and observed $\delta^{11}B$ values. Additionally, the program calculates the coefficient of determination ($R^2$), indicating the proportion of sample data variation explained by the simulated degassing model. All graphs are presented as $\delta^{11}B$ (in ‰) versus boron concentration (in ppm).

## 8.5 Results

In the following subsections, existing boron isotope data from Long Valley (Schmitt and Simon, 2004) are re-analyzed by examining each eruption individually. This approach contrasts with the original analysis by Schmitt and Simon (2004), in which eruptions were assessed collectively. By treating eruptions separately, this study aims to discover eruption-specific trends that may have been obscured in the aggregated dataset. The Long Valley data are furthermore studied using VolcDeGas to identify potential degassing trends, which are assessed from higher to lower concentrations. This pattern aligns with the chronological sequence of the degassing process, in which volatiles are lost over the course of degassing (Chapters 1.6 and 2.2). Subsequently, measured boron data of the BGM eruption are analyzed together with existing datasets of the hydrogen isotopic system. Finally, a theoretical model, based on natural parameters, is generated by VolcDeGas, and then interpreted.

### 8.5.1 Re-analysis of published boron data from Long Valley

In their study, Schmitt and Simon (2004), measured boron concentrations and isotopic compositions on numerous samples of several eruptions within the Long Valley complex, California, USA, using Secondary Ionization Mass Spectrometry (SIMS) and Positive Thermal Ionization Mass Spectrometry (PTIMS). However, the dataset was interpreted as a whole, without separating out individual eruptions. To address this issue, this work re-examines the geochemical data of the eruptions independently. This revised approach seeks to identify apparent degassing patterns that may have been overlooked when the eruptions were previously analyzed collectively.

Among the diverse eruptions investigated (Figures 8.2 and 8.3), only the South Deadman Creek eruption (Figure 8.3, Figure 8.2F) provided data from both quartz-hosted melt inclusions and matrix glasses (lava). This paired dataset captures a more complete record of the degassing process, as melt inclusions are associated with early-stage magma storage and initial degassing, while lavas reflect the late-stage ascent and eruption of the magma. For the Deer Mountain, Early Bishop Tuff, and Late Bishop Tuff eruptions (Figure 8.2C, D, E), boron isotope data are limited to quartz-hosted melt inclusions, whereas for the Older and Younger Glass Mountain eruptions (Figure 8.2 A, B), data are derived exclusively from matrix glass of lava samples.

Separate analyses of the melt inclusions (8.2C-E) reveal a boron concentration range of 50 ppm (42 - 92 ppm) and an isotopic variation of 7.2 ‰ in $\delta^{11}B$ (i.e., 0.3 - 7.5 ‰). In contrast, the South Deadman melt inclusions (Figure 8.2F) span over 36 ppm (39 - 75 ppm) and 4.3 ‰ in $\delta^{11}B$ (-0.5 - 3.8 ‰). The matrix glasses (Figure 8.2A, B) demonstrate a wider boron concentration range of 69 ppm (47 - 116 ppm) and boron isotopic values spanning over 7.4 ‰ (2.9 - 10.3 ‰), whereas South Deadman matrix glass samples contain a boron concentration variance of only 5 ppm (25 - 30 ppm) and an isotopic shift of up to ~3.7 ‰ in $\delta^{11}B$ (3.8 - 7.5 ‰). Interestingly, the boron concentrations in matrix glasses from lava samples often overlap with those in quartz-hosted melt inclusions, despite these two sample types representing distinct stages of magma degassing. In some cases, the minimum concentration in the matrix glasses even exceeds that of the melt inclusions.

Four Mono Craters samples were additionally analyzed in relation to D/H data and $H_2O$ content. The δD variance of these samples was detected as 50 ‰, associated with a nearly eight-fold depletion in $H_2O$ (0.72 - 0.1 wt.%). In contrast, $\delta^{11}B$ (2.6 - 3.9 ‰) and boron content (32 - 35 ppm) remained consistent within error margins (Schmitt and Simon, 2004).

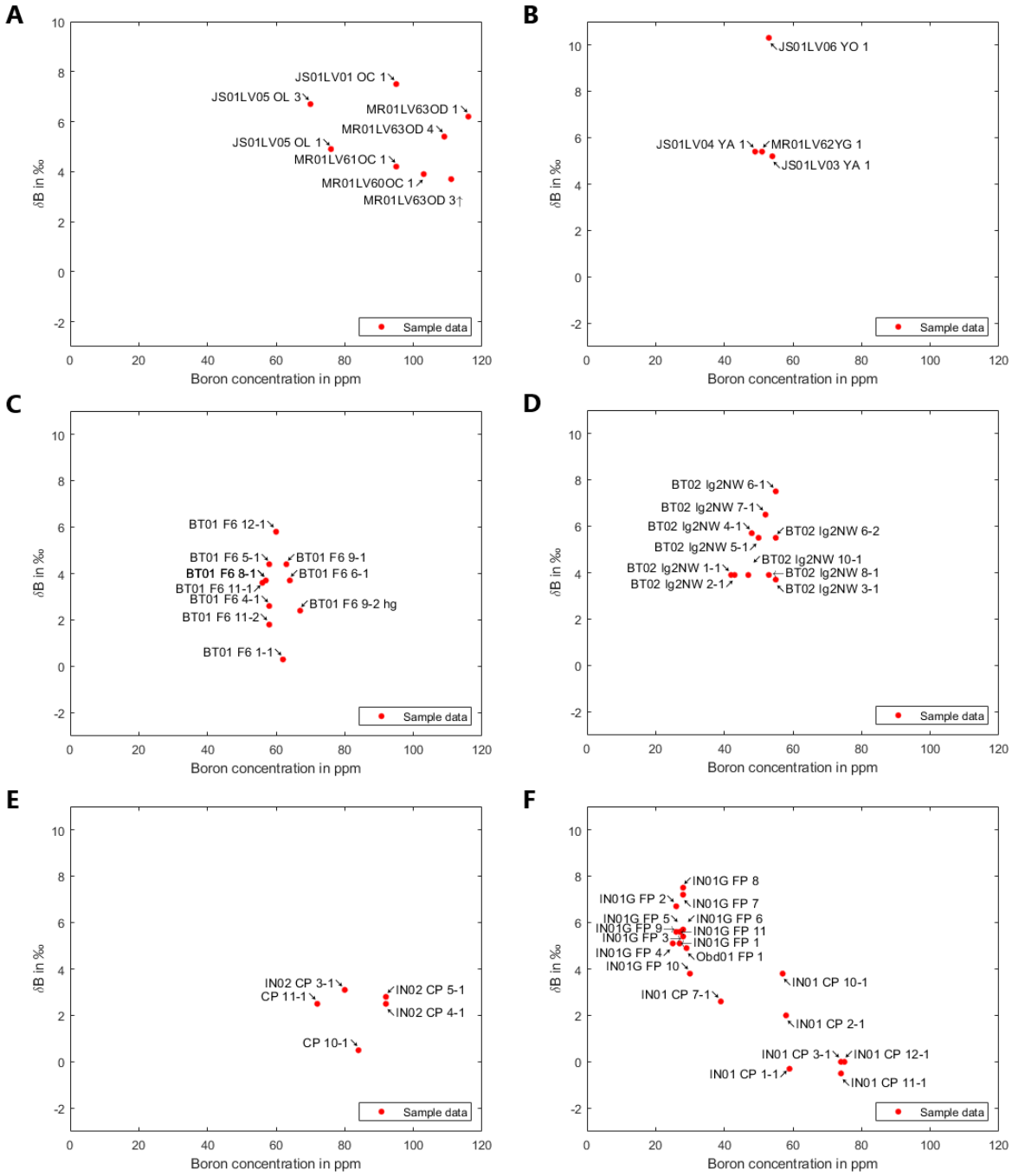


**Figure 8.2:** Plots presenting $\delta^{11}B$ (‰) and boron concentration (ppm) for individual eruptions in Long Valley, based on data from Schmitt and Simon (2004). Red dots portray the sample data points. Each sample is labeled with its appropriate tag. Frame [A] displays Older Mountain Glass matrix glass samples, [B] exhibits Younger Mountain Glass matrix glass samples, [C] and [D] depict Early and Late Bishop Tuff melt inclusions, respectively, whereas [E] represents Deer Mountain melt inclusions. Frame [F] includes South Deadman Creek samples, being the only eruption with a complete coherent trend containing both melt inclusions and matrix glasses (IN01 = melt inclusions; IN01G = matrix glasses)

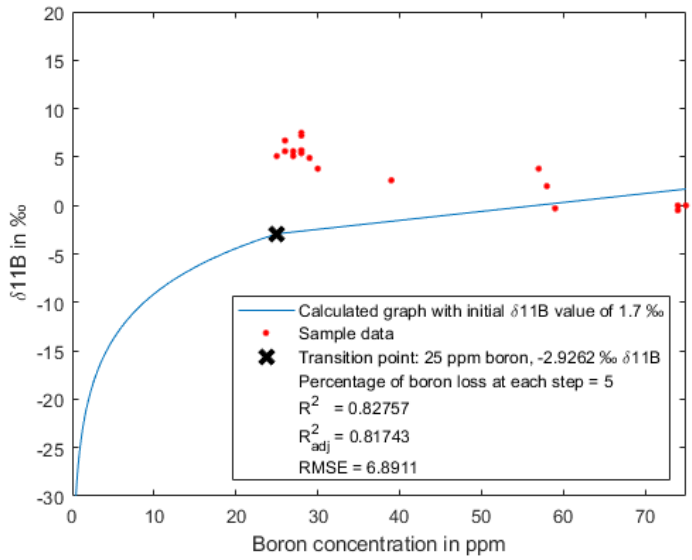


**Figure 8.3:** Best-fit VolcDeGas simulation of literature data from South Deadman Creek (Schmitt and Simon, 2004). The data points, exemplified as red dots, are based on $\delta^{11}B$ (‰) and boron concentration (ppm). The simulation illustrates a best-fit closed-to-batched degassing model with a variable step size, which was established to associate most closely with the hydrogen data of several other eruptions (Chapters 5 - 7). The initial boron concentration of this model is set at 75 ppm, which is the highest value observed in South Deadman Creek samples. The VolcDeGas program iteratively calculates the best-fit degassing system (blue curve) by utilizing minimum RMSE with variables such as initial $\delta^{11}B$ values and boron content, step size and natural data. The lower right box informs about the goodness-of-fit factors, transition points, initial $\delta^{11}B$ values, and boron loss percentages at each step.

Generally, $\delta^{11}B$ versus boron concentration trends portrayed in Figure 8.2 reveal significantly scattered data, hindering the extraction of meaningful results. An exception is the South Deadman Creek data (Figures 8.2F and 8.3), displaying an increasing $\delta^{11}B$ trajectory as the boron content is reduced. Other trends suggest neutral (Figure 8.2B, C), increasing (Figure 8.2A), or decreasing (Figure 8.2D, E) trajectories, with the caveat that such interpretations are speculative due to the highly dispersed data. Notably, the weak trends or outright scatter observed in the quartz-hosted melt inclusions (Figure 8.2C, D, E, F) contrast with the typical composition of melt inclusions, which generally trap pre-eruptive volatile species (e.g., Carroll and Holloway, 1994). As a result, melt inclusions are typically limited to elevated concentrations of these species (e.g., water or boron).

The overall best-fit degassing model to data of South Deadman Creek was computed by VolcDeGas and is presented in Figure 8.3. It involves a closed-to-batched system with variable step size, a system deemed highly effective for representing degassing behavior (see Chapters 5 - 7). Variables employed in VolcDeGas' calculations include an initial $\delta^{11}B$ range of -10 to +10 ‰ and an initial boron concentration of 75 ppm—corresponding to the sample with the highest concentration—with step sizes of 0.1 ppm, and a temperature of 810 °C. This

temperature is based on Fe-Ti oxide thermometry from melt inclusions of lavas (Vogel et al., 1989). As demonstrated in Figure 8.3, the observed trend outlined by the natural samples increases and is inverse to the ideal modeled degassing trend, which should inherently decrease as the remaining melt is successively depleted in both boron concentration and $^{11}B$ (Chapter 2.2). This incompatible fit is confirmed by the poor RMSE of 6.9.

### 8.5.2 Results of Big Glass Mountain boron measurements

The summarized sample data of the boron measurements are portrayed in Table 8.1 and visualized in Figure 8.4. Sample 7a2 (Figure 8.1 AS-1) was excluded owing to its low boron concentration, resulting in highly variable isotopic values possibly stemming from non-volcanic processes (e.g., environmental dust). The boron isotopic values of the remaining samples range from -5.1 ‰ to -3 ‰ of $\delta^{11}B$, while concentrations vary between 28.3 ppm to 31.7 ppm (Table 8.1).

As shown in Figure 8.4, the natural data present significant scatter and do not produce any consistent trend over the limited boron concentration range, which prevents the extraction of robust results. This is objectively supported by a linear regression model generated with MATLAB, which yields a nearly horizontal trend line and very low coefficients of determination ($R^2$ = 0.027 and $R^2_{adj}$ = -0.062), confirming the absence of any statistically significant pattern in the data. As an alternative approach, a direct comparison was made between the boron and hydrogen isotopic system. Accordingly, Figure 8.5 plots boron against water concentrations, while Figure 8.6 compares the isotopic signatures of boron with hydrogen. Since boron and hydrogen measurements are based on the same samples, a linear correlation would be anticipated if degassing were the primary driver of isotopic and concentration shifts within the boron system. This expectation is grounded on the established clear degassing trend in the hydrogen system (see Chapter 6).

To objectively evaluate correlations, in both figures (Figures 8.5 and 8.6) MatLab's own linear regression functions were applied providing the coefficient of determination ($R^2$) and adjusted coefficient of determination ($R^2_{adj}$) which are the most suitable factors for direct correlations between two datasets. In Figure 8.5, representing the boron vs. water concentrations, the coefficient of determination is very low ($R^2$ = 0.21; $R^2_{adj}$ = 0.14), which indicates that no significant correlation exists. This shows that boron loss did not occur continuously over the presumed degassing interval, contrary to the established boron degassing hypothesis (see Chapter 2.2), where volatiles are progressively lost from the melt. The relationship between the hydrogen and boron isotopic signature is even weaker with a $R^2$ of 0.016 and $R^2_{adj}$ of -0.073

(Figure 8.6). That negative adjusted coefficient of determination directly indicates that the explanatory variables lack statistical significance.

A best-fit degassing computation using “VolcDeGas” was not performed, as the high degree of data scatter, minimal variation over the assumed degassing path, and absence of a coherent trend rendered such a model infeasible. In summary, the natural data show no systematic relationship between boron concentration and $\delta^{11}B$, nor any correlation with the hydrogen isotopic system—which traces a coherent degassing history.

**Table 8.1:** Summary of boron concentration and $\delta^{11}B$ measurements obtained via SIMS for Big Glass Mountain obsidian samples (California, USA). Each value represents an average of several measurements conducted on individual homogeneous glass samples. The standard error of the mean (1 sm) is reported for both concentration and isotopic values.

| Sample name | B [ppm] | δB [‰] | 1 sm B [ppm] | 1 sm δB [‰] |
|---|---|---|---|---|
| 2b2 | 31.5 | -3.3 | 0.2 | 1.1 |
| 3b2/3b4 | 28.3 | -4.9 | 0.4 | 0.6 |
| 4b1 | 31.4 | -5.0 | 0.0 | 0.2 |
| 4b3 | 31.4 | -5.1 | 0.2 | 0.3 |
| 5a2 | 31.3 | -3.0 | 0.0 | 0.7 |
| 5a3 | 31.4 | -3.4 | 0.0 | 0.4 |
| 6b1 | 31.7 | -4.3 | 0.1 | 0.6 |
| 7b2 | 28.6 | -3.5 | 0.7 | 0.7 |
| 7b5 | 28.9 | -4.5 | 0.1 | 0.7 |
| 8a1 | 30.7 | -3.5 | 0.0 | 0.4 |
| 8a2 | 30.7 | -4.2 | 0.0 | 0.5 |
| 10b2 | 29.9 | -3.7 | 0.3 | 0.5 |
| 15a1 | 30.9 | -3.6 | 0.2 | 0.3 |

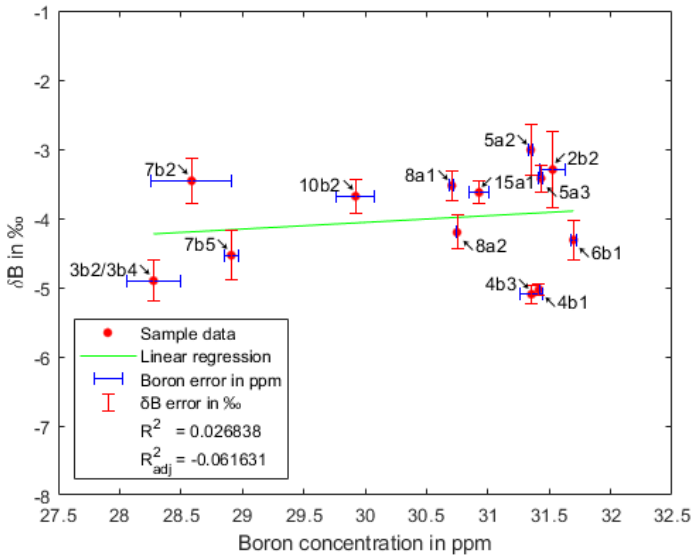


**Figure 8.4:** Graph of $\delta^{11}B$ (‰) vs. boron concentration (ppm) for Big Glass Mountain obsidian samples. Red dots represent SIMS data for individual samples. Blue error bars indicate the analytical uncertainty in boron concentration (ppm), while red error bars specify uncertainty in $\delta^{11}B$ (‰). Each sample is labeled with its identifier, and arrows indicate the corresponding data points. A linear regression calculated by MatLab, is displayed as a green line with the formula: y= -6.9619 + 0.096765 x. $R^2$ (0.027) and $R^2_{adj}$ (-0.062), are presented in the lower-left box.

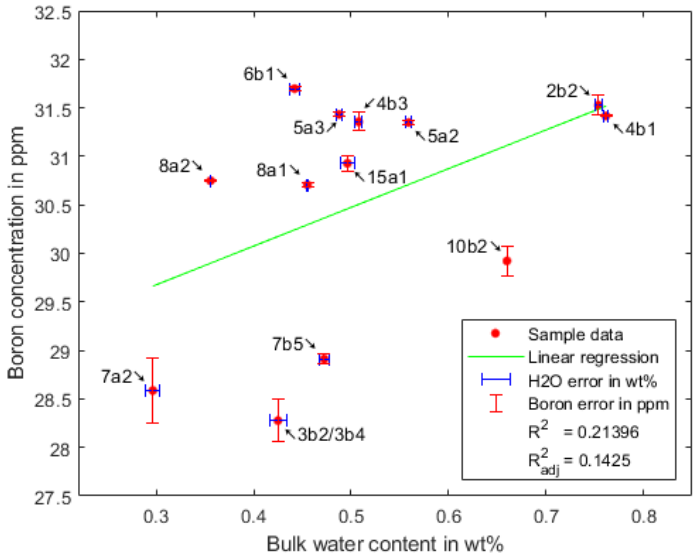


**Figure 8.5:** Plot exhibiting boron concentration (ppm) versus water content (wt.%) for Big Glass Mountain samples, illustrating their relationship. Boron concentrations were analyzed by SIMS, while water contents were obtained from previous FTIR measurements on the same samples (Chapter 6). Red dots represent distinct samples, with their identifying numbers attached in the diagram. Blue error bars specify FTIR uncertainty in water content, and red error bars indicate SIMS uncertainty in boron concentration. A linear regression calculated by MATLAB, is presented as a green line with the equation: y = 28.48 + 3.99 x. The $R^2$ (~0.21) and adjusted $R^2$ (~0.14), exposing the strength of correlation, are displayed in the lower-right box.

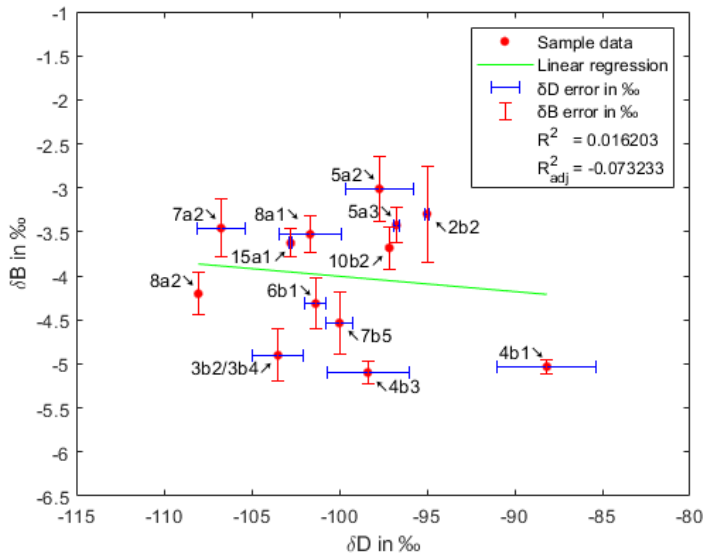


**Figure 8.6:** Graph depicting $\delta^{11}B$ (‰) versus δD (‰) for Big Glass Mountain samples, combining measurements from this chapter and of Chapter 6, respectively. Red dots represent individual sample data. Blue error bars exhibit TCEA measurement uncertainty in δD, while red error bars show SIMS uncertainty in $\delta^{11}B$. Each sample is labeled with its identifier. A linear regression calculated in MATLAB is plotted as a green line, with the formula: y = -5.742 - 0.017 x. The $R^2$ (0.016) and $R^2_{adj}$ (-0.073), are shown in the upper-right box.

### 8.5.3 Theoretical degassing models based on natural parameters

For comparison to natural systems, a theoretically simulated degassing trend for a one-stage open system ($\delta^{11}B$ vs. boron concentration), modeled with VolcDeGas, is illustrated in Figure 8.7. This simulation showcases one of the maximum possible isotopic shifts a boron system could theoretically achieve during degassing. Here, the interval was set to 0.01 ppm, the initial $\delta^{11}B$ value to 5 ‰ and the initial boron concentration to 100 ppm, which is the average of maximum concentrations reported by Schmitt and Simon (2004). The temperature is set as 800°C which is well within the temperature range of natural rhyolitic systems.

The modeled trend in Figure 8.7 is based solely on an idealized degassing formula and results in near-complete boron depletion. It displays a slight negative slope early in the degassing process and a later exponential steeper decline toward lower boron concentrations. This degassing behavior aligns with expectations for open systems involving a fluid/melt fractionation factor of over 1. The maximum isotopic variation generated in this model is approximately 60 ‰ $\delta^{11}B$ across the 100-ppm boron concentration range, and extending to a minimum boron concentration of about 0.1 ppm. This differs notably with the over 300 ‰ δD variation detected in hydrogen systems (refer to Chapter 5).

Given that boron concentrations in the analyzed samples never decrease below ~20 ppm, equivalent to 20 % of the initial boron content, the expected isotopic variations in natural degassing systems would amount to only ~11 ‰ of $\delta^{11}B$ within the 20 - 100 ppm range. In contrast, most natural hydrogen isotope systems undergo near-complete degassing, with $H_2O$ contents dropping down to ~0.05 wt.% from initial ~4 wt.% (e.g., Newman et al., 1988; Taylor, 1991; Cabrera et al., 2015; Shields et al., 2016), leaving only 1.25 % of its primary water content remaining in the melt (Chapters 6 and 7). Thus, the initial water content in natural rhyolitic systems is 400 times higher than that of boron. These results suggest that boron isotopic shifts associated with degassing appear to be minor in natural volcanic systems, particularly in comparison to the much larger fractionation observed in hydrogen isotopic systems.

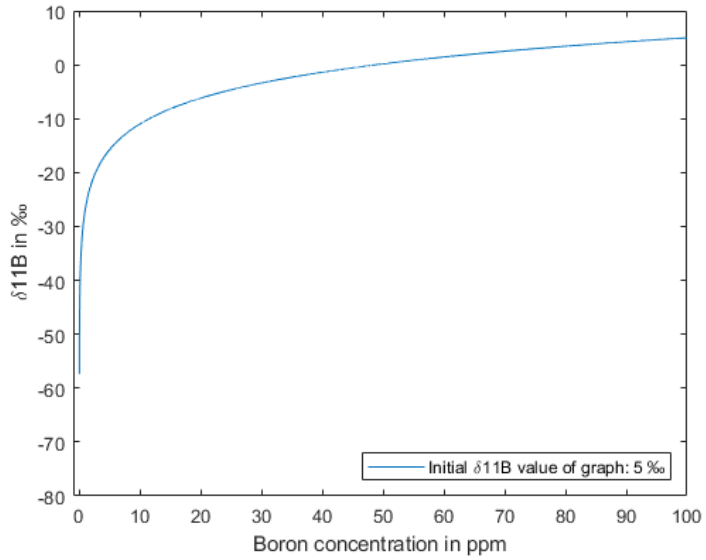


**Figure 8.7:** Modeled graph portraying $\delta^{11}B$ (‰) versus boron concentration (ppm), revealing the maximum possible isotopic fractionation of boron during degassing in rhyolitic melts. The blue curve represents a one-stage open-system degassing scenario, calculated by using the manual computation mode of VolcDeGas. The initial $\delta^{11}B$ is set at 5 ‰, and the initial boron concentration is estimated at 100 ppm, approximating an average of the highest concentrations observed in Long Valley samples (Schmitt and Simon, 2004).

## 8.6 Discussion

This section evaluates whether boron isotopes can trace syn-eruptive degassing processes in rhyolitic magmas. By interpreting theoretical degassing models, best-fit models to published data of Long Valley (Schmitt and Simon, 2004), and new data of the 1060 CE Big Glass Mountain eruption, California, the discussion explores the role of degassing in influencing boron systematics. It also considers whether other processes, such as crustal assimilation, magma mixing, or diffusion, may dominate boron concentration and isotopic shifts in natural settings.

As described in Chapter 2.2, boron is expected to fractionate during degassing—that is, as degassing progresses, boron and $^{11}B$ are successively lost from the melt, while the co-existing fluid phase becomes enriched in them. This expectation is primarily based on experimental results from Hervig et al. (2002) and Maner and London (2018). The following discussion therefore interprets the natural datasets in light of this fractionation hypothesis.

### 8.6.1 Long Valley data re-evaluation

Re-analyses of individual Long Valley eruptions via published boron isotope datasets (Schmitt and Simon, 2004), and best-fit models generated with VolcDeGas, reveal no evidence of boron isotope fractionation due to degassing (Figures 8.2 and 8.3). All eruptions, except for the South Deadman Creek eruption, demonstrate highly scattered data that prevent the identification of any coherent trend (Figure 8.2). Although the South Deadman Creek samples exhibit a clear pattern, the trend is inverse to that of the theoretical degassing model, thereby suggesting a non-degassing origin (Figure 8.3).

The results indicate that degassing is not the primary process controlling the observed boron isotopic shifts. That interpretation is supported by overlapping boron concentrations and $\delta^{11}B$ values between quartz-hosted melt inclusions and matrix glasses, as well as by high internal variability within melt inclusions. If degassing were the dominant factor driving boron shifts, it would be expected that melt inclusions—representing early degassing stages—retain higher boron concentrations and $\delta^{11}B$ values than degassed matrix glasses. Ideally, melt inclusions should also demonstrate limited variation in their data. This, in turn, implies that additional boron may have been incorporated into the melt at a later stage in the degassing history, creating a misleading impression that late-stage degassed samples resemble early-stage ones due to added boron. The absence of the predicted degassing patterns suggests that the boron record has been overprinted, and the chronological order of degassing may have been disrupted by other processes such as injection of mafic magma.

Additional insight into boron degassing behavior is obtained by samples from Mono Craters, where $\delta D$ and $H_2O$ contents were analyzed together with $\delta^{11}B$ and boron concentrations (Schmitt & Simon, 2004). Even though the dataset is limited to four samples, Schmitt and Simon (2004) still observed noticeable degassing-related variations in the hydrogen isotopic system, with $\delta D$ varying by 50 ‰ across a range of 0.72 to 0.1 wt.% $H_2O$. In contrast, they found no analogous degassing pattern in the boron isotopic system, where the data remained constant within analytical uncertainties. This discrepancy in behavior between hydrogen and

boron in the same samples provides further support for the conclusion that degassing is not a major factor affecting boron isotope systematics at Long Valley (Schmitt and Simon, 2004).

Several non-degassing related processes may likely explain the observed boron variations and lack of correlations. These include the injection of less evolved, mafic magma, and/or inheritance of slab-derived fluids into the rhyolitic reservoirs, prompting boron uptake and modification of the original magmatic isotopic signature. Other processes are the assimilation or partial melting of crustal rocks, both of which can be triggered by hot magma recharge. For instance, hydrothermally altered rocks, which are depleted in boron and $^{11}B$ due to preferential partitioning into the hydrous phase (e.g., Spivack and Edmond, 1987; Palmer and Swihart, 1996; Hervig et al., 2002; Schmitt and Simon, 2004), could fully melt and transfer this depleted signature into the melt. Conversely, partial melting of hydrothermally altered or other crustal rocks increases boron content and $^{11}B$ in the melt, since boron is generally incompatible in most silicate minerals (Schmitt and Simon, 2004).

Notably, Schmitt and Simon (2004) specifically proposed that the detected variations in $\delta^{11}B$ reflect assimilation of hydrothermally altered rocks following fresh rhyolite magma recharge. Although the present thesis implements a different methodological approach—i.e., here I have analyzed each eruption separately rather than treating all eruptions as an amalgam for elucidating degassing history (Schmitt and Simon, 2004)—it supports the plausibility of this hydrothermal assimilation scenario. Furthermore, while a magma injection process cannot be ruled out, the influence of subduction-related slab-derived fluids appears unlikely at Long Valley, due to the fact that this volcanic complex appears unrelated to an active subduction zone margin.

In summary, the re-evaluation of Long Valley data, supported by VolcDeGas best-fit modeling, indicates no compelling evidence for noticeable degassing-induced fractionation of boron isotopes. Instead, the boron isotopic composition in samples appears to reflect the effects of processes such as assimilation or possibly mafic magma interaction.

### 8.6.2 Big Glass Mountain boron data and correlation to hydrogen isotopes

This study measured $\delta^{11}B$ values and boron concentrations in glass samples from Big Glass Mountain (BGM). The results reveal that $\delta^{11}B$ values (-5.1 ‰ to -3 ‰) scatter across a narrow boron concentration range (28.3 ppm to 31.7 ppm), with no discernible trend. However, comparing this dataset to hydrogen isotope data measured on the same samples (Chapter 6), allows us to extract important information. Figures 8.6 and 8.7 reveal no correlation between

the boron and hydrogen systems. Given the strong degassing trend observed in the hydrogen system (Chapter 6), a corresponding pattern in the boron system would be anticipated if degassing significantly affected BGM's boron composition, but this is not observed. The characteristic volatile loss and isotopic fractionation associated with degassing appear to be absent—or at least obscured—in the samples.

The observed scatter in the boron isotopic system likely stems from the same factors discussed in Subsection 8.6.1. Mafic magma injection and mixing with rhyolitic melt could explain the data variability, a process which evidently occurred during the eruption of BGM (Donnelly-Nolan et al., 2016). In particular, injection during degassing could have prompted boron uptake into the melt together with isotopic mixing. Moreover, the addition of boron from slab-derived fluids with high boron contents and diverse $\delta^{11}B$ values remains plausible in light of the influence of the Cascadia Subduction Zone on the formation of Medicine Lake Volcano (e.g., Donnelly-Nolan et al., 2016). Such fluids are common in arc settings and could increase the melt's boron concentration while modifying its isotopic signature toward either higher or lower $\delta^{11}B$ values, depending primarily on the depth of fluid release from the subducting slab (e.g., Noll et al., 1996; Rosner et al., 2003; Savov et al., 2009; Pabst et al., 2012). That factor may be specifically relevant during the late stage of degassing, when the emptying magma chamber was being recharged. This scenario is particularly plausible, as "the presence of hydrous calcalkaline mafic lavas at MLV indicates that subduction-related processes (for example, slab fluids) operated to generate magmas like those erupted in late Holocene time" (Donnelly-Nolan et al., 2016).

The findings for BGM indicate that degassing did not significantly affect the boron isotopic system, reinforcing similar observations drawn from Long Valley rhyolites. Instead, the detected variations in boron concentrations and isotopic scatter are probably better explained by the combined effects of mafic magma injection, slab-derived fluids, and assimilation or partial melting. These processes appear to be the dominant factors responsible for the boron systematics at BGM.

### 8.6.3 Constraints on boron degassing: from theory to natural systems

To quantify the theoretical potential of boron isotope fractionation during degassing, an open-system degassing model (Figure 8.7) was generated with VolcDeGas over a concentration range between 0.1 and 100 ppm. This model predicts a maximum isotopic shift of 60 ‰, but only about 11 ‰ over the range of boron contents observed in natural rhyolitic systems (20 – 100 ppm), even under idealized conditions. In comparison, hydrogen isotopes generally exhibit

much more pronounced fractionations exceeding 300 ‰ of δD, as water contents drop from ~4 wt.% to ~0.05 wt.% during degassing, leaving only ~1.25% of the initial water content in the melt (Chapters 6 and 7). Because boron occurs at far lower initial concentrations (~400 times lower than water) it lacks the buffering capacity—i.e., the resistance to concentration and isotopic changes—of the hydrogen system. Therefore, the boron system is more susceptible than the hydrogen system to overprinting of its concentration and isotopic composition by processes such as crustal assimilation.

In addition to aforementioned processes like assimilation of crustal material or magma injection, other time-dependent and eruption related processes can lead to arrested or restricted equilibrium in boron's response to degassing. For example, a central—and potentially critical—factor affecting degassing characteristics are the slow diffusion rates of boron in rhyolitic melts (Section 2.2.1), as assessed by Spallanzani et al. (2022). These slow diffusion rates lead to prolonged timescales required for complete boron homogenization, that is the diffusion-driven "evening out" of concentration and isotopic gradients within the melt (Spallanzani et al., 2022). The homogenization time represents the "maximum time where any diffusion profiles may be retained and modelled" (Spallanzani et al., 2022), which in this context also includes the exsolution timeframe of boron during degassing (Spallanzani et al., 2022). This slow diffusion may result in retention of boron, specifically in degassed melts with lower water content and low decompression rates, where diffusion is even further reduced. Under such conditions boron may not exsolve efficiently and rapidly enough from the melt, limiting noticeable syn-eruptive, degassing-related fractionation effects in the boron isotopic system. Consequently, the duration of eruptive processes like magma ascent and decompression may be too short relative to boron diffusion timescales to produce substantial shifts in boron concentration and isotopic composition in preserved samples.

Another diffusion-related complication arises from the nature of the fractionation experiments used to determine the boron fractionation factor. The experiments conducted by Hervig et al. (2002) and Maner and London (2018)—whose alpha values were employed in this work—required equilibrium conditions. In the study by Maner and London (2018), the experiments were carried out over extended durations of 30 days (at 700-800°C), employing starting materials containing high water contents (~7 wt.%) and boron concentrations (2.5 and 5 wt.%). Under such controlled conditions, the inhibitory effects of slow boron diffusion—likely present in natural eruptive systems—may not have played a role thus resulting in a disconnect between experiments and nature.

In light of these insights, the natural boron concentration and isotopic data presented in the previous subsections can be further interpreted. As shown, the Long Valley and BGM boron data do not exhibit evidence of any influence of degassing, although such an effect is expected based on previous experimental studies (Hervig et al., 2002; Maner and London, 2018). While the theoretical simulations conducted in this section support the potential for boron isotope fractionation during degassing (Figure 8.7), they concurrently expose that such shifts are likely minimal (i.e., <11‰ $\delta^{11}B$) under natural conditions. In relation to the analyzed samples, this suggests that any subtle degassing-related isotopic shift may have been overprinted by processes already identified in earlier subsections. More importantly, the very slow diffusion of boron in rhyolitic melts may have limited—or nearly entirely prevented—degassing and associated isotopic fractionation over the timescale of the eruptions. As a result, these samples may have captured little to no record of degassing in the boron isotopic system and instead reflect the influence of non-degassing processes. In summary, the combined effects of inherently limited theoretical fractionation and diffusion-related inhibition likely prevented the boron system from tracking a discernible degassing pattern. Consequently, non-degassing processes remain the more plausible explanation for the variations observed in the natural boron data (e.g., crustal assimilation, injection of fresh magma and/or subduction-related fluids).

## 8.7 Conclusion

Detailed analyses of the BGM boron data obtained in this work, along with published Long Valley data (Schmitt and Simon, 2004), provide no compelling evidence for a detectable degassing history in the boron isotopic system, nor for degassing-induced variations in $\delta^{11}B$ and boron concentration. No correlation was detected between the hydrogen isotopic system—which records a comprehensive degassing history—and the boron isotopic system, despite both being measured on identical samples. Furthermore, theoretical modeling predicts only minor isotopic shifts from degassing when applying realistic parameters, while slow diffusion rates likely inhibit boron degassing during eruption altogether. These lines of evidence support the interpretation that the boron system remains largely unaffected by syn-eruptive degassing.

Instead, observed boron variations are primarily attributed to non-degassing processes. At BGM, these likely include the injection of mafic magma or subduction-related fluids, and possible crustal assimilation. At Long Valley, injection of mafic magma, and more specifically, the assimilation of hydrothermally altered rocks are plausible mechanisms. At both eruptive

complexes, the pre-eruptive signature of boron appears to be primarily preserved during degassing.

The perhaps most crucial factor controlling degassing behavior in the boron system is diffusion. The slow diffusion of boron in rhyolitic melts may inhibit effective degassing and isotopic fractionation over the timescale of an eruption. This limitation prevents the boron isotopic system from serving as a reliable tracer in studies of degassing during silicic eruptions.

## 8.8 Manual (boron)

This boron manual is based on the published program code of ”VolcDeGas: A program for modeling hydrogen isotope fractionation during degassing of rhyolitic melts” (Chapter 5) in Walter and Castro (2020), and is updated to include the boron isotopic system.

VolcDeGas was developed in MATLAB R2018a/b and is fully downwards compatible with MATLAB versions as early as R2012a. It requires the Signal Processing Toolbox as well as the Statistics and Machine Learning Toolbox. However, the compiled self-installer version does not require MATLAB and can run independently (Windows systems only).

The following files are necessary for running the program:

VolcDeGas.m
VolcDeGas.fig
VolcDeGasopion.m
VolcDeGasopion.fig

These files should be stored in a folder which is accessible by MATLAB (or added to the MATLAB path). The program can be launched by typing VolcDeGas in the MATLAB command window. Windows users can alternatively execute the compiled version by running VolcDeGas.exe. The download link for all files is: https://github.com/swalte0111/VolcDeGas-2.0-Hydrogen-and-Boron-.git

### 8.8.1 Code overview

VolcDeGas provides a user-friendly Graphical User Interface (GUI) to simply import datasets and modify parameters for analyzing degassing systems. The GUI includes buttons and fields with illuminating tooltips that direct the users through the programs functions and provide

additional guidance. Users can calculate one- and two-stage degassing histories either manually “by-hand” or automatically. The automatic mode establishes the best-fit degassing scenario by minimizing the Root-Mean-Square-Error (RMSE) between calculated degassing trends and natural data.

Users are advised to set broad parameter ranges, particularly for initial δD values, which control the generation of parallel graphs (e.g., -80 ‰ to -20 ‰ with a 1 ‰ interval) to ensure a wide range of modeled degassing histories. Extensive testing on rhyolitic systems has demonstrated excellent performance of the program, specifically in automatically identification of the best-matching degassing histories.

### 8.8.2 Usage instructions and input

The user must first select the isotopic system of interest (δD or δB) by clicking on the corresponding button in the top left of the GUI. Although the basic calculations for hydrogen and boron isotopic systems are similar, their terminology differs a bit. Therefore, the following paragraphs explain the usage of both systems.

It is important to clear the workspace by invoking the "Clear workspace for next run" button and closing all open figures, before initiating a new calculation. This step is particularly important when utilizing different step sizes or when switching between systems employing variable step sizes and systems which use fixed steps. For two-stage manual calculations, the workspace should only be cleared after completing the second-stage calculations, and other processes such as exporting of the calculated data to excel or making layout adjustments like font size changes.

The program is written in a user-friendly manner. That is that guidelines are provided to the user through tooltips that appear when hovering over buttons and fields, as well as via error messages. These features help to prevent mistakes, such as missing input variables or an incorrect sequence of controls. Conditional checks by if-loops and safeguards inserted in the code also mitigate the risk of crashes. For extensive computations which can be time-consuming and depend on the computer’s speed, a progress bar is displayed to inform about the program's status, signaling that the process is ongoing.

For any hydrogen system analysis, whether automatically or manual, it is generally advised that additional water speciation data is employed to calculate improved alpha factors. This data is imported by invoking the button “Input own speciation values …”, with an excel sheet, where

the first row of the sheet should contain the total water content in weight percent (wt.%), and the second row should list the molecular water content in wt.%. For boron system analyses, speciation data is not required, as these calculations rely solely on temperature input and are unrelated to concentration changes. When inputting natural δD or δB data by pressing the button: “Input excel”, the Excel sheet's first row must include bulk water content in wt.% or boron concentration in ppm, while the second row must contain the corresponding δD or δB values. This procedure is also a requirement for every automated calculation. In case the user applies speciation data to the hydrogen system, the alpha factor (α-factor) is calculated without reference to temperature, but the temperature field must still be filled with a placeholder value to ensure proper execution.

The program also accounts for specific constraints in the calculation process such as dividing by 0. For instance, if the final bulk water or boron content field (tagged with “From”) is set to 0, the program automatically replaces this value with one close to zero (0.00001) to prevent errors. Users are instructed to set the field to 0, as this yields accurate results without significantly increasing processing times.

The step size is another necessary parameter whereby changes in the step size interval have no effect on closed-system, and minimal effect open-system calculations. As excessively large step sizes can produce jagged, and less smooth graphs, users are encouraged to use smaller step sizes, such as 0.001 for water and 0.1 for boron to produce high resolution graphs, especially when employing automatic best-fit calculations. The batched system with variable step size dynamically adjusts step sizes during calculations, so the manual and fixed input values are not considered in this system. The batched system with constant step size, is the sole system heavily influenced by the selection of the step size interval.

In two-stage degassing systems, and for automatically computations, the transition point must be specified to account for closed-system limits. A pre-set value is applied in the program which is a rough estimate of the average transition point values based on past works. However, the suggested transition point, entered in the "Set most likely transition point" field, should always be lower than the highest natural data value. The program first calculates the best-fit closed-system trend up to the specified most likely transition point. It then determines the best-matching transition point along this closed-system trajectory for each two-stage system configuration. If the natural data is limited or scarce, a manual identification of the best-fit system may be required. This can be accomplished with the second GUI, "VolcDeGasopions," which provides supplementary features for manual adjustments, second stage calculations, data exportation, and layout customization.

By following these guidelines and employing the program's default values where applicable, users can accomplish optimal performance and correctness across various systems. In case of any unexpected behavior or program crashes, pressing "Clear workspace for next run" and closing all open figures will resolve most problems effectively.

# Chapter 9
# Conclusions and outlook

The primary aim of this thesis was to study rhyolitic eruption dynamics. Special emphasis was placed on degassing processes, primarily by employing the established hydrogen isotopic system. To address this, the program “VolcDeGas” was developed as a tool to iteratively model degassing histories using concentrations and isotopic signatures. Moreover, textural and depositional analyses, alongside isotopic signature and concentration measurements (processed through VolcDeGas), were conducted on the Big Glass Mountain eruption in California (1060 CE) and three eruptions on Lipari, Sicily (Rocche Rosse, Lami, Forgia Vecchia; ~1250 CE: Pistolesi et al., 2021). Finally, the practicability of applying boron isotopic systematics to support degassing-related research was examined.

The results provide important new insights into the behavior of rhyolitic volcanic systems during eruption and underscore the significance of degassing dynamics in shaping eruption styles. In particular, this work connects hybrid eruption sequences—characterized by simultaneous explosive and effusive activity—and the underlying chemical batched degassing system with eruptive processes such as fragmentation and sintering, and regassing. Additionally, the analyzed eruptions suggest that hybrid activity may have been more common in pre-historic eruptions than previously recognized, and that the Lipari eruptions were co-eruptive in nature. Finally, the boron system investigations reveal that boron and its isotopes cannot act as a reliable degassing tracer. Taken together, this thesis contributes to a more comprehensive understanding of eruptive behavior, progression, and timing. The guidelines developed within this thesis can support future research aimed at reconstructing eruption patterns, specifically those of hybrid activity.

### 9.1 Numerical approach to degassing systems

In this work, the VolcDeGas program was developed to model different rhyolitic degassing histories using the well-established hydrogen isotopic system (Chapter 5; Walter and Castro, 2020), which relies on δD values and water contents. The program furthermore provides best-fit analyses for natural data. It was later updated and applied to address boron isotopic systematics (Chapter 8; see also Section 9.4). Following the validation utilizing published data and models (Chapter 5), VolcDeGas was used to analyze theoretical degassing patterns and to examine several hydrogen isotopic datasets of different eruptions (Chapter 5 - 7 and Section

9.2). The program has been designed to be accessible to researchers with and without programming expertise, incorporating features like a Graphical User Interface (GUI), informative error messages and tooltips for each button. Coupled with its ability to rapidly and precisely compute hundreds of different degassing histories, the program provides a robust tool for analyzing eruptive processes. As a result, it has also been adopted by other researchers, such as Hudak et al. (2021).

Through numerical models on different degassing systems, VolcDeGas was used to study general degassing behaviors (Chapter 5). The results confirmed previously established trends for open and closed degassing systems, as described in numerous prior works (e.g., Taylor et al., 1983; Newman et al., 1988; Dobson et al., 1989; Giachetti et al., 2020). However, remarkable new patterns also came to light during this analysis. Contrary to previous assumptions, the open degassing system is only marginally affected by variations in simulated degassing step sizes, whereas the batched degassing system (Taylor, 1991) shows strong sensitivity to such changes. This flexibility allows the batched system to mimic both closed- and open-system behaviors, as well as all intermediate states.

To incorporate this component, the program was updated to model variable step size changes in the batched system, where water is lost as a percentage (variable step size) rather than a fixed aliquot (fixed step). This approach more accurately reproduces natural rhyolitic eruptive behavior, where explosive energy and gas output are typically greatest at the onset of an eruption and progressively decrease over the course of degassing. This change resulted in substantially improved fits with natural data as determined by VolcDeGas integrated best-fit calculations. Using the best-fit analyses, past literature data of various eruptions were investigated, revealing that numerous eruptions are best described by that batched degassing system with variable step size (Chapter 5). Specifically, the hydrogen isotope data of the hybrid eruption of Chaitén (2008), Chile (Castro et al., 2014)—which involved simultaneous explosive and effusive activity—aligns well with this model.

More broadly, this thesis demonstrates that batched degassing can effectively capture the eruptive transitions observed in the Chilean eruptions, revealing that changes in eruption style—from explosive to effusive—may occur more gradually than previously assumed. In particular, the variable-step batched model captures this continuous evolution in degassing behavior most realistically. It reflects the intermediate stages between fully closed and fully open systems (hybrid activity), along with the progressive loss of volatiles and eruptive energy observed during eruptions. Given the strong alignment between the new model and hybrid activity, it offers a robust theoretical background for understanding the dynamics of hybrid

eruptions in natural rhyolitic volcanic systems. The physical and textural manifestations of these processes are synthesized below in Section 9.2.

### 9.1.1 Implications

The validated performance and demonstrated applications of VolcDeGas underscore its potential as an important tool for volcanic hazard assessment and broader volcanological research. The program enables researchers to model various degassing systems with high precision, allowing the replica of closed-, open-, and batched-system behaviors. In turn, this enhances our ability to interpret eruption dynamics from geochemical data. A key outcome of this work is the refined batched degassing system, which better captures the progressive transition of eruption modes and gradual volatile release observed in hybrid systems.

## 9.2 Hybrid eruptions, cryptic fragmentation and regassing

Water contents and hydrogen isotopic compositions of the silicic, pre-historic eruptions of Big Glass Mountain (BGM) in California (1060 CE) and Lipari, Sicily (Rocche Rosse, Lami, Forgia Vecchia; ~1250 CE: Pistolesi et al., 2021) were measured—see Chapters 6 (Castro and Walter, 2021) and 7, respectively. The resulting data were then analyzed using VolcDeGas (Chapter 5; Walter and Castro, 2020), as detailed in the same studies. A particular focus was given to identifying potential hybrid activity amongst these two systems. Moreover, trends derived from hydrogen isotopic compositions and water contents, together with textural and depositional features of the BGM and Lipari eruptions (Chapters 6 and 7), were compared to those of the hybrid eruptions of Chaitén (2008) and Cordón Caulle (2011), both in Chile (Castro and Dingwell, 2009; Lara, 2009; Alfano et al., 2011; Schipper et al., 2013; Tuffen et al., 2013; Castro et al., 2014). These comparisons provide convincing evidence that the BGM and the Lipari eruptions included prolonged hybrid phases.

In addition to identifying hybrid activity in several pre-historic eruptions, this thesis also establishes a broader link connecting hybrid activity with the underlying batched degassing system, a combination of eruptive processes, and key textural and depositional features. In addition to the geochemical trends, evidence such as tuffisites, pyroclastic ridges within lava flows, and welded pyroclastic material mantling lava, indicate simultaneous explosive and effusive behavior. Furthermore, all of these observations could align with the “cryptic fragmentation” and sintering mechanisms (Gardner et al., 2018; Wadsworth et al., 2020; Schipper et al., 2021; Wadsworth et al., 2022). Such processes successively seal gas-escape pathways (e.g., conduits and tuffisites), leading to gas accumulation and periodic gas release

via explosive events that may clear these vents. Simultaneously, recurring sintering produces dense lava that eventually cools to obsidian (Wadsworth et al., 2020; Wadsworth et al., 2022; Foster et al., 2024). As tested in this PhD thesis, the periodic closing and opening of the system is best represented by a batched degassing system with variable step size.

Under the sintering conditions described above, another process may also occur: regassing (e.g., Giachetti et al., 2020). This work concludes that two samples from the Lipari eruptions, which exhibit significant elevated δD values (Table 7.1, Figure 7.7), may record regassed material. Regassing may transpire when volatiles are trapped by rapid sintering (e.g., within grains at the conduit walls or in tuffisites), creating temporary closed-system conditions that promote partial equilibrium. Under these conditions, hydrogen signatures from the trapped volatiles may be incorporated into the sample material at relatively constant water contents. Consequently, regassing may occur under the same conditions that drive hybrid activity.

### 9.2.1 Implications

The present thesis provides a comprehensive overview of hybrid activity by linking it to batched degassing, key textural observations and features, regassing, and the fragmentation and sintering mechanism (Gardner et al., 2018; Wadsworth et al., 2020; Schipper et al., 2021; Wadsworth et al., 2022). Collectively, these findings advance our understanding of volcanic processes, especially regarding eruptive behavior and its timing.

A novel contribution of this work is the identification of the isotopic signatures of regassing in some samples, thereby adding weight to an emerging hypothesis for silicic volcanism (e.g., “cryptic fragmentation” a la Wadsworth). In particular, the isotopic signatures of these samples must have been overprinted or modified by incorporation of previously exsolved gas. It is likely that many more samples with such signatures exist, but given the cost and time required to analyze large sample sets, these could not be identified. Nonetheless, these preliminary results underscore the potential for a new approach for identifying regassed material in hydrogen isotopic datasets. Future studies could benefit from larger datasets, which would allow more regassed samples to be identified and general geochemical pattern differences between affected and unaffected samples to be detected. For instance, such studies could quantify the regassing-induced increases of δD at distinctive water contents, providing a reference pattern. By this method other researchers could more easily associate outliers in their own natural hydrogen datasets with regassing signature.

The realization that hybrid activity may be more common than previously thought emphasizes the need for revising monitoring and forecasting strategies. Misinterpreting an ongoing eruption as having completely transitioned from an explosive activity to a less dangerous effusive phase, based solely on the appearance of lava effusion, could have serious consequences. Such errors in assessments may endanger lives, damage ecosystems, and disrupt economies (e.g., by affecting air traffic: Black et al., 2016, and local farming: Forte et al., 2018), if hazardous explosive activity persists alongside effusion. This highlights the critical importance of integrating hybrid activity into future volcanic risk evaluations.

In conclusion, this thesis not only contextualizes the hybrid eruption sequence but also presents practical guidelines for detecting such sequences in both past and future eruptions. These guidelines are based on geochemical, textural, and mechanistic indicators, reflecting the multifaceted nature of hybrid activity.

## 9.3 Co-eruptivity of Lipari, Sicily

The geochemical data and textural observations of the three eruptions at Lipari, together with previous literature findings (e.g., Cabrera et al., 2015; Shields et al., 2016; Pistolesi et al., 2021) show notable similarities among the three sites, indicating a shared eruptive history. Specifically, overlapping δD values, water contents, and a coherent degassing trend align with this interpretation. The data suggest that the eruption initiated with Forgia Vecchia erupting alongside Lami, followed by Rocche Rosse during later stages. This scenario implies that the conduits of Rocche Rosse and/or Lami may have operated as additional vents for the Forgia Vecchia eruption.

### 9.3.1 Implications

The study of Lipari's explosive and effusive products provides robust geochemical and textural evidence that the Rocche Rosse, Lami, and Forgia Vecchia eruptions may have been concurrent. This finding deepens our understanding of the northeastern volcanic complex of the island. If these eruptions were indeed contemporaneous rather than isolated events, the land area over which potential hazards would operate significantly increase, as underestimating the likelihood of multiple vents erupting simultaneously could lead to insufficient risk mitigation. Moreover, the results shed light on the volcanic dynamics of Lipari, indicating that the three volcanic centers may be connected through a joint eruption mechanism and a shared magma system. This in turn offers a range of valuable insights into

future threat assessments of the Lipari volcanic complex, ensuring that risk evaluations also account for the potential interaction between multiple eruption sites.

## 9.4 Boron isotopic system

Boron concentrations and isotopic signatures were analyzed to assess their potential to act as a tracer in researching rhyolitic degassing systematics (Chapter 8). Specifically, samples from the 1060 CE Big Glass Mountain (BGM) eruption in California, USA, were investigated. Additionally, the VolcDeGas program (Chapter 5; Walter and Castro, 2020) was updated to incorporate the calculations required to account for boron isotopic fractionation during degassing (Section 2.2.2). Data from BGM obtained in this thesis were too scattered to be effectively fit with VolcDeGas model outputs. However, using the program, best-fit models for literature data from various eruptions at Long Valley (Schmitt and Simon, 2004) alongside theoretical degassing simulations (Chapter 8) were generated.

Results indicate that no degassing trend can explain the patterns observed in either the literature or this study's data. In fact, the only detectable trend in Long Valley is inverse to the expected degassing trend. Both BGM and most of the literature datasets instead exhibit random scatter, often within minimal variations in boron contents and isotopic values. Comparisons between boron and hydrogen concentration and isotopic data from the BGM samples reveal no correlations.

As a result of the aforementioned findings, it is hypothesized that degassing, and subsequently also fractionation of boron, may be inhibited by its exceptionally slow diffusion rates in silicate melts (Spallanzani et al., 2022). Thus, effective degassing over the timescale of an eruption may not occur, primarily preserving the pre-eruptive boron signature in the magmatic glass.

### 9.4.1 Implications

Investigations into degassing systematics in the boron isotopic system indicate that boron is largely unaffected by volcanic degassing, most likely due to its slow diffusion rates. Instead, other boron sources and processes—such as crustal assimilation and/or partial melting, the introduction of magma, or fluids from subducting slabs—may exert predominant control over the boron content and isotopic composition observed in the volcanic glasses. This makes boron well suited for research unrelated to degassing, including investigations of hydrothermal environments, crust-mantle dynamics, fluid sources or reservoirs, and subduction-related processes, without the need to correct for degassing-related effects. Although this work does

not advocate for the use of the boron isotopic system as an alternative degassing tracer, it provides strong explanations for the inconsistency between theoretical models predicting boron degassing effects and the absence of systematic B-isotopic patterns in natural samples.

### 9.5 Future scientific questions

The hybrid eruption sequence is an area that warrants further research. Building upon the outcomes and methodologies presented in this thesis, and optionally utilizing VolcDeGas, future work should also investigate other well preserved pre-historic rhyolitic eruptions to detect hybrid activity. Examples of particularly promising sites include:

(1) The Kaharoa eruption (1315 CE), Tarawera volcano, Taupō Volcanic Zone, New Zealand. This eruption generated extensive pyroclastic deposits and lava flows. The possible presence of tuffisites (Horwell et al., 2025) makes it a great candidate for further studies.

(2) The Aluto volcanic complex, Main Ethiopian Rift, Ethiopia. Several rhyolitic eruptions have occurred here during the late Holocene, the most recent around 1450 CE. This relatively understudied complex (Hutchison et al., 2016) provides a rare chance to investigate multiple eruptive systems within a single volcanic center.

(3) The Havre volcano eruption (2012 CE), Kermadec arc ridge. This rhyolitic eruption is the largest submarine eruption recorded in historical times (e.g., Carey et al., 2014; Knafelc et al., 2022; Heap et al., 2025). Although the submarine setting makes sampling challenging—with deposits located 900 meters or more below the sea, which are also subjected to variable degrees of seawater alteration (e.g., Carey et al., 2014; Knafelc et al., 2022; Heap et al., 2025)—the relatively fresh deposits still provide important insights into submarine degassing systematics.

Confirming additional instances of explosive-effusive activity in other eruptions would further reinforce a central postulation of this work: that hybrid eruptions are more common than previously recognized.

Finally, a thorough investigation using high-T, high-P experiments could be a good test of the geochemical signatures resulting from sintering and regassing hypotheses. Well-designed sintering experiments with isotopically tagged fluid would allow us to quantify how hydrogen isotopes change during sintering in the presence of deuterium-enriched gas. The resulting data

could then be used to develop an empirically derived model for fractionation, accounting for P-T and composition conditions. This model, in turn, could be integrated into VolcDeGas to identify and integrate samples modified by regassing in suites of otherwise normally outgassed obsidians.

# References

Albert, P.G., Tomlinson, E.L., Smith, V.C., Di Traglia, F., Pistolesi, M., Morris, A., Donato, P., Rosa, R. de, Sulpizio, R., Keller, J., Rosi, M., Menzies, M., 2017. Glass geochemistry of pyroclastic deposits from the Aeolian Islands in the last 50 ka: A proximal database for tephrochronology. Journal of Volcanology and Geothermal Research 336, 81–107.

Alfano, F., Bonadonna, C., Volentik, A.C.M., Connor, C.B., Watt, S.F.L., Pyle, D.M., Connor, L.J., 2011. Tephra stratigraphy and eruptive volume of the May, 2008, Chaitén eruption, Chile. Bull Volcanol 73 (5), 613–630.

Alidibirov, M., Dingwell, D.B., 1996. Magma fragmentation by rapid decompression. Nature 380 (6570), 146–148.

Allard, P., Carbonnelle, J., Dajlevic, D., Le Bronec, J., Morel, P., Robe, M.C., Maurenas, J.M., Faivre-Pierret, R., Martin, D., Sabroux, J.C., Zettwoog, P., 1991. Eruptive and diffuse emissions of CO2 from Mount Etna. Nature 351 (6325), 387–391.

Anderson, C.A., 1933. Volcanic history of glass mountain, Northern California. American Journal of Science 5 (155), 485–506.

Anderson, S.W., Fink, J.H., 1989. Hydrogen-isotope evidence for extrusion mechanisms of the Mount St Helens lava dome. Nature 341 (6242), 521–523.

Anovitz, L.M., Elam, J.M., Riciputi, L.R., Cole, D.R., 2004. Isothermal Time-Series Determination of the Rate of Diffusion of Water in Pachuca Obsidian*. Archaeometry 46 (2), 301–326.

Anovitz, L.M., Grew, E.S. (Eds.), 1996. Boron. De Gruyter.

Aulock, F.W. von, Kennedy, B.M., Schipper, C.I., Castro, J.M., E. Martin, D., Oze, C., Watkins, J.M., Wallace, P.J., Puskar, L., Bégué, F., Nichols, A., Tuffen, H., 2014. Advances in Fourier transform infrared spectroscopy of natural glasses: From sample preparation to data analysis. Lithos 206-207, 52–64.

Barberi, F., Gandino, A., Gioncada, A., La Torre, P., Sbrana, A., Zenucchini, C., 1994. The deep structure of the Eolian arc (Filicudi-Panarea-Vulcano sector) in light of gravity, magnetic and volcanological data. Journal of Volcanology and Geothermal Research 61 (3-4), 189–206.

Barnes, J.D., Prather, T.J., Cisneros, M., Befus, K., Gardner, J.E., Larson, T.E., 2014. Stable chlorine isotope behavior during volcanic degassing of H2O and CO2 at Mono Craters, CA. Bull Volcanol 76 (3).

Barth, S., 1993. Boron isotope variations in nature: a synthesis. Geol Rundsch 82 (4).

Bernabò, B.L., 1978. Lipari, Vulcano, l'inferno e San Bartolomeo. Le Isole Eolie dal tardo antico ai Normanni. Archivio Storico Siracusano, 48–55.

Bigazzi, G., Bonadonna, F., 1973. Fission Track Dating of the Obsidian of Lipari Island (Italy). Nature 242 (5396), 322–323.

Billi, A., Barberi, G., Faccenna, C., Neri, G., Pepe, F., Sulli, A., 2006. Tectonics and seismicity of the Tindari Fault System, southern Italy: Crustal deformations at the transition between ongoing contractional and extensional domains located above the edge of a subducting slab. Tectonics 25 (2).

Bindeman, I.N., Hudak, M.R., Palandri, J.P., Qi, H., Milovsky, R., Hervig, R.L., Perfit, M.R., 2021. Rhyolitic and basaltic reference materials for TC/EA analysis: Investigation of water extraction and D/H ratios. Chemical Geology 583, 120486.

Bindeman, I.N., Kamenetsky, V.S., Palandri, J., Vennemann, T., 2012. Hydrogen and oxygen isotope behaviors during variable degrees of upper mantle melting: Example from the basaltic glasses from Macquarie Island. Chemical Geology 310-311, 126–136.

Bindeman, I.N., Lowenstern, J.B., 2016. Low-δD hydration rinds in Yellowstone perlites record rapid syneruptive hydration during glacial and interglacial conditions. Contrib Mineral Petrol 171 (11).

Black, B.A., Manga, M., Andrews, B., 2016. Ash production and dispersal from sustained low-intensity Mono-Inyo eruptions. Bull Volcanol 78 (8).

Blank, J.G., Stolper, E.M., Carroll, M.R., 1993. Solubilities of carbon dioxide and water in rhyolitic melt at 850°C and 750 bars. Earth and Planetary Science Letters 119 (1-2), 27–36.

Burgisser, A., Degruyter, W., 2015. Magma Ascent and Degassing at Shallow Levels, in: , The Encyclopedia of Volcanoes. Elsevier, pp. 225–236.

Cabrera, A., Weinberg, R.F., Wright, H.M., 2015. Magma fracturing and degassing associated with obsidian formation: The explosive–effusive transition. Journal of Volcanology and Geothermal Research 298, 71–84.

Carey, R.J., Wysoczanski, R., Wunderman, R., Jutzeler, M., 2014. Discovery of the Largest Historic Silicic Submarine Eruption. EoS Transactions 95 (19), 157–159.

Carroll, M.R., Holloway, J.R. (Eds.), 1994. Volatiles in Magmas. Reviews in Mineralogy & Geochemistry 30. De Gruyter.

Cashman, K.V., 1988. Crystallization of Mount St. Helens 1980?1986 dacite: A quantitative textural approach. Bull Volcanol 50 (3), 194–209.

Castro, J., Walter, S.C., 2021. Hybrid rhyolitic eruption at Big Glass Mountain, CA, USA. Volcanica 4 (2), 257–277.

Castro, J.M., Bindeman, I.N., Tuffen, H., Ian Schipper, C., 2014. Explosive origin of silicic lava: Textural and δD –H 2 O evidence for pyroclastic degassing during rhyolite effusion. Earth and Planetary Science Letters 405, 52–61.

Castro, J.M., Cordonnier, B., Schipper, C.I., Tuffen, H., Baumann, T.S., Feisel, Y., 2016. Rapid laccolith intrusion driven by explosive volcanic eruption. Nature communications 7, 13585.

Castro, J.M., Cordonnier, B., Tuffen, H., Tobin, M.J., Puskar, L., Martin, M.C., Bechtel, H.A., 2012. The role of melt-fracture degassing in defusing explosive rhyolite eruptions at volcán Chaitén. Earth and Planetary Science Letters 333-334, 63–69.

Castro, J.M., Dingwell, D.B., 2009. Rapid ascent of rhyolitic magma at Chaitén volcano, Chile. Nature 461 (7265), 780–783.

Castro, J.M., Gardner, J.E., 2008. Did magma ascent rate control the explosive-effusive transition at the Inyo volcanic chain, California. Geol 36 (4), 279.

Castro, J.M., Keller, F., Feisel, Y., Lanari, P., Helo, C., Mueller, S.P., Schipper, C.I., Thomas, C., 2020. Lightning-induced weathering of Cascadian volcanic peaks. Earth and Planetary Science Letters 552, 116595.

Castro, J.M., Manga, M., Martin, M.C., 2005. Vesiculation rates of obsidian domes inferred from H 2 O concentration profiles. Geophysical Research Letters 32 (21).

Castro, J.M., Mercer, C., 2004. Microlite textures and volatile contents of obsidian from the Inyo volcanic chain, California. Geophysical Research Letters 31 (18).

Castro, J.M., Schipper, C.I., Mueller, S.P., Militzer, A.S., Amigo, A., Parejas, C.S., Jacob, D., 2013. Storage and eruption of near-liquidus rhyolite magma at Cordón Caulle, Chile. Bull Volcanol 75 (4).

Chaussidon, M., Libourel, G., 1993. Boron partitioning in the upper mantle: An experimental and ion probe study. Geochimica et Cosmochimica Acta 57 (23-24), 5053–5062.

Cherniak, D.J., Hervig, R., Koepke, J., Zhang, Y., Zhao, D., 2010. Analytical Methods in Diffusion Studies. Reviews in Mineralogy and Geochemistry 72 (1), 107–170.

Chesterman, C.W., 1955. Age of the Obsidian Flow at Glass Mountain, Siskiyou County, California. American Journal of Science 253 (7), 418–424.

Chiodini, G., Paonita, A., Aiuppa, A., Costa, A., Caliro, S., Martino, P. de, Acocella, V., Vandemeulebrouck, J., 2016. Magmas near the critical degassing pressure drive volcanic unrest towards a critical state. Nature communications 7, 13712.

Cioni, R., CIVETTA, L., MARIANELLI, P., METRICH, N., SANTACROCE, R., Sbrana, A., 1995. Compositional Layering and Syn-eruptive Mixing of a Periodically Refilled Shallow Magma Chamber: the AD 79 Plinian Eruption of Vesuvius. Journal of Petrology 36 (3), 739–776.

Cortese, M., Frazzetta, G., La Volpe, L., 1986. Volcanic history of Lipari (Aeolian Islands, Italy) during the last 10,000 years. Journal of Volcanology and Geothermal Research 27 (1-2), 117–133.

Crozier, J., Tramontano, S., Forte, P., Oliva, S.J.C., Gonnermann, H.M., Lev, E., Manga, M., Myers, M., Rader, E., Ruprecht, P., Tuffen, H., Paisley, R., Houghton, B.F., Shea, T., Schipper, C.I., Castro, J.M., 2022. Outgassing through magmatic fractures enables effusive eruption of silicic magma. Journal of Volcanology and Geothermal Research 430, 107617.

Davì, M., Rosa, R. de, Barca, D., 2009. A LA-ICP-MS study of minerals in the Rocche Rosse magmatic enclaves: Evidence of a mafic input triggering the latest silicic eruption of Lipari Island (Aeolian Arc, Italy). Journal of Volcanology and Geothermal Research 182 (1-2), 45–56.

Davì, M., Rosa, R. de, Donato, P., Sulpizio, R., 2011. The Lami pyroclastic succession (Lipari, Aeolian Islands): A clue for unravelling the eruptive dynamics of the Monte Pilato rhyolitic pumice cone. Journal of Volcanology and Geothermal Research 201 (1-4), 285–300.

Deegan, F.M., Troll, V.R., Whitehouse, M.J., Jolis, E.M., Freda, C., 2016. Boron isotope fractionation in magma via crustal carbonate dissolution. Scientific reports 6, 30774.

DeGroat, P.J., 1997. Degassing and rehydration of silicic magmas and glasses. PhD thesis.

DeGroat-Nelson, P.J., Cameron, B.I., Fink, J.H., Holloway, J.R., 2001. Hydrogen isotope analysis of rehydrated silicic lavas: implications for eruption mechanisms. Earth and Planetary Science Letters 185 (3-4), 331–341.

Della Ventura, G., Marcelli, A., Bellatreccia, F., 2014. SR-FTIR Microscopy and FTIR Imaging in the Earth Sciences. Reviews in Mineralogy and Geochemistry 78 (1), 447–479.

Dingwell, D.B., 1996. Volcanic Dilemma--Flow or Blow? Science 273 (5278), 1054–1055.

Dingwell, D.B., 1998. Magma degassing and fragmentation: recent experimental advances. Developments in Volcanology 4, 1–23.

Dingwell, D.B., Romano, C., Hess, K.-U., 1996. The effect of water on the viscosity of a haplogranitic melt under P-T-X conditions relevant to silicic volcanism. Contrib Mineral Petrol 124 (1), 19–28.

Dobson, P.F., Epstein, S., Stolper, E.M., 1989. Hydrogen isotope fractionation between coexisting vapor and silicate glasses and melts at low pressure. Geochimica et Cosmochimica Acta 53 (10), 2723–2730.

Domanik, K.J., Hervig, R.L., Peacock, S.M., 1993. Beryllium and boron in subduction zone minerals: An ion microprobe study. Geochimica et Cosmochimica Acta 57 (21-22), 4997–5010.

Donnelly-Nolan, J.M., Champion, D.E., Grove, T.L., 2016. Late Holocene volcanism at Medicine Lake volcano, northern California Cascades. Professional paper / U.S. Department of the Interior, U.S. Geological Survey 1822. U.S. Department of the Interior U.S. Geological Survey, Reston, Virginia, 59 pp.

Donnelly-Nolan, J.M., Grove, T.L., Lanphere, M.A., Champion, D.E., Ramsey, D.W., 2008. Eruptive history and tectonic setting of Medicine Lake Volcano, a large rear-arc volcano in the southern Cascades. Journal of Volcanology and Geothermal Research 177 (2), 313–328.

Donnelly-Nolan, J.M., Nathenson, M., Champion, D.E., Ramsey, D.W., Lowenstern, J.B., Ewert, J.W., 2007. Volcano Hazards Assessment for Medicine Lake Volcano, Northern California.

Dutrow, B.L., Henry, D.J., 2011. Tourmaline: A Geologic DVD. ELEMENTS 7 (5), 301–306.

Edmonds, M., Wallace, P.J., 2017. Volatiles and Exsolved Vapor in Volcanic Systems. ELEMENTS 13 (1), 29–34.

Eichelberger, J.C., 1975. Origin of andesite and dacite: Evidence of mixing at Glass Mountain in California and at other circum-Pacific volcanoes. Geol Soc America Bull 86 (10), 1381.

Eichelberger, J.C., 1995. Silicic Volcanism: Ascent of Viscous Magmas from Crustal Reservoirs. Annu. Rev. Earth Planet. Sci. 23 (1), 41–63.

Eichelberger, J.C., Carrigan, C.R., Westrich, H.R., Price, R.H., 1986. Non-explosive silicic volcanism. Nature 323 (6089), 598–602.

Eichelberger, J.C., Westrich, H.R., 1981. Magmatic volatiles in explosive rhyolitic eruptions. Geophysical Research Letters 8 (7), 757–760.

Farquharson, J.I., Tuffen, H., Wadsworth, F.B., Castro, J.M., Unwin, H., Schipper, C.I., 2022. In-conduit capture of sub-micron volcanic ash particles via turbophoresis and sintering. Nature communications 13 (1), 4713.

Fink, J.H., Anderson, S.W., Manley, C.R., 1992. Textural constraints on effusive silicic volcanism: Beyond the permeable foam model. J. Geophys. Res. 97 (B6), 9073–9083.

Forni, F., Lucchi, F., Peccerillo, A., Tranne, C.A., Rossi, P.L., Frezzotti, M.L., 2013. Chapter 10 Stratigraphy and geological evolution of the Lipari volcanic complex (central Aeolian archipelago). Memoirs 37 (1), 213–279.

Forte, P., Castro, J.M., 2019. H2O-content and temperature limit the explosive potential of rhyolite magma during Plinian eruptions. Earth and Planetary Science Letters 506, 157–167.

Forte, P., Domínguez, L., Bonadonna, C., Gregg, C.E., Bran, D., Bird, D., Castro, J.M., 2018. Ash resuspension related to the 2011–2012 Cordón Caulle eruption, Chile, in a rural community of Patagonia, Argentina. Journal of Volcanology and Geothermal Research 350, 18–32.

Foster, A., Wadsworth, F.B., Tuffen, H., Unwin, H.E., Humphreys, M.C.S., 2024. Evidence for the formation of silicic lava by pyroclast sintering. Nature communications 15 (1), 5347.

Foster, G.L., Marschall, H.R., Palmer, M.R., 2018. Boron Isotope Analysis of Geological Materials, in: Marschall, H., Foster, G. (Eds.), Boron Isotopes, vol. 120. Advances in Isotope Geochemistry. Springer International Publishing, Cham, pp. 13–31.

Friedman, I., Smith, R.L., 1958. The deuterium content of water in some volcanic glasses. Geochimica et Cosmochimica Acta 15 (3), 218–228.

Gardner, J.E., 2007. Bubble coalescence in rhyolitic melts during decompression from high pressure. Journal of Volcanology and Geothermal Research 166 (3-4), 161–176.

Gardner, J.E., Hilton, M., Carroll, M.R., 1999. Experimental constraints on degassing of magma: isothermal bubble growth during continuous decompression from high pressure. Earth and Planetary Science Letters 168 (1-2), 201–218.

Gardner, J.E., Hilton, M., Carroll, M.R., 2000. Bubble growth in highly viscous silicate melts during continuous decompression from high pressure. Geochimica et Cosmochimica Acta 64 (8), 1473–1483.

Gardner, J.E., Llewellin, E.W., Watkins, J.M., Befus, K.S., 2017. Formation of obsidian pyroclasts by sintering of ash particles in the volcanic conduit. Earth and Planetary Science Letters 459, 252–263.

Gardner, J.E., Wadsworth, F.B., Llewellin, E.W., Watkins, J.M., Coumans, J.P., 2018. Experimental sintering of ash at conduit conditions and implications for the longevity of tuffisites. Bull Volcanol 80 (3).

Giachetti, T., Gonnermann, H.M., 2013. Water in volcanic pyroclast: Rehydration or incomplete degassing? Earth and Planetary Science Letters 369-370, 317–332.

Giachetti, T., Gonnermann, H.M., Gardner, J.E., Shea, T., Gouldstone, A., 2015. Discriminating secondary from magmatic water in rhyolitic matrix-glass of volcanic pyroclasts using thermogravimetric analysis. Geochimica et Cosmochimica Acta 148, 457–476.

Giachetti, T., Hudak, M.R., Shea, T., Bindeman, I.N., Hoxsie, E.C., 2020. D/H ratios and H2O contents record degassing and rehydration history of rhyolitic magma and pyroclasts. Earth and Planetary Science Letters 530, 115909.

Giordano, D., Romano, C., Papale, P., Dingwell, D.B., 2004. The viscosity of trachytes, and comparison with basalts, phonolites, and rhyolites. Chemical Geology 213 (1-3), 49–61.

Giordano, D., Russell, J.K., Dingwell, D.B., 2008. Viscosity of magmatic liquids: A model. Earth and Planetary Science Letters 271 (1-4), 123–134.

Gonfiantini, R., Tonarini, S., Gröning, M., Adorni-Braccesi, A., Al-Ammar, A.S., Astner, M., Bächler, S., Barnes, R.M., Bassett, R.L., Cocherie, A., Deyhle, A., Dini, A., Ferrara, G., Gaillardet, J., Grimm, J., Guerrot, C., Krähenbühl, U., Layne, G., Lemarchand, D., Meixner, A., Northington, D.J., Pennisi, M., Reitznerová, E., Rodushkin, I., Sugiura, N., Surberg, R., Tonn, S., Wiedenbeck, M., Wunderli, S., Xiao, Y., Zack, T., 2003.

Intercomparison of Boron Isotope and Concentration Measurements. Part II: Evaluation of Results. Geostandards and Geoanalytical Research 27 (1), 41–57.

Gonnermann, H.M., 2015. Magma Fragmentation. Annu. Rev. Earth Planet. Sci. 43 (1), 431–458.

Gonnermann, H.M., Manga, M., 2003. Explosive volcanism may not be an inevitable consequence of magma fragmentation. Nature 426 (6965), 432–435.

Gonnermann, H.M., Manga, M., 2007. The Fluid Mechanics Inside a Volcano. Annu. Rev. Fluid Mech. 39 (1), 321–356.

Gottsmann, J., Dingwell, D.B., 2001. The cooling of frontal flow ramps: a calorimetric study on the Rocche Rosse rhyolite flow, Lipari, Aeolian Islands, Italy. Terra Nova 13 (3), 157–164.

Hammer, J.E., Rutherford, M.J., 2002. An experimental study of the kinetics of decompression-induced crystallization in silicic melt. J. Geophys. Res. 107 (B1).

Heap, M.J., Mitchell, S.J., Carey, R.J., Kushnir, A.R., 2025. Influence of cristobalite and diktytaxitic textures on the physical properties of submarine rhyolite lavas from Havre volcano (Kermadec volcanic arc, Pacific Ocean). Journal of Volcanology and Geothermal Research 466, 108392.

Heap, M.J., Tuffen, H., Wadsworth, F.B., Reuschlé, T., Castro, J.M., Schipper, C.I., 2019. The Permeability Evolution of Tuffisites and Implications for Outgassing Through Dense Rhyolitic Magma. JGR Solid Earth 124 (8), 8281–8299.

Heiken, G., 1978. Plinian-type eruptions in the medicine lake highland, california, and the nature of the underlying magma. Journal of Volcanology and Geothermal Research 4 (3-4), 375–402.

Hervig, R.L., Moore, G.M., Williams, L.B., Peacock, S.M., Holloway, J.R., Roggensack, K., 2002. Isotopic and elemental partitioning of boron between hydrous fluid and silicate melt. American Mineralogist 87 (5-6), 769–774.

Hobiger, M., Sonder, I., Büttner, R., Zimanowski, B., 2011. Viscosity characteristics of selected volcanic rock melts. Journal of Volcanology and Geothermal Research 200 (1-2), 27–34.

Holloway, J.R., 1981. Volatile Interactions in Magmas, in: Saxena, S.K., Newton, R.C., Navrotsky, A., Wood, B.J. (Eds.), Thermodynamics of Minerals and Melts, vol. 1. Advances in Physical Geochemistry. Springer New York, New York, NY, pp. 273–293.

Holloway, J.R., Blank, J.G., 1994. Chapter 6. APPLICATION OF EXPERIMENTAL RESULTS TO C-O-H SPECIES IN NATURAL MELTS, in: Carroll, M.R., Holloway, J.R. (Eds.), Volatiles in Magmas. Reviews in Mineralogy & Geochemistry 30. De Gruyter, pp. 187–230.

Horwell, C.J., Emerson, H.M., Ashwell, P., Damby, D.E., Self, S., Nattrass, C., Carey, R., Houghton, B., 2025. The crystalline silica respiratory hazard from rhyolitic lava dome eruptions in New Zealand's Taupo Volcanic Zone: A case study from the 1315 CE Kaharoa eruption. Journal of Volcanology and Geothermal Research 461, 108309.

Hudak, M.R., Bindeman, I.N., Loewen, M.W., Giachetti, T., 2021. Syn-Eruptive Hydration of Volcanic Ash Records Pyroclast-Water Interaction in Explosive Eruptions. Geophysical Research Letters 48 (23).

Hutchison, W., Pyle, D.M., Mather, T.A., Yirgu, G., Biggs, J., Cohen, B.E., Barfod, D.N., Lewi, E., 2016. The eruptive history and magmatic evolution of Aluto volcano: new insights into silicic peralkaline volcanism in the Ethiopian rift. Journal of Volcanology and Geothermal Research 328, 9–33.

Ihinger, P.D., Hervig, R.L., McMillan, P.F., 1994. Chapter 2. ANALYTICAL METHODS FOR VOLATILES IN GLASSES, in: Carroll, M.R., Holloway, J.R. (Eds.), Volatiles in Magmas. Reviews in Mineralogy & Geochemistry 30. De Gruyter, pp. 67–122.

Ihinger, P.D., Zhang, Y., Stolper, E.M., 1999. The speciation of dissolved water in rhyolitic melt. Geochimica et Cosmochimica Acta 63 (21), 3567–3578.

Jaupart, C., Allègre, C.J., 1991. Gas content, eruption rate and instabilities of eruption regime in silicic volcanoes. Earth and Planetary Science Letters 102 (3-4), 413–429.

Jochum, K.P., Stoll, B., Herwig, K., Willbold, M., Hofmann, A.W., Amini, M., Aarburg, S., Abouchami, W., Hellebrand, E., Mocek, B., Raczek, I., Stracke, A., Alard, O., Bouman, C., Becker, S., Dücking, M., Brätz, H., Klemd, R., Bruin, D. de, Canil, D., Cornell, D., Hoog, C.-J. de, Dalpé, C., Danyushevsky, L., Eisenhauer, A., Gao, Y., Snow, J.E., Groschopf, N., Günther, D., Latkoczy, C., Guillong, M., Hauri, E.H., Höfer, H.E., Lahaye, Y., Horz, K., Jacob, D.E., Kasemann, S.A., Kent, A.J.R., Ludwig, T., Zack, T., Mason, P.R.D., Meixner, A., Rosner, M., Misawa, K., Nash, B.P., Pfänder, J., Premo, W.R., Sun, W.D., Tiepolo, M., Vannucci, R., Vennemann, T., Wayne, D., Woodhead, J.D., 2006. MPI-DING reference glasses for in situ microanalysis: New reference values for element concentrations and isotope ratios. Geochem. Geophys. Geosyst. 7 (2), n/a-n/a.

Kasemann, S., Meixner, A., Rocholl, A., Vennemann, T., Rosner, M., Schmitt, A.K., Wiedenbeck, M., 2001. Boron and Oxygen Isotope Composition of Certified Reference Materials NIST SRM 610/612 and Reference Materials JB-2 and JR-2. Geostandards NEwsletter 25 (2-3), 405–416.

Katsui, Y., Katz, H.R., 1967. Lateral Fissure Eruptions in the Southern Andes of Chile. Journal of the Faculty of Science, Hokkaido University 13 (4), 433–448.

Keller, J., 2002. Lipari's Fiery Past: Dating the Medieval Pumice Eruption of Monte Pilato.

Knafelc, J., Gust, D., Bryan, S.E., Anderson, M., Cathey, H.E., 2022. Petrogenesis of Havre Volcano in the Kermadec Arc: 2012 Eruption of a Chemically Homogeneous Rhyolite. Front. Earth Sci. 10.

Kolzenburg, S., Ryan, A.G., Russell, J.K., 2019. Permeability evolution during non-isothermal compaction in volcanic conduits and tuffisite veins: Implications for pressure monitoring of volcanic edifices. Earth and Planetary Science Letters 527, 115783.

Konstantinos, T., 2017. Behaviour of Boron Isotopes During Magmatic Degassing and Application to B-Rich Volcanic Glass from Lesbos, Greece. Master Thesis, Uppsala, 70 pp.

Kowalski, P.M., Wunder, B., 2018. Boron Isotope Fractionation Among Vapor–Liquids–Solids–Melts: Experiments and Atomistic Modeling, in: Marschall, H., Foster, G. (Eds.), Boron Isotopes, vol. 6. Advances in Isotope Geochemistry. Springer International Publishing, Cham, pp. 33–69.

Lange, R.L., Carmichael, I.S.E., 1990. CHAPTER 2. THERMODYNAMIC PROPERTIES OF SILICATE LIQUIDS WITH EMPHASIS ON DENSITY, THERMAL EXPANSION AND COMPRESSIBILITY, in: NICHOLLS, J., Russell, K. (Eds.), Modern Methods of Igneous Petrology. De Gruyter, pp. 25–64.

Lanzafame, G., Bousquet, J.C., 1997. The Maltese escarpment and its extension from Mt. Etna to Aeolian Islands (Sicily): importance and evolution of a lithosphere discontinuity. Acta Vulcanol 1997 (9), 113–120.

Lara, L.E., 2009. La erupcion 2008 del volcan Chaiten, Chile: informe preliminar. Andgeo 36 (1).

Lara, L.E., Naranjo, J.A., Moreno, H., 2004. Rhyodacitic fissure eruption in Southern Andes (Cordón Caulle; 40.5°S) after the 1960 (Mw:9.5) Chilean earthquake: a structural interpretation. Journal of Volcanology and Geothermal Research 138 (1-2), 127–138.

Liu, Y., Zhang, Y., Behrens, H., 2005. Solubility of H2O in rhyolitic melts at low pressures and a new empirical model for mixed H2O–CO2 solubility in rhyolitic melts. Journal of Volcanology and Geothermal Research 143 (1-3), 219–235.

Luhr, J.F., 2001. Glass inclusions and melt volatile contents at Parícutin Volcano, Mexico. Contrib Mineral Petrol 142 (3), 261–283.

Maner, J.L., London, D., 2018. Fractionation of the isotopes of boron between granitic melt and aqueous solution at 700 °C and 800 °C (200 MPa). Chemical Geology 489, 16–27.

Marschall, H., Foster, G. (Eds.), 2018. Boron Isotopes. Advances in Isotope Geochemistry. Springer International Publishing, Cham.

Marschall, H.R., Altherr, R., Rüpke, L., 2007. Squeezing out the slab — modelling the release of Li, Be and B during progressive high-pressure metamorphism. Chemical Geology 239 (3-4), 323–335.

Marschall, H.R., Wanless, V.D., Shimizu, N., Pogge von Strandmann, P.A., Elliott, T., Monteleone, B.D., 2017. The boron and lithium isotopic composition of mid-ocean ridge basalts and the mantle. Geochimica et Cosmochimica Acta 207, 102–138.

Martin, E., Bindeman, I., Balan, E., Palandri, J., Seligman, A., Villemant, B., 2017. Hydrogen isotope determination by TC/EA technique in application to volcanic glass as a window into secondary hydration. Journal of Volcanology and Geothermal Research 348, 49–61.

Mazzuoli, R., Tortorici, L., Ventura, G., 1995. Oblique rifting in Salina, Lipari and Vulcano islands (Aeolian islands, southern Italy). Terra Nova 7 (4), 444–452.

Melson, W.G., Saenz, R., 1973. Volume, energy and cyclicity of eruptions of Arenal volcano, Costa Rica. Bull Volcanol 37 (3), 416–437.

Meyer, C., Wunder, B., Meixner, A., Romer, R.L., Heinrich, W., 2008. Boron-isotope fractionation between tourmaline and fluid: an experimental re-investigation. Contrib Mineral Petrol 156 (2), 259–267.

Miller, C.D., 1985. Holocene eruptions at the Inyo volcanic chain, California: Implications for possible eruptions in Long Valley caldera. Geol 13 (1), 14.

Navon, O., Lyakhovsky, V., 1998. Vesiculation processes in silicic magmas. SP 145 (1), 27–50.

Newman, S., Epstein, S., Stolper, E., 1988. Water, carbon dioxide, and hydrogen isotopes in glasses from the ca. 1340 A.D. eruption of the Mono Craters, California: Constraints on degassing phenomena and initial volatile content. Journal of Volcanology and Geothermal Research 35 (1-2), 75–96.

Ninkovich, D., Sparks, R.S.J., Ledbetter, M.T., 1978. The exceptional magnitude and intensity of the Toba eruption, sumatra: An example of the use of deep-sea tephra layers as a geological tool. Bull Volcanol 41 (3), 286–298.

Nolan, G.S., Bindeman, I.N., 2013. Experimental investigation of rates and mechanisms of isotope exchange (O, H) between volcanic ash and isotopically-labeled water. Geochimica et Cosmochimica Acta 111, 5–27.

Noll, P.D., Newsom, H.E., Leeman, W.P., Ryan, J.G., 1996. The role of hydrothermal fluids in the production of subduction zone magmas: Evidence from siderophile and chalcophile trace elements and boron. Geochimica et Cosmochimica Acta 60 (4), 587–611.

Ogburn, S.E., Loughlin, S.C., Calder, E.S., 2015. The association of lava dome growth with major explosive activity (VEI ≥ 4): DomeHaz, a global dataset. Bull Volcanol 77 (5), 2.

Okumura, S., 2005. Molar absorptivities of OH and H2O in rhyolitic glass at room temperature and at 400-600 C. American Mineralogist 90 (2-3), 441–447.

Pabst, S., Zack, T., Savov, I.P., Ludwig, T., Rost, D., Tonarini, S., Vicenzi, E.P., 2012. The fate of subducted oceanic slabs in the shallow mantle: Insights from boron isotopes and light

element composition of metasomatized blueschists from the Mariana forearc. Lithos 132-133, 162–179.

Pallister, J.S., Diefenbach, A.K., Burton, W.C., Muñoz, J., Griswold, J.P., Lara, L.E., Lowenstern, J.B., Valenzuela, C.E., 2013. The Chaitén rhyolite lava dome: Eruption sequence, lava dome volumes, rapid effusion rates and source of the rhyolite magma. Andgeo 40 (2).

Palmer, M.R., Swihart, G.H., 1996. Chapter 13. BORON ISOTOPE GEOCHEMISTRY: AN OVERVIEW, in: Anovitz, L.M., Grew, E.S. (Eds.), Boron. De Gruyter, pp. 709–744.

Pennisi, M., Leeman, W., Tonarini, S., Pennisi, A., Nabelek, P., 2000. Boron, Sr, O, and H isotope geochemistry of groundwaters from Mt. Etna (Sicily)—hydrologic implications. Geochimica et Cosmochimica Acta 64 (6), 961–974.

Pistolesi, M., Rosi, M., Malaguti, A.B., Lucchi, F., Tranne, C.A., Speranza, F., Albert, P.G., Smith, V.C., Di Roberto, A., Billotta, E., 2021. Chrono-stratigraphy of the youngest (last 1500 years) rhyolitic eruptions of Lipari (Aeolian Islands, Southern Italy) and implications for distal tephra correlations. Journal of Volcanology and Geothermal Research 420, 107397.

Qi, H., Coplen, T.B., Gehre, M., Vennemann, T.W., Brand, W.A., Geilmann, H., Olack, G., Bindeman, I.N., Palandri, J., Huang, L., Longstaffe, F.J., 2017. New biotite and muscovite isotopic reference materials, USGS57 and USGS58, for δ2H measurements–A replacement for NBS 30. Chemical Geology 467, 89–99.

Richet, P., Whittington, A., Holtz, F., Behrens, H., Ohlhorst, S., Wilke, M., 2000. Water and the density of silicate glasses. Contrib Mineral Petrol 138 (4), 337–347.

Richter, F.M., Liang, Y., Minarik, W.G., 1998. Multicomponent diffusion and convection in molten MgO-Al2O3-SiO2. Geochimica et Cosmochimica Acta 62 (11), 1985–1991.

Romine, W.L., Whittington, A.G., 2015. A simple model for the viscosity of rhyolites as a function of temperature, pressure and water content. Geochimica et Cosmochimica Acta 170, 281–300.

Rosner, M., Erzinger, J., Franz, G., Trumbull, R.B., 2003. Slab-derived boron isotope signatures in arc volcanic rocks from the Central Andes and evidence for boron isotope fractionation during progressive slab dehydration. Geochem. Geophys. Geosyst. 4 (8), 297.

Ruch, J., Vezzoli, L., Rosa, R. de, Di Lorenzo, R., Acocella, V., 2016. Magmatic control along a strike-slip volcanic arc: The central Aeolian arc (Italy). Tectonics 35 (2), 407–424.

Rust, A.C., Cashman, K.V., 2007. Multiple origins of obsidian pyroclasts and implications for changes in the dynamics of the 1300 B.P. eruption of Newberry Volcano, USA. Bull Volcanol 69 (8), 825–845.

Rust, A.C., Cashman, K.V., Wallace, P.J., 2004. Magma degassing buffered by vapor flow through brecciated conduit margins. Geol 32 (4), 349.

Ryan, A.G., Russell, J.K., Nichols, A.R.L., Hess, K.-U., Porritt, L.A., 2015. Experiments and models on H2O retrograde solubility in volcanic systems. American Mineralogist 100 (4), 774–786.

Saubin, E., Tuffen, H., Gurioli, L., Owen, J., Castro, J.M., Berlo, K., McGowan, E.M., Schipper, C.I., Wehbe, K., 2016. Conduit Dynamics in Transitional Rhyolitic Activity Recorded by Tuffisite Vein Textures from the 2008–2009 Chaitén Eruption. Front. Earth Sci. 4.

Savov, I.P., Leeman, W.P., Lee, C.-T.A., Shirey, S.B., 2009. Boron isotopic variations in NW USA rhyolites: Yellowstone, Snake River Plain, Eastern Oregon. Journal of Volcanology and Geothermal Research 188 (1-3), 162–172.

Scaillet, B., Clemente, B., Evans, B.W., Pichavant, M., 1998. Redox control of sulfur degassing in silicic magmas. J. Geophys. Res. 103 (B10), 23937–23949.

Schipper, C.I., Castro, J.M., Kennedy, B.M., Tuffen, H., Whattam, J., Wadsworth, F.B., Paisley, R., Fitzgerald, R.H., Rhodes, E., Schaefer, L.N., Ashwell, P.A., Forte, P., Seropian, G., Alloway, B.V., 2021. Silicic conduits as supersized tuffisites: Clastogenic influences on shifting eruption styles at Cordón Caulle volcano (Chile). Bull Volcanol 83 (2).

Schipper, C.I., Castro, J.M., Tuffen, H., James, M.R., How, P., 2013. Shallow vent architecture during hybrid explosive–effusive activity at Cordón Caulle (Chile, 2011–12): Evidence from direct observations and pyroclast textures. Journal of Volcanology and Geothermal Research 262, 25–37.

Schmidt, C., Thomas, R., Heinrich, W., 2005. Boron speciation in aqueous fluids at 22 to 600°C and 0.1 MPa to 2 GPa. Geochimica et Cosmochimica Acta 69 (2), 275–281.

Schmitt, A.K., Simon, J.I., 2004. Boron isotopic variations in hydrous rhyolitic melts: A case study from Long Valley, California. Contributions to Mineralogy and Petrology 146 (5), 590–605.

Scott, W.E., 1987. Holocene rhyodacite eruptions on the flanks of South Sister volcano, Oregon, in: , The Emplacement of Silicic Domes and Lava Flows, vol. 212. Geological Society of America Special Papers. Geological Society of America, pp. 35–54.

Self, S., 1992. Krakatau revisited: The course of events and interpretation of the 1883 eruption. GeoJournal 28 (2).

Seligman, A.N., Bindeman, I., van Eaton, A., Hoblitt, R., 2018. Isotopic insights into the degassing and secondary hydration of volcanic glass from the 1980 eruptions of Mount St. Helens. Bull Volcanol 80 (4).

Seligman, A.N., Bindeman, I.N., Watkins, J.M., Ross, A.M., 2016. Water in volcanic glass: From volcanic degassing to secondary hydration. Geochimica et Cosmochimica Acta 191, 216–238.

Shields, J.K., Mader, H.M., Caricchi, L., Tuffen, H., Mueller, S., Pistone, M., Baumgartner, L., 2016. Unravelling textural heterogeneity in obsidian: Shear-induced outgassing in the Rocche Rosse flow. Journal of Volcanology and Geothermal Research 310, 137–158.

Sigmundsson, F., Hreinsdóttir, S., Hooper, A., Arnadóttir, T., Pedersen, R., Roberts, M.J., Oskarsson, N., Auriac, A., Decriem, J., Einarsson, P., Geirsson, H., Hensch, M., Ofeigsson, B.G., Sturkell, E., Sveinbjörnsson, H., Feigl, K.L., 2010. Intrusion triggering of the 2010 Eyjafjallajökull explosive eruption. Nature 468 (7322), 426–430.

Silver, L., Stolper, E., 1985. A Thermodynamic Model for Hydrous Silicate Melts. The Journal of Geology 93 (2), 161–177.

Silver, L.A., Ihinger, P.D., Stolper, E., 1990. The influence of bulk composition on the speciation of water in silicate glasses. Contrib Mineral Petrol 104 (2), 142–162.

Spallanzani, R., Koga, K.T., Cichy, S.B., Wiedenbeck, M., Schmidt, B.C., Oelze, M., Wilke, M., 2022. Lithium and boron diffusivity and isotopic fractionation in hydrated rhyolitic melts. Contrib Mineral Petrol 177 (8).

Sparks, R., 1978. The dynamics of bubble formation and growth in magmas: A review and analysis. Journal of Volcanology and Geothermal Research 3 (1-2), 1–37.

Sparks, R.S.J., Barclay, J., Jaupart, C., Mader, H.M., Phillips, J.C., 1994. Chapter 11a. PHYSICAL ASPECTS OF MAGMA DEGASSING I. Experimental and theoretical constraints on vesiculation, in: Carroll, M.R., Holloway, J.R. (Eds.), Volatiles in Magmas. Reviews in Mineralogy & Geochemistry 30. De Gruyter, pp. 413–446.

Sparks, S.R.J., Sigurdsson, H., Wilson, L., 1977. Magma mixing: a mechanism for triggering acid explosive eruptions. Nature 267 (5609), 315–318.

Spivack, A., Edmond, J., 1987. Boron isotope exchange between seawater and the oceanic crust. Geochimica et Cosmochimica Acta 51 (5), 1033–1043.

Spivack, A.J., Berndt, M.E., Seyfried, W.E., 1990. Boron isotope fractionation during supercritical phase separation. Geochimica et Cosmochimica Acta 54 (8), 2337–2339.

Stolper, E., 1982. The speciation of water in silicate melts. Geochimica et Cosmochimica Acta 46 (12), 2609–2620.

Stolper, E., 1989. Temperature dependence of the speciation of water in rhyolitic melts and glasses. American Mineralogist 74 (11-12), 1247–1257.

Taylor, B.E., 1991. Degassing of Obsidian Dome rhyolite, Inyo volcanic chain, California. Geological Survey of Canada (3), 339–353.

Taylor, B.E., Eichelberger, J.C., Westrich, H.R., 1983. Hydrogen isotopic evidence of rhyolitic magma degassing during shallow intrusion and eruption. Nature 306 (5943), 541–545.

Tonarini, S., Forte, C., Petrini, R., Ferrara, G., 2003. Melt/biotite 11B/10B isotopic fractionation and the boron local environment in the structure of volcanic glasses. Geochimica et Cosmochimica Acta 67 (10), 1863–1873.

Trumbull, R.B., Slack, J.F., 2018. Boron Isotopes in the Continental Crust: Granites, Pegmatites, Felsic Volcanic Rocks, and Related Ore Deposits, in: Marschall, H., Foster, G. (Eds.), Boron Isotopes, vol. 56. Advances in Isotope Geochemistry. Springer International Publishing, Cham, pp. 249–272.

Tuffen, H., Dingwell, D., 2005. Fault textures in volcanic conduits: evidence for seismic trigger mechanisms during silicic eruptions. Bull Volcanol 67 (4), 370–387.

Tuffen, H., Dingwell, D.B., Pinkerton, H., 2003. Repeated fracture and healing of silicic magma generate flow banding and earthquakes? Geol 31 (12), 1089.

Tuffen, H., James, M.R., Castro, J.M., Schipper, C.I., 2013. Exceptional mobility of an advancing rhyolitic obsidian flow at Cordón Caulle volcano in Chile. Nature communications 4, 2709.

Ventura, G., 2013. Chapter 2 Kinematics of the Aeolian volcanism (Southern Tyrrhenian Sea) from geophysical and geological data. Memoirs 37 (1), 3–11.

Vogel, T.A., Eichelberger, J.C., Younker, L.W., Schuraytz, B.C., Horkowitz, J.P., Stockman, H.W., Westrich, H.R., 1989. Petrology and emplacement dynamics of intrusive and extrusive rhyolites of Obsidian Dome, Inyo Craters Volcanic Chain, eastern California. J. Geophys. Res. 94 (B12), 17937.

Wadsworth, F.B., Llewellin, E.W., Castro, J.M., Tuffen, H., Schipper, C.I., Gardner, J.E., Vasseur, J., Foster, A., Damby, D.E., McIntosh, I.M., Boettcher, S., Unwin, H.E., Heap, M.J., Farquharson, J.I., Dingwell, D.B., Iacovino, K., Paisley, R., Jones, C., Whattam, J., 2022. A reappraisal of explosive–effusive silicic eruption dynamics: syn-eruptive assembly of lava from the products of cryptic fragmentation. Journal of Volcanology and Geothermal Research 432, 107672.

Wadsworth, F.B., Llewellin, E.W., Vasseur, J., Gardner, J.E., Tuffen, H., 2020. Explosive-effusive volcanic eruption transitions caused by sintering. Science advances 6 (39).

Wadsworth, F.B., Witcher, T., Vossen, C.E.J., Hess, K.-U., Unwin, H.E., Scheu, B., Castro, J.M., Dingwell, D.B., 2018. Combined effusive-explosive silicic volcanism straddles the multiphase viscous-to-brittle transition. Nature communications 9 (1), 4696.

Walter, S., Castro, J., 2020. VolcDeGas: A program for modelling hydrogen isotope fractionation during degassing of rhyolitic melts. Volcanica 3 (1), 155–168.

Walter, S.C., 2017. Sebastian Walter Simulation of Degassing and Isotope Fractionation of Hydrogen in Rhyolitic Melts A Study of Big Glass Mountain, CA;. MA thesis, Mainz, 89 pp.

Waters, L.E., Andrews, B.J., Lange, R.A., 2015. Rapid Crystallization of Plagioclase Phenocrysts in Silicic Melts during Fluid-saturated Ascent: Phase Equilibrium and Decompression Experiments. Journal of Petrology 56 (5), 981–1006.

Waters, L.E., Lange, R.A., 2016. No effect of H2O degassing on the oxidation state of magmatic liquids. Earth and Planetary Science Letters 447, 48–59.

Watkins, J.M., Gardner, J.E., Befus, K.S., 2017. Nonequilibrium degassing, regassing, and vapor fluxing in magmatic feeder systems. Geology 45 (2), 183–186.

Watkins, J.M., Manga, M., DePaolo, D.J., 2012. Bubble geobarometry: A record of pressure changes, degassing, and regassing at Mono Craters, California. Geology 40 (8), 699–702.

Watt, S.F.L., Pyle, D.M., Mather, T.A., Martin, R.S., Matthews, N.E., 2009. Fallout and distribution of volcanic ash over Argentina following the May 2008 explosive eruption of Chaitén, Chile. J. Geophys. Res. 114 (B4).

Wilson, L., 1976. Explosive Volcanic Eruptions--III. Plinian Eruption Columns. Geophysical Journal International 45 (3), 543–556.

Woods, A.W., Koyaguchi, T., 1994. Transitions between explosive and effusive eruptions of silicic magmas. Nature 370 (6491), 641–644.

Wunder, B., Meixner, A., Romer, R.L., Wirth, R., Heinrich, W., 2005. The geochemical cycle of boron: Constraints from boron isotope partitioning experiments between mica and fluid. Lithos 84 (3-4), 206–216.

Zhang, Y., 1999. H 2 O in rhyolitic glasses and melts: Measurement, speciation, solubility, and diffusion. Reviews of Geophysics 37 (4), 493–516.

Zhang, Y., Cherniak, D.J., 2010. Diffusion in Minerals and Melts: Introduction. Reviews in Mineralogy and Geochemistry 72 (1), 1–4.

Zhang, Y., Gan, T., 2022. Diffusion in Melts and Magmas. Reviews in Mineralogy and Geochemistry 87 (1), 283–337.

Zhang, Y., Stolper, E.M., Wasserburg, G.J., 1991. Diffusion of water in rhyolitic glasses. Geochimica et Cosmochimica Acta 55, 441–456.

# Appendix: Supplementary Material of Chapter 7

The following figures were submitted as supplementary material for the study presented in Chapter 7 (Walter et al., *under review*)

**Contents:**

**Figure S1:** Photographs of tephra outcrops from Rocche Rosse, Forgia Vecchia and Lami eruptions

**Figure S2:** Additionally modeled best-fit degassing trends to Rocche Rosse, Forgia Vecchia and Lami eruptions with the VolcDeGas program


**Figure S1:** Photographs of tephra outcrops from the [A] Forgia Vecchia, [B] Lami, and [C] Rocche Rosse eruptions showing the sampling locations on Lipari, Sicily. At each site, samples were collected from each stratigraphic layer, with one bag containing a mixture of bulk material (pumice, obsidian chips, and lithic fragments), and another bag exclusively containing hand-picked obsidian shards. The stratigraphic layers are marked directly in the image for clarity.

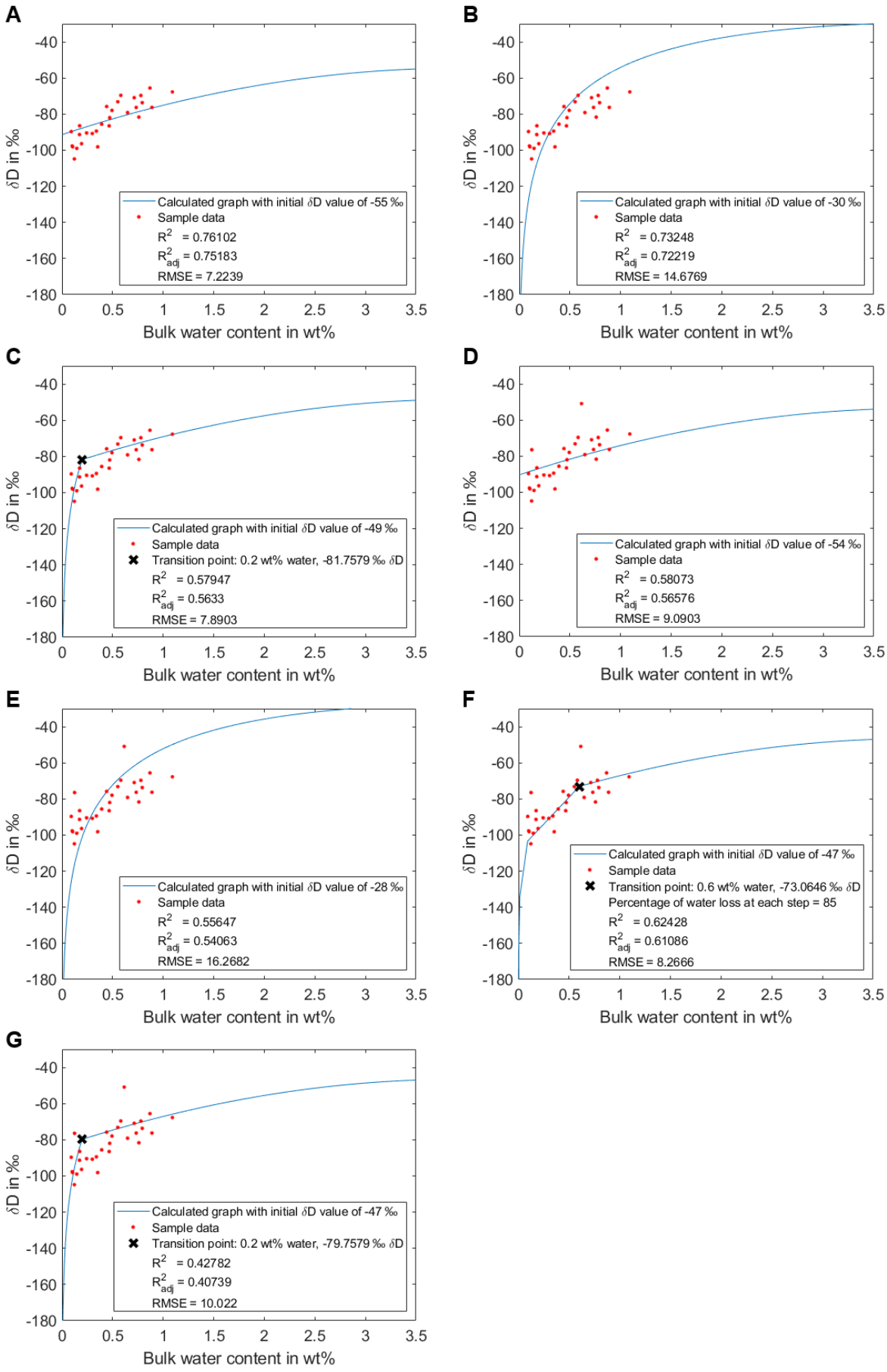


**Figure S2:** [Caption on next page]

**Figure S2:** Figure presenting additional modeled degassing graphs of Rocche Rosse, Lami and Forgia Vecchia eruptions depicting δD versus $H_2O$ relations. The models are generated using the VolcDegas program (Walter and Castro, 2020), employing variables such as initial water content, step size, water speciation values and natural data to iteratively model and identify the best-fit between natural sample data (red points) and calculated degassing data (blue line) by exploiting the minimum Root-Mean-Square-Error (RMSE). All models are based on an initial water content of 3.5 wt.% and a step size of 0.001 wt.%. For each graph, a box on the lower right provides additional information such as RMSE, $R^2$, percentage of water loss and transition points for two-stage systems. The graphs are divided into two groups: Frames [A]-[C] depict the degassing systems excluding outliers FV-1a12 and RR-1a1 while panels [D]-[G] include them. Frame [A] portrays a purely closed system which yields a moderate (RMSE of 7.2 but a strong coefficient of determination ($R^2$) of ~0.76. Panel [B] represents an open system which achieves a poor RMSE exceeding 14 but a reasonable $R^2$ of ~0.73. Panel [C] displays a closed-to-open system, producing a suboptimal RMSE of ~7.9 and a weak $R^2$ of around 0.58. The inclusion of outliers ([D]-[G]) in the models exhibits diminished metrics: Panel [D] presenting the closed system, yields a relatively high RMSE of 9.1 and a reduced $R^2$ of 0.58, while the open system [E] exhibits the worst RMSE at 16.3 and a low $R^2$ of 0.56. Frame [F], exhibiting a closed-to-batched system with variable step size, slightly improves the RMSE to 8.3 and yields an $R^2$ of 0.62. Lastly, panel [G] shows a closed-to-open system with the high RMSE of 10 and the weakest $R^2$ of ~0.43. These observations, together with results from Figure 8 of the study, illustrate that the most accurate models are those utilizing batched degassing with variable step size. This system effectively represents the hybrid degassing systematics characterized by simultaneous explosive and effusive eruptions. The geochemical patterns in the graph, reflected by natural data, are best represented by the batched model which illustrates a gradual transition between degassing modes rather than a sharp ‘kink’. This behavior aligns with the essential features of the batched system, being the repetitive accumulation of gases under closed-system conditions which are periodically released through explosive events, resulting in a steady decline in explosive activity and a subsequent shift toward effusive conditions.

# Acknowledgement

I would like to express my sincere gratitude to my PhD supervisor, Jonathan Castro, who introduced me to the fascinating world of volcanology.

With your guidance and support I was able to evolve as a scientist, deepening my understanding of eruptive processes and dynamics. You also initiated numerous projects that form the foundation of this thesis. I am especially thankful for the continuous mentorship, the fresh insights, and the scientific ideas we could explore and openly discuss that resulted in the development and testing of new hypothesis. Specifically, I want to thank you for the invaluable assistance with scientific writing and the opportunity to gain hands-on experience during our enjoyable sampling campaign at Lipari, where I refined my fieldwork procedures. Thank you for the opportunity to work with you and to learn from the vast expertise of an outstanding, experienced scientist.

I am also grateful to Klemens Seelos for teaching me MATLAB programming—a skill that has proven critical in solving complex scientific questions—especially in connection with isotope geology and degassing studies.

Tobias Häger, thank you for helping me whenever some critical problems arose with the FTIR which sometimes were solved with simply “patting” the FTIR at a specific point.

I would like to thank all my colleagues at the Institute of Geoscience in Mainz, too many to name them all individually. Special thanks are due to Christoph Helo for the valuable scientific discussions and laboratory assistance, to Sabine Fohrman for her essential help with administrative matters, contracts, and ensuring that lab supplies were always available, and to Gregor Weber and Étienne Le Glas for insightful discussions about science and scientific writing.

Finally, I wish to express my genuine gratitude to my family, especially my parents, who supported and encouraged me throughout my whole PhD journey.